FLOWS

Final Report

AE3200: Design Synthesis Exercise

DSE Group 10

Delft University of Technology

TU Delft

This page intentionally left blank.

FLOWS
Final Report

by

DSE Group 10

Hugo Bruins	5445116
Carel van Daelen	5257816
James Dunselman	5289815
Wouter Eijkelenkamp	5312264
Rik Keulemans	5321174
Alex Nedelcu	5466946
Branco van Rijn	5176212
Guglielmo De Stefano	5544831
Agustín Strik	5220912
Luke Willigenburg	5341434

Version Control

Version	Date	Description
1.0	19.06.2024	First draft

Instructors:	Matteo Pini & Carlo De Servi
Coaches:	Chandrasekar Medipati & Jane Pauline Ramirez
Project Duration:	04-2024 - 06-2024
Faculty:	Faculty of Aerospace Engineering

Cover:	Final design of the FLOWS UAV
Style:	TU Delft Report Style, with modifications by Daan Zwaneveld

TU Delft

Executive Overview

This document provides an overview of Phases Four (Detailed Design) and Five (Final Design) of the FLOWS mission. The objective of project FLOWS is to design a flood forecasting, warning, and response system centered around a versatile, cost-effective unmanned aerial vehicle. The most prominent contribution to the design process documented in this report is represented by the final design of the airborne segment, together with the results of aerodynamic, structural, economic, and sustainability analyses.

Initial Sizing Results

The starting point for the design of all subsystems was the preliminary aircraft design. Several concepts capable of Vertical Take-Off and Landing (VTOL) were considered and after a trade-off a conventional fixed wing-VTOL concept was chosen. Using a self-made iterative sizing program, a preliminary design was obtained. This led to a Maximum Take-Off Weight (MTOW) of $247.9\,\mathrm{kg}$, with a maximum modular payload mass of $40\,\mathrm{kg}$. The wing of the preliminary design had an aspect ratio of 20 to ensure high endurance, and featured a wingspan of $9.891\,\mathrm{m}$.

Based on initial calculations, a maximum VTOL thrust of $2917\,\mathrm{N}$ and a maximum horizontal thrust of [1] were found, which would be used to size the propulsion system. Afterwards, a sensitivity analysis of the design was performed, determining the most influential input parameters. This analysis revealed that the propulsion system is critical, and thus this would be the primary focus of the detailed design phase.

Payload, Communication, and Data Handling

The payload design consists of a monitoring payload and an intervention payload. The monitoring payload includes sensors for measuring water levels, riverbed topography, and surface debris. It uses the RIEGL VQ-840-GE LiDAR for shallow water penetration, and the Trillium LV-25 camera for photogrammetry and debris identification. The intervention payload bay is modular, with a mass limit of $31\,\mathrm{kg}$ and volume limit of 630x250x420mm.

The communication system's starting point was determining data rates for the monitoring payload and control systems. Video compression and minimum required frame rates were established. A novel LiDAR data compression technique led to the selection of the Saab RVC-E computer, resulting in $11.4\,\mathrm{pts/m^2}$ LiDAR point density, $2.82\,\mathrm{cm}$ visible light photogrammetry resolution and $10.0\,\mathrm{cm}$ for infrared.

The minimum required downlink data rate was found to be $2.95\,\mathrm{Mbps}$, with a safety factor of 2. Redundancy is provided by a direct link radio system and a satellite link with a $10\,\mathrm{Mbps}$ limit, resulting in a total downlink data rate of $5\,\mathrm{Mbps}$. Any extra bandwidth will increase the frames per second for the operator camera. Lastly, the open source DRONECAN framework was chosen for robust, redundant, and bidirectional communication between subsystems, facilitated by CAN compatible components.

Propulsion System Design

The component selection for the vehicle propulsion system encompassed the choice of propellers, electric motors and electronic speed controllers. First, the requirements for the propulsion system upon which the selection was to be based upon were identified, formalized, and rationalized.

The next step was the selection of both the horizontal and vertical propeller. Possible methods of propeller selection were discussed and evaluated based on their ability to verify that the performance requirements could be met. This led to the choice of the Fluxer 63x22 Pro for the vertical propellers,

[1] https://www.overleaf.com/project/664ee793a36b698e5407de7a#section.3.46.2

providing each a peak continuous thrust of $392.4\,\mathrm{N}$, and the $1.4\,\mathrm{m}$ diameter three-bladed X-PROP for the horizontal propeller, providing a peak continuous thrust of $853.5\,\mathrm{N}$.

Consequently, it was found that motors that matched the expected power density were inadequate in terms of power production and weight. This led to exploring alternative motor configuration options, but in the end it was determined that the quadcopter design was most efficient, and heavier, more powerful motors were chosen. The Emrax 188 family of motors was chosen. The vertical motors are air cooled Emrax 188, with a peak continuous power of $27\,\mathrm{kW}$, while the horizontal motor is an Emrax 188 with combined cooling, with a peak continuous power of $37\,\mathrm{kW}$. The electronic speed controller selection followed, and the AMPX 90A HV ESC resulted as the lightest and best performing option, with an amperage of $180\,\mathrm{A}$ and a voltage of $440\,\mathrm{V}$.

Electrical Power System Design

This chapter details the design of the electrical power system for the UAV, emphasizing reliable power distribution and management. It features a series-hybrid configuration where an engine provides mechanical shaft power to a DC generator, producing electrical power for various subsystems. Four UAVHE RW1-79 Aircooled Wankel Gensets were selected as the generator assembly, providing a total output of 64 kW to meet peak power demands.

The power transmission system includes high-voltage and low-voltage circuits to ensure effective power distribution to propulsion and other subsystems. High-voltage transmission utilizes relays and microcontrollers for unregulated power to electronic speed controllers, while low-voltage needs are managed by a VisionAirtronics 1800W Power Distribution Unit. Redundancy is enhanced by a secondary battery that ensures system control during power failures. All components are commercial off-the-shelf (COTS), streamlining the verification process. Verification methods include practical demonstrations in a specialized electrical testing facility to ensure compliance with design requirements.

Wing Design

The NACA65(3)-618 airfoil was selected for its large lift coefficient and endurance at monitoring speed, and further optimized to meet aerodynamic requirements. A wingbox design with two shear panels was chosen for high resistance against bending, twist, and shear. Aluminum 6061-T6 was chosen as structural material due to its high recycling rate, specific strength, and specific stiffness. The total wing structural mass amounts to $27.79\,\mathrm{kg}$. The aileron was sized to provide a roll rate of 30° in 1.5 seconds, with a surface area of $0.08\,\mathrm{m}^2$ and a hinge moment of $12\,\mathrm{Nm}$ at the most constraining load. The SD-01B actuator was selected to provide this torque.

Stability, Balance and Tail Design

An in-house tool was developed to simultaneously address the positioning of VTOL engines, landing gear, wing layout, and boom mass estimation. Using this tool, a twin-boom separated conventional low tail design was finalized due to the large boom spacing resulting from the VTOL propellers.

The tool provided a comprehensive wing group layout and landing gear position visualized in a simplified 3-view plot. Internal and external validation processes ensured satisfactory results for vertical stabilizer sizing, while adjustments are needed for horizontal stabilizer sizing. Additionally, a dynamic stability analysis using an OpenVSP model revealed an initial unstable Dutch roll, which was resolved by incorporating a 1.5-degree anhedral angle.

Fuselage Design

The design of the fuselage was initiated by the determination of the position of the components within the fuselage. As a starting point for the fuselage layout, the payload bay and landing gear were considered. From here, all other subsystems and components were positioned according to their requirements. The decision has been made to implement a retractable nose landing gear, to refrain from

obstructing the field of view of the monitoring and control camera. To save weight, the main landing gear is non-retractable. In addition, due to the many cutouts required by the individual components of the UAV, the skin is only required to carry aerodynamic loads.

Then, the loads throughout the fuselage were analyzed. Multiple load cases were assessed, including a $3.6\,\mathrm{g}$ airborne maneuver, a $2.0\,\mathrm{g}$ impact landing, and compressive forces from the pusher propeller. From these load cases, the critical cases were detected, by which the fuselage structure was sized. An additional safety factor of 1.5 was employed. The final fuselage structure consists of five frames, which allow for the retaining of the cylindrical shape. The frames are kept together by five longerons, positioned such that the load transfer between fuselage and wing is optimized. These components are manufactured from aluminum, and have a total structural mass of $42.75\,\mathrm{kg}$.

Ground System and Operations

To ensure versatile operations, a mobile ground station is included in the system. This allows for quick relocation using existing infrastructure, meaning the UAV can be dispatched from a variety of locations, assuming tactical positions near a risk or disaster area. This mobile ground station will fit inside a $12\,\mathrm{m}$ sea container, allowing it to be transported according to the road haul regulations. The container is separated into two distinct sections, the first being the operational headquarters of the mission, and the second being the deployable landing platform and UAV storage. The ground system allows for on-site repairs and refueling of the UAV. By incorporating this flexibility into the system, a larger variety of missions can be performed.

Two distinct operational modes were determined. First, the monitoring mission profile was identified, during which the UAV is capable of monitoring areas for over $10.5\,\mathrm{hours}$. The second profile is the intervention mission, which is a fast-response mission. This mission type allows for quick delivery of humanitarian aid resources to the determined location, as it can cover distances of $200\,\mathrm{km}$ in under $45\,\mathrm{minutes}$. When performing this mission type, the UAV is capable of being loaded with its modular payload of up to $31\,\mathrm{kg}$. After delivering this payload, it will cruise back to the ground station at its monitoring altitude and speed.

Technical Risk Assessment

Along the development of the detailed design, technical risks have been identified and assessed to accommodate for the integration of mitigation strategies into the design. This chapter summarizes the initial risk identification from the Fault Tree Analysis (FTA), after which their assessment and required mitigation have been tabulated. Finally, the pre- and post-mitigation risk maps show that all risks have successfully been mitigated to an acceptable risk level. To testify to the impact of the risk assessment on the design, numerous references to risk controls can also be found throughout the report.

Lifecycle Assessment

Once a complete overview of the final design was obtained, the lifecycle of the system was analyzed. Researching material procurement led to the decision of sourcing aluminium from countries such as Norway or Sweden, as this minimizes the emissions, and therefore the carbon footprint.

Next, the manufacturing and assembly methods to produce the structural frame out of the aluminum were detailed, From the manufacturing material waste estimation and the expected final part mass, an Al6061 mass of $83.46\,\mathrm{kg}$ was obtained. Using this, an emission analysis for both the production process and the operations of the system could be carried out, focusing on carbon dioxide emissions. First, the production of the structural frame was calculated to produce $494.6\,\mathrm{kg}$ of CO_2 emissions. For the operations of the system, carbon dioxide emissions for both the monitoring and intervention missions were calculated to be $58.4\,\mathrm{kg}$ and $44.3\,\mathrm{kg}$ respectively.

Finally, the recycling and reuse procedure once the system reaches end-of-life conditions were explored. The conclusion was reached that after a nominal operational lifetime, the entirety of the com-

ponents making up the system could be recycled or reused.

Economic Analysis

With a finalized design, the market position of the final product was further analyzed. First, a detailed cost breakdown of the total project cost - composed of capital expenses and operational costs - was computed. This resulted in a fixed operation cost of €120k and an additional €181k per unit. Meanwhile, capital expenditures consisted of a fixed €783.5k and an additional €281.7k per unit. The unit price would consequently be equal to the variable capital expenditures, or higher if profit was desired.

To analyze the demand of the product, a market analysis and customer case studies were performed, revealing a discernible gap on the flood monitoring, riverbed topography, and flood response market as well as possible customers from both the public sector (FEMA) and private sector (Allianz SE) who would be interested in purchasing several units. However, FLOWS may be challenged in having no pre-existing customer relationships or competition in the monitoring systems market.

Final Design

The complete airborne segment of the UAV, with a maximum take-off weight of 272.1 kg and a wingspan of 9.89 m, was analyzed. All components, with their specific quantity, mass, power consumption, and cost, were detailed. Aerodynamic analysis using the OpenVSP program revealed a zero-lift drag coefficient of CD0 = 0.0196 and a maximum lift-to-drag ratio of over 28. Fuel mass for both design missions was calculated, and a maximum endurance of over 23 hours was found, with the UAV capable of carrying a maximum fuel weight of 41.91 kg. In case of an intervention mission, the UAV can carry $31.7\,\mathrm{kg}$ of extra payload to aid the mission. The requirement compliance matrix details the verification state of stakeholder, system, and mission requirements. The text also discusses design limitations and recommendations for future development, including the integration strategy for the final design, which is represented in Figure 1.

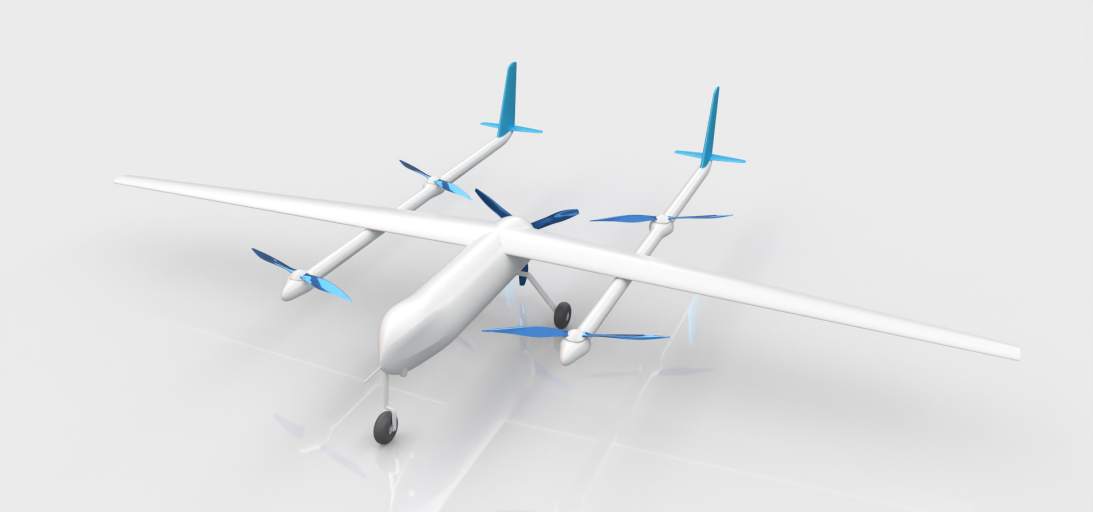

Figure 1: Render of the final design of the UAV.

Project Conclusion

The conclusion of the report contains a discussion of further steps in the design process, represented through a design and development logic diagram. Validation activities were also discussed, such as field testing, operational testing, simulations, and environmental testing. The expected costs for these validation methods were also quantified, and their timeline was addressed through a Gantt chart.

Contents

1 | Project Introduction and Objectives

Around the world, no less than 23% of the world's population is exposed to significant flooding risk [1]. As anthropological climate forcings continue to increase temperature variability, and thus affect the global water cycle [1], this portion of the population is slated to increase. To adapt to often catastrophic flooding events, humanity has developed complex flood monitoring, forecasting, and warning systems, which rely on fixed stream stage sensors to obtain data about water levels. Although they reliably provide real-time information, these systems require significant investments in the manufacturing and mounting of a large number of sensors, and only cover fixed geographical areas [2].

In this context, a system based on an unmanned aerial vehicle that can fulfill mobile flood monitoring capabilities was proposed, taking the name FLOWS (**FL**ood F**O**recasting, **W**arning, and Re**S**ponse). The following mission need statement was thus defined for the FLOWS design project [3]:

FLOWS-MNS: Design a system to monitor water levels and riverbed topography, provide early warning for floods, investigate waterborne debris, and support response efforts.

In consultation with the client, this mission need statement was refined into a project objective statement, by including the project development conditions, as well as certain imposed design guidelines:

FLOWS-POS: The project objective is to design an all-weather, cost-effective UAV and supporting infrastructure for flood forecasting, warning, and response with 10 students in 10 weeks.

Therefore, the purpose of the system is to detect floods by visual monitoring of the operational area, allowing for rapid detection of any irregularities or forthcoming danger and ample time for decision-makers to initiate warning and response procedures. The system is also expected to intervene directly, supporting first responders in their efforts through the deployment of a humanitarian aid drop. Based on these project objectives, a comprehensive requirement analysis was performed, resulting in the list of stakeholder (purple), mission (orange), and system (blue) requirements shown in Table 1.1 [3]. These requirements act as the baseline of the design process documented in this report.

Table 1.1: Identified stakeholder, mission, and system requirements.

ID	Requirement description	Origin	Type
R-STK-1	The system shall effectively monitor landscape.	STK-5	Key
R-STK-2	The system shall quickly provide data for warning about flood risk.	STK-1	Key
R-STK-3	The system shall aid in maintaining lives and the surrounding environment.	STK-1,2	Key
R-STK-4	The system shall have affordable operational costs.	STK-1	Driver
R-STK-5	The system shall be able to be deployed and operated in a variety of environments.	STK-1	Driver
R-STK-6	The system shall not endanger the civilians in the region where it operates and the first responders active in the area.	STK-2,4	Key
R-STK-7	The system shall not compromise the functioning of other flood prevention and protection systems.	STK-1	Key
R-STK-8	The system shall operate according to existing UAV regulations.	STK-3	Driver
R-STK-9	The system components shall be reusable at end of life.	STK-1	Driver
R-MIS-1	The system shall allow for total airborne operational endurance of no less than 10 hours at the lowest latitude-related flyability conditions as described by FAA weather tolerance data.	R-STK-1	Driver
R-MIS-2	The system shall allow for monitoring of water levels, riverbed topography, surface debris, and stationary flood protection mechanisms.	R-STK-1	Key
R-MIS-3	The system shall allow for remote control and data transmission from a range of no less than $200\,\mathrm{km}$.	R-STK-2	Driver

Continued on next page

Table 1.1: Identified stakeholder, mission, and system requirements.

ID	Requirement description	Origin	Type
R-MIS-4	The system shall allow for the continuous transmission of data about monitored areas to the ground segment.	R-STK-2	Key
R-MIS-5	The system shall allow for vertical take-off and landing from any ground surface at lowest latitude-related flyability conditions as described by the FAA weather tolerance data.	R-STK-5	Driver
R-MIS-6	The system shall allow for deployment and operations under moderate to high turbulence conditions as described by the FAA weather tolerance data.	R-STK-5	Key
R-MIS-7	The system shall allow for safe autonomous landing in case of propulsion system failure.	R-STK-6	Key
R-MIS-8	The payload shall comply with existing EASA UAV regulations.	R-STK-8	Driver
R-MIS-9	The system shall allow for reuse or recycling of all assembly components at end of life according to ISO-14001:2015.	R-STK-9	Key
R-MIS-10	The system shall allow for versatile payload loading.	R-STK-3	Driver
R-SYS-1	The system shall have a maximum wind resistance of $14\,\mathrm{m/s}$.	R-MIS-6	Key
R-SYS-2	The system shall have a precipitation tolerance of $50\,\mathrm{mm/h}$.	R-MIS-6	Key
R-SYS-3	The system shall have an onboard data storage of TBD.	R-MIS-3	Driver
R-SYS-4	The propulsion system shall be able to transition between VTOL and horizontal flight.	R-MIS-5	Driver
R-SYS-5	The system shall have an operational temperature range of -20 $^{\circ}C$ to 46 $^{\circ}C$.	R-MIS-1	Key
R-SYS-7	The UAV shall have a modular sensing payload system with predefined interfaces for data and power.	R-MIS-10	Key
R-SYS-8	The UAV shall have a modular intervention payload bay.	R-MIS-10	Key
R-SYS-9	The UAV shall have an autonomous landing mode.	R-MIS-6	Key
R-SYS-10	The UAV shall have a manual flying mode.	R-MIS-4	Key
R-SYS-11	The system flight profile shall be dynamically stable.	R-MIS-2	Driver
R-SYS-12	The system flight profile shall be controllable.	R-MIS-2	Driver
R-SYS-13	The software related to the control of the UAV shall have a Design Assurance Level (DAL) of Level A	R-MIS-8	Driver
R-SYS-14	The UAV shall not produce more than $130\,\mathrm{dB}$ measured at $100\,\mathrm{m}$ from the ground.	R-MIS-8	Key
R-SYS-15	The UAV shall be capable of a glide ratio of 22 at a velocity of no more than $40\,\mathrm{m/s}$	R-MIS-7	Key
R-SYS-16	The UAV shall be capable of a horizontal landing from gliding flight.	R-MIS-7	Driver

This design report is organized as follows. Chapter 2 describes the initial sizing of the airborne segment, from which subsystem requirements were derived. Then, Chapter 3 covers the development of the payload, together with the communications and data handling system. The detailed design of the propulsion system and of the electrical power system are presented in Chapter 4 and Chapter 5 respectively.

The airborne segment is then subdivided into three groups: the wing group, discussed in Chapter 6, the VTOL boom and tail group, discussed in Chapter 7, and the fuselage group, discussed in Chapter 8. Chapter 7 also covers the stability and controllability of the aircraft.

The design continues with Chapter 9, which describes the design of the ground segment and of the operational profile. The following chapters cover holistic aspects of the system: Chapter 10 assesses operational risks, Chapter 11 documents the multidimensional lifecycle analysis performed, and Chapter 12 presents the economic aspects of the design, including an estimate of the cost and the market segmentation. Finally, Chapter 13 provides an overview of the final design and its compliance with the design constraints and Chapter 14 concludes the report with further steps for the project.

2 | Initial Sizing Results

This chapter describes the initial results that were used as a baseline for the detailed design phase. Section 2.1 presents the selected conceptual configuration for the airborne segment, while Section 2.2 describes the initial sizing process and results and Section 2.3 describes the verification procedures applied to this process. Finally, the interrelations between each individual subsystem to be designed are discussed in Section 2.4 with the help of an N2 chart.

2.1. Conceptual Configuration Selection

The conceptual design phase included a comprehensive trade-off being performed to select the configuration of the airborne segment. The results of this trade-off are presented briefly in Table 2.1.

Table 2.1: Conceptual design trade-off scores [4].

Criterion	Aircraft stability	Aerodynamic performance	Complexity	Reliability	TOTAL
Weight	30%	30%	20%	20%	
Tiltrotor	3. Only two vertical rotors, limited VTOL stability	1. Massive rotors cause performance penalty	2. Large rotation mechanism	2. Low TRL, complex certification	2.00
Fixed wing-VTOL	4. Multicopter and generous stability margin	3. Increased drag due to VTOL motors	4. No large mechanisms	4. No compromises in reliability	3.70
Tail-sitter	2. Heavy tail and unstable in bad weather	4. No performance loss from VTOL	4. No large mechanisms	2. No VTOL redundancy	3.00
Flying wing-VTOL	2. Inherent longitudinal instability, multicopter	4. Best-in-class aerodynamic performance	3. Complex manufacturing process	4. No compromises in reliability	3.20
Tiltrotor canard	2. Inherent small stability margin, multicopter	2. Large rotors cause performance penalty	2. Large rotation mechanism	2. Low TRL, complex certification	2.00

Based on the trade-off results in Table 2.1 and a subsequent sensitivity analysis, it was found that the **conventional fixed wing-VTOL** strawman concept represented the most robust option. The fixed wing-VTOL configuration was therefore used as the baseline for the preliminary design process.

2.2. Initial Sizing

After the conventional fixed wing-VTOL concept was selected, a sizing procedure was created. Its outputs represent a preliminary wing geometry and a subsystem mass budget, to act as a starting point for the detailed design. Due to the limited amount of design constraints and top level design requirements there was a very large design space. Therefore, the decision was made to create a sizing tool which would allow for rapid changes in the initial design, giving the design team the option to test several designs in quick succession.

2.2.1. Sizing Procedure

The first step in the sizing procedure was a Class-I weight estimation based on a relation between payload mass and maximum take off weight (MTOW). A literature study was performed and UAVs with similar missions were selected to create a statistical regression relation. With the payload being an input parameter, an initial estimate for the MTOW is obtained. Based on this MTOW, an assumed stall speed and an assumed aspect ratio, an initial estimate for the wing surface area is then calculated.

Using estimates for the Oswald efficiency factor and the zero lift drag coefficient, an estimate can then be made for the drag at different speeds. This was used to compute the required thrust and power at design-critical velocities.

After obtaining an initial MTOW and a preliminary wing geometry, a more accurate estimation of the MTOW was obtained using a Class II weight estimation. The weight estimation relationships used were specifically designed for preliminary UAV sizing [5]. The maximum thrust and power requirements calculated in the first step were then used to size the propulsion system. Since vertical take-off and landing was found to require far more power than traditional take off, this was an important aspect of the design and several propulsion configurations were considered and automatically sized [6].

Thirdly, the fuel mass was calculated for all possible propulsion systems. This fuel mass was based on two possible missions, one involving a payload being delivered at maximum speed to a destination located at the maximum operational range of the aircraft, and the other mission being a pure monitoring mission without an intervention payload, with an endurance of 10 hours. The propulsion system capable of performing both missions at the lowest weight was ultimately picked as the best propulsion system.

Finally, a new MTOW was calculated and the wing was resized, with the process being repeated iteratively until convergence of the MTOW. After a preliminary design was obtained, a sensitivity analysis was performed by varying all input parameters within a certain range and calculating the effect of that parameter variation on the MTOW.

2.2.2. Sizing Results

With the iterative sizing tool, a preliminary low-fidelity system-level design was obtained. The aspect ratio was set relatively high, as this improved endurance at low speeds, and it was found that a series-hybrid propulsion configuration was the lightest option. This propulsion configuration uses separate electric motors to drive all propellers and power is provided by a gas generator assembly operated on hydrocarbon fuels. The preliminary design parameters are available in Table 6.6, with all values containing four significant figures.

Table 2.2: Preliminary system characteristics.

Aircraft geometry	**Value**	**Mass**	**Value**	**Performance**	**Value**
Wingspan [m]	9.891	Maximum take-off mass [kg]	247.9	Maximum horizontal thrust [N]	316.2
Wing surface area [m^2]	4.892	Modular payload mass [kg]	40.00	Maximum horizontal power [kW]	26.35
Aspect ratio [-]	20.00	Instruments mass [kg]	10.00	Maximum VTOL thrust [N]	2917
Mean chord [m]	0.4945	Operating empty mass [kg]	161.0	Maximum VTOL power [kW]	71.33
Taper ratio [-]	0.4000	Structures mass [kg]	86.38	Maximum endurance thrust [N]	119.7
1/4 chord sweep [deg]	0.000	Wing mass [kg]	34.42	Maximum endurance power [kW]	4.633
Fuselage length [m]	3.300	Fuselage mass [kg]	35.86	Maximum speed [m/s]	83.33
Average fuselage diameter [m]	0.5000	VTOL boom mass [kg]	7.803	Monitoring speed [m/s]	38.71
Vertical tail arm [m]	2.200	Nacelle mass [kg]	5.725	Stall speed [m/s]	26
Horizontal tail arm [m]	1.800	Empennage mass [kg]	2.586	Maneuvering speed [m/s]	50.69
Vertical tail area [m^2]	0.5107	Fixed equipment mass [kg]	25.58	CL/CD at max endurance [-]	20.31

Aircraft Geometry	Value	Mass	Value	Performance	Value
Horizontal tail area [m^2]	0.5498	Propulsion system mass [kg]	49.04	CL at max speed [-]	0.1582
		Fuel mass [kg]	76.87	CD at max speed [-]	0.02058
		Battery mass [kg]	20.09	CL max [-]	1.200

With the system properties calculated, a preliminary performance analysis on the aircraft endurance and load regime was performed, with the results available in Figure 2.2 and Figure 2.1 respectively. The loads shown in the load diagram are required as a starting point for the structural analysis of the wing, fuselage and landing gear. And the payload endurance diagram shows what different missions can be performed.

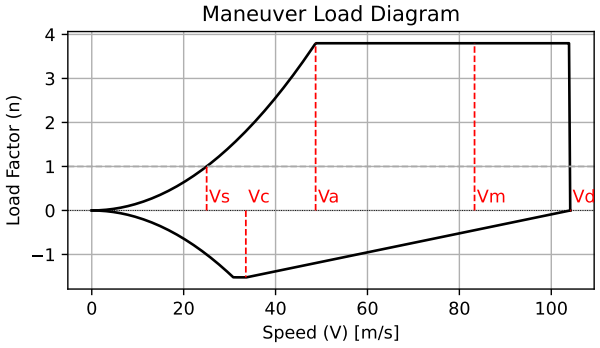

Figure 2.1: Preliminary V-n diagram.

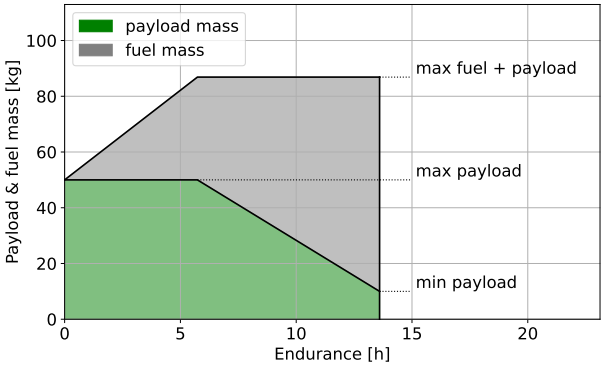

Figure 2.2: Preliminary payload-endurance diagram.

As the design focuses on two separate mission profiles, the combination of payload and fuel required for the maximum speed mission results in a higher MTOW than the total fuel for the maximum endurance mission, resulting in additional mass being available for fuel. Therefore, as seen in Figure 2.2, the maximum endurance was calculated to go beyond the required $10\,\mathrm{h}$, pushing towards $13.5\,\mathrm{h}$.

2.3. Initial Sizing Verification

The iterative sizing tool was implemented in a large Python program, requiring significant computational effort and development time. For this reason, attention was dedicated to the code and calculation verification of the software. To guarantee the correctness of the code, internal verification was performed through unit testing with the pytest library, achieving a total coverage (percentage of lines tested) of 79%. A convergence analysis was also applied to the maximum take-off weight calculation, ensuring that convergence of each individual subsystem (wing, fuselage, propulsion etc.) could be evaluated.

In order to estimate the effects of the assumed values of input parameters, a sensitivity analysis was performed. This was done by varying the input parameters of the design and calculating its effect on the MTOW. The results of the sensitivity analysis of the initial design are presented in Figure 2.3.

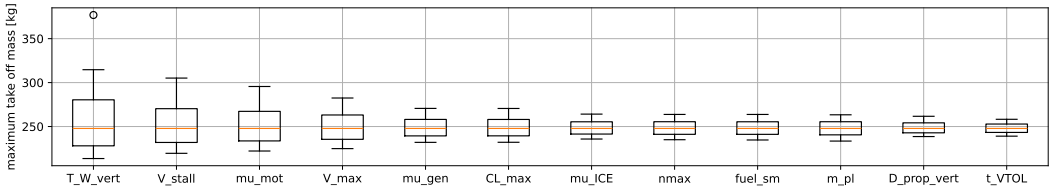

Figure 2.3: Sensitivity analysis of initial design.

The most influential parameters of the sizing program were set by requirements such as the thrust over weight during vertical flight (T_W_vert), the stall speed (V_stall) and the maximum speed (V_max). The most influential parameters that could change are the various efficiencies related to the propulsion system. These efficiencies are the electric motor efficiency, the generator efficiency and the internal combustion engine (ICE) efficiency. For this reason, the design of the power generation and propulsion system and of the wing became design priorities for the detailed design process, as discussed below. Finally some other parameters are shown in Figure 2.3 which are: nmax (maximum load factor, which is set by regulations), fuel_sm (fuel safety margin), m_pl (modular payload mass, which is to be maximized), D_prop_vert (diameter of vertical propellers) and t_VTOL (time of a vertical climb maneuver).

2.4. Subsystem Detail Design Interactions

With the initial sizing complete, it was decided to develop an N2 chart, which describes the interactions between each individual subsystem from a design standpoint. It is available in Figure 2.4 below.

Payload and Supporting Subsystems			Payload and subsystem mass, volume		Payload and subsystem mass, location
	Propulsion and Power	Fuel volume	Generator assembly, motor and power architecture mass, volume	Vertical and horizontal propeller diameter, motor mass, volume	Generator assembly and motor mass
		Wing Design			Control surfaces, nose-wing distance
			Fuselage Design	propulsion system mass, fuel mass	Fuselage length, horizontal motor position
				Tail Design	Tail layout, nose-tail distance
		Wing longitudinal position		Tail volume, longitudinal position	Stability and Control

Figure 2.4: System N2 diagram.

As observed in the N2 diagram, the design of the wing, fuselage, and tail require significant inputs from the payload, propulsion, and power design processes, with these aspects in turn requiring no inputs. For these reasons, despite the concurrent engineering methodology, these subsystems were afforded premier importance, as proven by the following three chapters.

3 | Payload, Communications, and Data Handling

This chapter presents the design of the monitoring payload, as well as critical supporting subsystems. Section 3.1 describes the selected monitoring payload, while Section 3.2 discusses the flexible intervention payload. Then, Section 3.3 presents the requirements for the three designed subsystems: Attitude Determination and Control, Command and Data Handling, and Telemetry and Telecommunications. The internal data flows are analyzed in Section 3.4, and the communications system is designed in Section 3.5, with the internal communications protocol discussed in Section 3.6. Finally, the verification process for these subsystems is described in Section 3.7.

3.1. Monitoring Payload Design

The monitoring payload is a FLOWS mission-specific payload designed to measure riverbed topography, measure water levels, create a three-dimensional map and identify waterborne debris. To do this, two off-the-shelf components are required; A multi-spectral camera gimbal and a bathymetric LIDAR. A set of requirements was identified for the overall monitoring payload, as shown in Table 3.1.

Table 3.1: Overall monitoring payload requirements.

ID	Requirement description	Origin
RPA-MON-1	The monitoring payload shall have a mass no more than $10\,\mathrm{kg}$.	**R-MIS-1**, **R-SYS-7**
RPA-MON-2	The monitoring payload shall be operated at up to $40\,\mathrm{m/s}$.	**R-SYS-1**
RPA-MON-3	The monitoring payload shall contain available off-the-shelf components.	**R-STK-4**
RPA-MON-4	The monitoring payload shall be operated at up to $500\,\mathrm{m}$ altitude.	**R-STK-1**
RPA-MON-5	The monitoring payload shall be safe to operate at an altitude no less than $50\,\mathrm{m}$.	**R-STK-6**

- **RPA-MON-1** stems from the initial sizing performed in Chapter 2, and the statistical mass estimation [4].
- **RPA-MON-2** & **RPA-MON-4** stem from the monitoring conditions set in Chapter 2.
- **RPA-MON-3** follows from the intention to achieve a readily available final design.
- **RPA-MON-5** follows from the intention to achieve a final design that meets safety standards.

With these requirements set as a baseline, the design process for each individual payload component continues with the definition of individual requirements.

3.1.1. Multi-spectral Camera Gimbal Selection

The requirements in Table 3.2 were identified for the camera gimbal, with rationales available below.

Table 3.2: Multi-spectral camera gimbal requirements.

ID	Requirement description	Origin
RPA-CAM-1	The multi-spectral camera shall be stabilized during flight.	**R-STK-2**, **R-MIS-2**
RPA-CAM-2	The multi-spectral camera shall be able to find waterborne debris no smaller than $25\,\mathrm{cm}^2$ during day- and nighttime operations.	**R-STK-5**, **R-MIS-2**
RPA-CAM-3	The multispectral camera has a frame rate capable of providing no less than 80% image overlap at monitoring speed.	**R-STK-1**, **R-MIS-2**
RPA-CAM-4	The multispectral camera shall create photogrammetry data with a horizontal accuracy of no less than $0.3\,\mathrm{m}^2$.	**R-STK-1**, **R-MIS-2**

- **RPA-CAM-1** is required to ensure no blurring occurs in data capture.
- **RPA-CAM-2**, **RPA-CAM-3**, and **RPA-CAM-4** set the performance limit for the monitoring capabilities, ensuring a minimum observation resolution, high image overlap, and continuous footage.

With the above requirements in mind, it was decided that minimizing the weight of the multi-spectral camera gimbal would be the most important sizing parameter. This would most easily be achieved using a camera already integrated with a gimbal, as these systems typically weigh less than the sum of their parts. Besides this, the infrared camera needed to be on the long wave infrared (LWIR) spectrum, as it is an infrared variant capable of performing in the dark, which is required for nighttime operation, without compromising weight.

The camera chosen is the Trillium HD25LV, as it is one of the lightest multi-spectral camera gimbals on the market capable of fulfilling the mission requirements discussed above [1]. As the main utility of this camera will be aerial mapping by photogrammetry, it is necessary to determine the required frame rate for optimal mapping as well as a lower data production rate for its maximum field of view (FOV) of $13.7\,^{\circ}$. The horizontal resolution is given in Table 3.7.

3.1.2. LIDAR Selection

The requirements in Table 3.3 were identified for the LIDAR, with rationales available below.

Table 3.3: LIDAR requirements.

ID	Requirement description	Origin
RPA-LID-1	The LIDAR shall capture an average point density of no less than $10\,\mathrm{pts/m^2}$, and a minimum point density of no less than $5\,\mathrm{pts/m^2}$.	**R-MIS-2**
RPA-LID-2	The LIDAR shall have a maximum water penetration depth of no less than 1 Secchi Depth in optimum conditions.	**R-MIS-2**

- **RPA-LID-1** and **RPA-LID-2** are performance requirements that guarantee that the LIDAR obtains river topography data in sufficient resolution [7].

Using these requirements, commercially available bathymetric LIDAR systems were compared. It was found that there were no bathymetric LIDAR systems capable of adhering to the altitude, velocity, weight, and point density requirements at the same time. Therefore, the search was extended to sensors capable of fulfilling three of the aforementioned requirements.

With the multispectral camera gimbal selected with a mass of $0.35\,\mathrm{kg}$ in Section 3.1.1, a maximum available mass remained of $9.65\,\mathrm{kg}$. This sets a hard requirement on the maximum mass of the LIDAR for which the propulsion and endurance of the UAV were sized. For the data cloud to be capable of creating a detailed enough riverbed model, there was no room to decrease the point density requirement. The search for a suitable bathymetric LIDAR therefore resulted in a trade-off of altitude and velocity.

The final selection for the bathymetric LIDAR is the RIEGL VQ-840GE. This system weighs $9.5\,\mathrm{kg}$ and has no limit on velocity [8]. It is however not able to penetrate water at an altitude of $500\,\mathrm{m}$. Following consultation with the company, a recommendation of a maximum altitude of $150\,\mathrm{m}$ was given to ensure the required water surface penetration [9]. Furthermore, the RiPARAMETER software was used to confirm that the requirements on point density are met for the selected altitude and velocity settings [9]. However, the monitoring altitude requirement therefore was be lowered to $150\,\mathrm{m}$ for the UAV to be able to adequately monitor the riverbed topography.

The RIEGL VQ-840-GE is rated for maximum water depth penetration at a pulse repetition rate of $50\,\mathrm{kHz}$ [8]. At an altitude of $75\,\mathrm{m}$ the water penetration depth reaches 2 Secchi Depths for bright targets for clear atmospheric conditions [8], with a Secchi depth representing the depth at which

[1] `https://www.trilliumeng.com/gimbals/hd25`

a standard black and white disc deployed in water is no longer visible to the human eye. The water penetration depth can be reduced from its optimum by multiple parameters, including light-attenuating sediment, poor weather, distance, and surface reflectivity.

The monitoring altitude of $150\,\mathrm{m}$ is two times as high as the optimum altitude for the VQ-840-GE, leading to reductions in the laser energy even under optimum measurement conditions. To model this attenuation, the Bouguer-Lambert Law will be used, linking the loss of light intensity due to propagation through a medium. The intensity of the laser beam is first calculated using Equation 3.1, starting with the pulse energy, then the pulse power and area.

$$E_{pulse} = \frac{P_{ave}}{PPR} \qquad P_{pulse} = \frac{E_{pulse}}{\tau_{pulse}} \qquad A_{pulse} = \pi \cdot \frac{D_{pulse}^2}{4} \qquad I_0 = \frac{P}{A} \tag{3.1}$$

where P_{ave} is the maximum average power of $30\,\mathrm{mW}$, PPR is the pulse repetition rate of $50\,\mathrm{kHz}$, τ_{pulse} is the pulse duration of $15\,\mathrm{ns}$, and D_{pulse} is the pulse footprint at $150\,\mathrm{m}$ of $150\,\mathrm{mm}$ [8]. The pulse energy E_{pulse} in J, pulse power P_{pulse} in W, pulse area A_{pulse} in m^2 and intensity of the laser beam at the water surface due to divergence I_0 in W/m^2 are subsequently calculated, leading to a value of $22\,637\,\mathrm{W/m^2}$ for I_0. This value is not attenuated, only distributed over the area. With the laser beam intensity calculated, the Bouguer-Lambert law in Equation 3.2 can be used to calculate the attenuation effect:

$$I(z) = I_0 e^{-\mu z} \tag{3.2}$$

where I_0 is the initial intensity in W/m^2, z is the distance the light beam travels through the medium in m, and μ is the atmospheric attenuation constant in km^{-1}, with values ranging from $0.05 - 0.125 km^{-1}$ depending on aerosols in the environment [2]. With the lowest value selected for a conservative result, the intensity at $150\,\mathrm{m}$ becomes $I(150m) = 22\,468\,\mathrm{W/m^2}$.

The effect of attenuation is thus observed to be minimal in optimum conditions. However, this represents the maximum expected performance, leading to a penetration of two Secchi depths. Due to aerosols, weather, and changes in water clarity, laser intensity is expected to decrease exponentially. Regardless, due to its power and wavelength, the laser is classified as a Class 3B laser product according to IEC60825-1:2014 [8]. This laser has a Nominal Ocular Hazard Distance (NOHD) of 15 meters. Beyond the NOHD, the laser will fall within the Maximum Permissible Exposure (MPE), meaning it will not be biologically harmful to the human eye.

With the power performance estimated, the monitoring resolution of the LIDAR needs to be calculated and discussed. The topographic map produced is directly impacted by the point density, as data between points needs to be interpolated. This point density is dependent on covered swath length, field of view, flight speed, scan rate, and pulse repetition rate.

The RIEGL VQ-840-GE has a variable field of view (FOV) of $\pm 20\,^\circ$, meaning the maximum total angle is $40\,^\circ$, with the highest average point density only available at this field of view. This is because decreasing the FOV does not change the scan pattern, instead cutting it short at the edges. At an altitude of $150\,\mathrm{m}$, this will lead to a swath width w_s of $109.2\,\mathrm{m}$.

The VQ-840-GE uses a near elliptical scanning pattern with a higher point concentration near the edges shown in Figure 3.1. This distribution deposits more points near the edges due to the way ellipses are drawn. To calculate the point density distribution of the LIDAR scanner, a program developed by RIEGL that calculates the scanning parameters called RiPARAMETER was used. This software uses the exact scanning pattern of the LIDAR and yields the point density distribution over the swath width of the scan.

[2] https://apps.dtic.mil/sti/tr/pdf/ADA325417.pdf

The scan rate in lines per second was optimized for uniform distributions at the middle of the scan, where the point density is lowest. At a scan rate of 77.6 full rotations per second, the lowest point density, which appears in the middle of the scan, is made uniform, as shown in Figure 3.2 [8]. A uniform point distribution means the distance between points on a scan line is equal to the line spacing, which optimizes the distribution over the entire resulting point cloud.

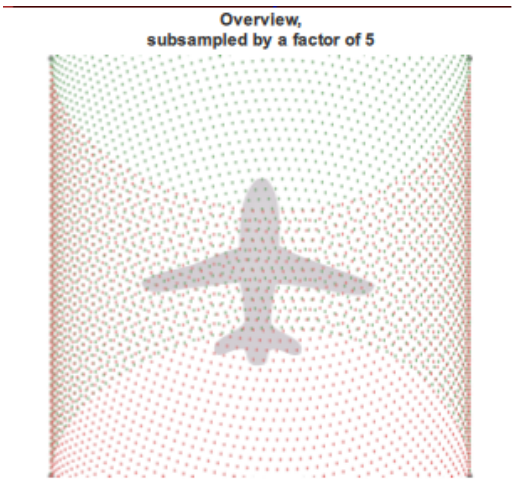

Figure 3.1: RIEGL VQ-840-GE elliptical LIDAR scan pattern[8].

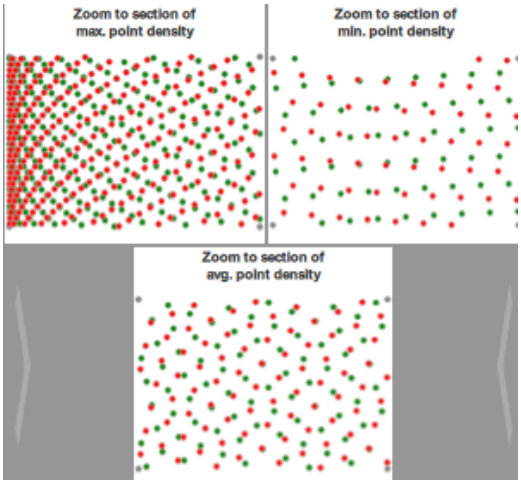

Figure 3.2: Highest, lowest, and average point distribution at monitoring conditions [8].

The average point density of the point cloud was calculated to be equal to $11.4\,\mathrm{pts/m^2}$, with the maximum point density at the edges being $184\,\mathrm{pts/m^2}$ and the minimum point density in the middle of the wath being $7.4\,\mathrm{pts/m^2}$. These densities fulfill **RPA-LID-1** and allow the construction of a digital terrain model of the riverbed topography.

To construct the point cloud from the monitoring data, additional specialized software will be required, for example, the proprietary RiPROCESS with the addon RiHydro [9]. This software can analyze point cloudes by computing the laser beam's refraction at the air-water interface and the lower propagation speed within the water column, obtaining a geometrically accurate point cloud.

3.2. Intervention Payload Design

The intervention payload is to be designed to provide humanitarian aid to civilians or to first responders and is limited by the design of the fuselage and propulsion system. This payload can be delivered through the use of VTOL, allowing the UAV to hover near enough to the ground not to require a parachute. From the initial sizing, the requirements in Table 3.4 were defined.

Table 3.4: Intervention payload requirements.

ID	Requirement description	Origin
RPA-INT-1	The intervention payload shall weigh no more than $31.7\,\mathrm{kg}$.	**R-SYS-8**, **R-MIS-10**
RPA-INT-2	The intervention payload shall be no larger than 780x460x310 mm.	**R-SYS-8**
RPA-INT-3	The intervention payload shall allow for mounting to the release mechanism.	**R-MIS-10**
RPA-INT-4	The intervention payload shall remain mounted until released by UAV operator.	**R-STK-6**
RPA-INT-5	The intervention payload shall be content-agnostic.	**R-SYS-8**

- **RPA-INT-1** follows from the final mass allocation discussed in the budget breakdown in Chapter 13.
- **RPA-INT-2** follows from the payload bay size calculated in Chapter 8.
- **RPA-INT-3**, **RPA-INT-4** & **RPA-INT-5** guarantee that any actual humanitarian aid that fits the mass and volume constraint can be loaded and released as desired.

These requirements allow the operator of the UAV to load any type of humanitarian aid that fits the constraints. Two potential options have been explored by the design team.

The first intervention payload is a deployable life raft, capable of auto-inflation. This payload can be dropped near civilians to help them reach safer locations from a flooded area. A suitable liferaft that meets all requirements is a LALIZAS ISO RACING Liferaft [3]. Specifically, the six-person version meets both the weight and size requirements of the intervention payload, with a mass of $30\,\mathrm{kg}$ and a volume of 630x250x420 mm.

The second intervention payload is a transceiver mounted to the UAV capable of connecting devices of civilians on the ground to communication networks during power outages, making communication with first responders possible. The technology is still quite novel, with no clear options existing off-the-shelf, but is being developed by multiple companies [4], [10], and can be expected to become commercially available in the coming years.

3.3. Subsystem Requirements

The fixed subsystems in the airborne segment are defined as the Attitude Determination and Control (ADC), Telemetry and Telecommunications (TTC), and the Command and Data Handling (CDH) subsystem. In Table 3.5 below, the requirements for each subsystem are listed, including the system requirement from which they are derived.

Table 3.5: Identified fixed subsystem requirements

ID	Requirement description	Origin
RFS-ADC-1	The ADC subsystem shall be able to determine its altitude with a relative accuracy of no more than 5%.	**R-SYS-9**, **R-SYS-10**
RFS-ADC-2	The ADC subsystem shall be able to control its altitude with a relative accuracy of no more than 5%.	**R-SYS-12**, **RFS-ADC-1**
RFS-ADC-3	The ADC subsystem shall be able to determine its longitudinal and latitudinal position with an accuracy of no less than $7\,\mathrm{m}$.	**R-SYS-9**, **R-SYS-10**
RFS-ADC-4	The ADC subsystem shall be able to control its longitudinal and latitudinal position with an accuracy of no less than $7\,\mathrm{m}$.	**R-SYS-12**, **RFS-ADC-3**
RFS-ADC-5	The ADC subsystem shall be able to determine its airspeed with an accuracy of no more than $1.3\,\mathrm{m/s}$.	**R-SYS-9**, **R-SYS-10**
RFS-ADC-6	The ADC subsystem shall be able to control its airspeed with an accuracy of no more than $1.3\,\mathrm{m/s}$.	**R-SYS-12**, **RFS-ADC-5**
RFS-ADC-7	The ADC subsystem shall be able to determine its attitude with an accuracy of no more than $1\,°$ under high turbulence conditions.	**R-SYS-9**, **R-SYS-10**
RFS-ADC-8	The ADC subsystem shall be able to control its attitude with an accuracy of no more than $1\,°$ under high turbulence conditions.	**R-SYS-12**
RFS-TTC-1	The TTC subsystem shall be able to send no less than $6\,\mathrm{Mbps}$ to the ground segment.	**R-MIS-3**, **R-MIS-4**
RFS-TTC-2	The TTC subsystem shall be able to receive incoming commands from the ground segment.	**R-SYS-12**, **RFS-TTC-1**
RFS-TTC-3	The TTC subsystem shall have a data link with the ground station of no less than $200\,\mathrm{km}$.	**R-MIS-3**
RFS-TTC-4	The video generated by the infrared and visual light control camera shall be sent to the ground station at a frame rate of no less than $4\,\mathrm{Hz}$.	**R-SYS-12**
RFS-TTC-5	The video generated by the infrared and visual light monitoring camera shall be sent to the ground station at a frame rate of no less than $5.4\,\mathrm{Hz}$.	**R-SYS-12**
RFS-CDH-1	The CDH subsystem shall be able to process all generated payload data.	**R-SYS-12**, **RFS-TTC-4**

Continued on next page

[3] https://www.lalizas.com/product/143-yachting/6384-lalizas-international-liferaft-iso-raft-racing
[4] https://about.att.com/innovationblog/cows_fly

Table 3.5: Identified fixed subsystem requirements

ID	Requirement description	Origin
RFS-CDH-2	The CDH subsystem shall be able to store all generated payload data on board of the UAV.	**R-SYS-3**, **RFS-CDH-1**
RFS-CDH-3	The CDH subsystem shall be able to process all generated flight data on board of the UAV.	**R-SYS-9**
RFS-CDH-4	The CDH subsystem shall be able to store all flight data on board of the UAV.	**R-SYS-9**, **RFS-CDH-3**

- **RFS-ADC-1**, **RFS-ADC-3** and **RFS-ADC-5** represent basic expected UAV functionalities, which are required for the mission as well as the control and operation of the airborne segment.
- **RFS-ADC-2**, **RFS-ADC-4** and **RFS-ADC-6** flow from the previous three requirements, as controlling the aircraft is necessary in order to perform the mission.
- **RFS-ADC-7** flows from **R-STK-5**, as the UAV will be operating under adverse conditions. In these situations it is important that the UAV is capable of determining its attitude.
- **RFS-ADC-8** flows from the previous requirement, as controlling the UAV in these high turbulence conditions is integral to the success of the mission.
- **RFS-TTC-1** flows from mission requirements **R-MIS-3** and **R-MIS-4**, stating it should maintain a link for flight and monitoring data, with the data rate determined from Section 3.4. **RFS-TTC-2** follows from the same mission requirements.
- **RFS-TTC-3** flows from the distance at which the UAV shall be controllable as defined in **R-MIS-3**.
- **RFS-TTC-4** follows from requirement **R-MIS-2**, allowing for continuous monitoring operations.
- **RFS-CDH-1** flows from **RFS-TCC-4**, requiring the data to be processed on board before being sent to the ground station.
- **RFS-CDH-2** guarantees that the UAV can process flight data on board, which allows for autonomous operations, along with processed data being transmitted to the ground station.
- **RFS-CDH-3** allows for autonomous operations, as data can stored on board the UAV. In addition, this mitigates risk in case of loss of communication (**TRRC-13**).

Before the subsystems can be sized, a trade-off is required with respect to data processing. This can occur either at the ground station or at the airborne segment. The former suggests that all monitoring data is transmitted to the ground station, which imposes more strict requirements on the TTC subsystem. The latter, on the other hand, suggests that limited data is transmitted, which imposes more strict requirements on the CDH subsystem but alleviates TTC requirements. In literature, it is argued that onboard data pre-processing is vital and increases reliability of the communication link [11] [12]. Therefore, the data flows will be analyzed and processed accordingly in Section 3.4, after which it is to be transmitted with available market options in Section 3.5.

3.4. Data Flow Analysis

In order to determine the data flows generated by the components in the UAV that needs to be both processed (CDH) and communicated (TTC), it is important to assess each component that generates data. The control and monitoring camera can be split into two distinct parts, namely, the visible sensor and the infrared (heat) sensor. In addition, the LIDAR system and the flight computer are assessed.

Multi-spectral Control Camera

The first Trillium HD25 camera will be employed for controlling the UAV itself, flowing into both the flight computer and directly to the operator. The visible sensor of the camera has a resolution of 1280 by 720 pixels. As it is a color image, each pixel contains 24 bits [5]. Furthermore, the camera has a maximum frame rate of $30\,\mathrm{Hz}$, meaning 30 images per second are taken. Multiplying these numbers, the bit rate can be determined in bits per second.

The infrared camera has a given resolution of 640 by 512 pixels, and each pixel consists of 14 bits

[5] http://preservationtutorial.library.cornell.edu/intro/intro-04.html

[6]. Again, this camera implements a frequency of $30\,\mathrm{Hz}$. Similarly to the visible light sensor, it can be converted to mega- or gigabits. The results of this calculation can be found in Table 3.6. As these data rates are quite large, it is important to consider methods of compression or reduction. These methods, along with their compression factors are given as follows.

H.264 Compression

The selected camera system employs a built in encoding of the video footage, which is the standard H.264 codex. The compression factor of this system is variable, but estimates can be made based on empirical data [13]. The concept of motion factor can be considered, taking a value of 1, 2 or 4 depending on the amount of movement in the video. Because this scaling is highly subjective and the UAV will be flying at high speeds, it is assumed that the motion factor of the UAV camera footage is the maximum possible of 4 [13]. Then, the compressed bit rates can be determined. In Equation 3.3, H and W represent the height and width of the footage in pixels. FR represents the frame rate, and MF gives the motion factor. Finally, 0.07 is the empirically determined scaling factor.

$$Bitrate_{compressed} = H \cdot W \cdot FR \cdot MF \cdot 0.07 \tag{3.3}$$

For HD footage of 1280 x 720 pixels, with a frame rate of 30 frames per second and a motion factor of 4, this leads to a compressed bit rate of $7.74\,\mathrm{Mbps}$. This coincides with a compression factor of 86. As this empirical relation is determined for color footage, it cannot be immediately applied to the infrared camera output. To convert this, the ratio between the bits per pixel should be taken into account. This ratio is $14/24$, which should be multiplied by the compressed data rate as given in Equation 3.3. Again, assuming a motion factor of 4, this leads to compressed long-wave infrared footage of $1.61\,\mathrm{Mbps}$ and a compression factor of 86.

Reduction of Frame Rate and Resolution

It is also important to assess the required frame rate and resolution for the operator to operate the UAV. Experiments have been performed on the effect of reduced frame rates and resolution on human performance. From this, it has been estimated that the UAV is still controllable at a framerate of $4\,\mathrm{Hz}$, with the resolution allowing for reduction [14]. From this, it has been decided to reduce the frame rate to a minimum of 4 frames per second and to reduce the resolution of the visible light camera by half. This leads to visible light camera footage of 640 by 360 pixels and a frame rate of 4. Using Equation 3.3, this leads to a new compressed bit rate of $258\,\mathrm{kbps}$, for a relative compression factor of 30. For the infrared camera, with a frame rate of 4, this leads to a bit rate of $214\,\mathrm{kbps}$. Summing up, the total to-be-transmitted bit rate for UAV controlling is $581\,\mathrm{kbps}$, an additional compression factor of 7.5.

Bitrate Overview

In Table 3.6, an overview is given of the compressed data rate from the flight control cameras. This table shows the adjusted resolution and frame rate, as well as the total bitrate.

Table 3.6: Comparison between uncompressed and compressed bitrates of visible light and infrared control cameras

Sensor	Visible light (Uncompressed)	Visible light (Compressed)	Infrared (Uncompressed)	Infrared (Compressed)
Resolution [pixels]	1280x720	640x360	640x512	640x512
Bits per pixel	24	24	14	14
Frame rate [Hz]	30	4	30	4
Bit-rate [Mbps]	664	0.258	138	0.214

From this, it is shown that the data from the visible light camera is compressed by a total compression factor of 2580, whereas the data from the infrared camera is compressed by a total compression factor of 645.

[6] https://www.flir.com/support-center/oem/how-many-bits-per-pixel-is-the-digital-output/

Multi-spectral Monitoring Camera

The second camera is used for in-flight terrain monitoring and photogrammetry. As this camera is the same as that used for flight control, it produces the same data rates. However, as its application is different, the data output has different requirements. Similar to the controlling camera, it uses the H.264 codex, leading to a compression factor of 86, both for the visual light and infrared camera.

Photogrammetry Frame Rate

The required frame rate dictates the data rate of the camera. Assuming the monitoring altitude is no less than 150 meters, and the FOV is set to its maximum at $13.7\,°$, the width of the measured surface, called the swath width can be calculated using the tangent function. Half of the angle ($6.85\,°$) with an adjacent side length of $150\,\mathrm{m}$ leads to half a swath of $18.0\,\mathrm{m}$. This means the total minimum swath will be $36\,\mathrm{m}$. From literature, $80\,\%$ is taken as a frontal overlap percentage for photogrammetry [15]. This means that for every $20\,\%$ of the swath, a photo should be taken, which leads to an interval of $7.2\,\mathrm{m}$. As the UAV will have a maximum cruise speed of $40\,\mathrm{m/s}$, this leads to one image every $0.18\,\mathrm{s}$, or a minimum frame rate of $5.56\,\mathrm{Hz}$. This same frame rate can be employed for the Infrared camera.

To ensure a detailed photogrammetry map, the choice has been made to not diminish the resolution of the footage. This leads to a compression factor of $30/5.56$, or 5.4. This is valid for both the visual light sensor and the infrared sensor.

Bitrate Overview

Table 3.7 shows the properties of the compressed data stream from the monitoring camera. It also shows the horizontal resolution, which is calculated by dividing the swath by the number of pixels.

Table 3.7: Comparison between uncompressed and compressed bitrates of visible light and infrared monitoring cameras

Sensor	Visible light (Uncompressed)	Visible light (Compressed)	Infrared (Uncompressed)	Infrared (Compressed)
Resolution [pixels]	1280x720	1280x720	640x512	640x512
Bits per pixel	24	24	14	14
Frame rate [Hz]	30	5.4	30	5.4
Bit-rate [Mbps]	664	1.43	138	0.30
Horizontal Resolution [cm]	2.82	2.82	10.0	10.0

From this, it is shown that the data from the visible light camera and the infrared camera are both compressed by a total compression factor of 464. This leads to a maximum total data rate for photogrammetry of $1.73\,\mathrm{Mbps}$.

LIDAR Data Rate

The LIDAR data rate depends on the Field of View (FoV) and Pulse Repetition Rate (PRR). As changing the FoV only cuts off the laser, without narrowing the distribution, any angle below the maximum of $40\,°$ cuts off points from the edges. As mentioned in Section 3.1.2, the best Pulse Repetition Rate (PPR) for water depth penetration was $50\,\mathrm{kHz}$, but the maximum PPR the RIEGL VQ-840-GE is capable of creating is $100\,\mathrm{kHz}$. The maximum PPS yields a maximum data rate of $13.3\,\mathrm{GB/h}$ or $3.69\,\mathrm{MB/s}$. Multiplying by 8, a data rate of $29.6\,\mathrm{Mbps}$ is obtained.

LIDAR Data Compression

By far the largest source of data within the UAV is the LiDAR, with a maximum data generation rate of $29.6\,\mathrm{Mbps}$. This is too much raw data to communicate with the ground station, and for that reason it is important to compress this data on board. Novel methods for real-time data compression of LIDAR generated point clouds are necessary, which leads to compression factors between 40 and 90 [16]. Implementing the lowest compression factor, a bit rate of $0.74\,\mathrm{Mbps}$, or $0.092\,\mathrm{MB/s}$ is found. However, as this compression is not built into the selected LIDAR system, it is important to determine the computational requirements for the compression. In the research, the assumed compression factor was reached using the Nvidia Jetson TX2 platform. After looking into the compression computer, it has been determined that this same computer can be used aboard the UAV, due to its small size,

relatively low power usage and proven functionality [7]. SAAB supplies this computer in a rugged housing, with ports compatible with the other used equipment [8]. This computer has a maximum power consumption of $25\,\mathrm{W}$ and a mass of $1.2\,\mathrm{kg}$. The ruggedized design of this system ensures that it is able to withstand vibrations, g-forces and is not susceptible to moisture.

Flight Computer

The Flight Computer, composed of the VECTOR-600 and VECTOR-MCC, processes camera data used for pilot control, IMU data, and control commands to subsequently control the attitude of the aircraft and the pilot control camera. In addition, the VECTOR-600 has built-in sensor redundancy (**TRRC-11**) and contains an autopilot, which allows for autonomous operations (**TRRC-13**) which can be taken over by the operator mid-flight. IMU and altitude data is sampled at a maximum of $500\,\mathrm{Hz}$ with a 12-bit resolution, producing a maximum data rate of $0.006\,\mathrm{Mbps}$. Given its negligible magnitude with respect to other data rates, this data is directly fed to the antenna.

3.5. Communications System Sizing

With all outgoing data determined, it is important to establish a link margin to ensure that the data can be transmitted in a variety of circumstances, such as bad weather (**TPRC-26**). A typical signal-to-noise ratio margin for UAV's for satellite communications is set as $3.0\,\mathrm{dB}$ [17]. Converting this to a percentage, an increase of $3.0\,\mathrm{dB}$ leads to a total link margin of $100\,\%$ of the original link budget. Effectively, the possible data bandwidth should be twice of what is required by the subsystems.

Given the compressed bit rates found from the previously listed components, i.e. the data rate of the control camera DR_C, monitoring camera DR_M, LIDAR sensor DR_L, and the flight computer DR_F, the total data rate DR (in Mbps) is computed:

$$DR = DR_C + DR_M + DR_L + DR_F$$
$$DR = (0.258 + 0.214) + (1.43 + 0.30) + 0.74 + 0.006 = 2.948$$

The communication system must thus be able to transmit a data rate of $2.95\,\mathrm{Mbps}$. Including the previously determined link margin, this becomes $5.90\,\mathrm{Mbps}$.

Design Options

The communication link required for the relay of payload data and flight data is a common problem among UAV's. This is due to a limited frequency and bandwidth availability whilst also having to cover a long distance. Although wireless links such as IEEE 802.11 and IEEE 802.16 are commonly used in UAV applications, these do not have enough signal strength to cover the desired distance. High-frequency (HF) and very high-frequency (VHF) bands - in the order of MHz - are more suitable, but have become too crowded for use [11]. Therefore, frequencies in the order of GHz with more available bandwidth are investigated, such as the L-band. Two feasible options are presented: either the UAV can directly communicate with the ground station, or the UAV can establish communication using an earth-orbiting satellite as medium.

While satellite communication may aid in covering long distances, this comes at the cost of significantly lower data rates [18]. Satellites with a larger orbit altitude show to have an improved transmission and receiving data rate, but this comes at the cost of the round-trip latency, which is the time delay for a signal to travel between UAV and ground station [12]. As a compromise between both requirements, it is decided to make use of the existing O3b mPOWER satellite infrastructure flying at Medium Earth Orbit (MEO). This makes use of the Ka-band, establishing a communication link of $10\,\mathrm{Mbps}$ at a transmission frequency of $30\,\mathrm{GHz}$ and a receiving frequency of $20\,\mathrm{GHz}$. This is performed using the MICRO SAT from GetSAT. The satellite connection will have a latency of $150\,\mathrm{ms}$ [9].

[7] https://www.nvidia.com/en-us/autonomous-machines/embedded-systems/jetson-tx2/

[8] https://www.saab.com/globalassets/products/support-and-services/vehicle-electronics-solutions/oflf-1507-1-rvc-e-product-sheet.pdf&ved=2ahUKEwiC14Osh7iGAxXR8QIHHYpmDp4QFnoECCYQAQ&usg=AOvVaw0jzg0O8_hblfUoWsNbm0y5

[9] https://www.ses.com/o3b-mpower

For the sake of redundancy (**TPRC-44**), a direct link between the UAV and the ground station is also established by means of an air-to-ground transponder, the Airmobi Swiftlink P43, which establishes a $200\,\mathrm{km}$ communication link, with a maximum of $15\,\mathrm{Mbps}$ at a working frequency of $1.4\,\mathrm{GHz}$ (L-BB).

It can be seen that the minimum bandwidth is obtained from the satellite connection using the O3b infrastructure. The bandwidth of $10\,\mathrm{Mbps}$ is significantly higher than the determined downlink bandwidth required. Half of this difference ($4.10\,\mathrm{Mbps}$) can therefore be used to increase the frame rate of the control camera, which would make it more pleasant to fly for the UAV operator. Reassessing the frame rate, it is found that the data rate per frame is $0.116\,\mathrm{Mb/frame}$. Dividing the remaining bandwidth ($2.05\,\mathrm{Mbps}$) by this amount gives a frame rate of 17.7. Therefore, it can be said that at optimal bandwidth, the control camera monitored by the UAV pilot can transmit footage at a diminished resolution, at a frame rate of $17.7\,\mathrm{Hz}$.

3.6. Internal Communication Protocol

Between the flight computer/mission computer and the various subsystems operating during flight, bidirectional data flows are required. Uplinks need to be used to provide information on subsystem status, and downlinks need to be used to control these subsystems. For this reason, it was decided to make use of a Controller Area Network (CAN)-based internal communication system, namely the open-source DRONECAN framework [10].

DRONECAN allows for robust and redundant multidirectional communication between decentralized peers, with each peer (node) exhibiting a unique node identifier. Both message broadcasting and service invocation capabilities are available, allowing for data exchange and control. For each communication type, a predefined set of data structures is used, with minimal bitrate required.

By selecting components that are CAN-compatible such as the VECTOR-600 and the VECTOR-MCC, the DRONECAN architecture acts as the internal data handling system as shown in Figure 3.3. The data handling diagram in Figure 3.3 includes data rates for all data flows above $0.1\,\mathrm{Mbps}$, with any lower data rates (e.g. binary relay control flows) being considered negligible at this design stage.

3.7. Payload and Subsystem Verification

To guarantee compliance with requirements set on the payload and fixed subsystems described above, the verification methods set in Table 3.8 can be used. Importantly, a requirement set in Section 3.1 has changed to match components because available parts were found to be limiting. The updated requirement is set below, and is expected to impact the mission profile discussed in Chapter 9:

RPA-MON-4: The monitoring payload shall be operated at up to $150\,\mathrm{m}$ altitude.

Table 3.8: Payload and fixed subsystem verification methods.

ID	Verification method	Discussion
RPA-MON-1	Inspection	Place monitoring payload components on a scale.
RPA-MON-2	Test	Perform measurements at monitoring velocity and check if monitoring data is satisfactory.
RPA-MON-3	Analysis	Check that the parts are not created in house.
RPA-MON-4	Demonstration	Perform measurements at monitoring altitude and check if monitoring data is satisfactory.
RPA-MON-5	Analysis	Check classification of the laser to ensure safety at a distance of $50\,\mathrm{m}$.
RPA-CAM-1	Analysis	Analyze the critical vibrations encountered during measurement and test gimbal stability with vibration test bench.

Continued on next page

[10] https://dronecan.github.io/

Table 3.8: Payload and fixed subsystem verification methods.

ID	Verification method	Discussion
RPA-CAM-2	Test	Submerge objects of varying size in water and test if they are identifiable at a distance equivalent to the monitoring altitude.
RPA-CAM-3	Analysis	Calculate required framerate and check camera specifications.
RPA-CAM-4	Test	Perform measurements at monitoring conditions and verify the horizontal resolution.
RPA-LID-1	Analysis	Calculate the point densities at monitoring conditions using RiPARAMETER.
RPA-LID-2	Test	Measure the Secchi Depth and perform measurements to compare if penetration depth is adequate.
RPA-INT-1	Inspection	Place intervention payload on a scale.
RPA-INT-2	Inspection	Measure physical dimensions of the intervention payload.
RPA-INT-3	Demonstration	Mount the intervention payload to the release structure and demonstrate deployment.
RPA-INT-4	Test	Fly a mission with intervention payload in a location clear of civilians and check if payload remains attached.
RPA-INT-5	Demonstration	Replace an intervention payload content piece with another.
RFS-ADC-1	Test	Perform a flight test at known altitudes and determine whether the altimeter performs adequately.
RFS-ADC-2	Demonstration	Perform a flight test and demonstrate that the UAV is capable of adjusting its altitude as required.
RFS-ADC-3	Test	Test the GPS receiver in both a stationary and mobile environment to check for satisfactory results.
RFS-ADC-4	Demonstration	Perform a flight test and demonstrate that the UAV is capable of changing its position as required.
RFS-ADC-5	Test	Mount the pitot tube and flight computer in a wind tunnel at varying air speeds and compare the pitot tube measurements.
RFS-ADC-6	Demonstration	Perform a flight test and demonstrate that the UAV is capable of adjusting its airspeed as required.
RFS-ADC-7	Test	Perform a test flight in turbulent conditions to check compliance of this requirement.
RFS-ADC-8	Test	Perform a test flight in turbulent conditions to check compliance of this requirement.
RFS-TTC-1	Demonstration	Demonstrate that the CDH subsystem is capable of sending the required bit rate to the ground segment at large distance.
RFS-TTC-2	Demonstration	Demonstrate that the CDH subsystem is capable of receiving the required bit rate from the ground segment at large distance.
RFS-TTC-3	Test	Perform a test flight continuously flying further from the ground station to determine its maximum range.
RFS-TTC-4	Demonstration	Demonstrate that the data rate from the payload fits within the link budget and can be sent.
RFS-CDH-1	Test	Perform a test with the payload outputting data at its maximum rate, to see if the compression computer functions as required.
RFS-CDH-2	Test	Run the payload at maximum rate for the rated duration and check whether flight computer has sufficient capacity.
RFS-CDH-3	Test	Perform a test with the ADC outputting data at its maximum rate, to see if the compression computer functions as required.
RFS-CDH-4	Test	Run the ADC at maximum rate for the rated duration and check whether flight computer has sufficient capacity.

Certain tests described above (e.g. for **RFS-ADC-5**) can be straightforwardly performed in the facilities of the Faculty of Aerospace Engineering at TU Delft, with individual components being inspected or tested as required. However, other tests, such as for **RPA-INT-4**, require the complete assembly of the system and a mock mission. For such tests, a range with free airspace, such as the local range at ASK 't Harde, could be rented out to perform system-level tests.

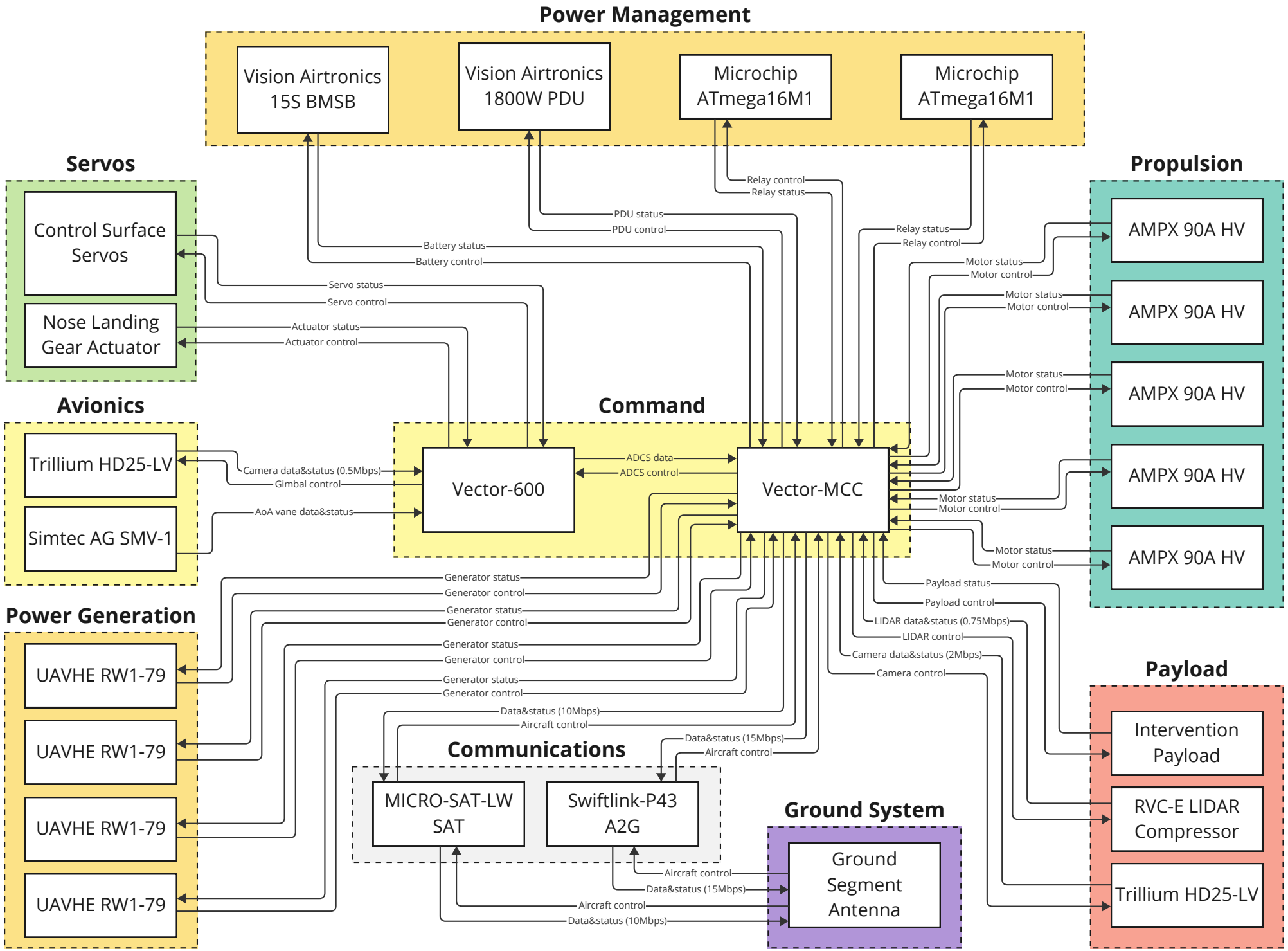

Figure 3.3: Data Handling Diagram

4 | Propulsion System Design

In this chapter, the design of the propulsion subsystem is presented. First, the requirements relevant to the propulsion subsystem are formulated and rationalized in Section 4.1. Then, the propeller assemblies and motors are selected in Section 4.2 and Section 4.3 respectively, followed by the selection of the electronic speed controllers in Section 4.4. A noise estimation of the propulsion system is carried out in Section 4.5. Lastly, the verification of the selected system is explored in Section 4.6.

4.1. Propulsion Subsystem Requirements

The subsystem requirements for the propulsion architecture are identified and shown in Table 4.1.

Table 4.1: Propulsion subsystem requirements.

ID	Requirement description	Origin
RPR-PRP-1	The vertical propellers shall provide a total continuous thrust of no less than $2920\,\mathrm{N}$.	**R-MIS-5**
RPR-PRP-2	The horizontal propeller shall provide a continuous thrust of no less than $320\,\mathrm{N}$.	**R-MIS-1**
RPR-PRP-3	Each vertical propeller shall have 2 blades.	**R-SYS-1**
RPR-PRP-4	Each vertical propeller shall have a total mass of no more than $1.1\,\mathrm{kg}$.	**R-MIS-5**
RPR-PRP-5	The horizontal propeller shall have a mass of no more than $1.4\,\mathrm{kg}$.	**R-MIS-1**
RPR-MOT-1	The vertical electric motors shall provide a total continuous mechanical power output of no less than $50\,\mathrm{kW}$.	**R-MIS-5**
RPR-MOT-2	The horizontal electric motor shall provide a continuous mechanical power output of no less than $50\,\mathrm{kW}$.	**R-MIS-1**
RPR-MOT-3	The vertical electric motors shall have a total mass of no more than $9.6\,\mathrm{kg}$.	**R-MIS-5**
RPR-MOT-4	The horizontal electric motor shall have a mass of no more than $3.1\,\mathrm{kg}$.	**R-MIS-1**
RPR-COM-1	Each individual component shall be available commercially.	**R-MIS-9**

- **RPR-PRP-1** and **RPR-PRP-2** follow from the need to provide sufficient thrust for all operations. The leading vertical thrust requirement is based on the thrust required for VTOL, while the horizontal thrust requirement is set from the thrust for maximum speed. This stems from the design choice of a load factor of no less than n = 1.2
- **RPR-PRP-3** results from the possibility of orienting two-bladed propellers in free-stream direction to minimize drug.
- **RPR-MOT-1** and **RPR-MOT-2** flow from the power required for the propellers to achieve the thrust mentioned in **RP-PRP-1** and **RPR-PRP-2**.
- **RPR-PRP-4**, **RPR-PRP-5**, **RPR-MOT-3** and **RPR-MOT-4** all follow from the initial allocated mass budgets determined in the initial sizing of the propulsion system in Chapter 2.
- **RPR-COM-1** follows from the top-level design intention to rely on proven, already existing components.

4.2. Propeller Design

The propeller selection process depends on the configuration of the horizontal propeller, with either tractor or pusher architectures being available. In the former, the propeller is usually placed at the front of the vehicle, and it pulls the aircraft forward, while in the latter the propeller pushes the aircraft forward and is usually placed at the back of the vehicle[1].

The application of pusher or tractor configuration depends on operational considerations to be made[2]. First of all, pusher propellers are the preferred configuration for first person view (FPV) drones, espe-

[1] https://mail.supermotoxl.com/resources/guides-tutorial/r-c-models-fpv-uav-diy-how-to-tips/pusher-vs-tractor-propeller-configuration.html

[2] https://airplaneacademy.com/pusher-vs-puller-propeller-aircraft-compared/

cially the ones relying on video footage, such as the FLOWS mission as well. This is because placing the propeller forward would lead to obstructing the view of the sensing equipment. However, pusher propellers result in significantly lower clearance for horizontal landing, which is important to guarantee glide landing capabilities in case of propulsion system failure. Furthermore, the pusher receives disturbed airflow, leading to induced vibrations and increased noise.

The trade-off to be made leaves a decision between potentially compromising the monitoring mission, or increasing the difficulty of the design to account for the pusher configuration - leading to the selection of the pusher propeller. This configuration requires a cooled electric motor, as while in a tractor configuration air cooling happens naturally, for a pusher configuration that is not often the case, so special attention must be placed on ensuring that the motor powering the horizontal propeller is able to be adequately cooled [3].

With the configuration selected, the propeller selection method relies on calculating the thrust that a commercially-available propeller is able to produce when provided with a certain value for mechanical power and RPM. This process is documented for both the vertical and horizontal propellers below.

4.2.1. Vertical Propeller Selection

Four possible approaches were considered for the selection of the vertical propeller [19].

1. The first approach would rely on power estimates from ideal Actuator Disk Theory (ADT) to determine the necessary propeller size to fulfill the thrust requirement. This method outputs the ideal propeller thrust given the power provided, so it is considered non-conservative, especially at low advance ratios (such as during vertical take-off), where the actual efficiency of a propeller is far lower than the ADT estimate[4].
2. The second approach relies on applying Blade Element Momentum Theory (BEMT), a highly accurate method that requires aerodynamic and geometric airfoil data. These propeller geometry characteristics are not provided by any propeller manufacturer, and any approximations cannot be verified to be representative of the selected component[5].
3. The third approach involves the use of a TU Delft-developed program which makes use of BEMT but corrects for compressibility and root-tip effects[6]. However, this program also requires complete geometric data to be provided.
4. The fourth approach is to rely on test data provided by propeller manufacturers. These tests usually make use of a specific motor, and do not run to maximum supported thrust settings. Regardless, the thrust produced for a certain power and RPM setting can be identified, and similar motors that provide the same mechanical power and RPM can be assumed to result in similar thrust ratings. These tests are typically performed on fixed thrust benches, aligning with VTOL conditions. However, the level of accuracy of the estimation cannot be guaranteed.

Given the timeframe of the project, it was decided to pursue the fourth approach, as other approaches would either provide wholly inaccurate results (ADT) or require impossible to determine inputs (BEMT). Test data was gathered for several motor-propeller combinations, and the input and output power were related to the thrust obtained. By interpolating these quantities, the required thrust could be used as input, and the propeller efficiency and required motor power obtained as output.

An extensive market study was performed, and the Fluxer 63x22 Pro propeller from MAD Components, shown in Figure 4.1, was found to satisfy **RPR-PRP-1**[7]. The 63x22 Pro was demonstrated to achieve a thrust rating beyond the required $727\,\mathrm{N}$ when combined with the MAD Components M50C60 PRO IPE 10KV brushless drone motor, as shown in Figure 4.2.

[3] https://1000aircraftphotos.com/HistoryBriefs/CessnaXMC.htm
[4] https://web.mit.edu/16.unified/www/FALL/thermodynamics/notes/node86.html
[5] http://wwwmdp.eng.cam.ac.uk/web/library/enginfo/aerothermal_dvd_only/aero/propeller/prop1.html
[6] https://data.4tu.nl/datasets/e748a68d-5f15-4757-b904-880bcec8217b
[7] https://store.mad-motor.com/products/mad-m50c60-pro-ipe-for-the-electric-manned-drone-e-vtol-and-paratrike

Figure 4.1: Image of the Fluxer 63x22 Pro.

MAD M50C60 IPE 10KV **FLUXER** PRO 63x22 **AMPX** 90A (100S) **100S** MAX 131°C

Throttle [%]	Voltage [V]	Current [A]	Input Power [W]	Output Power [W]	Torque [N×m]	RPM	Thrust [kgf]	Efficiency [%]	Efficiency [gf/W]
continuous operation									
25	399.3	2.76	1102.1	563.4	6.960	773	10	51.1	9.3
30	399.4	4.42	1765.3	1024.1	10.360	944	16	58.0	8.8
35	398.9	6.4	2553.0	1664.7	14.360	1107	21	65.2	8.4
40	398.9	9.28	3701.8	2562.9	19.150	1278	29	69.2	7.7
45	399	13.06	5210.9	3842.7	25.220	1455	38	73.7	7.2
50	399.1	17.36	6928.4	5258.4	31.150	1612	46	75.9	6.7
55	398.9	22.5	8975.3	6971.5	37.740	1764	56	77.7	6.2
short term operation									
60	398.9	28.5	11368.7	9051.0	45.110	1916	66	79.6	5.8
65	398.9	35.55	14180.9	11364.7	52.810	2055	76	80.1	5.4
70	398.8	42.35	16889.2	13570.5	59.390	2182	87	80.4	5.2
75	398.2	50.75	20208.7	16255.9	67.200	2310	98	80.4	4.9
80	397.9	51.23	20384.4	16822.3	67.610	2376	99	82.5	4.8
85	397.8	60.58	24098.7	19093.6	75.250	2423	109	79.2	4.5

Figure 4.2: Fluxer 63x22 Pro test data with M50C60 PRO.

It was observed that the M50C60 PRO motor is stated to be incapable of delivering the required power in Figure 4.2 for more than 30 seconds, which means that an alternative which can continually provide the required mechanical power and RPM needs to be selected. This is discussed in Section 4.3 below.

4.2.2. Horizontal Propeller Selection

As the horizontal propeller operates at velocities from $26\,\mathrm{m/s}$ to $83.3\,\mathrm{m/s}$, the stationary test bench is not considered an accurate representation. Furthermore, using Blade Element Momentum Theory remains impossible due to the lack of available lift polar data for off-the-shelf propellers.

As the operational velocities during cruise have higher advance ratios, it is considered that the efficiencies calculated with Actuator Disk Theory will approach reality [19]. A relation between the thrust coefficient, the advance ratio, the propeller efficiency, and the pitch angle was found for the three-bladed TU Delft X-Prop propeller in Figure 4.3a [20], as shown in Figure 4.3b and Figure 4.3c. Because it is the only propeller for which sufficient data to perform this analysis was found, it is considered an off-the-shelf component and will be analyzed in what follows.

(a) Image of a scaled-down three-bladed X-PROP in low-speed wind tunnel.

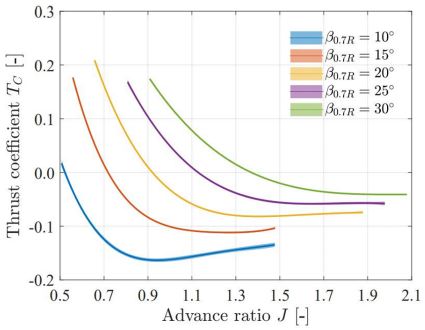

(b) Relation between three bladed X-Prop thrust coefficient and advance ratio for varying blade pitch.

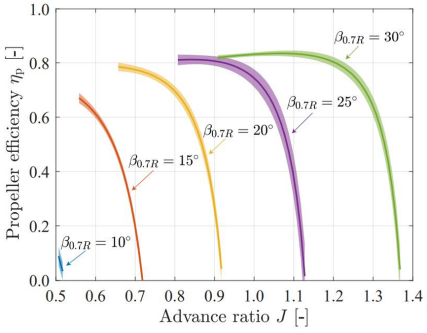

(c) Relation between three-bladed X-Prop propeller efficiency and advance ratio for varying blade pitch.

Figure 4.3: X-PROP propeller characteristics [20].

For the final performance analysis of the airborne segment, the propeller efficiency is required. Based on the comprehensive X-PROP data, this can be calculated from the thrust coefficient T_C obtained in Equation 4.1:

$$T_C = \frac{T}{0.5\rho V^2 A} \tag{4.1}$$

where T_C is the thrust coefficient, T is the required thrust in Newton, ρ is the air density in kg/m^3, V is the flight velocity in m/s and A is the disc area of the propeller in m^2. Three conditions are evaluated:

1. Stall conditions occur at $V_{stall} = 26\,\mathrm{m/s}, \rho_{stall} = 1.225\,\mathrm{kg/m^3}, T_{stall} = 110\,\mathrm{N}$.

2. Monitoring conditions occur at $V_{monitor} = 40\,\mathrm{m/s}, \rho_{monitor} = 1.225\,\mathrm{kg/m^3}, T_{monitor} = 150\,\mathrm{N}$.
3. Maximum velocity conditions occur at $V_{max} = 83.3\,\mathrm{m/s}, \rho_{max} = 0.9093\,\mathrm{kg/m^3}, T_{stall} = 400\,\mathrm{N}$.

With these conditions, the following area-normalized thrust coefficients are obtained:

$$T_{C_{stall}} = \frac{0.1267}{A} \qquad T_{C_{monitor}} = \frac{0.1531}{A} \qquad T_{C_{maximum}} = \frac{0.2657}{A} \tag{4.2}$$

To limit the highest thrust ratio to fall within the graphs of Figure 4.3b, a diameter of $1.4\,\mathrm{m}$ is needed to provide sufficient surface area. Advance ratios of 0.9 to 1.1 were found for thrust coefficients of 0.1726 and 0.0803 respectively. Using the plotted graphs, efficiencies can be found at these advance ratios. It should be mentioned that the efficiencies are calculated for $30\,\frac{\mathrm{m}}{\mathrm{s}}$, however, the efficiency is expected to improve for higher Mach numbers [20].

The three-bladed TU-Delft X-Prop in Figure 4.3a, with a diameter of $1.4\,\mathrm{m}$ and a 70% Chord angle of $28\,°$, was found to give the highest efficiencies, with 84% at maximum velocity at $3000\,\mathrm{m}$ altitude and 82% at monitoring and stall speed at sea level. The final propeller selection is shown in Table 4.2.

Table 4.2: Selected propeller data.

Application	Thrust required [N]	Selected propeller	Peak continuous thrust [N]	Weight [kg]
Horizontal	315.8	1.4m 3-Bladed XPROP	392.4	≈ 3.5
Vertical	726.9	Fluxer 63x22 Pro	853.5	1.08

4.3. Electric Motor Selection

For the selection of the electric motors, propulsion system requirements **RPR-MOT-1**, **RPR-MOT-2**, **RPR-MOT-3**, **RPR-MOT-4** and **RPR-COM-1** from Section 4.1 were considered as leading.

A comprehensive market study was performed to identify possible options that match the required power density and maximum continuous power production. Several motors with similar power density properties were found, but either at smaller scales[8] or at larger scales[9]. In particular, no UAV application exists that can continuously provide the required power at the desired weight rating, as shown during the selection of the vertical propellers.

Three alternatives were therefore explored to ensure that the stringent requirement for vertical take-off and landing capabilities is met. They are described below:

1. The options of hexacopter and octocopter, employing 6 and 8 separate electric motors respectively, were explored in the hopes that lighter motors at a similar power density would be able to satisfy the requirements. These configurations were found to significantly increase required structural mass, as well as the complexity of the design. In both cases, no motors could be found that would have allowed to maintain performance at a lower weight than the standard quadcopter configuration.
2. Another option that was explored was coaxial propellers, which are also often employed in vehicles capable of VTOL. While the main advantage of such a configuration consists of providing an increase in lift considering the increase in weight and volume, it comes at an increase in power consumption, which again makes this layout less efficient than the standard quadcopter configuration [21].
3. Heavier, more powerful electric motors with high power density were identified, which satisfy maximum continuous power requirements even with steep increases in maximum take-off mass.

Though the third option was found to the mass of the propulsion system, it was the only one that allowed for the design process to continue with COTS components, and so it was chosen. The

[8] https://eansys.de/Power-to-weight-analysis-of-brushless-outrunner-engines
[9] https://emrax.com/

selected motors for both horizontal and vertical propulsion, alongside the power provided and weight, are shown in Table 4.3. The relation between the shaft RPM and the power it provides is shown in Figure 4.4, while a picture of the motor itself is displayed in Figure 4.5 [10].

Table 4.3: Electric motor selection.

Application	Power required [kW]	Selected motor	Peak continuous power [kW]	Weight [kg]
Horizontal	30	EMRAX 188 CC	37	7.6
Vertical	12.5	EMRAX 188 AC	27	7.1

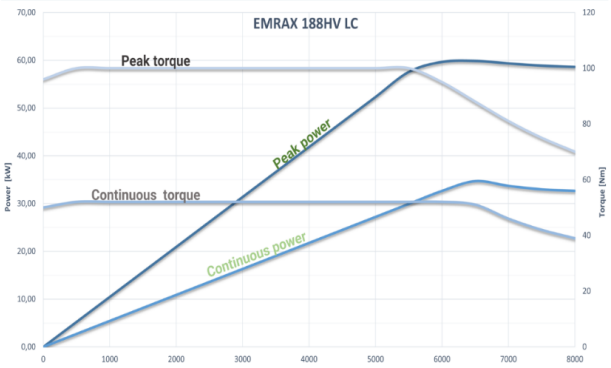

Figure 4.4: Power as a function of RPM for EMRAX 188.

Figure 4.5: EMRAX 188 motor.

It is important to note that the EMRAX 188 CC was selected for the horizontal propeller not only because it is able to satisfy the power requirement, but also because it presents cooling features (CC = combined cooling) needed for a pusher propeller configuration [10]. However, taking into account **R-SYS-2**, the ingress protection rating[11] of both the air-cooled and combined cooling EMRAX motors needs to be evaluated. The motors present an IP21 rating, which indicates protection against solid foreign objects of $12.5\,\mathrm{mm}$ diameter and greater and protection against vertically falling water drops. Because the vehicle is expected to operate in turbulent weather, each component exposed to the outside must have significantly better resistance to debris or rain in order to ensure continuous and safe operations so, appropriate housing and protection is to be considered in their integration in the structure discussed in Chapter 7.

4.4. Electronic Speed Controller Selection

With the electric motors selected, their specifications can be used to determine the performance requirements of the electronic speed controllers, as defined in Table 4.4.

Table 4.4: Propulsion subsystem requirements

ID	Requirement description	Origin
RPR-ESC-1	Each vertical electronic speed controller shall be able to withstand a continuous voltage of 384 V.	**R-MIS-5**
RPR-ESC-2	The horizontal electric motor shall be able to withstand a continuous voltage of 384 V.	**R-MIS-1**
RPR-ESC-3	The vertical electronic speed controllers shall provide a continuous current of 42 A.	**R-MIS-5**
RPR-ESC-4	The horizontal electric motor shall provide a continuous current of 84 A.	**R-MIS-1**
RPR-ESC-5	Each vertical electronic speed controller shall have a total mass of no more than 1.1 kg.	**R-MIS-5**
RPR-ESC-6	The horizontal electric motor shall have a mass of no more than 1.1 kg.	**R-MIS-1**

[10] https://emrax.com/e-motors/emrax-188/
[11] https://www.iec.ch/ip-ratings

- **RPR-ESC-1** and **RPR-ESC-2** follow from the power that the electronic speed controllers must be able to handle in order to control the EMRAX electric motors.
- **RPR-ESC-3** and **RPR-ESC-4** are derived from the amperage necessary to transfer power to the EMRAX electric motors.
- **RPR-ESC-5** and **RPR-ESC-6** follow from the initial allocated mass budgets determined in the initial sizing of the propulsion system.

The initial and best candidate for the ESC choice is the same controller used in the collection of the performance data of the vertical propeller explained in Section 4.2.1, that being the AMPX 90A HV shown in Figure 4.6 [11]. Further research to find better alternatives was carried out, but no other option is able to deliver the same performance of the AMPX at a lower or equal weight.

Figure 4.6: AMPX 90A HV.

The performance data of the AMPX 90A HV is shown in Table 4.5[12].

Table 4.5: Electronic speed controller selection.

Application	Voltage required [V]	Current required [A]	ESC chosen	Voltage provided [V]	Amperage provided [A]	Weight [kg]
Horizontal	384	84	AMPX 90A HV	440	180	1.8
Vertical	384	42	AMPX 90A HV	440	180	1.8

4.5. Noise Estimation

According to system requirement **R-SYS-16**, the vehicle must not produce more than $130\,\mathrm{dB}$ of noise measured at $100\,\mathrm{m}$ from the ground, ensuring that the noise levels produced during operations are safe for civilians within its range of action[13]. With components making up the propulsion system selected, a noise estimation has been performed to ensure compliance with this requirement.

The noise produced by the propellers will be estimated by determining a number of partial noise levels and connection factors, related to the configuration and the operating parameters of the propeller in use by means of available propeller noise test data, gathered both in static and flight conditions [22]. From these graphical relations, the following steps for propeller noise estimation can be defined [22]:

1. Determine the rotational tip Mach number.
2. Calculate partial levels FL1 (propeller power input and rotational tip speed), FL2, (diameter and number of blades), and FL3, (atmospheric absorption and spherical spread of sound).
3. Calculate the correction factor DI for directivity pattern, based on angle from the propeller axis.
4. Calculate the correction factor NC for the number of propellers.
5. Calculate the Perceived Noise Level (PNL) correction.
6. Total propeller noise is given by $FL1 + FL2 + FL3 + DI + NC + PNL$.

For the analysis of the noise produced by vertical and horizontal propellers, the VTOL and monitoring scenarios were considered, as those are the stages in the mission profile where the vehicle is closest to the height level specified by the requirement. At maximum speed, when the propellers would be producing the most noise, the vehicle is traveling at an altitude of $h_{V_{max}} = 3000m$, which considered sufficient for attenuation. Furthermore, the noise produced by the electric motors was found to be low enough to be neglected in this analysis [14].

Below, the list of inputs needed for the computation is given in Table 4.6, while the values for the partial and total noise levels for both conditions are shown in Table 4.7 [22]. The units used in the graphical relations were chosen to portray the data for repeatability.

[12] https://www.mad-motor.com/products/foc-90a-100sesc

[13] https://rnid.org.uk/information-and-support/ear-health/protect-your-hearing/how-loud-is-too-loud/

[14] See footnote 9

Table 4.6: Noise estimation inputs.

Input	Monitoring	VTOL	Unit
Propeller diameter	4.59	5.17	ft
Number of blades	3	2	-
RPM	1500	2200	rpm
Power input (per propeller)	30	17	hp
Location of noise measuring point	492, 90	328, 180	$[ft, °]$
Flight speed	74	4	kts
Ambient temperature	59	59	$°F$
Number of propellers	1	4	-

Table 4.7: Propulsion system noise levels.

Parameter	Monitoring	VTOL	Unit
FL1	55	60	dB
FL2	11	13	dB
FL3	-10	21	dB
DI	0	-4	dB
NC	0	6	dB
PNL	3	1	dB
Total	**59**	**97**	dB

With final total noise values of $59\,\mathrm{dB}$ and $97\,\mathrm{dB}$ for the horizontal and vertical propulsion systems respectively, it can be concluded that both flight conditions will respect the noise requirement.

4.6. Propulsion System Verification

The verification method for each propulsion system requirement, alongside explanations for practical application, are available in Table 4.8.

Table 4.8: Propulsion system verification methods.

ID	Verification method	Discussion
RPR-PRP-1	Demonstration	Simulate thrust performance with BEMT software and test thrust produced by the propeller in static and dynamic conditions.
RPR-PRP-2	Demonstration	Simulate thrust performance with BEMT software and test thrust produced by the propeller in static and dynamic conditions.
RPR-PRP-3	Inspection	Count the number of blades.
RPR-PRP-4	Inspection	Place propeller on a scale.
RPR-PRP-5	Inspection	Place propeller on a scale.
RPR-MOT-1	Demonstration	Connect electric motor to power supply, measure torque and revolutions per minute to compute mechanical power produced.
RPR-MOT-2	Demonstration	Connect electric motor to power supply, measure torque and revolutions per minute to compute mechanical power produced.
RPR-MOT-3	Inspection	Place electric motor on a scale.
RPR-MOT-4	Inspection	Place electric motor on a scale.
RPR-ESC-1	Demonstration	Connect ESC to power supply and measure voltage drop.
RPR-ESC-2	Demonstration	Connect ESC to power supply and measure voltage drop.
RPR-ESC-3	Demonstration	Connect ESC to power supply and measure current output.
RPR-ESC-4	Demonstration	Connect ESC to power supply and measure current output.
RPR-ESC-5	Inspection	Place ESC on a scale.
RPR-ESC-6	Inspection	Place ESC on a scale.
RPR-COM-1	Analysis	Check that the components are not designed in-house.

The methods proposed in Table 4.8 take into account that the components to be tested are all COTS, meaning that they can be purchased and direct testing of performance can be carried out. An exception to this is the horizontal propeller, which is not directly available for direct testing, hence why an alternative procedure of verification using BEMT software was proposed. Testing of the propellers can be carried out in the Faculty of Aerospace Engineering at TU Delft by means of propeller test rigs, with the additional use of a wind tunnel to simulate dynamic conditions [15]. The facilities for direct testing of the electric motors and the electronic speed controllers are discussed later in the verification of the electrical power system in Section 5.3.

[15] https://www.tudelft.nl/lr/organisatie/afdelingen/flow-physics-and-technology/flight-performance-propulsion/flight-performance/propeller-aerodynamics/facilities/propeller-test-rigs

5 | Electrical Power System Design

This chapter covers the design of the electrical power system. Based on the system-level power requirements, the generator assembly is designed in Section 5.1. Then, the power management and transmission system is documented in Section 5.2, together with the system-level electrical block diagram. Finally, verification methods are discussed in Section 5.3.

The electrical power system relies on a series-hybrid configuration, consisting of an engine that provides mechanical shaft power to a DC generator. The generator transforms mechanical power into electrical power, distributing it further to the other subsystems.

In the design of the electrical power system, it was decided to pursue a flow-down methodology. First, the generator assembly was designed based on high-level power requirements. Then, the transmission system was designed based on the individual requirements for each power consuming subsystem. All components were selected off-the-shelf, with significant effort being dedicated to integration within the internal CAN data flow system as described in Chapter 3.

5.1. Generator Assembly Design

The generator assembly provides a continuous power output to the subsystems described in Chapter 3 and the propulsion system described in Chapter 4 among others. Based on the maximum power consumption for each such component, the requirements for the generator assembly were defined and are available in Table 5.1 below.

Table 5.1: Generator assembly requirements.

ID	Requirement description	Origin
REP-GEN-1	The generator assembly shall produce no less than $51.8\,\mathrm{kW}$ continuously.	**RPR-MOT-1**
REP-GEN-2	The generator assembly shall weigh no more than $35\,\mathrm{kg}$.	Mass Budget
REP-GEN-3	The generator assembly shall be composed of COTS components.	**R-MIS-9**

- **REP-GEN-1** follows from the total power required for the maximum power scenario as discussed in Chapter 2, which includes vertical take-off with all subsystems operating at maximum power.
- **REP-GEN-2** follows from the mass allocation for the generator assembly in the preliminary sizing in Chapter 2.
- **REP-GEN-3** follows from the top-level design intention to rely on proven, already existing components.

A comprehensive study of the generator market was performed, with particular focus on new developments specifically for UAV's. However, it was found that most generators were either sized for different, far smaller applications (for example, the Pegasus Aeronautics GE70 providing a meager $4\,\mathrm{kW}$ [1]) or dangerously exceeding the weight allocation (such as the $40\,\mathrm{kW}$ LaunchPoint HPS400 Genset [2]). The search was further limited by the inability to select generators based on turboshafts or similar, as the generator needs to run even when the horizontal propulsion system is inactive.

During the market study, the UAVHE RW1-79 Aircooled Wankel Genset was found to demonstrate excellent power density beyond any other option (up to $3\,\mathrm{kW/kg}$) [3]. However, its maximum continuous power output was only $16\,\mathrm{kW}$, less than a third of the required $51\,\mathrm{kW}$. For this reason, it was decided to select four such generators working in parallel to constitute the generator assembly, resulting in a maximum continuous power output of $64\,\mathrm{kW}$. Though the official datasheet describes a component

[1] https://www.pegasusaero.ca/ge70
[2] https://launchpointeps.com/gensets
[3] https://uavhe.eu/products/rw1-79/

mass of $5.2\,\mathrm{kg}$, UAVHE has provided an estimate of $9\,\mathrm{kg}$ for a fully integrated generator, including cooling assembly, vibration supports and fuel and power lines [23] - slightly above the allocation of $35\,\mathrm{kg}$. The overall properties of the generator assembly are available in Table 5.2, with a representation of an individual generator in Figure 5.1 [23].

Table 5.2: Generator assembly properties [23].

Property	Value	Unit
Mass	36	kg
Maximum continuous power	64	kW
Specific fuel consumption	0.255	kg/kWh
Maximum output voltage	384	V
Length	177	mm
Width	197	mm
Height	162	mm

Figure 5.1: UAV RW1-79 generator [23].

The values in Table 5.2 include an engine control unit compatible with the CAN protocol, as well as the air cooling intake (which is to be added to the final assembly) [23]. The brake-specific fuel consumption allows for the calculation of the fuel mass and volume required, which is performed in the sizing of the fuel tank in Chapter 6. Finally, the generator can transmit power through 16 channels at different voltages ($14.4\,\mathrm{V}$, $28\,\mathrm{V}$, $48\,\mathrm{V}$, $192\,\mathrm{V}$, $384\,\mathrm{V}$), which allows for a straightforward connection to the transmission system [23].

5.2. Transmission System Design

From the power requirements of each individual subsystem and the power output of the selected generator assembly, the power transmission system requirements were defined, as shown in Table 5.3. Importantly, during the design process, it was also decided to include a small-scale secondary battery within the power transmission system, allowing for the airborne segment to be controllable in case of power generation failure, as discussed further below.

Table 5.3: Transmission system requirements.

ID	Requirement description	Origin
REP-TRA-1	The transmission system shall distribute no less than $12.5\,\mathrm{kW}$ to each vertical motor speed controller.	**RPR-MOT-1**
REP-TRA-2	The transmission system shall distribute no less than $30\,\mathrm{kW}$ to the horizontal motor speed controller.	**RPR-MOT-2**
REP-TRA-3	The transmission system shall distribute no less than $0.3\,\mathrm{kW}$ to the monitoring payload.	**R-SYS-7**
REP-TRA-4	The transmission system shall distribute no less than $0.196\,\mathrm{kW}$ to the avionics.	**R-SYS-10**
REP-TRA-5	The transmission system shall distribute no less than $1\,\mathrm{kW}$ to the servos.	**RT-AERO-2**
REP-TRA-6	The transmission system shall be composed of COTS components.	**R-MIS-9**
REP-BAT-1	The batteries shall have a capacity of no less than **TBD** Wh.	**R-MIS-7**
REP-BAT-2	The batteries shall be COTS components.	**R-MIS-9**

- **REP-TRA-1**, **REP-TRA-2**, **REP-TRA-3**, **REP-TRA-4**, and **REP-TRA-5** flow directly from the maximum power rating for each individual component as selected in Chapter 3, Chapter 4 and Chapter 6.
- **REP-BAT-1** follows from the contingency strategy (**TRRC-23**) for the risk of power generation and/or propulsion failure. A secondary battery can be used to power system avionics and control surface servos for a limited duration to ensure the possibility of a glide landing. Its required capacity is dependent on the power it has to provide and the duration of the maneuver, and has been therefore set as TBD pending further analysis.

- **REP-TRA-6** and **REP-BAT-2** follow from the top-level design intention to focus on proven, already existing components.

Two transmission architectures are required: between the generators and the propulsion system (high current, high voltage) and between the generators and other subsystems (medium current, low voltage).

The high-voltage transmission circuit relies on several relays connected to a microcontroller to provide unregulated high-voltage current to the five electronic speed controllers. The transmission lines are redundant, so that each generator can transmit power to each electronic speed controller. The added mass in wiring and relays is considered justified by the ability to still provide significant power to the vertical/horizontal motors even in the case of individual generator failure.

Though the electronic speed controllers act as voltage regulators for the high-voltage transmission circuit, a specialized regulator is required for the low-voltage path. Therefore, the VisionAirtronics 1800W Power Distribution Unit (PDU) was selected to manage this path, allowing for two 24-48V inputs and six regulated outputs [4]. The PDU weighs $2.7\,\mathrm{kg}$ and is CAN-compatible.

As discussed above, a secondary battery has been selected to guarantee redundancy in case of power generation failure. The MaxAmps Li-ion 2800 10S1P 36V battery pack provides a total of $100.8\,\mathrm{Wh}$, covering all non-propulsion system power consumption for more than three minutes [5]. Pending further analysis, this capacity is considered sufficient to cover airborne segment control during an emergency glide landing. A lightweight battery management system was also selected in the CAN-compatible VisionAirtronics 15S BMSB, allowing for monitoring, self-balaning and recharge of the battery [6]. The battery weighs $0.48\,\mathrm{kg}$, while the battery management system weighs less than $0.3\,\mathrm{kg}$. The three main components are shown in Figure 5.2 below.

(a) VisionAirtronics 1800W PDU[1]

(b) MaxAmps Li-ion 2800 10S1P 36V[2]

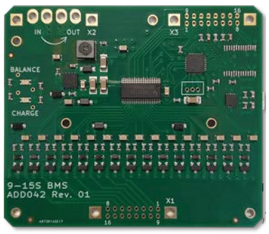

(c) VisionAirtronics 15S BMSB[3]

Figure 5.2: Power transmission system components.

The six output lines from the PDU were distributed to the individual components according to their consumption requirements, as shown in Figure 5.3 below. Though the microcontrollers for generator distribution were selected as the Microchip ATmega16M1[7], and step-down voltage converters were selected as the Wurth Elektronik 173011235 Power Module[8], further wiring and relay components were not selected in detail, as highly specific wiring and integration topologies are considered outside the scope of this report. The wires were sized for the lowest lowest multiple of $0.5\,\mathrm{A}$ higher than the required passing current, with a wiring mass estimate of 20% of the mass of each component, or a total of $9.1\,\mathrm{kg}$, being developed based on literature [24]. Though this estimate is considered to be quite above the actual required wiring, it provides a buffer for relays and power converters, and will thus be used in the final mass estimation.

[4] https://vat.aero/1800w-power-distribution-unit/
[5] https://maxamps.com/collections/10s-36v-li-ion/products/li-ion-2800-10s1p-36v-battery-pack
[6] https://vat.aero/15s-balancer-product-brief-v1-4/
[7] https://www.microchip.com/en-us/product/ATmega16M1
[8] https://www.we-online.com/en/components/products/

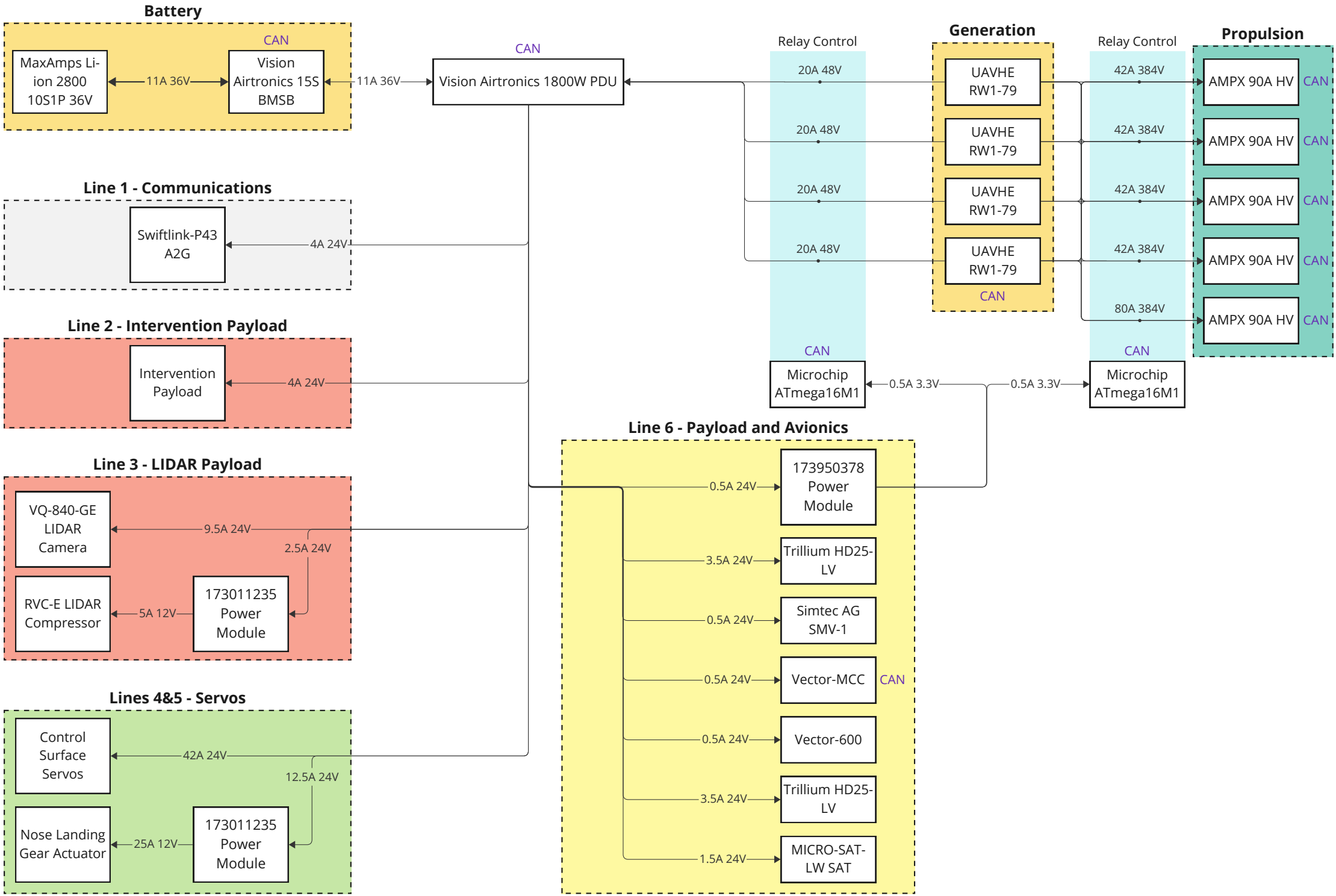

Figure 5.3: Electrical Block Diagram

5.3. Electrical Power System Verification

The electrical power system consists entirely of COTS components. This means that verifying its requirements is a straightforward process, starting with purchasing the required components, and providing a safe experimental environment to perform the practical demonstration of requirement compliance. The verification methods for each requirement are described in Table 5.4, together with a short breakdown of the practical verification procedure.

Table 5.4: Electrical power system verification methods.

ID	Verification method	Discussion
REP-GEN-1	Demonstration	Integrate individual generators into combined assembly, connect to load, and measure total current and voltage while running at maximum continuous power condition.
REP-GEN-2	Inspection	Place generator assembly on a scale.
REP-GEN-3	Analysis	Check that the components are not designed in-house.
REP-TRA-1	Demonstration	Integrate generator assembly with wire/relay transmission line, connect to each electronic speed controller, and measure current and voltage while running at maximum power requirement.
REP-TRA-2	Demonstration	Integrate generator assembly with wire/relay transmission line, connect to electronic speed controller, and measure current and voltage while running at maximum power requirement.
REP-TRA-3	Demonstration	Integrate generator assembly with wire/relay transmission line, connect to power distribution unit, connect to monitoring payload, and measure current and voltage while running at maximum power requirement.
REP-TRA-4	Demonstration	Integrate generator assembly with wire/relay transmission line, connect to power distribution unit, connect to avionics, and measure current and voltage while running at maximum power requirement.
REP-TRA-5	Demonstration	Integrate generator assembly with wire/relay transmission line, connect to power distribution unit, connect to servos, and measure current and voltage while running at maximum power requirement.
REP-TRA-6	Analysis	Check that the components are not designed in-house.
REP-BAT-1	Demonstration	Integrate battery pack into battery management system, connect to load, and measure total current and voltage while timing discharge.
REP-BAT-2	Analysis	Check that the components are not designed in-house.

In practical terms, the detailed verification procedures require access to an electrical testing facility, including an insulated test stand, a voltmeter, adequate non-conductive clothing, and a variable load that can run up to $64\,\mathrm{kW}$. Such a facility can be found in the Faculty of Electrical Engineering, Mathematics, and Computer Science at the TU Delft, namely the Electrical Energy Conversion Laboratory. This laboratory is specialized in the testing of rotating electric machines, with significant experience in aviation component testing [9] that can also be used in the testing of the electric motors and electronic speed controllers selected in Chapter 4.

[9] https://www.tudelft.nl/en/eemcs/the-faculty/departments/electrical-sustainable-energy/dc-systems-energy-conversion-storage/electrical-sustainable-power-lab/electrical-energy-conversion-laboratory/

6 | Wing Design

The design of the wing starts with the development of the requirements in Section 6.1. Then,Section 6.2 presents the aerodynamic design, including the selection and optimization of the airfoil geometry. The subsequent structural design of the wingbox, ribs, skin, and fuel tank is covered in Section 6.3, with Section 6.4 providing the final results and Section 6.5 describing the sizing of the ailerons. Finally, Section 6.6 presents verification methods for the subsystem requirements, as well as aerodynamic and structural verification methodologies pursued directly by the design team.

6.1. Wing Requirements

The design of the wing starts with requirements for aerodynamic and structural performance. The airfoil to be selected should fit the diverse flight profile, with a sufficiently high maximum lift coefficient to achieve the low imposed stall speed of $25\,\mathrm{m/s}$ and high efficiency at the top speed of $83.3\,\mathrm{m/s}$. The requirements for the wing section are presented in Table 6.1.

Table 6.1: Wing section requirements.

ID	Requirement description	Origin
RWI-AER-1	The $C_{L_{max}}$ of the aircraft shall be at least 1.2.	**R-SYS-4**
RWI-AER-2	The C_L achieved at the top speed of $83.3\,\mathrm{m/s}$ at $3000\,\mathrm{m}$ shall be at least 0.159.	**R-STK-2**
RWI-STR-1	The structure shall not yield under the maximum load circumstance.	**R-STK-5**
RWI-STR-2	The wingtip shall not deflect more than 10% of the wingspan when performing a $3.6\,\mathrm{g}$ pull-up maneuver.	**R-STK-5**
RWI-STR-3	The wing structure shall have a precipitation tolerance of no less than $50\,\mathrm{mm/h}$.	**R-SYS-2**
RWI-STR-4	The wing structure shall store the fuel and necessary fuel systems.	
RWI-AIL-1	The aileron shall provide a roll rate of $30°$ in 1.5 seconds [25].	**R-SYS-12**
RWI-AIL-2	The aileron shall have a maximum downwards deflection of °15.	**R-SYS-12**
RWI-AIL-3	The aileron shall have a maximum upwards deflection of 75% of the maximum upwards deflection to account for adverse yaw.	**R-SYS-12**
RWI-AIL-4	The aileron chord shall be 20% of the chord of the wing.	**R-SYS-12**
RWI-AIL-5	The aileron shall not be placed in the same spanwise position as the booms supporting the propellers.	**R-SYS-12**
RWI-AIL-6	The aileron shall have an outward location fixed at 4.5 meters along the span, to create a maximal moment arm while leaving space at the tip of the wing.	**R-SYS-12**

- **RWI-AER-1** has to be met in order to fly at stall speed.
- **RWI-AER-2** is set to ensure equilibrium during flight at the top speed flight profile.
- **RWI-STR-1** is crucial to maintain the aerodynamic shape of the wing and produce lift.
- **RWI-STR-2** stems from the fact that too much deflection could lead to aerodynamic losses.
- **RWI-STR-3** needs to be met to meet **R-SYS-2**.
- **RWI-STR-4** results from the decision to store the fuel in the wing.
- **RWI-AIL-1** will ensure that the UAV will be sufficiently controllable during monitoring flight.
- **RWI-AIL-2** should be met in order to create a sufficient moment arm to meet **RWI-AIL-1**.
- **RWI-AIL-3** should be met to counter adverse yaw during rolling.
- **RWI-AIL-4** should be met in order to create a large enough moment arm to meet **RWI-AIL-1** while limiting the power required for the servo.

- **RWI-AIL-5** needs to be met in order to prevent structural interference, which would also impact control performance.
- **RWI-AIL-6** flows down directly from **RWI-AIL-4** and **RWI-AIL-5**.

6.2. Wing Aerodynamic Design

The aerodynamic design of the wing begins with the selection of the airfoil. To this end, the literature-recommended approach is to start by selecting a standard airfoil, then optimize its geometry to reach the desired aerodynamic properties [26]. The option space was restricted to NACA-series airfoils to reduce the required effort, and the various NACA number series were themselves evaluated.

In literature, the 4-digit, 5-digit, 6-digit, and 7-digit series are generally evaluated based on stall characteristics, maximum lift coefficient, drag performance, and pitching moment [27]. A synthesis of the advantages and disadvantages of each airfoil series is available in Table 6.2.

Table 6.2: Airfoil series properties [26, 27].

Series	Advantages	Disadvantages	Discussion
4-digit	High stall resistance, gradual drag increase with lift.	Relatively low maximum lift coefficient and high drag.	Typically used in light training aircraft and tailplanes.
5-digit	Best in class maximum lift coefficient.	Low stall resistance and high drag.	Typically used for wings requiring high lift performance.
6-digit	High maximum lift coefficient, with extended laminar boundary layer resulting in best-in-class drag performance over limited performance conditions.	High pitching moment and low stall resistance.	Typically used in high-speed applications, significant design experience.
7-digit	Low drag over limited performance conditions and low pitching moment.	Low maximum lift coefficient and low stall resistance.	Rarely used, little design experience.

During the design process, the 4-digit and 7-digit series were excluded from the option space, due to their low maximum lift coefficient, which is considered critical to counteract UAV mass. In comparing the 5-digit and 6-digit series, though the 5-digit shows higher maximum lift coefficients, the 6-digit series, critically, allows for redesign of the geometry to capture the laminar flow regime and optimize performance for a limited range of operation conditions [26]. Due to their high maximum lift coefficient and optimization potential, the NACA 6-series were therefore selected and actual airfoil options were explored.

6.2.1. Initial Airfoil Selection and Performance

Airfoil selection is performed according to the operational regime of the aircraft, in this case with principal focus on obtaining high endurance at monitoring speed. The operational regime for airfoil selection is represented by the Reynolds number. As the UAV is to monitor at around $38\,\mathrm{m/s}$ between $50\,\mathrm{m}$ and $500\,\mathrm{m}$ altitude, the Reynolds number it will encounter is calculated as:

$$\mathrm{Re} = \frac{\rho v l}{\mu} = \frac{v l}{\nu} \approx 1.3 \cdot 10^6 \tag{6.1}$$

where ρ is the air density, v is the free stream velocity, l is the chord length of the airfoil, μ is the dynamic viscosity, and ν is the kinematic viscosity.

With this Reynolds number, a database of NACA 6-digit series airfoils was sorted for $\frac{CL^3}{CD^2}$, which is the parameter to be maximized to ensure high endurance [28]. The best-performing airfoil on this parameter was found to be the NACA65(3)-618 (shown in Figure 6.1) and thus this airfoil was analyzed to check whether it could meet the Class-II sizing requirements. The airfoil geometry was inserted into the XFLR5 aerodynamic analysis program as a three-dimensional flying wing with the same parameters as in Chapter 2. The performance of the airfoil between Reynolds numbers of $5 \cdot 10^5, 1 \cdot 10^6$ and $4 \cdot 10^6$ is presented in Figure 6.2.

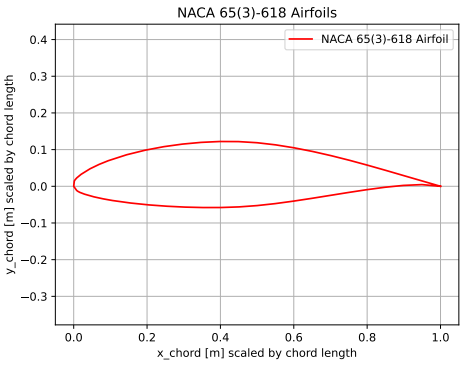

Figure 6.1: NACA65(3)-618 airfoil.

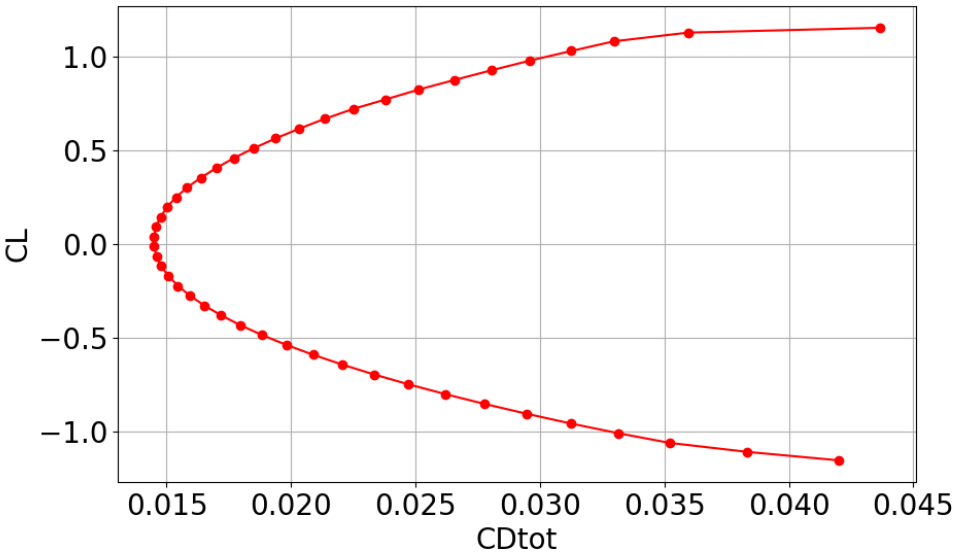

Figure 6.2: NACA 65(3)-618 airfoil performance analysis.

From Figure 6.2, the flying wing can be observed to satisfy the $\frac{C_L}{C_D}$ requirement and for the C_L at monitoring and maximum speed. However, as for the maximum lift coefficient, it does not reach $C_{L_{max}} = 1.2$ for the lower Reynolds number (stall-critical). Therefore, the optimization algorithm in XFLR5 has been used to optimize for a higher $C_{L_{max}}$.

6.2.2. Airfoil Optimization

The XFLR5 program allows for the geometry to be optimized for a certain parameter, in this case obtaining $C_{L_{max}} = 1.5$ at $\alpha = 5$ and a Reynolds number of $1 \cdot 10^6$, the closest to the monitoring conditions. The swarm-type algorithm was used in optimization [29], resulting in the geometry in Figure 6.3. The optimized airfoil is more slender and shows a more pronounced camber, with its performance shown in Figure 6.4.

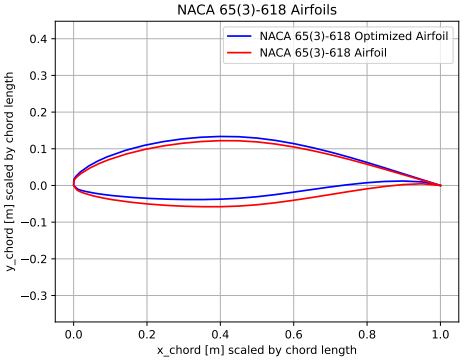

Figure 6.3: Optimized airfoil.

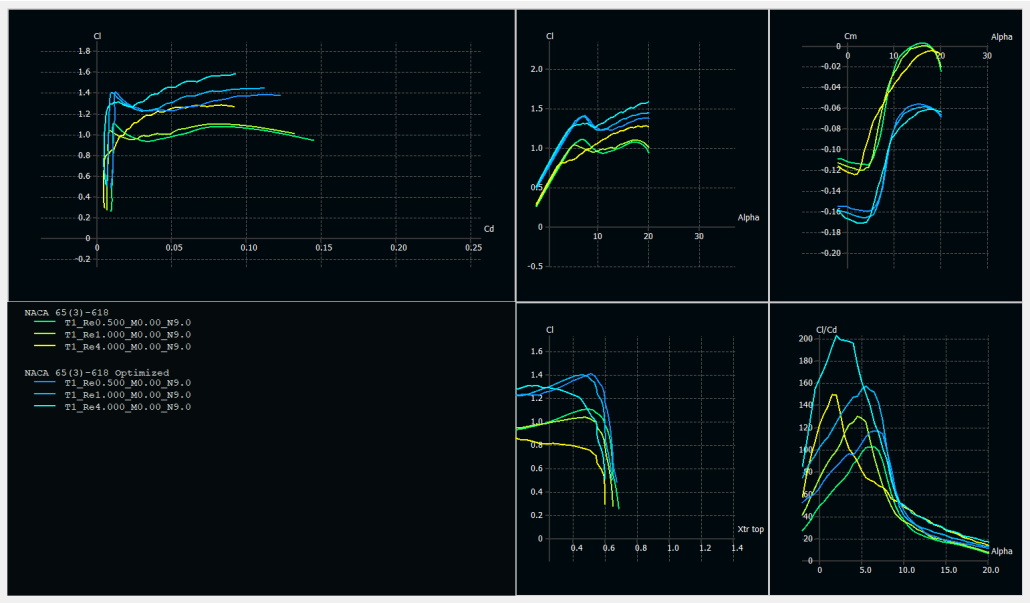

Figure 6.4: Performance for the NACA 65(3)-618 airfoil (green) and its optimized version (blue).

As seen from Figure 6.4, the entire range of C_L shifts upwards, meaning a higher C_L is obtained at a similar α and a higher $C_{L_{max}}$. It now also passes the $C_{L_{max}}$ requirement and improves the glide ratio, increasing endurance even further (**TRRC-8**). This optimized version of the NACA 65(3)-618 fulfils all set performance requirements, and was therefore chosen for the wing design.

6.3. Wing Structural Design Methodology

The selection of the airfoil allowed for the wing structure to be designed. Given the requirements for transportability, a modular wing design was pursued, with a rigid middle wing integrated within the fuselage and detachable sections closer to the wingtip. The detachable sections are split just after the booms that connect the VTOL motors and the empennage. This configuration, ensures that all fuel can be stored in the middle part of the wing, without integration of the fuel lines being required during every assembly (**TRRC-5**). Additionally, loads caused by the VTOL motors and tail can be transferred to the fuselage through an integrated connection, resulting in lighter structures being required when compared to a discontinuous part.

The strength and stiffness of the wing is provided by a wingbox, representing a closed-section structure rigid in shear, beinding and torsion [5]. Its design starts with the geometrical configuration layout.

6.3.1. Wingbox Geometry

The positioning of the wing box is determined by the shape of the airfoil. A Python program has been created to precisely calculate the wing box placement. First, the 2D airfoil is plotted, with coordinates retrieved from Airfoiltools' online database [1]. Subsequently, the optimized NACA 65(3)-618 airfoil coordinates are acquired from XFLR 5, as elaborated in Section 6.2.2. These coordinates are imported into Python and harmonized to a chord length of 1 meter. Consequently, the coordinates are mapped to the appropriate coordinate system, yielding the 2D airfoil coordinates at the root. The root chord length is determined by the mean chord, derived from the ratio of the wing area to the wingspan.

An important step is to identify the location of the front and aft spars in the wing, as this determines the entire geometry of the wingbox. For preliminary UAV design, literature gives a front spar position at 20% of the chord length and an aft spar placement at 70% of the chord length [5]. The front spar is positioned at a relatively high thickness of the wing to accommodate a larger wing box and spar. Sufficient space is also allocated for the placement of ailerons near the aft spar.

[1] http://airfoiltools.com

These percentages are fixed along the entire wingspan, so the spar spacing is strictly determined by the chord length at each location. In turn, this allows for the calculation of the leading edge and trailing edge sweep using geometry. The leading edge sweep will be important for calculating the corner coordinates of the wingbox and the x-position of the leading edge mean aerodynamic chord.

As previously explained, the spacing between the spars depends on the chord length. The chord length can be calculated as a function of the spanwise location y, span b, and taper ratio λ, as shown in Equation 6.2.

$$c_y = c_{root}\left(1-(1-\lambda)\frac{y}{\frac{b}{2}}\right)dy \tag{6.2}$$

The x-coordinates of the leading edge and trailing edge at a specific location along the span are determined using leading edge sweep geometry. Subsequently, the coordinates of the front and aft spars are derived from these values. A vertical straight line is then drawn, intersecting the upper and lower airfoils at this location. The points of intersection serve as the coordinates for the corners of the wingbox and are denoted as $z_{upper_{front}}$, $z_{lower_{front}}$, $z_{upper_{aft}}$, and $z_{lower_{aft}}$.

Since the chord length varies along the wingspan and due to the presence of sweep, the enclosed area of the wingbox reduces towards the wingtip. The volume of the wingbox is calculated using Equation 6.3:

$$\int_0^{y_{boom}} \frac{(z_{upper_{front}}(y)-z_{lower_{front}}(y))+(z_{upper_{aft}}(y)-z_{lower_{aft}}(y))}{2} c_{root}\left(1-(1-\lambda)\frac{y}{\frac{b}{2}}\right)dy \tag{6.3}$$

As mentioned in Section 6.3.7, the fuel will be stored up to the tail boom. Therefore, the upper limit of Equation 6.3 is the position of the boom y_boom, and the lower limit is the root chord location. When determining the enclosed area of the wingbox in the code, a straight line is drawn between $z_{upper_{front}}$ and $z_{upper_{aft}}$, and another straight line is drawn between $z_{lower_{front}}$ and $z_{lower_{aft}}$ to represent the upper and lower plates of the wingbox.

The side view of the wingbox can be seen in Figure 6.5a, and a 3D visualization of the wingbox along the span is displayed in Figure 6.5b. These representations are simplified, as in reality the upper and lower airfoil sheets are used to enclose the wingbox instead of flat plates. This means that the wingbox volume calculated using this method is underestimated, resulting in a conservative allocation for the fuel storage volume in Section 6.3.7.

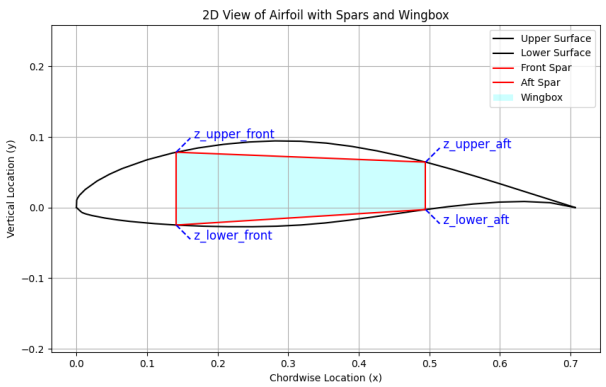

(a) Sideview of the wingbox at the root of the wing.

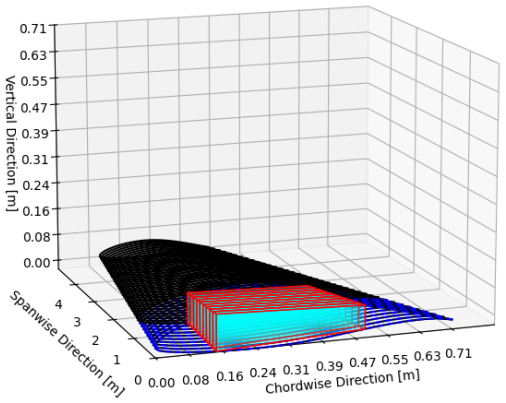

(b) 3D visualization of the wingbox along the wingspan.

Figure 6.5: Wingbox positioning

With the modeled wingbox geometry defined, the structural design can continue. A skin-panel method was used to simulate the wingbox and obtain its resistance to shear and bending as a function of the material properties and section thicknesses [30, 5]. The wingbox was divided into an upper and lower cap and two shear webs.

6.3.2. Structural Model Assumptions

To calculate the structure and mass of the wing, several assumptions were made, simplifying the model. They are described below:

- **A-WS-01** : A safety factor of 1.5 is applied to the limit lift and thrust loads to satisfy safety design regulations (**TPRC-43**) [2].
- **A-WS-02** : Each VTOL propeller is assumed to produce same thrust.
- **A-WS-03** : Only the half-span of the wing is modelled, and is split into 100 segments to be analyzed.
- **A-WS-04** : The lift is considered to act in the vertical plane.
- **A-WS-05** : The wingbox cross-section is idealized as rectangular. In reality, the top and bottom panels follow the shape of the airfoil.
- **A-WS-06** : The wingbox is modeled as a cantilever beam, fixed at the fuselage connection.
- **A-WS-07** : The bending loads are assumed to be fully carried by the top and bottom panel of the wingbox [5].
- **A-WS-08** : The shear loads are assumed to be carried fully by the shear webs [5].
- **A-WS-09** : The shear webs are assumed to be one panel, with the height being the average of the two panels [5].

These assumptions are expected to make the design more conservative, and are to be verified in Section 6.6.

6.3.3. Load Analysis

The most constraining load cases were analyzed, together with the stationary taxi case, in order to calculate the deflection of the wing before vertical take-off. The load cases are described below:

- Positive 3.6g maneuver at MTOW. In this case, the lift, wing structure weight, and boom mass play a role. The fuel tanks are assumed to be empty, since otherwise the load case would be less critical, due to the fuel relieving stress on the wing.
- Negative 1.52g maneuver at MTOW. In this case, all forces act in the negative direction: Lift, weight, boom weight, and fuel weight.
- Vertical flight with a thrust-to-weight ratio of 1.2. This case was chosen as it applies different point loads on the structure than during conventional flight. The following loads are applied here: thrust due to the VTOL propellers, boom weight, and wing weight.
- Stationary taxi. When the aircraft is stationary, only the wing weight, boom weight, and fuel are applied.

During these load cases, the following loads were identified. The first load identified is the lift force. The total lift distributed over the wing should equal the weight of the aircraft multiplied by the load factor, with the distribution calculated during the XFLR5 analysis performed in Section 6.2. The lift value at any point on the span can be seen in Equation 6.4, where $L(y)$ is the lift at a specific span position, $L_{local}(y)$ is the local lift again at a specific span position, and F_{max} is the total maximum load of the wing either positive or negative. L_{local} is important for the distribution throughout the span but not as a value of itself as it is normalized in the model.

[2] https://www.law.cornell.edu/cfr/text/14/25.303

$$L(y) = \frac{L_{local}(y) * F_{max}}{\int_0^{b/2} L_{local(y)}\, dy} \tag{6.4}$$

The weight of the wing is considered distributed over the wing and proportional to the chord. Due to the small value of the wing mass compared to the ultimate load of the lift see, the proportional distribution is considered acceptable. The weight of the wing is defined as Equation 6.5, where $W_{wing}(y)$ is the weight at a specific span position, $c(y)$ is the chord at a specific span position, and W_{wing} is the total wing weight.

$$W_{wing}(y) = \frac{c(y) * W_{wing}}{\int_0^{b/2} c(y) dy} \tag{6.5}$$

The boom weight is considered as a point mass at the corresponding distance from $b = 0$. It consists of the weight of the boom, the vertical propulsion system, and the tail. The boom weight F_{boom} points in the negative z direction and is defined as shown in Equation 6.6, where the weights of the boom, VTOL propulsion system and empennage are summed up. During VTOL, a point load is set again at the corresponding boom distance shown in Equation 6.7. The VTOL thrust points in the positive z direction. A reaction force and moment is added at the root as well, so that the structure is in equilibrium.

$$F_{boom} = W_{boom} + W_{prop} + W_{empennage} \tag{6.6}$$

$$T_{VTOL} = T/W * MTOW \tag{6.7}$$

The shear force can be calculated for a distributed load and for point loads. The shear at any point on the wing due to a point load can be calculated as shown in Equation 6.8, where $V_{point}(y)$ is the shear force at a specific span position, F is the point force applied and y_0 is the distance where the point force is applied [30]. For the lift and weight distributed load, Equation 6.9 can be used, where $V_{\text{dsitributed}}(y)$ is the shear force, and $w(y)$ is the distributed load [30].

$$V_{point}(y) = +F(y > y_0) \tag{6.8}$$

$$V_{dsitributed}(y) = \int_0^y w(y)\, dy \tag{6.9}$$

The moment $M(y)$at any point on the wing is the integral of the shear force throughout the span of the wing, shown in Equation 6.10 [30]. The area moment of inertia needed I_x to resist the moment can be calculated as shown in Equation 6.11, where y_c is the maximum distance of the wingbox to the centroid of said wingbox, and σ_{yield} is the yield stress of the material [30]. The yield stress was chosen as a failure mode, as it must follow **RWI-STR-1**. The centroid is calculated assuming that all panels have the same thickness. In reality this is not the case, but it is considered sufficiently accurate as the top and bottom panels and the left and right shear webs have equal thicknesses, as further discussed in Section 6.3.4.

$$M(y) = \int_y^{b/2} V(y)\, dy \tag{6.10}$$

$$I_{xx}(y) = \frac{M(y) * y_c}{\sigma_{yield}} \tag{6.11}$$

6.3.4. Wingbox Structural Design

The wingbox is defined as a top and bottom panel and two shear panels. To reduce the degrees of freedom of the design, it is decided that the top and bottom panels shall have the same thickness, and the shear webs are treated as one panel as assumed in **A-WS-09**. The panels are split in point masses to ease the calculation of the area moment of inertia. Due to the high calculation speed, 1000 point masses are assumed, over a maximum distance of $0.5\,\mathrm{m}$. The area of each panel is split over the point masses equally.

For the top and bottom panel, the area moment of inertia normalized with thickness I_{xxt} is calculated as shown in Equation 6.12. In this case a 1mm thickness t is chosen, p is the amount of point masses,

$y_c(n)$ is the distance from the point mass to the centroid, and l is the length of the top or bottom panel [5]. Due to the linear relationship between thickness and area moment of inertia, The necessary thickness $t_{bending}(y)$ at each point on the span for the top and bottom panel can be calculated as shown in Equation 6.13 [5].

$$I_{xxt} = \sum_{n=0}^{p} \frac{y_c(n)^2 * l * t}{p} \tag{6.12}$$

$$t_{bending}(y) = \frac{I_{xx}(y)}{I_{xxt}(y)} \tag{6.13}$$

The thickness of the shear panels can be calculated by simplifying the shear stress equations for a rectangular cross-section. Equation 6.14 shows the simplified equation, where $t_web(y)$ is the necessary thickness needed of the web together at each point on the span, h_{spar} is the average height of the spar, and $\tau_{strength}$ is the shear strength of the material [30]. When calculating the thickness, the model rounds $t_{bending}(y)$ and $t_{web}(y)$ up to the nearest multiple of $0.1\,\mathrm{mm}$, to account for manufacturing tolerances.

$$t_{web}(y) = \frac{3 * V(y)}{2 * h_{spar}\tau_{strength}} \tag{6.14}$$

With the thickness calculated for yielding calculated, the stiffness-driven design studies the deflection of the wing as a function of distance from the root chord. The first step is to calculate the derivative of the deflection $\Delta z'(k)$ due to a specific moment M calculated previously in Equation 6.10, shown in Equation 6.15 [5]. This is done for each section Δy span-wise, which if the semi-span divided by the amount of sections. k is the specific section, with 1 being the section at the root and 100 the last section at the tip. $\Delta z'(k)$ is thus a numerical integration starting from the root. The actual deflection $\Delta z(k)$ can straightforwardly be calculated by numerically integrating again throughout the span, shown in Equation 6.16 [5].

$$\Delta z'(k) = -\sum_{i=1}^{k} \frac{M(i)}{E * I_{xx}(i)} * \Delta y \tag{6.15}$$

$$\Delta z(k) = \sum_{i=1}^{k} \Delta z'(k) * \Delta y \tag{6.16}$$

6.3.5. Rib Structural Design

Ribs are used to support the aerodynamic shape of the wing and to transfer the loads from the skin to the wingbox [31]. The study of rib spacing and thickness is complex and requires extensive calculations and design choices such as cutouts, truss structure design, variable rib spacing, or rib configuration [31] and is thus considered beyond the scope of this design report. Nonetheless, a specific spacing must be chosen to have a complete structural design. A total of 10 ribs per semi-span was chosen, with a thickness of $2\,\mathrm{mm}$ and evenly spaced [5].

6.3.6. Skin Design

The leading and trailing edge of the wing are not part of the wingbox, and must transfer the local aerodynamic loads to the ribs and wingbox. For aluminum plates, literature recommends a minimum thickness of $0.4\,\mathrm{mm}$ to transfer shear, hence this value is chosen for the skin thickness [32].

6.3.7. Fuel Tank Design

The maximum fuel mass required is calculated in Chapter 13 to be equal to $41.91\,\mathrm{kg}$. Assuming a density of $800\,\mathrm{kg/m^3}$ for kerosene-based jet fuel[3], this would result in a required storage volume of $60\,\mathrm{L}$. The total volume of the inner wingbox segment is equal to $82.46\,\mathrm{L}$ starting from the root chord, which should comfortably allow for all required fuel to be stored. Additional volume is expected to be required for fuel pumps and lines, as well as specialized fuel tank diaphragms. To ensure that trapped fuel mass is reduced to an absolute minimum, the ribs are to be thinned down on the bottom panel. Further discussion of the layout is available in Chapter 13.

[3] https://chemicalsafety.ilo.org/dyn/icsc/showcard.display?p_lang=en&p_card_id=0663&p_version=2

6.4. Wing Structural Design Results

The yield and deflection of the wingbox depend entirely on the structural material, which is to be selected based on specific strength. Though composites show best-in-class performance, they are currently impossible to recycle [33], and their use would result in a breach of **R-MIS-9**. For this reason, a standard aerospace aluminum alloy was selected, namely Aluminum 6061-T6, which shows high strength and stiffness, and high recycling fraction [33]. It has the following properties[4]:

- Density: $2700\,\mathrm{kg/m^3}$
- Tensile yield strength: $276\,\mathrm{MPa}$
- Shear strength: $207\,\mathrm{MPa}$
- Elastic modulus: $68.9\,\mathrm{GPa}$

With the material selected, Figure 6.6 shows the four analyzed critical cases. Each plot shows the distributed loads, the point loads, and the final shear. A dotted line is drawn at z=0 to differentiate positive and negative loads. All external loads have been multiplied with the safety factor of 1.5 mentioned in **A-WS-01**. In the 3.6g and the VTOL maneuver, the reaction force must be negative to counteract the positive shear force. The other two cases create a positive shear force at the root, hence a negative reaction force is needed. The maximum shear force on the wingbox occurs during a 3.6g maneuver and its magnitude is $6598\,\mathrm{N}$.

Figure 6.6: Forces and final shear plotted over the semi-span.

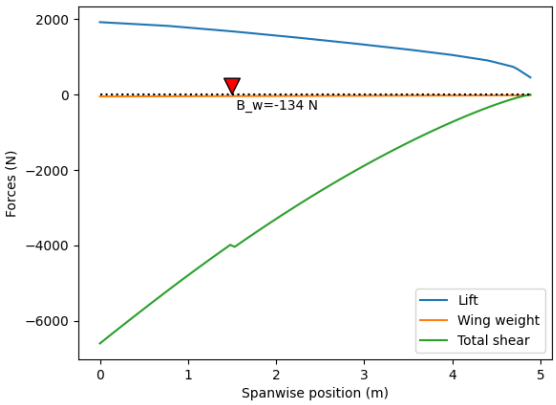

(a) 3.6g pull-up maneuver.

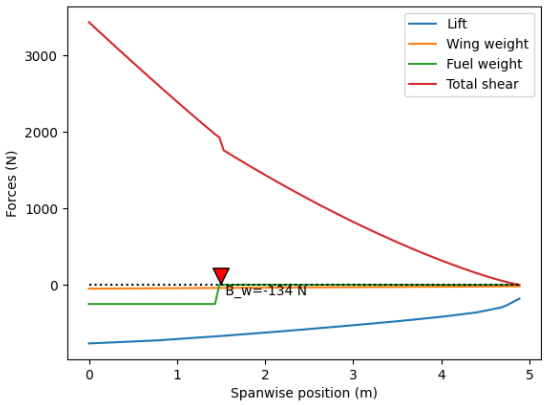

(b) -1.52g pull-down maneuver.

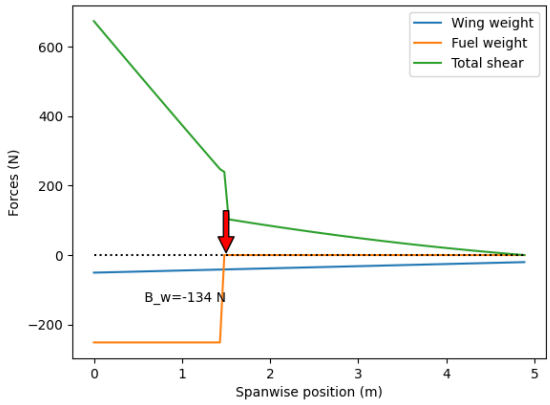

(c) Stationary taxi.

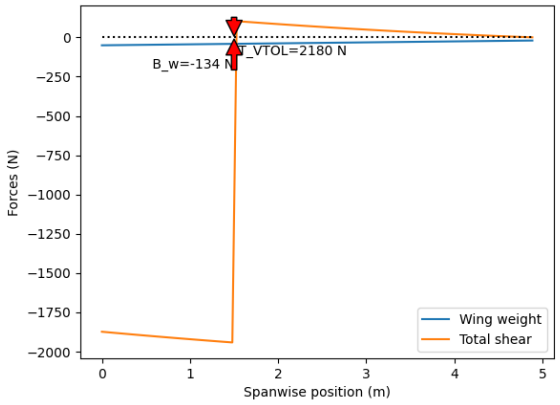

(d) VTOL maneuver.

[4] https://www.aerospacemetals.com/wp-content/uploads/2023/06/Aluminum-6061-T6-6061-T651.pdf

The bending moment for each case can then be calculated, as shown in Figure 6.7a. The maximum moment is again found during a 3.6g maneuver and is $13\,851\,\mathrm{Nm}$ at the root. This load case is used to calculate the thickness needed for the structure to not yield, according to requirement **RWI-STR-1**. Figure 6.7b shows the necessary thickness of the top and bottom panel as well as the shear panels. Due to the fact that sheet metal is not manufactured for any thickness, a thickness rounded to $0.5\,\mathrm{mm}$ is used. When a thinner sheet metal can be used, a connection must be made between the two different thickness sheets. The thickness of the sheets ranges from $2.5\,\mathrm{mm}$ to $0.5\,\mathrm{mm}$.

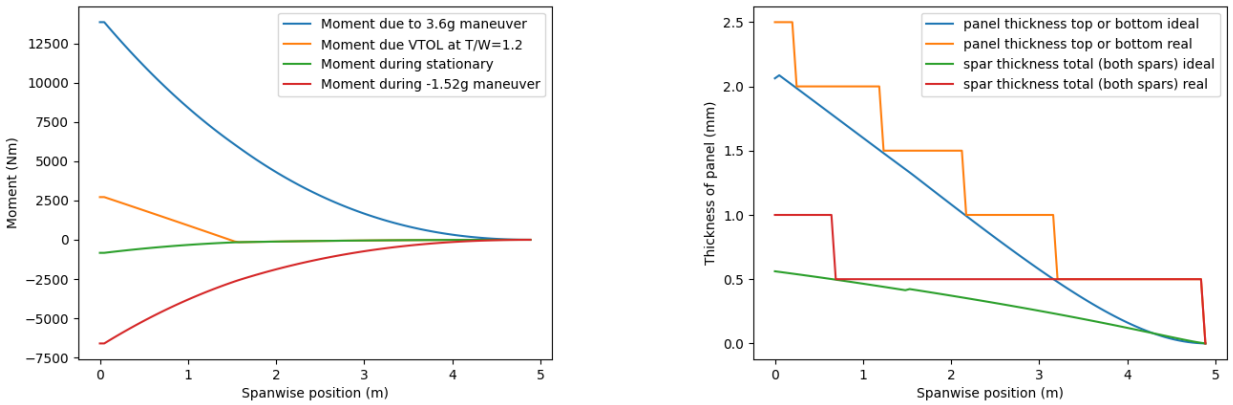

(a) Bending moment diagram of the semi-span wing.

(b) Thickness needed for the 4 panels of the wingbox.

Figure 6.7: Bending moment of the four loading cases and the necessary thickness to withstand the maximum load.

The deflection of the four cases is shown in Figure 6.8a, with the cross-section of the root chord available in Figure 6.8b. The highest positive deflection happens again during a 3.6g maneuver and equals $918\,\mathrm{mm}$. This deflection complies with requirement **RWI-STR-2** as it is less than $10\% * \text{span} = 989\,\mathrm{mm}$.

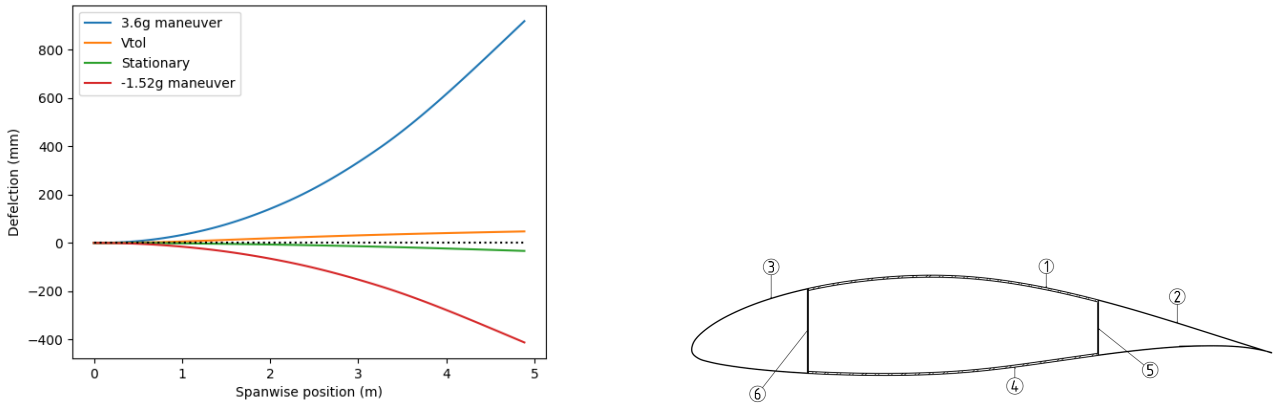

(a) Wing deflection of the semi-span during the four cases

(b) Cross-section of the root chord

Figure 6.8: Wing deflection and cross-section of the wing

In Figure 6.8b, the bubbles represent the following parts of the wing structure:

- **1:** Top wingbox panel, ranging from $2.5\,\mathrm{mm}$ to $0.5\,\mathrm{mm}$
- **2:** Trailing edge skin, $0.4\,\mathrm{mm}$
- **3:** Leading edge skin, $0.4\,\mathrm{mm}$
- **4:** Bottom wingbox panel, ranging from $2.5\,\mathrm{mm}$ to $0.5\,\mathrm{mm}$
- **5:** Back spar, ranging from $1\,\mathrm{mm}$ to $0.5\,\mathrm{mm}$
- **6:** Front spar, ranging from $1\,\mathrm{mm}$ to $0.5\,\mathrm{mm}$

The final mass of the wing structure amounts to $27.79\,\mathrm{kg}$. The mass includes the wingbox, skin, and ribs. A more detailed depiction of the structural parts is shown in Table 6.3.

Table 6.3: Total structural mass of the wing.

Part	Mass [kg]
Wingbox	19.55
LE skin	2.36
TE skin	3.10
Ribs	2.78
Total structure	**27.79**

6.5. Aileron Sizing

Another important aspect of the wing design is the design of the ailerons, which provide roll control to the UAV. The requirements of the aileron are shown in Table 6.1. With these constraints in place, the aileron size can be calculated [25]. Starting with the roll rate L of an aircraft that is defined as:

$$L = qS_{\text{ref}}b\left(C_{l_{\delta_a}}\delta_a + C_{l_p}\frac{Pb}{2V}\right) \tag{6.17}$$

Assuming a steady state roll, the roll rate does not change over time. This means that $\dot{P} = 0$ and $L = 0$, resulting in Equation 6.18:

$$C_{l_{\delta_a}}\delta_a + C_{lp}\frac{Pb}{2V} = 0 \tag{6.18}$$

Where δ_a and P are set by the requirements and V is always known. This means that the roll damping coefficient C_{l_p} and $C_{l_{\delta_a}}$ can be used to calculate the placement of the ailerons along the span.

$$C_{l_p} = \frac{dC_l}{d\left(\frac{Pb}{2V}\right)} = -\frac{4\left(c_{l_\alpha} + c_{d_0}\right)}{S_{\text{ref}}b}\int_0^{b/2} y^2 c(y)\,dy \tag{6.19a}$$

$$C_{l_{\delta_a}} = \frac{dC_l}{d\delta_a} = \frac{2c_{l_\alpha}\tau}{S_{\text{ref}}b}\int_{b_1}^{b_2} c(y)y\,dy \tag{6.19b}$$

where τ is the aileron effectiveness that is estimated from Figure 6.9 using the aileron chord to wing chord ratio. Now, as all variables in Equation 6.19a are known, and the only free variable in Equation 6.19b is b_1, this can be calculated relatively easily through Equation 6.18.

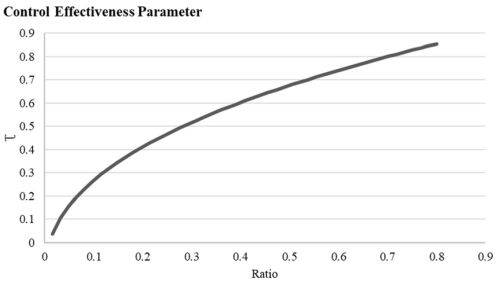

Figure 6.9: Aileron effectiveness [34]

With the aileron dimensions calculated, the hinge moment it creates can be determined, allowing for the control surface actuator to be selected. The hinge moment can be calculated as follows:

$$M_h = C_{m_\delta} q_\infty S_{ref}\delta c \tag{6.20}$$

where C_{m_δ} is the hinge moment coefficient, typically ranging from -0.5 to 0.5, q_∞ is the free stream velocity, S_{ref} is the surface area of the aileron, c is the chord length of the aileron, and δ is the aileron deflection. Finally, the final values for the aileron sizing and placement are shown in Table 6.4.

Table 6.4: Aileron properties.

Parameter	Value
Aileron chord as wing chord fraction	$20\,\%$
Aileron length	$1.09\,\mathrm{m}$
Aileron Surface	$0.08\,\mathrm{m}^2$
b_1 (inner spanwise coordinate)	$3.41\,\mathrm{m}$
b_2 (outer spanwise coordinate)	$4.5\,\mathrm{m}$
Maximum hinge moment	$12\,\mathrm{N\,m}$

With the maximum hinge moment calculated, the control servos for the ailerons can be selected. After a market study, the UAVOS SD-01B was selected, and is capable of developing a maximum continuous torque of $15.5\,\mathrm{Nm}$ with a power consumption of $100\,\mathrm{W}$, satisfying the requirement. The SD-01B was therefore included in the component inventory and in the power allocation in Chapter 5.

6.6. Wing Design Verification

To guarantee compliance with the wing requirements in Table 6.1, several verification methods were defined. They are shown in Table 6.5.

Table 6.5: Wing design verification methods.

ID	Verification method	Discussion
RWI-AER-1	Analysis, Test	Perform CFD simulations on the model, then perform wind-tunnel test to obtain accurate C_L values.
RWI-AER-2	Analysis, Test	Perform more extensive CFD simulations on the model, then perform wind-tunnel test to get accurate C_L/C_D values.
RWI-STR-1	Analysis, Test	Analyze wing structure with high-fidelity techniques, then manufacture and test prototype.
RWI-STR-2	Analysis, Test	Analyze wing structure with high-fidelity techniques, then manufacture and test prototype.
RWI-STR-3	Analysis, Test	Analyze wing structure with high-fidelity techniques, then manufacture and test prototype.
RWI-STR-4	Demonstration	Fill up tanks to maximum capacity.
RWI-AIL-1	Demonstration	Perform a flight test to demonstrate rolling capabilities.
RWI-AIL-2	Demonstration	Deflect the aileron and check its maximum downwards deflection.
RWI-AIL-3	Demonstration	Deflect the aileron and check its upwards deflection compared to the maximum downwards deflection.
RWI-AIL-4	Inspection	Measure the dimensions of the aileron.
RWI-AIL-5	Inspection	Check that the position does not overlap with the booms.
RWI-AIL-6	Inspection	Measure and verify that the distance is correct.

Though certain verification methods in Table 6.5 require dedicated mechanical/weather testing facilities (for example, the Delft Aerospace Structures and Materials Laboratory in the Faculty of Aerospace Engineering at TU Delft), certain verification procedures have already been performed by the design team.

6.6.1. Aerodynamic Verification

A computational fluid dynamics analysis was performed on a preliminary model of the detailed design using the OpenVSP software. OpenVSP has a tool called VSPAero, which is a potential flow aerodynamics tool developed by Dave Kinney at NASA Ames [35]. As this tool is widely used for CFD analysis and aerodynamic performance prediction, verification and validation have already been performed and documented by other instances by comparing simulation data to flight data [36]. This makes sure that it can be used for this project, as time constraints prevent verification and validation from being done by the design team.

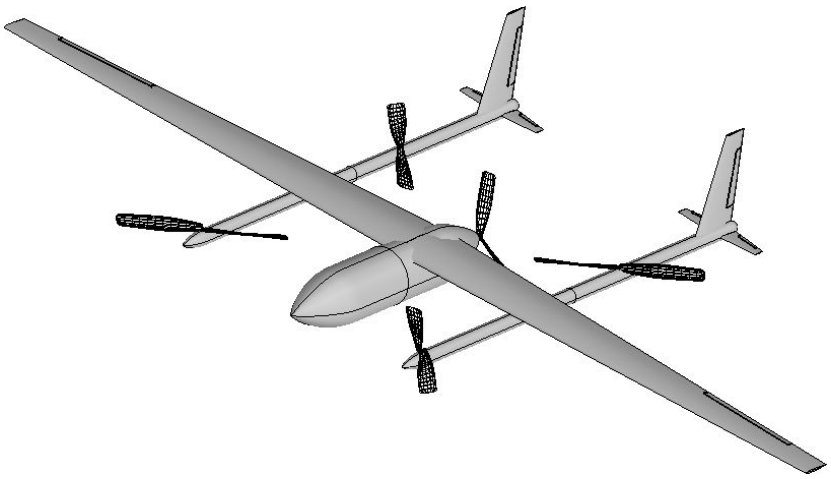

Figure 6.10: UAV model used for simulation in VSPAero.

As OpenVSP allows for modeling of the entire UAV and not just of the wings, the simulated values will be more accurate. The model used for simulation is shown in Figure 6.10. OpenVSP allows for either the Vortex Lattice Method (VLM) or the Panel Method. Only the VLM can analyze supersonic flow, and the panel method can more accurately capture the fluid interaction between components and handle the effects of model thickness and volume. As the FLOWS UAV will not reach supersonic speeds, the panel method is chosen because it will provide more accurate data [37].

The aerodynamic simulation in OpenVSP was performed, and performance metrics were obtained. The lift and drag polars that are obtained from this analysis are shown in Figure 6.11a and Figure 6.11b, respectively. These are simulated over various Reynolds numbers, ranging from $5e^5$ until $4e^6$, as these include both the situation in which the UAV will be monitoring and the situation where the UAV will reach its top speed.

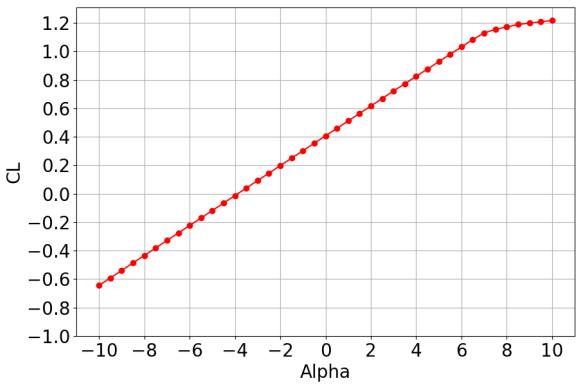

(a) Lift polar over a range of Angles of Attack.

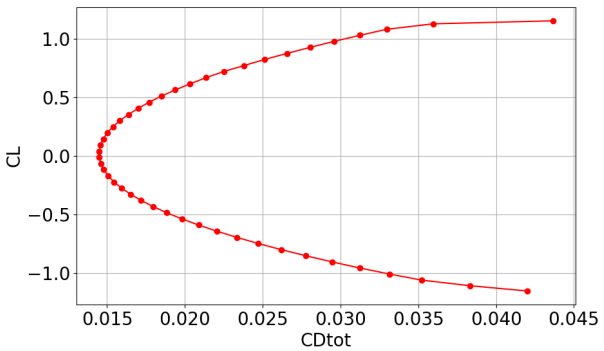

(b) Lift polar over a range of Drag Polars.

Figure 6.11: Lift and drag polar obtained in OpenVSP.

The aerodynamic data obtained from OpenVSP, including the parameters in Figure 6.11, were used to verify the initial airfoil lift and drag calculation in XFLR5, as well as to obtain higher-fidelity results for the final system sizing in Chapter 13. A more detailed discussion of the impact of these aerodynamic results is provided in Chapter 13.

6.6.2. Structural Model Internal Verification

The first verification method for the structural simulation involves simple unit tests to ensure that the code and calculations are correctly implemented. Simple point and distributed loads were applied to verify the shear and moment calculations. A simple I-beam was also used to verify the thickness needed and moment of inertia needed for a certain moment. Hand calculations were used to verify the model. Furthermore, the deflection was verified in a similar manner.

Figure 6.12a shows the shear force and moment for a $3\,\mathrm{m}$ long cantilever beam fixed at the root. A

$5\,\mathrm{N}$ point load is applied at the edge pointing upwards. The reaction force is thus $5\,\mathrm{N}$ in the negative direction. This gives a negative jump at the root and a positive jump at the tip. The magnitude is $5\,\mathrm{N}$ which correlates to the standard formulas of a cantilever beam [30]. The moment as explained in Equation 6.10, should be the integral of the shear force. In this case at the root, the moment equals $15\,\mathrm{Nm}$, this is because the shear force creates a moment and thus a reaction moment of the same amount must be applied on the root.

Figure 6.12b shows a similar test, but with a distributed load of $5\,\mathrm{N/m}$, along the span. The shear and moment in this case also follow the expected values from the standard formulas [30].

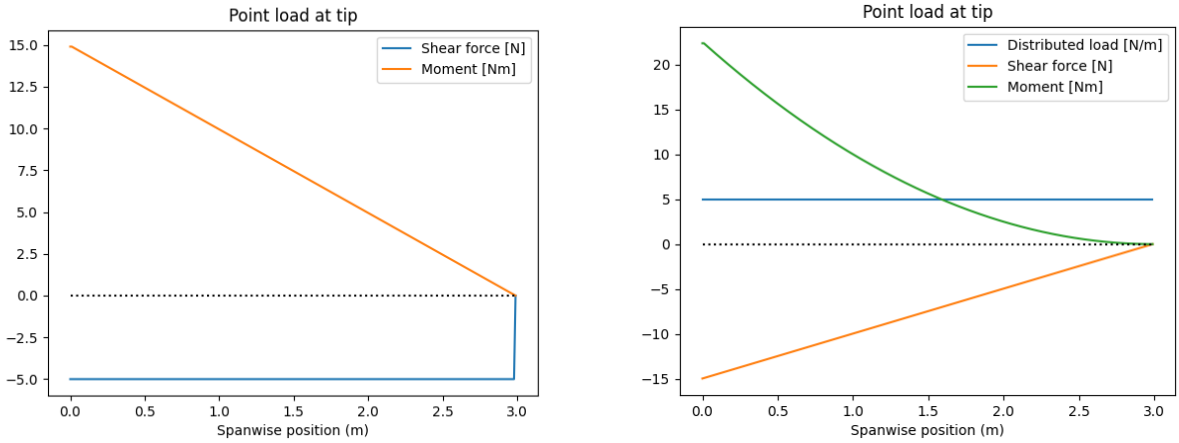

(a) Point load applied on a cantilever beam.

(b) Distributed load applied on a cantilever beam.

Figure 6.12: Two simple test cases to verify the structural model of the wing.

A sensitivity analysis was also performed to verify that changes in input parameters had the expected effect. All input parameters were varied by $\pm 10\,\%$ and their effect on the calculated wing box mass was analyzed. As expected, only the parameters related to the pull up maneuver had effect on the wing box mass, as the wing box is sized for this extreme case. The parameters that had effect on the final mass are shown in Table 6.6. An increase in either load factor, safety factor, or MTOW had the same effect on the wing box mass, which is to be expected, as they are multiplied to find the loading on the wing. Similarly, the yield stress had the same relative effect, only with a different sign, as an increase in yield strength is beneficial to the design. In Figure 6.13, the effect of the thickness variability of the spars is shown. In general, if the thickness variation is lower, the wing box mass is also lower, which is to be expected.

Table 6.6: Sensitivity of the structural model.

Variable	**+10 %**	**-10 %**
ultimate load factor	+7.94	-8.44
safety factor	+7.94	-8.44
thickness variability	1.24	-2.02
yield stress	-7.94	+8.44
material density	+10	-10
MTOM	+7.94	-8.44

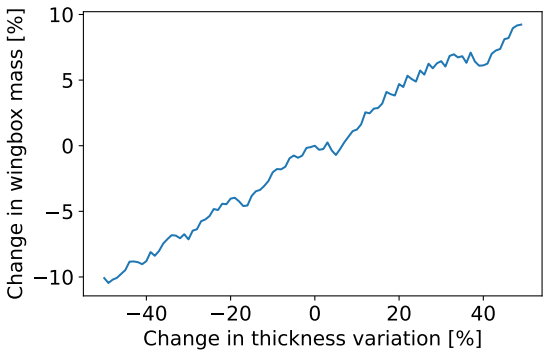

Figure 6.13: Change in wingbox mass due to a thickness variation change

6.6.3. Structural Model External Verification

As described in the verification strategy for **RWI-STR-1** and **RWI-STR-2**, the wingbox structural design can be verified with an external solver. The ANSYS Mechanical suite was chosen to perform this verification. Due to the limited scope of the project, it was decided to limit the analysis to the most critical aspects of the structural design, namely the maximum maneuver lift load and the maximum take-off taxi load cases on the wingbox.

The model of the wingbox (without the leading and trailing edges, which have not been designed at a structural level) was used as input geometry, with Al6061-T6 (elastic modulus of $69\,\mathrm{GPa}$, Poisson Ratio of 0.33) being assigned to the geometry. A fine tetragonal mesh was applied to the wingbox, with $0.5\,\mathrm{cm}$ elements being selected due to the thinness of the wing. This mesh was observed to converge to the solution in $7\,\mathrm{min}$, and is represented in Figure 6.14.

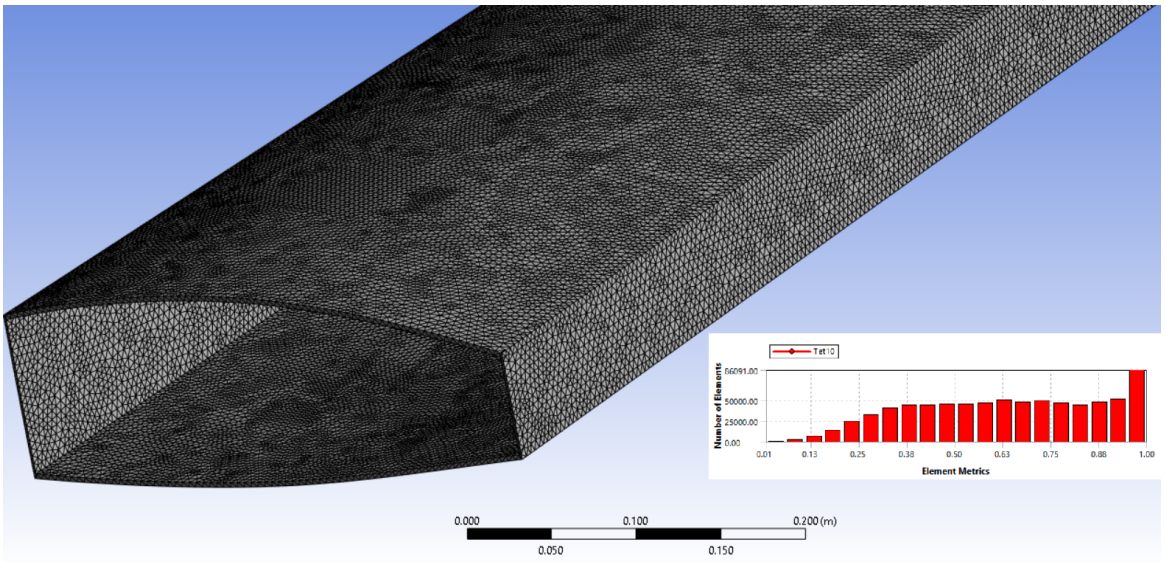

Figure 6.14: Wingbox finite element analysis mesh. Skewness metrics for mesh elements on the right side.

Figure 6.14 includes an overview of element skewness. High element skewness can result in unrealistic deformation values. It may be observed that only 9 percent of elements have a skewness above 0.9, with these elements being observed to be found closer to the wingtip (around areas with lower thickness). In spite of the high computational effort required, it was decided to maintain the high mesh resolution to avoid even higher skewness metrics.

To simulate the real world scenario, two load cases were selected, namely maximum lift force at a load factor of $3.6\,\mathrm{G}$ and maximum weight force during taxi. These load factors are considered the most constraining for the design, not only for the wing itself, but also for the design of the landing gear (which needs to allow for wingtip clearance) and fuselage structural integration.

The maximum lift force load case was simulated in a conservative manner through the application of two equivalent distributed $1412\,\mathrm{Pa}$ loads on the lower and upper flange of the wingbox. Fixed boundary conditions were applied to the root chord connection, to simulate the other side of the wing and fuselage integration. Standard Earth Gravity was also applied, as the operational altitudes are considered negligible from the perspective of gravitational attraction. The maximum deflection and maximum equivalent stress for this case are shown in Figure 6.15.

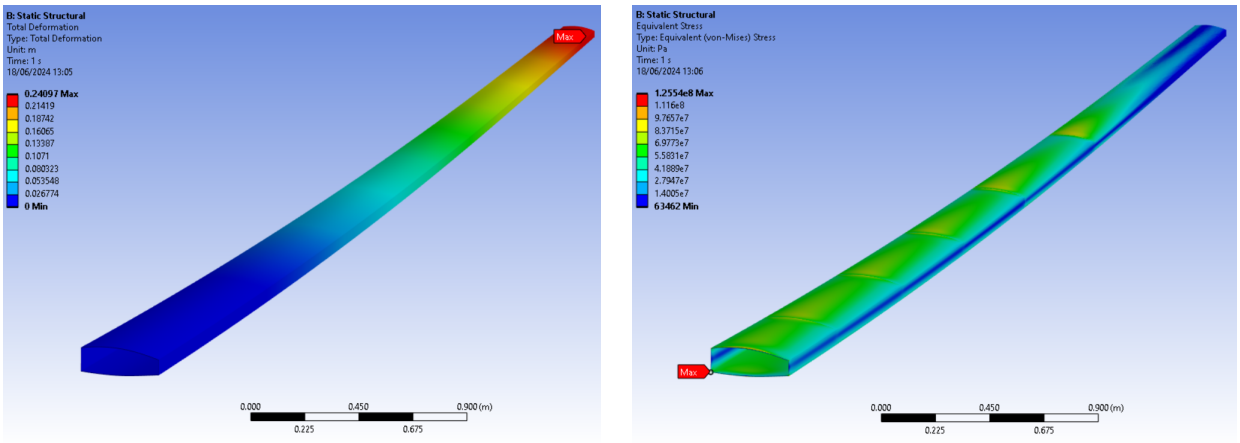

(a) Maximum lift load deformation (exaggerated).

(b) Maximum lift load equivalent stress.

Figure 6.15: Wingbox finite element analysis for maximum lift load case.

The maximum take-off weight during taxi load case was simulated in a conservative manner through the application of Standard Earth Gravity, together with an equivalent point load (simulating the leading and trailing edge, control surfaces, and fuel) of $500\,\mathrm{N}$, positioned at the centroid of the fuel tank. The same fixed boundary condition was applied as in the maximum lift force case. The maximum deflection and maximum equivalent stress for this case are shown in Figure 6.16.

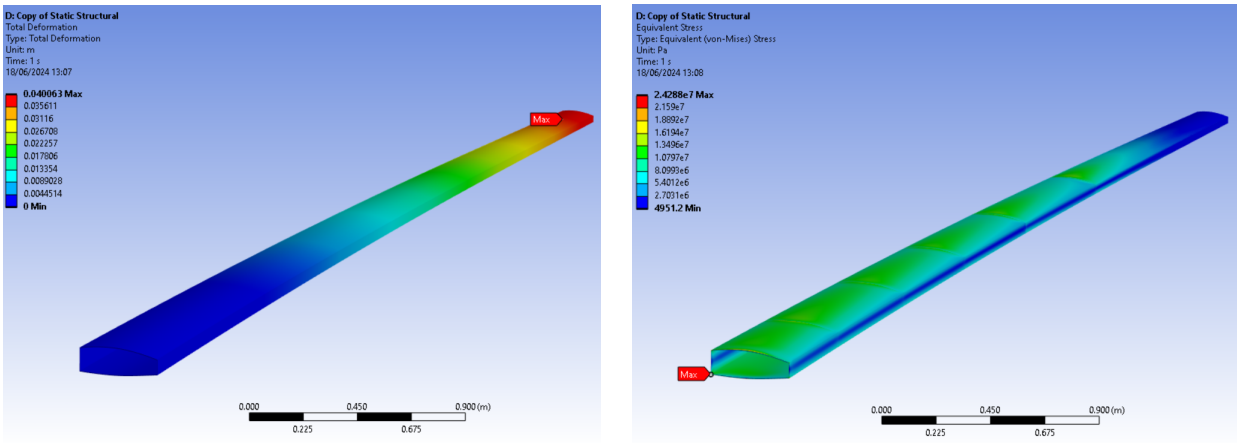

(a) Maximum take-off weight deformation (exaggerated).

(b) Maximum take-off weight equivalent stress.

Figure 6.16: Wingbox finite element analysis for maximum take-off weight case.

As demonstrated by the results in Figure 6.15 and Figure 6.16, the static finite element analysis shows that the preliminary wingbox structural design is highly conservative, with lower deflections and stresses calculated than expected. Both load cases show deflections below the requirements, and maximum equivalent stresses below the yield stress of the material. However, by only performing a static structural analysis, other aspects can be neglected, such as vibrational or buckling resistance.

The ANSYS Workbench has also allowed for a modal analysis and a linear eigenvalue buckling analysis to be performed. The modal analysis studies the first two vibrational modes for the wingbox, with results shown in Figure 6.17.

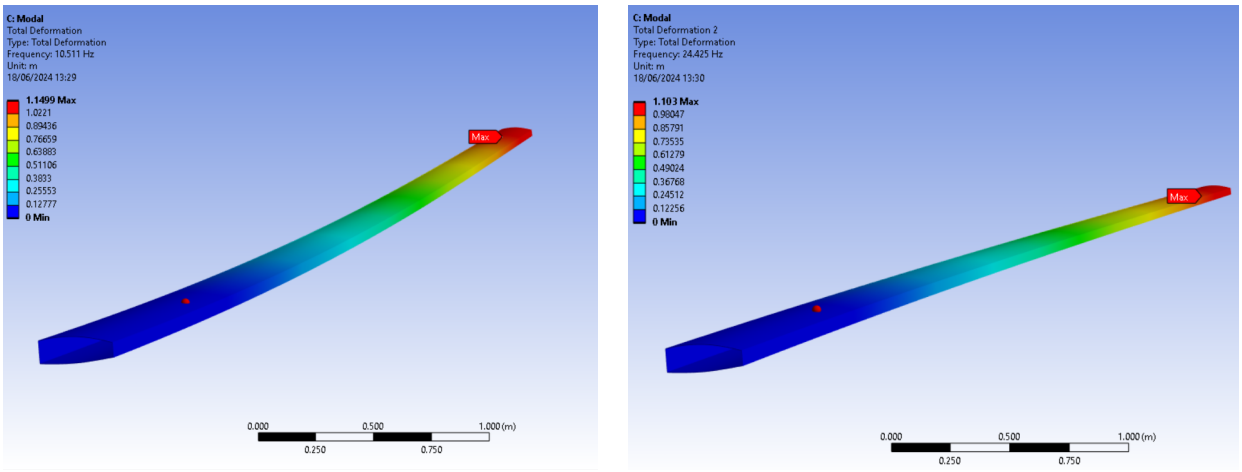

(a) Wingbox first vibrational mode. **(b)** Wingbox second vibrational mode.

Figure 6.17: Wingbox modal analysis results.

As observed in Figure 6.17, the first vibrational mode represents vertical bending (at a frequency of $10.5\,\mathrm{Hz}$), while the second mode represents lateral bending (at a frequency of $24.4\,\mathrm{Hz}$. Further vibrational modes divided the wingspan into several wavelengths, representing unrealistic vibrational results for an aeroelastic forcing. For further study, these results can be compared to a coupled fluid-structure analysis to evaluate the impact of aeroelastic effects on the structure.

For the eigenvalue buckling analysis, the same constraints and loading case as in the maximum lift load case were applied (with this being the most constraining load case), with the first buckling mode shown in Figure 6.18.

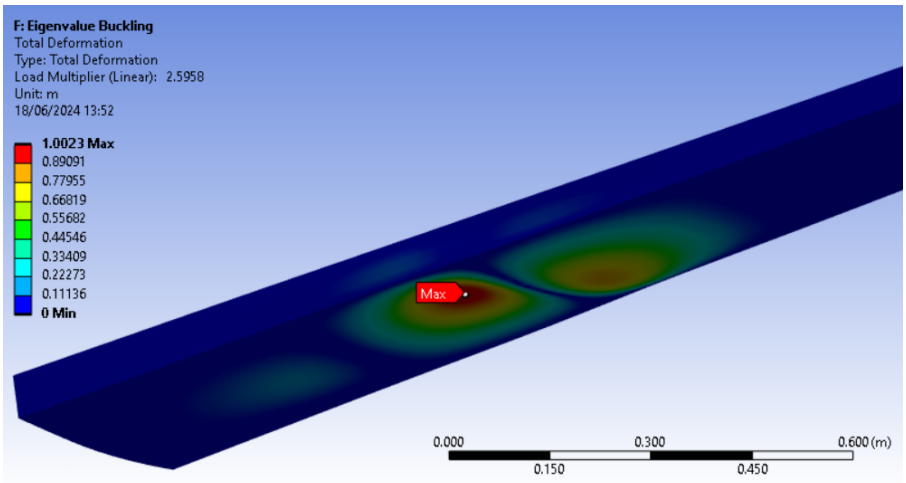

Figure 6.18: Local wingbox panel buckling.

Figure 6.18 shows that the lower wingbox panels show significant risk of local buckling, in agreement with the maximum stress points found in Figure 6.15b. The load multiplication factor for this mode was found to be equal to 2.6, which means that the applied load needs to be multiplied with this factor for the buckling mode to occur. Though the load factor is greater than 1, it is recommended that further analysis is performed to ensure that buckling does not occur over the operational lifetime.

The finite element analysis has allowed for the structural design of the wingbox to be verified independently. As discussed in Table 6.5, further verification involves continued analysis of the entire wing structure, as well as static, vibration, and fatigue testing in a dedicated facility.

7 | Stability, Balance and Tail Design

This chapter starts with Section 7.1, which covers the requirements on the balancing aspect of the aircraft. Next, Section 7.2 describes the empennage configuration choice. Section 7.3 provides a high-level flowchart of the balancing tool methodology, and Section 7.4 describes the nomenclature and reference frames used for the sizing equations. Following this, Section 7.5 describes the process of positioning the VTOL propellers, landing gear, and computing the tail arm, while Section 7.6 goes over the horizontal tail sizing and wing positioning methodology. Section 7.7 describes the vertical tail sizing methodology, and Section 7.8 sizes the booms based on the loads of the empennage and VTOL propellers.

Following all this work, the results of the balancing tool are compiled in Section 7.9. These results are then verified using internal tests and an external verification method in Section 7.10 and Section 7.11. Thereafter, Section 7.12 analyzes the final configuration for dynamic stability, and Section 7.13 provides preliminary sizing of empennage control surfaces. Finally, Section 7.14 analyzes the wind resistance of the UAV, and Section 7.15 provides an overview of future verification strategies.

7.1. Stability and Balance Requirements

The stability and balance analyses require that well-defined requirements are set on the tail, propulsion system, and landing gear. These are identified in Table 7.1.

Table 7.1: Identified requirements for subsystems related to stability and balance analysis.

ID	Requirement description	Origin
RTL-AER-1	The aircraft shall be longitudinally statically stable.	**R-SYS-11**
RTL-AER-2	The aircraft shall be controllable at stall velocity.	**R-SYS-12**
RTL-AER-3	The aircraft shall be statically laterally stable.	**R-SYS-11**
RTL-AER-4	The empennage shall not be in the wake of the wing during a stall.	**RTL-AER-2**
RTL-AER-5	The aircraft shall have a wind resistance of $14\,\mathrm{m/s}$ in vertical flight	**R-SYS-1**
RTL-AER-6	The aircraft shall have a wind resistance of $14\,\mathrm{m/s}$ in horizontal flight.	**R-SYS-1**
RTL-STR-1	The tail boom shall twist no more than 1° at the ultimate empennage load.	**R-STK-5**
RTL-STR-2	The tail boom angle shall be no more than 1° at the position of the tail at the ultimate empennage load in both the longitudinal and lateral direction.	**R-STK-5**
RTL-STR-3	The tail boom shall withstand the stresses at the ultimate empennage load.	**R-STK-5**
RPR-BAL-1	The VTOL engines shall be balanced about the center CG position.	**R-MIS-5**
RPR-CSH-1	The vertical and horizontal propellers shall not clash during transition.	**R-MIS-5**
RLG-BAL-1	The aft landing gear shall account for a scrape angle of no less than 12°.	**R-SYS-16**
RLG-BAL-2	The nose landing gear shall carry between $8\,\%$ and $15\,\%$ of the total aircraft weight	**R-SYS-16**.

- **RTL-AER-1**, **RTL-AER-2**, and **RTL-AER-3** are all required for making the aircraft flyable in horizontal and transition phases.
- **RTL-AER-4** ensures that the aircraft does not enter a so-called deep stall at a high angle of attack, which keeps the aircraft controllable [38].
- **RTL-AER-5** and **RTL-AER-6** stem from **R-SYS-1** to make sure both flight modes can resist wind.
- **RTL-STR-1** and **RTL-STR-2** are there to reduce fatigue effects on the empennage. If stiffness is not considered, the tail boom will flutter when the elevator and rudder are actuated.
- **RTL-STR-3** ensures that no structural failure of the empennage can happen, which would likely cause full mission failure.
- **RPR-BAL-1** is required to make maximal use of the vertical thrust during takeoff and landing. Without having the engines balanced, the engine that is furthest from the CG has to reduce thrust to keep the engine balanced.
- **RLG-BAL-1** and **RLG-BAL-2** are set to obtain satisfactory landing gear placement in the case of horizontal landing (**TRRC-12**) [39].

A clear takeaway from the requirements presented in Table 7.1 is that the design of the VTOL booms, empennage, landing gear position, and the stability analysis are all interdependent. The aircraft can be balanced manually and iterated using a high-fidelity stability program, but moving one part of the aircraft would shift the aerodynamic center and CG, requiring other components to shift along or to be resized, and these interactions are not captured by such high-fidelity software.

Therefore, it is necessary to first obtain an initial optimum of the layout by using a lower fidelity but faster empirical estimation method in an independently developed **balancing tool**. This initial estimate of the full layout can then be used as input for higher fidelity balancing and stability CFD tools, to make smaller final adjustments, and prevent a garbage-in, garbage-out scenario.

7.2. Empennage Configuration Selection

Before designing the balancing tool, first the attachment method of the empennage should be considered. For this, there are two primary options: A quad-plane layout where the empennage is attached to an extended fuselage or a twin-boom layout where the empennage is attached to the wings, as shown in Figure 7.1.

Figure 7.1: Left: Twin boom configuration, Right: Quadplane configuration [40]

In literature, the configurations in Figure 7.1 are found to perform similarly when it comes to aerodynamic performance [40]. However, this research did not consider structural weight, where Roskam argues that in some cases, using a unique combination of structural components, weight savings can be made [41, p. 249].

In the case of this aircraft, the fuselage layout is quite compact, as discussed in Chapter 8, so extending it to add the empennage would shift the CG backward as the engine and landing gear moves along, resulting in a mostly empty section of the fuselage. Therefore, the twin-boom configuration was selected, as the booms used to support the vertical motors can be extended to also support the tail

surfaces. Before choosing how the tail surfaces should be attached to the booms, first, the required tail surface areas must be computed.

7.3. Balancing Tool Flowchart

Sizing the tail surfaces for a twin-boom configuration is highly dependent on many aspects of the aircraft, except for the fuselage attached to the main wing. In Figure 7.2 on the next page, the final general sizing methodology is shown.

The balancing tool starts with inputs. All inputs are parametric and can be easily adjusted during the concurrent engineering iteration process. The main input is the fuselage shape and CG range, as well as the main wing shape and CG range. Also, the size and mass of the VTOL propellers and aft landing gear is given as an important input. Furthermore, initial parameters have to be set for the boom and empennage shape.

The main part of the optimization is that first, the wing position is varied over every position along the length of the fuselage, as noted in BT.1.1. Next, for each wing position, the CG location is iterated within a separate loop which is visible in BT.1.2.1. This is done as the aft landing gear and VTOL engine positioning (BT.1.2.1 and BT.1.2.3) move the CG but are also positioned based on the CG.

After this, the required boom length is determined, which is used for the scissor plot generation in BT.1.3, which analyses the limits of the horizontal stabilizer area based on stability and control, for different positions of the CG. After the scissor plot is completed and the CG range is known, the minimum required horizontal stabilizer size can be computed for that specific wing position, as shown in BT.1.4.

Next, after all possible wing positions are evaluated, the optimal wing position is extracted based on the minimum required horizontal tail area, as visible in BT.1.5. For this optimal wing position, the horizontal and vertical stabilizer size is computed as shown in BT.1.6.1 and BT.1.6.2.

Following this, using the size of the vertical and horizontal stabilizers, a mass estimation can be done for the stabilizers as shown in TS.1.7.2. Additionally, with the size and position of the wing, vertical stabilizer, horizontal stabilizer, and VTOL engines, the required thickness of the tail boom can be computed based on the ultimate tail loads, which can be used to compute the mass of the tail boom as shown in BT.1.7.1.

Finally, with the updated mass of the boom and empennage, the program is iterated until all masses and stabilizer areas converge. After iteration, the complete layout of the aircraft is visualized in a 3-view drawing plot. Additionally, the final scissor plot with the final CG range is visualized. Furthermore, a plot of the required horizontal stabilizer area for different positions of the wing is provided. Next to that, a plot is provided that shows the convergence of the stabilizer areas and boom mass within the global iterations.

This final layout of the aircraft can then be used as input for the external verification procedure. This starts by modeling the aircraft in openVSP, as shown in BTV.2.1. using this model, the static stability of the aircraft can be evaluated as shown in BTV.2.2. Following this, the dynamic stability is evaluated in BTV.2.3. If either the dynamic stability or static stability is not satisfactory, the relevant wing platform parameters for either the main wing or tail can be adjusted, as shown in BTV.2.4. If everything is satisfactory the final layout can be frozen, as visible in BTV.2.5.

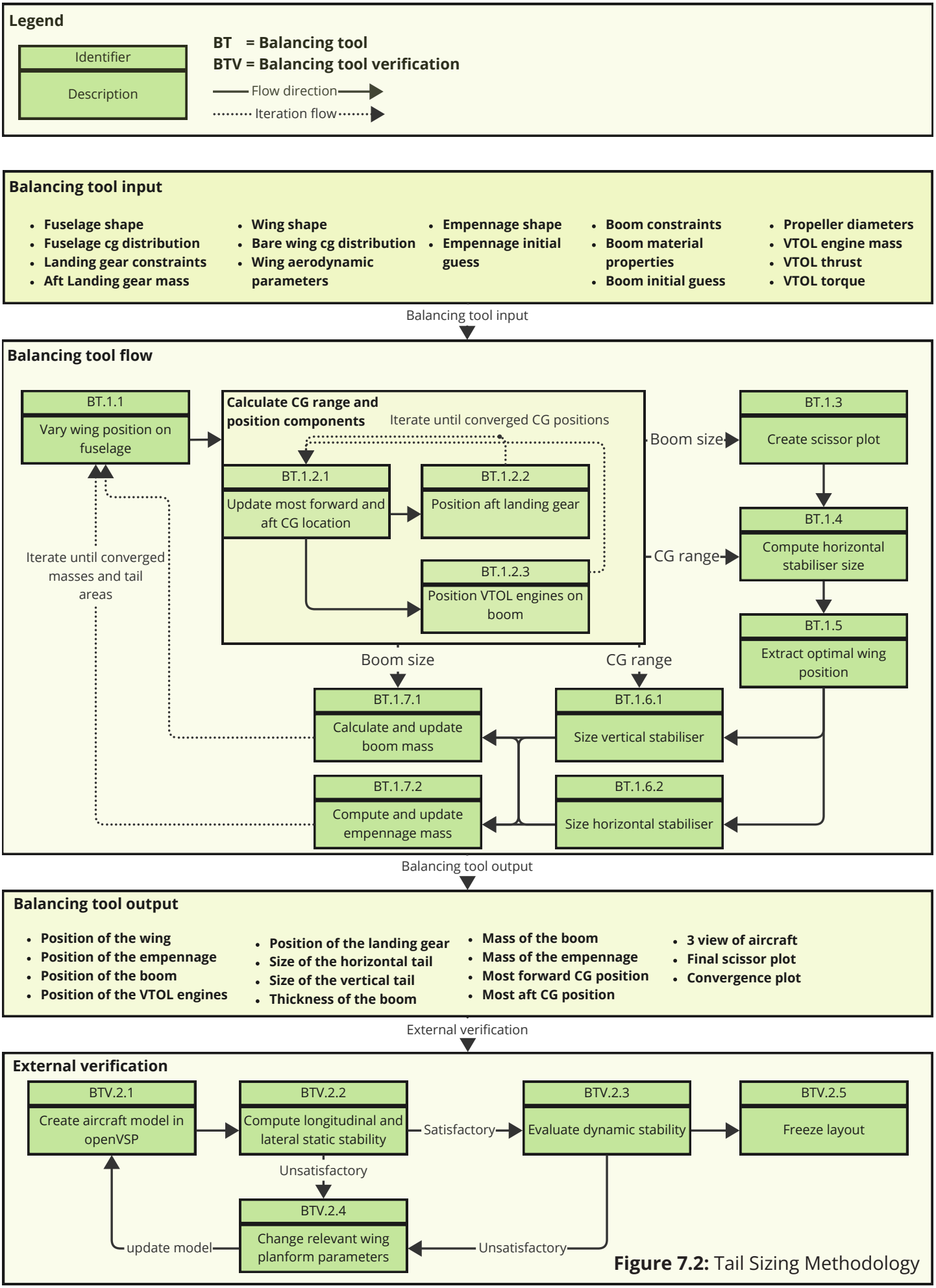

Figure 7.2: Tail Sizing Methodology

7.4. Nomenclature and Reference Frames

Since many equations in this chapter repeat symbols, the symbol explanation has been moved into a nomenclature to maintain a flow in the report. For these, some terms have the same meaning but apply to different parts of the aircraft, such as the lift slope gradient C_{L_α}. For this there are four distinct subscripts $C_{L_{\alpha_w}}$, $C_{L_{\alpha_{wf}}}$, $C_{L_{\alpha_h}}$, and $C_{L_{\alpha_v}}$. These subscripts mean wing, wing-fuselage combination, horizontal stabilizer, and vertical stabilizer respectively. Similar subscripts except for wf are used for wing platform geometry of the wing, horizontal and vertical stabilizers as well.

Symbol	Name	Unit
$x_{\text{cg}}^{\mathbb{F}}$	x position of the center of gravity in reference frame $\mathbb{F}$	m
m	mass	kg
b	Wingspan of a wing planform	m
S	Wing planform surface area	m^2
A	Aspect ratio of a wing planform	$-$
λ	Wing planform taper ratio	$-$
c_r, c_t, c_b	Wing planform root chord, tip chord, and chord at boom location	m
$\bar{c}$	Wing planform mean aerodynamic chord	m
Λ_n	Wing planform sweep at position n, which is a fraction of the chord with respect to the leading edge	$^\circ$
y_{mac}	y position (in wing planform reference frame) of the mean aerodynamic chord	m
l_h, l_v, h_h	Arm of the aerodynamic center of the horizontal stabilizer and vertical stabilizer to the center of gravity, and height of the horizontal stabilizer compared to the wing	m
F_{tail}	Tail arm to fuselage length ratio	$-$
$C_{L_{\alpha_h}}$, $C_{L_{\alpha_v}}$, $C_{L_{\alpha_w}}$, $C_{L_{\alpha_{wf}}}$	Lift gradient of a 3d wing platform for the horizontal tail, vertical tail, wing, and wing-fuselage combination.	rad^{-1}
$\frac{d\epsilon}{d\alpha}$, $\frac{\partial\sigma}{\partial\beta}$	Downwash and sidewash gradient of the wing and fuselage on the empennage	$-$
$\frac{V_h}{V}$, $\frac{V_v}{V}$	Velocity ratio of horizontal and vertical stabilizers compared to freestream velocity	$-$
$x_{ac}^{\mathbb{F}}$	Position of the aerodynamic center where there is no change in moment with a change in angle of attack in reference frame $\mathbb{F}$.	m
$C_{L_{\text{max}}}$	Maximum lift coefficient the aircraft is able to produce	$-$
$C_{L_{\text{h, min}}}$	Minimum lift coefficient the horizontal stabilizer is able to produce	$-$
$C_{M_{\text{ac}}}$	Moment coefficient at the aerodynamic center.	$-$
η	Airfoil lift slope efficiency factor compared to theoretical 2π	$-$
β	Mach number correction factor $\sqrt{1-M^2}$	$-$
b_f, h_f, l_f	Fuselage width, height and length	m
S_{net}	Wing surface area after subtracting the area of intersection of fuselage and booms from the wing	m^2
M	Mach number of the aircraft	$-$
$\Delta_{f1}\frac{x_{ac}}{\bar{c}}$	Aerodynamic center shift caused by the fuselage and boom shape	$-$
C_{L_0}	Lift coefficient at zero angle of attack	$-$
$\Delta_{f2}\frac{x_{ac}}{\bar{c}}$	Aerodynamic center shift caused by the lift loss at the fuselage position	$-$
$\Delta_f C_{m_{ac}}$	Moment coefficient shift due to the fuselage and booms	$-$
C_{n_β}	Stability coefficient responsible for the weathervane effect	rad^{-1}
S_{fs}	Surface area of the side of the fuselage	m^2
h_{f1}, h_{f2}	Height of the fuselage at 25% and 75% of the fuselage length	m
b_{f1}, b_{f2}	Width of the fuselage at 25% and 75% of the fuselage length	m
B_p	Number of blades on the propeller	$-$
l_p, D_p	Distance of the (tractor) propeller to the center of gravity, Propeller diameter	m
n_v, η_v	DATCOM correction factors for short fuselages and sidewash respectively	$-$
$\frac{z_w}{z_f}$	The ratio of the wing position, computed from the centerline of the fuselage where downwards is positive, to the fuselage height in the wing region	$-$

In the balancing tool, many calculations rely on geometry and positioning relative to components. In this section, all relevant reference frames with computations will be explained.

CG Balancing: Fuselage and Wing Reference Frames

The main CG range computation relies on both the fuselage group and the wing group. For the fuselage group CG reference frame, the computation is performed from where the shell of the fuselage starts. For the wing CG reference frame, all computations are performed relative to the leading edge of the mean aerodynamic chord (lemac).

The main cg locations can be computed using the left of Equation 7.1, where all positions have to be with respect to the same reference frame $\mathbb{F}$. To convert between the lemac and fuselage reference frame, the right of Equation 7.1 was used. Here the superscript represents the reference frame and the subscript represents the component, where c is an arbitrary component.

$$x_{cg}^{\mathbb{F}} = \frac{\sum x_i^{\mathbb{F}} m_i}{\sum m_i} \qquad\qquad x_c^{\text{lemac}} = x_c^{\text{fuselage}} - x_{\text{lemac}}^{\text{fuselage}} \tag{7.1}$$

Wing Planform Geometry Reference Frame

Many different geometric aspects of the wing and tail surfaces are required for different computations. All wing platforms are assumed to be conventional and straight-tapered. For the main wing, the aspect ratio, surface area, and taper ratio are known; with these, all other relevant parameters can be computed using Equation 7.2, and the sweep at any point of the chord can be computed using the left of Equation 7.3. The right of Equation 7.3 is used to compute the position of the mean aerodynamic chord on the span of the platform [42, p. 236].

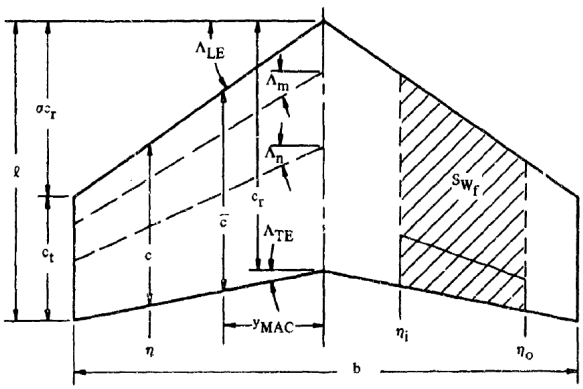

Figure 7.3: Conventional, straight-tapered platform geometric definition [42, p. 236].

$$A = \frac{b^2}{S} \qquad \bar{c} = \frac{2}{3} c_r \frac{1+\lambda+\lambda^2}{1+\lambda} \qquad c_r = \frac{2S}{b(1+\lambda)} \qquad c_t = \lambda c_r \tag{7.2}$$

$$\tan\Lambda_n = \tan\Lambda_m - \frac{4}{A}\left[(n-m)\frac{1-\lambda}{1+\lambda}\right] \qquad \frac{y_{\text{mac}}}{\frac{b}{2}} = \frac{1}{3}\left(\frac{1+2\lambda}{1+\lambda}\right) \tag{7.3}$$

7.5. Mass Iteration and Component Positioning

VTOL Propeller Positioning

To make maximal use of the VTOL thrust, the VTOL propellers have to be balanced between the most forward and most aft CG. One technicality is that the propeller should not overlap with the wing. Design variables for this are the distance of the boom from the center of the fuselage, y_b, and the minimum allowed horizontal clearance of the VTOL propeller to the wing, cw. If the CG is aft of the wing, the aft VTOL propellers has to be moved far back to keep balance, the opposite happens if the CG is far in front, this effect can be seen in Figure 7.4, which is the output of a system test for the propeller positioning.

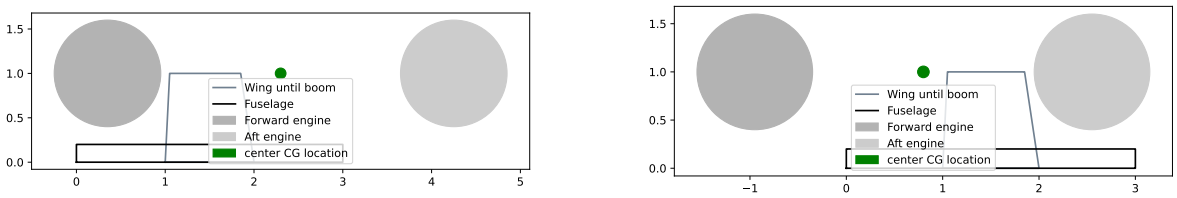

Figure 7.4: Effect of the center of gravity position on the propeller positioning. Left: center of gravity behind the wing, right: center of gravity in front of the wing.

Landing Gear Positioning

The aft landing gear is positioned based on scrape angles, for which literature recommends $12°$ to $15°$ as a good design range [39, p. 26]. Since $15°$ requires the tallest landing gear, this will be used in the balancing analysis. The theory behind this is visualized in Figure 7.5, where there is a $15°$ vertical line originating from the center of gravity, and another $15°$ line originating from the aft scrape point of the aircraft.

Meanwhile, the front landing gear should carry $8\,\%$ to $15\,\%$ of the total weight of the aircraft [39, p. 28]. The $8\,\%$ quantity is limited by the most aft position of the CG and the $15\,\%$ is limited by the most forward CG position. The valid range can also be found in Figure 7.5.

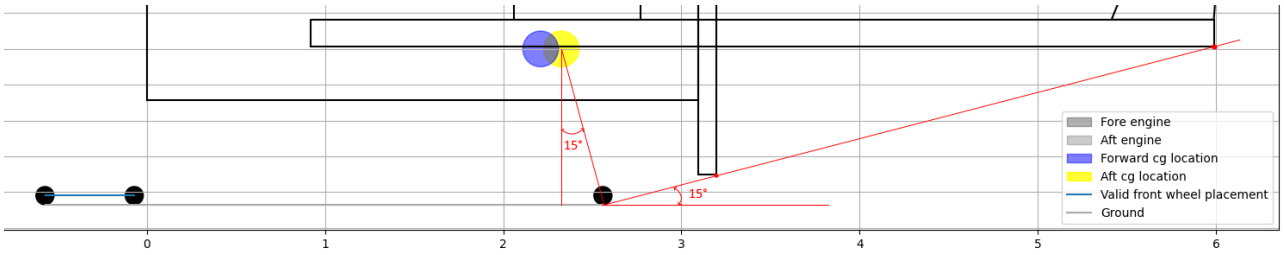

Figure 7.5: Scrape angle requirement visualized as part of the program output, the $15°$ angle for the scrape point is extracted from the most limiting case: either the propeller or the end of the boom.

From this, it was found that the forward landing gear will be placed in the nose of the fuselage and is fixed in the fuselage layout. The program input is adjusted to include the fuselage weight without the aft landing gear, as that is positioned and iterated inside of the program.

Stabilizer Positioning

Determining an optimal tail lever is a delicate balance of structural mass, aerodynamic efficiency, and stability. A common approach for estimating the tail arm is to use empirical data, specifically the ratio of fuselage length to the tail arm. Existing research can be found on determining such ratios for conventional single-tail aircraft [43]. However, for vehicles with a twin-boom configuration, there is no literature available.

As there are many existing designs available for the chosen configuration, this ratio was determined manually by gathering a top profile or side profile of twelve similar UAVs and collecting the length in pixels of the fuselage (l_f), distance between the leading edge of the wing and horizontal stabilizer, chord length at the boom of the wing and horizontal stabilizer, c_{b_w} and c_{b_w}. With this l_h was approximated using Equation 7.4, which was used to get the fraction F_{tail} as shown in Equation 7.5.

$$l_h \approx x_{LE_{b_h}} - x_{LE_{b_w}} - \frac{1}{4}c_{b_w} + \frac{1}{4}c_{b_h} \qquad (7.4)$$

$$F_{\text{tail}} \approx \frac{l_h}{l_f} \qquad (7.5)$$

With this, the results can be found in Table 7.3. The twelve UAVs include five fixed-wing non-VTOL UAVs, five fixed-wing hybrid electric VTOL UAVs, and two fully electric fixed wing-VTOL UAVs. When

only the results of the five hybrid electric UAVs the sample standard deviation shrinks significantly. With this, a good initial estimate for the tail arm will be used as 1.062 times the fuselage length.

Table 7.3: Tail arm to fuselage ratio for similar UAVs

	Average F_{tail}	**Standard deviation σ**
All Twelve UAVs	0.985	0.149
Five Hybrid Electric UAVs	1.062	0.067

For the stabilizer positioning, l_h is by definition the distance from the quarter chord point of the horizontal stabilizer to the center of gravity [44], that is also how it was positioned on the aircraft.

Center of Gravity Iteration

Since the VTOL propellers and aft landing gear move with the center of gravity but are also placed using the center of gravity, the positioning is iterated until the relative change is 1×10^{-5} %, this typically occurs after no more than 13 iterations per wing position.

7.6. Wing Positioning and Horizontal Stabilizer Sizing

In aerospace design, scissor plots are typically used to optimize the horizontal stabilizer area [26, p. 328]. The main purpose of is to see how x_{cg} influences the required tail area. The program output can be seen in Figure 7.6. If the wing is too far forward, the tail area is governed by stability, whereas if the wing is too far aft the tail area is governed by maneuverability. The center of gravity range should fit between the stability and maneuverability boundaries.

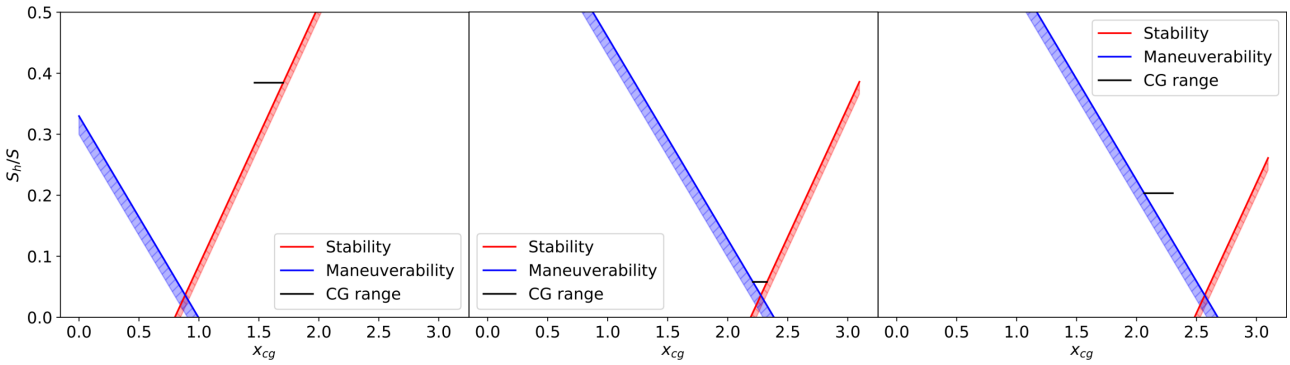

Figure 7.6: Scissor plot program output, left: wing positioned too far forward. Center: wing positioned optimally, right: wing positioned too far aft.

The stability line is defined using Equation 7.6 [45]. This includes a stability margin of 0.05. The steeper the slope of the stability line with respect to x_{cg}, the more constraining the stability limit becomes. Components that negatively affect the slope are the fuselage wing combination lift gradient and the downwash of the main wing onto the tail. Having a higher lift gradient on the horizontal stabilizer and a larger tail arm positively affects the slope.

$$\frac{S_h}{S} = \frac{1}{\frac{C_{L_{\alpha_h}}}{C_{L_{\alpha_{wf}}}}\left(1 - \frac{d\epsilon}{d\alpha}\right)\frac{l_h}{\bar{c}}\left(\frac{V_h}{V}\right)^2} x_{cg}^{\text{fuselage}} - \frac{x_{\text{ac, wf}}^{\text{fuselage}} - 0.05}{\frac{C_{L_{\alpha_h}}}{C_{L_{\alpha_{wf}}}}\left(1 - \frac{d\epsilon}{d\alpha}\right)\frac{l_h}{\bar{c}}\left(\frac{V_h}{V}\right)^2} \tag{7.6}$$

.

Meanwhile, the maneuverability line is computed using Equation 7.7 [45], which is based on being able to maneuver the aircraft during stall [26]. An aircraft with a higher tail minimum lift coefficient will have a shallower slope.

$$\frac{S_h}{S} = \frac{1}{\frac{C_{L_{\text{h, min}}}}{C_{L_{\text{wf, max}}}}\frac{l_h}{\bar{c}}\left(\frac{V_h}{V}\right)^2} x_{cg}^{\text{fuselage}} + \frac{\frac{C_{M_{\text{ac, wf}}}}{C_{L_{\text{wf, max}}}} - x_{\text{ac, wf}}^{\text{fuselage}}}{\frac{C_{L_{\text{h, min}}}}{C_{L_{\text{wf, max}}}}\frac{l_h}{\bar{c}}\left(\frac{V_h}{V}\right)^2} \tag{7.7}$$

Stability Parameters

Stabilizer Shape

The results of the balancing tool itself constrained the tail configuration. Initially, the plan was to connect the horizontal stabilizers, as is done in many fixed-wing VTOL aircraft. However as the design matured, the propeller diameter increased, increasing the boom spacing. This high boom spacing made it so that if the horizontal stabilizer were connected to both booms, the width of the stabilizer would become only $0.05\,\mathrm{m}$, with a length of $2.8\,\mathrm{m}$, or an aspect ratio of 56 This was deemed structurally unfeasible. Therefore the stabilizers were not connected to one another.

Next, a choice had to be made on the layout of the tail. Due to the large difference in vertical and horizontal stabilizer area, a V-tail would cause unusual control coupling due to the very high required dihedral angle. Leaving only conventional options. A high tail was impossible due to **RTL-AER-4**, the vertical tail height would put it in the wake of the main wing [38], another reason is inherent flutter issues with the T-tail configuration [46], which is not deemed acceptable on top of possible flutter issues introduced with the twin-boom configuration.

With this in mind, the horizontal tail was placed on the boom. An asymmetric layout was considered to put the tail surface further out of the boom wake, but this increased the boom mass due to the additional stabilizer torque. Therefore the final tail configuration was chosen as a twin-boom disconnected conventional low tail.

For the empennage airfoil, a symmetric NACA0012 profile was selected, symmetric airfoils are a typical choice for stabilizers, as adequate performance is required in both deflection directions of the control surfaces [26]. The horizontal stabilizer aspect ratio was fixed at 5, with a taper ratio of 0.5 and a quarter chord sweep angle of $5°$, which are typical values for single-engine aircraft [47]. The vertical stabilizer shape was also selected based on typical values for aircraft [47]. It has a much lower aspect ratio of 2, to ensure a high stall angle of attack. The taper ratio is also selected as 0.5 and the quarter chord sweep is put as $20°$ to further increase the stall angle of attack for low-velocity high sideslip conditions [45].

Velocity at Tail Location

For the low tail configuration, the velocity fraction on the tail compared to freestream velocity is assumed as $\frac{V_h}{V}$, $\frac{V_v}{V}$ = 0.85. This is considered the most conservative value [45].

Horizontal Lift Slope Estimation

To estimate the lift lope of the horizontal tail, and later for the vertical tail, the Helmbold Diedrich formula (Equation 7.8) was used [48]. The computation of the airfoil efficiency and mach number correction factor is also shown.

$$C_{L_{\alpha_h}} = \frac{2\pi A_h}{2 + \sqrt{4 + \left(\frac{A_h \beta}{\eta_h}\right)^2 \left(1 + \frac{\tan^2\left(\Lambda_{0.5c_h}\right)}{\beta^2}\right)}} \qquad \eta = \frac{C_{l_a}}{2\pi\beta} \qquad \beta = \sqrt{1 - M^2} \tag{7.8}$$

Tailless Lift Slope Estimation

The lift slope of the wing-fuselage combination can be estimated using Equation 7.9[26, p. 479]. This equation is valid for near-circular fuselage cross-sections, for $b_f/b < 0.2$, and for a fuselage with no aft upsweep.

$$C_{L_{\alpha_{wf}}} = C_{L_{\alpha_w}} \left(1 + 2.15\frac{b_f}{b}\right) \frac{S_{\text{net}}}{S} + \frac{\pi}{2C_{L_{\alpha_w}}} \frac{b_f^2}{S} \tag{7.9}$$

In the case of this aircraft, the computation is performed with b_f including the diameter of the two booms, and the area of the booms also included in S_{net}. Not including these additions would be non-conservative as the effects are destabilizing.

Downwash Estimation

The downwash can be estimated using Equation 7.10 [49, p. 278]. Here the three constants can be computed using Equation 7.11. K_a depends on the aspect ratio of the wing A, K_λ depends only on the wing taper ratio λ and K_h depends on the horizontal and vertical distance of the tail l_h and h_h. Also, the ratio of lift coefficients was approximated using the Prandl Glauert correction [28, p.754]. Note that A, λ and b are all with respect to the wing in this equation.

$$\frac{d\epsilon}{d\alpha} = 4.44 \left[K_{A_w} K_{\lambda_w} K_h \cos \Lambda_{0.25c_w}^{0.5}\right]^{1.19} \frac{C_{L_{\alpha_{w,M=M}}}}{C_{L_{\alpha_{w,M=0}}}} \tag{7.10}$$

$$K_A = \frac{1}{A} - \frac{1}{1+A^{1.7}} \qquad K_\lambda = \frac{10-3\lambda}{7} \qquad K_h = \frac{1-\frac{h_h}{b}}{\frac{2l_h}{b}^{1/3}} \qquad \frac{C_{L_{\alpha_{w,M=M}}}}{C_{L_{\alpha_{w,M=0}}}} \approx \frac{1}{\beta} \tag{7.11}$$

Aerodynamic Center Prediction

The aerodynamic center without the fuselage as a percentage of the chord can be extracted from the airfoil. However, the fuselage and engine booms will also cause a shift in the aerodynamic center. This shift due to the fuselage can be estimated using Equation 7.12 [26, p. 480].

$$\frac{x_{ac}^{\text{lemac}}}{\bar{c}}_{wf} = \frac{x_{ac}^{\text{lemac}}}{\bar{c}}_{w} + \Delta_{f1}\frac{x_{ac}^{\text{lemac}}}{\bar{c}} + \Delta_{f2}\frac{x_{ac}^{\text{lemac}}}{\bar{c}} \tag{7.12}$$

The individual contributions can be computed using Equation 7.13 [26, p. 480], where Δ_{f1} is the shift due to the nose of the fuselage based on empirical data. Δ_{f2} considers the lift loss near the center of the wing due to the fuselage, but since the quarter chord sweep is zero, the contribution is also zero. These computations are also computed for each boom, as it cannot be ignored due to the destabilizing effect.

$$\Delta_{f1}\frac{x_{ac}^{\text{lemac}}}{\bar{c}} = -\frac{1.8}{C_{L_{\alpha_{wf}}}}\frac{b_f h_f l_{fn}}{S\bar{c}} \qquad \Delta_{f2}\frac{x_{ac}^{\text{lemac}}}{\bar{c}} = \frac{0.273}{1+\lambda}\frac{b_f c_g (b-b_f)}{\bar{c}^2(b+2.15b_f)}\tan\Lambda_{c/4} \tag{7.13}$$

Maneuverability Parameters

Maximum Tailless Lift and Minimum Stabilizer Lift

The maximum lift coefficient of the tailless aircraft is already defined as 1.2 in Chapter 6. That leaves the minimum lift coefficient of the horizontal stabilizer. For this, a value of -0.8 is assumed for a fixed adjustable stabilizer [25].

Moment Coefficient at Aerodynamic Center Estimation

The moment coefficient at the aerodynamic center of the wing-fuselage combination can be estimated using Equation 7.14 [26, p. 480]. The moment coefficient of the wing was extracted using the data from Chapter 6.

The contribution due to the fuselage can be computed using Equation 7.15 [26, p. 480]. The top profile is assumed to be a box around the geometry of the fuselage, which is conservative as it increases the moment contribution compared to the real value. The lift slope at zero angle of attack was also extracted from Chapter 6.

$$C_{M_{\text{ac, wf}}} = C_{M_{\text{ac, w}}} + \Delta_f C_{M_{\text{ac}}} \tag{7.14}$$

$$\Delta_f C_{M_{\text{ac}}} = -1.8\left(1 - \frac{2.5b_f}{l_f}\right)\frac{\pi b_f h_f l_f}{4Sc}\frac{C_{L_0}}{C_{L_{\alpha_{wf}}}} \tag{7.15}$$

7.7. Vertical Tail Sizing

The vertical tail is sized by evaluating the total C_{n_β} of the aircraft, as shown in Equation 7.16, the vertical tail can be sized such that the total is at least $C_{n_\beta} = 0.057$ [50].

$$C_{n_\beta} = C_{n_{\beta_f}} + C_{n_{\beta_p}} + C_{n_{\beta_i}} + C_{n_{\beta_v}} \tag{7.16}$$

Negative Contributions

For this, there are negative contributions due to the fuselage shape, propeller, and wing location, which are shown in Equation 7.17 to Equation 7.18. The fuselage contribution depends on the shape of the fuselage, while the wing location contribution depends only on low, mid or high wing.

A note must be placed on the propeller contribution, as it is derived from a tractor propeller configuration, which is destabilizing. For a pusher configuration propeller, it instead has a stabilizing effect [51, p. 321], therefore this term will be ignored to remain conservative. The fuselage contribution only depends on the geometry of the fuselage and the location of the CG.

$$C_{n_{\beta_f}} = -K_\beta \frac{S_{fs} l_f}{Sb} \left(\frac{h_{f_1}}{h_{f_2}}\right)^{\frac{1}{2}} \left(\frac{b_{f_2}}{b_{f_1}}\right)^{\frac{1}{3}} \qquad K_\beta = 0.3\frac{x_{cg}}{l_f} + 0.75\frac{h_f}{l_f} - 0.105 \tag{7.17}$$

$$C_{n_{\beta_p}} = -0.053 B_p \sum \frac{l_p D_p^2}{Sb} \qquad C_{n_{\beta_i}} = -0.017, \text{ high wing} \tag{7.18}$$

The positive contribution caused by the vertical tail can be computed using Equation 7.19. Here n_v is 1 when the vertical stabilizer span to fuselage diameter ratio is greater than 3.5 [49, p. 385]. Furthermore, the function relies on the lift slope of the vertical tail, $C_{L_{\alpha_v}}$, which was computed using Equation 7.8.

The sidewash together with the efficiency factor can be computed using Equation 7.20, requiring the wing geometry but also the surface area of the vertical wing. Here $\frac{z_w}{z_f}$ is equal to -0.5 for a high wing configuration [48]. Both equations were solved simultaneously to gain the required surface area of the vertical stabilizer.

$$C_{n_{\beta_v}} = n_v C_{L_{\alpha_v}} \eta_v \left(1 - \frac{\partial\sigma}{\sigma\beta}\right) \frac{V_v}{V}^2 \frac{S_v l_v}{Sb} \tag{7.19}$$

$$\eta_v \left(1 - \frac{\partial\sigma}{\sigma\beta}\right) = 0.724 + 3.06\frac{S_v}{S}\frac{1}{1+\cos\Lambda_{c/4}} + 0.4\frac{z_w}{z_f} + 0.009A \tag{7.20}$$

It should be noted that the estimation of the DATCOM method on which this equation is based generally underpredicts the actual $C_{n_{\beta_v}}$ compared to CFD [48] and having a higher value is generally better for lateral gust recovery [44]. Therefore the $C_{n_{\beta_v}}$ will be sized to exactly converge to 0.057.

7.8. Tail Boom Structural Design

For the structural analysis of the boom, new symbols were used on top of the already existing symbols. These symbols are summarized below:

Symbol	Name	Unit
T_F, T_A	Thrust of the most forward and aft engines	N
F_v, F_h	Force output of the vertical and horizontal stabilizers	N
F_c	Reaction force at the center of the wing at the boom attachment point	N
τ_F, τ_A	Torque output of the most forward and aft engines	$\mathrm{N\,m}$
M_{x_c}, M_{y_c}	Reaction moment about the x-axis and y-axis at the center of the wing at the boom attachment point	$\mathrm{N\,m}$
d_{e_F}, d_{e_A}	Distance from the center of the wing at the boom attachment point to the forward and aft engines	m
d_h	Distance from the center of the wing at the boom attachment point to the center of the horizontal stabilizer	m
$\theta_x, \theta_{\text{req}}$	Twist angle of the boom and allowable twist angle of the boom.	rad
E, G	Elastic and shear modulus of the material	$\mathrm{N\,m^{-2}}$

Continued on next page

Symbol	Name	Unit
I, J	Second moment of area of the cross-section and polar moment of area, xx, and yy subscripts indicate relevant the centroidal axis	m^4
t, t_b	Thickness of the boom	m
R_b	Radius of the boom	m
ϕ_z	Twist angle due to torsion of the boom	rad
σ_z	Internal normal stress that runs axially through the boom	$\mathrm{N\,m^{-2}}$
M_x, M_y	Internal moment of the boom about the x and y axis	$\mathrm{N\,m}$
τ_{xy}	Internal shear of the boom	$\mathrm{N\,m^{-2}}$
σ_{mises}	Combined von misses stress on the boom	$\mathrm{N\,m^{-2}}$
σ_h	Hoop normal stress that follows the radius circumferentially of the boom	$\mathrm{N\,m^{-2}}$
m_b, m_e	Mass of the boom and empennage	kg
L_b	Total length of the boom	m
ρ	Density of the material	$\mathrm{kg\,m^{-3}}$
ρ_e	Density of the empennage	$\mathrm{kg\,m^{-2}}$

The boom was modeled using the free body diagram shown in Figure 7.7, which is a combined loading case. The attachment point was assumed to be clamped at the center of where it is attached to the wing. This is conservative as realistically this load would be distributed over a larger area. The vertical tail load was assumed to coincide with the load of the horizontal tail, this is also conservative as this increases the internal moment.

For the boom geometry, a thin-walled tube was chosen, as tubes are the most efficient shape for torsional loading [52], and tubes also handle biaxial bending loads well due to the concentrated material at a good distance from the neutral axis and the radial symmetry. The boom material was chosen to be the same as the wing material from Chapter 6, to prevent possible galvanic corrosion [53].

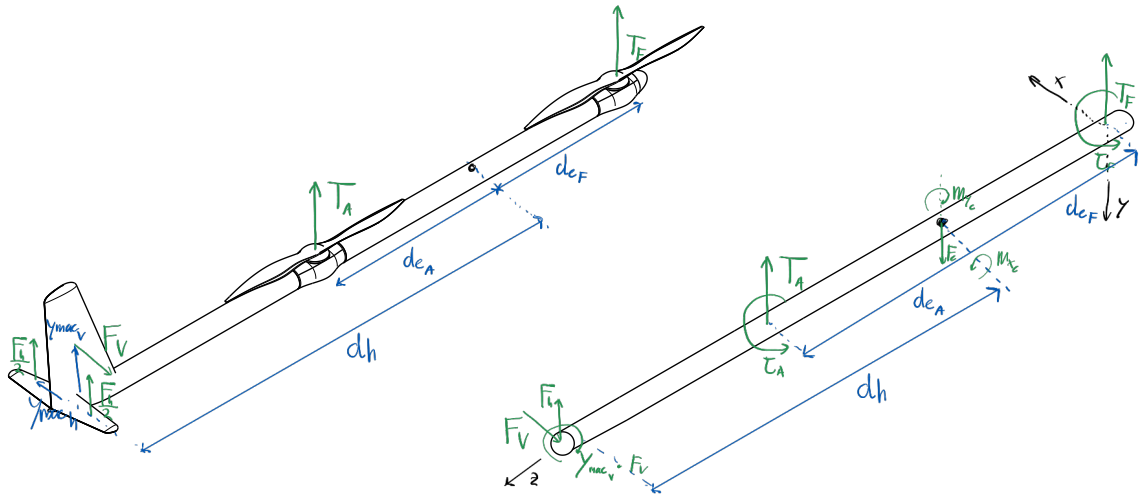

Figure 7.7: Free body diagram of the boom

In terms of loads, the maximum VTOL thrust force and torque were taken from Chapter 4. Analyzing the ultimate tail loads rigorously requires detail that is not known yet at this stage of the design [54, p. 115-160]. To simplify it, the maximum tail loads were extracted using Equation 7.21, for which sea level conditions at intervention velocity were taken as limiting cases. The equation is multiplied by another safety factor of 1.5.

$$F_h = 1.5 \cdot \frac{1}{2}\rho V^2 S_h C_{L_{h\mathrm{max}}} \qquad F_v = 1.5 \cdot \frac{1}{2}\rho V^2 S_v C_{L_{v\mathrm{max}}} \tag{7.21}$$

With this free-body diagram, the internal moments along the boom were extracted using Macaulay step functions [52].

Angle-constrained Thickness

By integrating the internal moment and setting $\theta(z)EI$ at the boundary condition to zero to extract the integration constant, $\theta(z)EI$ can be extracted [52]. Since E is known by material selection, and I is a function of thickness (Equation 7.23 and boom diameter, with this, the minimum thickness can be solved for resulting in Equation 7.24. This bending angle was also analyzed for the angle about the y-axis (longitudinal), where x and y are interchanged in the equations.

$$\frac{d}{dz}\left(\theta_x(z)\right) EI_{\text{xx}} = M_x(z) \quad (7.22) \qquad I_{\text{xx}} = \pi R_b^3 t \quad (7.23) \qquad t_{\text{min}} = \frac{(\theta(z)EI_{\text{xx}})_{\text{max}}}{E\pi R_b^3 \theta_{\text{req}}} \quad (7.24)$$

Twist-constrained Thickness

Since there is torsion on the boom also, the twist has to be computed. For a radially symmetric beam under constant torsion the twist can be computed using Equation 7.25 [52], the polar moment of inertia can be computed using Equation 7.26. With these combined and substituting the torque and distance from Figure 7.7 the minimum thickness for the twist constraint can be computed using Equation 7.27.

$$\phi_z = \frac{TL}{GJ} \quad (7.25) \qquad J = 2\pi R_b^3 t \quad (7.26) \qquad t_{\text{min}} = \frac{y_{\text{mac}_v} F_v d_h}{2\pi R_b^3 \phi_{\text{req}} G} \quad (7.27)$$

Stress-constrained Thickness

The biaxial symmetric bending stress can be computed using Equation 7.28 [31]. Here first the general symmetric biaxial bending equation is taken. Since the cross section is radially symmetric x and y can be converted to polar coordinates. Then by taking the derivative with respect to α the position along the cross-section where the maximum stress occurs can be computed. Since I_{xx} is equal to I_{yy} the equation can be simplified.

$$\sigma_z = \frac{M_x y}{I_{\text{xx}}} + \frac{M_y x}{I_{\text{yy}}} \longleftrightarrow x = \cos\alpha, y = \sin\alpha \longleftrightarrow \alpha_{\sigma_{z_{\text{max}}}} = \arctan\frac{M_x I_{\text{yy}}}{M_y I_{\text{xx}}} = \arctan\frac{M_x}{M_y} \quad (7.28)$$

There is also shear loading due to torsion, which can be computed using Equation 7.29 [52] which applies for radially symmetric cross sections. The internal shear flow is constant facing in the direction of the torque [52].

The stress in a thin-walled pipe under combined stress can be found using Equation 7.30 [55], which is derived from the von Mises stress criterion. In this yield criterion, if the von Mises stress exceeds the yield stress of the material, the material will deform plastically. Hoop stresses (σ_h) were ignored as the tube is not pressurized, simplifying the equation.

$$\tau_{\text{xy}} = \frac{TR_b}{J} = \frac{y_{\text{mac}_v} F_v R_b}{J} \quad (7.29) \qquad \sigma_{\text{mises}} = \sqrt{\sigma_h^2 + \sigma_z^2 - \sigma_h\sigma_z + 3\tau_{\text{xy}}^2} \quad (7.30)$$

Now to solve for the thickness, observe that Equation 7.23 and Equation 7.26 both depend on thickness. Therefore, to extract the minimum required thickness, a numerical Newton-Raphson solver [56] was used. The maximum allowed stress was divided by a safety factor of 1.5.

Extracting the minimum required thickness is done by gathering the maximum non-dimensional bending and twist angles, and maximum moments along the boom, and extracting the minimum thicknesses based on the four criteria presented by **RTL-STR-1**, **RTL-STR-2** and **RTL-STR-3**. From these four thicknesses, the highest minimum thickness is extracted and then rounded upward to the nearest $0.1\,\text{mm}$. This rounding is done to stay conservative and to account for manufacturing tolerances.

Mass Extraction

With all the geometry defined, the mass is extracted and updated. The mass updates are only done after the optimum is found to go into the next iteration. The mass of the boom was computed using Equation 7.31.

Next, the mass of the empennage was estimated using an empirical estimation for aluminum empennages, as the loads on the empennage are still uncertain. An estimation was used where the density

of an aluminum empennage is approximately 1 pound per square foot ($4.88\,\mathrm{kg\,m^{-2}}$)[5] as can be seen in Equation 7.32. This method fits quite well the trendline of several other tactical UAVs [57].

$$m_b = 2\pi R_b t_b L_b \rho \tag{7.31}$$

$$m_e = (S_h + S_v)\rho_e \tag{7.32}$$

7.9. Balancing Tool Results

The inputs for the program were the final fuel mass and velocities from Chapter 2, the final propeller sizes, VTOL engine masses, engine thrust and torques from Chapter 4, the final wing parameters and material properties from Chapter 6, and finally, the final aft landing gear mass and final fuselage shape and mass distribution from Chapter 8.

In terms of design parameters, a boom diameter of $0.15\,\mathrm{m}$ was chosen, increasing this further would decrease the boom mass and thickness, at the cost of aerodynamic drag. $0.15\,\mathrm{m}$ turned out to result in a reasonable thickness-to-diameter ratio that is manufacturable and where buckling has a low probability. Decreasing it beyond this would increase the structural mass and likely have consequences to the drag as the engine diameter of $0.188\,\mathrm{m}$ would cause significant bulges on the boom.

A boom distance of $1.4\,\mathrm{m}$ and a propeller wing clearance of $0.15\,\mathrm{m}$ was chosen to ensure that the aircraft still fits in the ground station and the propellers do not clash. The final output for the 3-view drawing of the program can be seen in Figure 7.8.

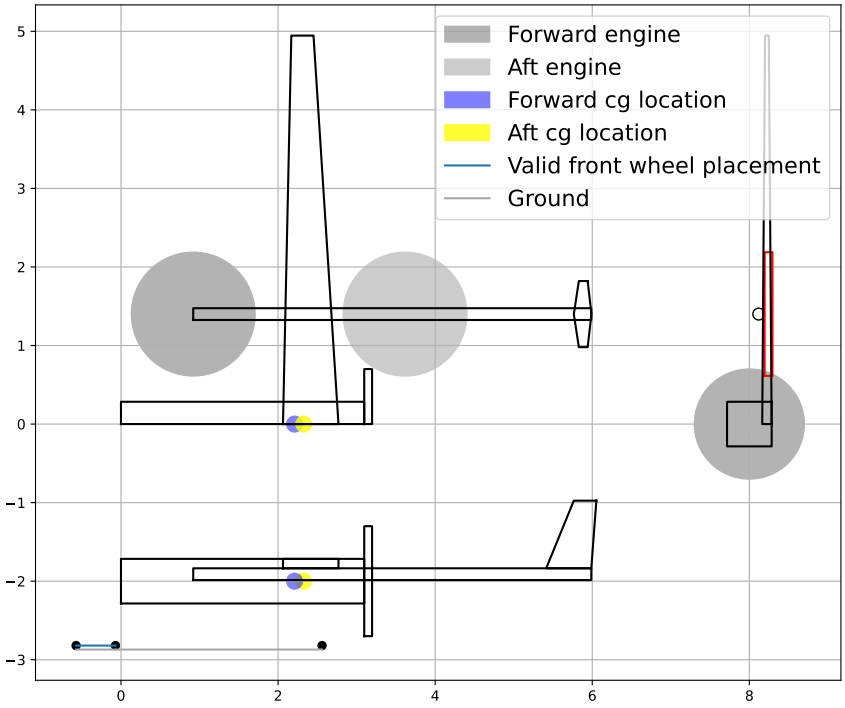

Figure 7.8: Final 3-view drawing output of the balancing tool.

The geometric relations can be extracted directly from Figure 7.8, as the aspect ratio is equal and dimensions and relative positioning are true to the output. The total horizontal and vertical tail surface area was found as $0.283\,\mathrm{m^2}$ and $0.741\,\mathrm{m^2}$, resulting in a mass of $2.5\,\mathrm{kg}$ per boom. The boom thickness was found as $4.2\,\mathrm{mm}$, resulting in each bare boom weighing $8.7\,\mathrm{kg}$. This implies that the total mass of each boom and tail including VTOL propulsion is $27.4\,\mathrm{kg}$.

7.10. Internal Balancing Tool Verification

The final main version of the tool relies on 29 functions that incorporate the equations and methods shown so far. For these functions, unit tests were performed to ensure the output was reasonable.

One finding from the unit testing is that the downwash estimation from Equation 7.10 was underpredicting the downwash by $40\,\%$ compared to a CFD paper [58] analyzing the downwash of a similar high aspect ratio UAV. With this result, the downwash equation was multiplied by a factor of 1.4 to compensate.

Next to the unit tests, system tests were performed. An example of such a system test was already visible in Figure 7.4, which was used to verify correct behavior of the VTOL engine positioning. Another system test is manually measuring the scrape angle output of the final program. Other system tests include the behavior of the bending moments and angles over the tail boom, an example can be seen in Figure 7.9. Primary checks for this were 0 bending moment at the free ends of the boom, correct function behavior after integration, and a zero angle at the boundary condition.

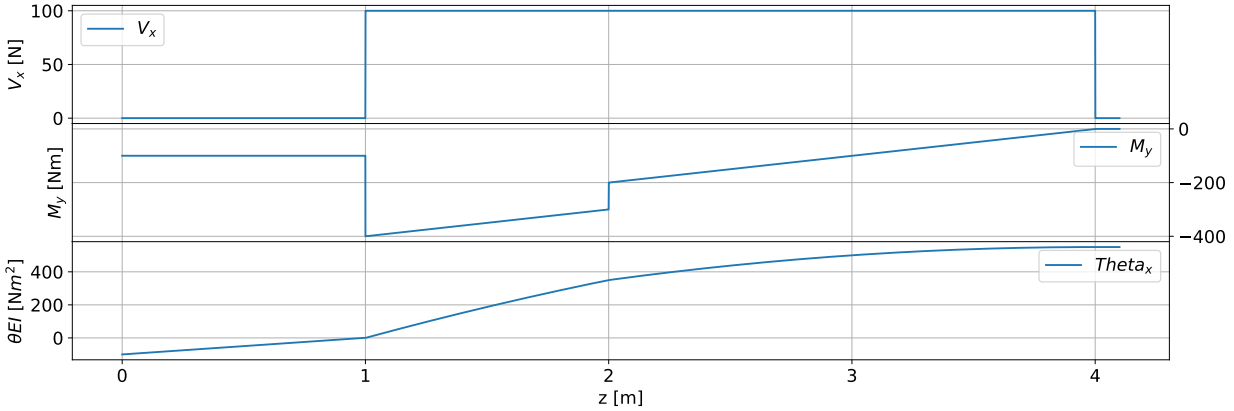

Figure 7.9: Example of system test output of the internal shear in the x direction, moment about the y-axis, and angle about the y-axis. For this test $d_{e_f} = d_{e_a} = 1\,\mathrm{m}$, $\tau_a = \tau_f = 100\,\mathrm{N\,m}$, $F_v = 100\,\mathrm{N}$, $d_h = 3\,\mathrm{m}$.

Another system test was performed to analyze the convergence of the program based on initial conditions. A visual method was used by plotting the relative difference between the previous value, as shown in Figure 7.10. It can be seen that the convergence is well-behaved and that the program correctly ends when the difference in tail surface area is $1 \times 10^{-5}\,\%$. It was also tested if the program converges to the same values with unusual initial conditions. For example, if the initial mass of the boom starts as $100\,\mathrm{kg}$, the program still converges to the same final result.

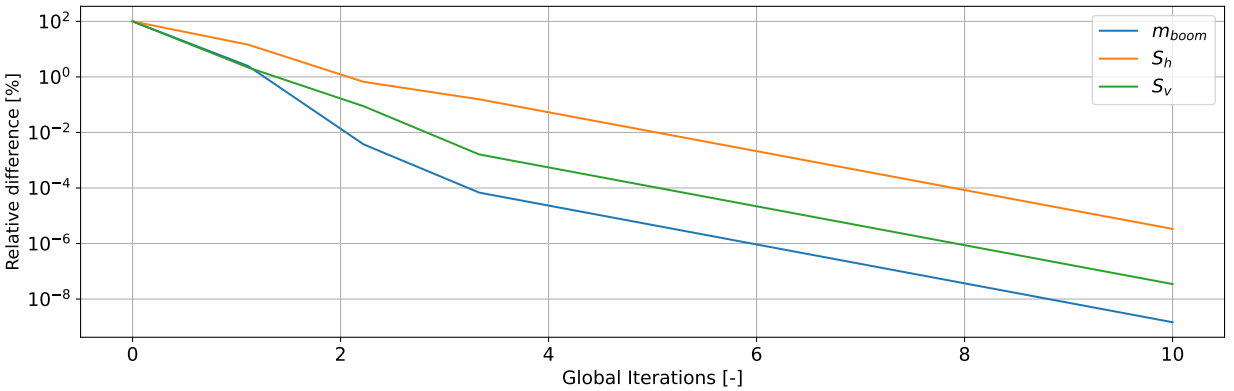

Figure 7.10: Convergence of the program. The y-axis shows the relative difference between the previous values in percentages. For this plot, the initial mass of the boom and tail surface areas were set as 0.

As a crude validation method, a final check on the tail volume coefficients was compared to values in literature. The tail volume coefficients can be computed using Equation 7.33 [47]. The final tail volume coefficient for the horizontal tail was found to be 0.3628 , and for the vertical tail, it was 0.0504 For the horizontal stabilizer, typical values for a single-engine aircraft range between 0.46 and 1.07 [47]. For the vertical stabilizer, the values range between 0.024 and 0.087 [47]. While the vertical stabilizer

size falls within the expected range, the horizontal stabilizer volume is underpredicted compared to empirical numbers.

$$\mathbb{V}_h = \frac{l_h S_h}{S\bar{c}} \qquad \mathbb{V}_v = \frac{l_v S_v}{Sb} \tag{7.33}$$

7.11. External Balancing Tool Verification

The final geometry output of the aircraft was input into openVSP, similarly to the procedure discussed in Chapter 6. with this the static stability derivatives C_{M_α} were extracted to verify the longitudinal static stability and the C_{n_β} of the whole aircraft was extracted to verify the vertical tail sizing method.

The angle of attack for the horizontal stabilizer was swept within the operational range of $-3°$ and $15°$ for the most aft (destabilizing) CG position. Initially, this resulted in a negative (stable) C_{M_α}, but there was no trim point over the whole range. To create a trim point that matched the optimal angle of attack value at the monitoring speed, the angle of incidence of the horizontal tail was adjusted. A satisfactory trim point was found with an angle of incidence of the tail at $-5°$, resulting in a trim angle of attack of $3.5°$. The C_{M_α} curve is visualized in Figure 7.11. Regressing the slope yields a C_{M_α} value of $-0.832\,\mathrm{rad}^{-1}$, which is a typical value for a stable conventional aircraft [44]. This verifies **RTL-AER-1**.

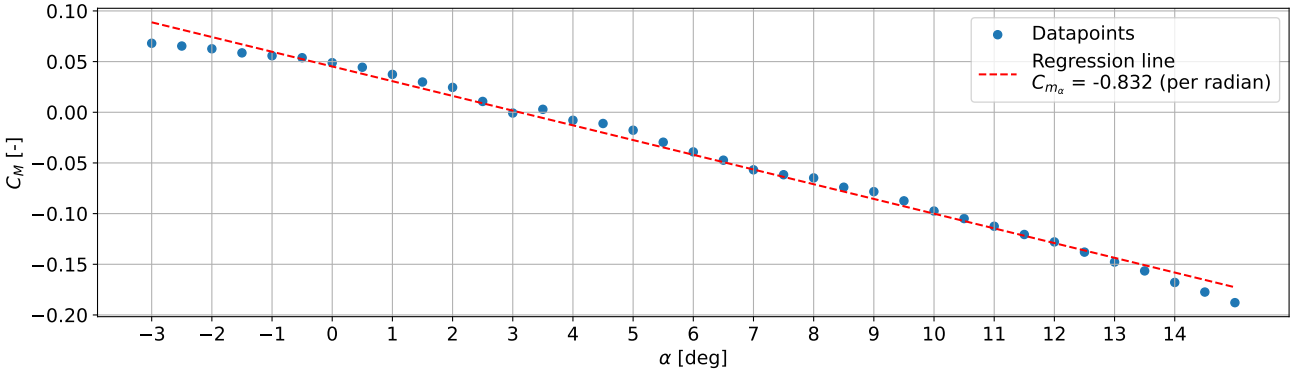

Figure 7.11: C_{m_α} curve of the full aircraft from the OpenVSP model

For the vertical stabilizer, the lateral stability derivatives can also be extracted from openVSP with the internal stability file output. The C_{n_β} was extracted for an angle of attack of $0°$ and at a sideslip angle of $0°$. With this, a value of 0.067 was extracted. This is only $16\,\%$ larger than the 0.057 value that the vertical stabilizer was sized for. The larger value was expected and also beneficial as noted in the methodology. A positive C_{n_β} indicates lateral static stability verifying **RTL-AER-3**.

During verification, three major weaknesses of the balancing tool were identified. They are discussed below:

- **Empennage load prediction:** The way the code is written as of now, is that the framework for calculating the boom thickness already exists, and the modularity of the code allows further modifications to the tail load estimation to be added to the program as the flight envelope of the UAV matures during detail design.
- **Underprediction of horizontal tail volume:** The tail volume coefficient was compared to single-engine, crewed aircraft from an old design book. The mission, regulations, and aircraft geometry of such planes are vastly different. One example of a difference with such aircraft would be their inclusion of high lift devices, which dramatically restrict the maneuverability line [45]. Furthermore, the code can be improved in the future to include other restrictions for tail size, such as out-of-trim maneuverability [26].
- **Tail incidence angle**: An incidence angle of $-5°$ is deemed unacceptable. The values found in the literature were no lower than $-3°$ [47]. This likely indicates a wing placement that is too far

aft, causing controllability issues. For this the methods for predicting the aerodynamic center of the wing-fuselage combination could be further improved. To reduce the angle of incidence required, the airfoil can also be adjusted to contain negative camber [45].

7.12. Dynamic Stability Analysis

The analysis of the stability of the aircraft continued with the assessment of dynamic stability. To simulate and analyze the stability properties of the UAV, symmetrical and asymmetrical equations of motion were used to see how the UAV behaves under such perturbations. Five different eigenmotions exist, of which two are symmetric and caused by pitch perturbations, and three are asymmetric due to roll and yaw perturbations:

Symmetrical eigenmotions:

- Short period oscillation
- Phugoid motion

Asymmetrical eigenmotions:

- Aperiodic roll motion
- Dutch roll motion
- Spiral motion

All required stability coefficients to analyze the aircraft eigenmotions were extracted directly from the VSPAero aerodynamic model as described in Chapter 6. Since there are limitations to the VSPAero stability derivative outputs for unsteady derivatives, that for example rely on $\dot{\alpha}$ or $\dot{\beta}$, simplified representations of the equations of motions for the eigenmotion analysis had to be derived.

7.12.1. Symmetrical Equations of Motion

The equations used to simulate the symmetrical eigenmotions are depicted in matrix form in Equation (7.34) [44]:

$$\begin{bmatrix} C_{X_u} - 2\mu_c D_c & C_{X_\alpha} & C_{Z_0} & 0 \\ C_{Z_u} & C_{Z_\alpha} + (C_{Z_{\dot{\alpha}}} - 2\mu_c)D_c & -C_{X_0} & C_{Z_q} + 2\mu_c \\ 0 & 0 & -D_c & 1 \\ C_{M_u} & C_{M_\alpha} + C_{M_{\dot{\alpha}}} D_c & 0 & C_{M_q} - 2\mu_c K_Y^2 D_c \end{bmatrix} \begin{bmatrix} \hat{u} \\ \alpha \\ \theta \\ \frac{q\bar{c}}{V} \end{bmatrix} = 0 \tag{7.34}$$

Simplified Short Period Oscillation

When the angle of attack is increased for a short period, the UAV will undergo a short period of oscillation as it tries to dampen this sudden disturbance. This motion typically happens over a very short time, therefore a constant velocity is assumed at this airspeed. Consequently, $\hat{u} = 0$, and the first column can be disregarded. Additionally, due to this constant velocity assumption, the forces in the X_B direction should remain in equilibrium, so the first row of the matrix can also be neglected. Assuming initial steady flight, where γ_0 and C_{X_0} are both 0, the kinematic relation $-D_c\theta + \frac{qc}{V}$ can also be disregarded[44]. This simplifies the equation of motion to the system shown in Equation 7.35:

$$\begin{bmatrix} C_{Z_\alpha} + (C_{Z_{\dot{\alpha}}} - 2\mu_c)D_c & C_{Z_q} + 2\mu_c \\ C_{M_\alpha} + C_{M_{\dot{\alpha}}} D_c & C_{M_q} - 2\mu_c K_Y^2 D_c \end{bmatrix} \begin{bmatrix} \alpha \\ \frac{q\bar{c}}{V} \end{bmatrix} = 0 \tag{7.35}$$

The eigenvalues of this simplified matrix can be extracted and define the behavior of the motion. If the real part of these eigenvalues is negative, the aircraft is stable.

Simplified Phugoid Motion

The phugoid is the steady-state oscillation that occurs after the disturbance of the short-period motion. In the phugoid motion, the angle of attack is approximately constant, dropping $\dot{\alpha}$. Additionally, the pitch rate is very low, therefore the time rate of change coefficients $D_c(\frac{q\bar{c}}{V})$ and $D_c\alpha$ can be ignored. Finally, C_{z_q} can also be neglected as it is significantly smaller than 2μ. This leads to the following simplified equations of motion for the phugoid [44]:

$$\begin{bmatrix} C_{Xu} - 2\mu_c D_c & C_{X_\alpha} & C_{Z_0} & 0 \\ C_{Z_u} & C_{Z_\alpha} & 0 & 2\mu_c \\ 0 & 0 & -D_c & 1 \\ C_{m_u} & C_{m_\alpha} & 0 & C_{m_q} \end{bmatrix} \begin{bmatrix} \hat{u} \\ \alpha \\ \theta \\ \frac{q\bar{c}}{V} \end{bmatrix} = 0 \tag{7.36}$$

7.12.2. Asymmetrical Equations of Motion

The equations used to simulate the asymmetrical eigenmotions are depicted in matrix form in Section 7.12.2 [44]:

$$\begin{bmatrix} C_{Y_\beta} + \left(C_{Y_{\dot{\beta}}} - 2\mu_b\right) D_b & C_L & C_{Y_p} & C_{Y_r} - 4\mu_b \\ 0 & -\frac{1}{2} D_b & 1 & 0 \\ C_{l_\beta} & 0 & C_{l_p} - 4\mu_b K_X^2 D_b & C_{l_r} + 4\mu_b K_{XZ} D_b \\ C_{n_\beta} + C_{n_{\dot{\beta}}} & 0 & C_{n_p} + 4\mu_b K_{XZ} D_b & C_{n_r} - 4\mu_b K_Z^2 D_b \end{bmatrix} \begin{bmatrix} \beta \\ \phi \\ \frac{pb}{2V} \\ \frac{rb}{2V} \end{bmatrix} = \begin{bmatrix} -C_{Y_{\delta_a}} & -C_{Y_{\delta_r}} \\ 0 & 0 \\ -C_{l_{\delta_a}} & -C_{l_{\delta_r}} \\ -C_{n_{\delta_a}} & -C_{n_{\delta_r}} \end{bmatrix} \begin{bmatrix} \delta_a \\ \delta_r \end{bmatrix}$$

Which can also be simplified for the specific asymmetric eigenmotions.

Simplified Aperiodic Roll Motion

The aperiodic roll motion describes the transient damping of roll rate under a sudden roll disturbance. The yawing moment is neglected, so all components due to sideslip angle β and $\frac{rb}{2V}$ disappear. The equations for lateral force and the yawing moment can be disregarded as well. Therefore, only the second and the third row remain, and as the roll angle ϕ does not appear in the third row, the relation $-\frac{1}{2} D_b \phi + \frac{pb}{2V}$ may be removed [44]. This leaves Equation 7.37 for the simplified representation.

$$\left(C_{l_p} - 4\mu_b K_X^2 D_b\right) \frac{pb}{2V} = 0 \tag{7.37}$$

Simplified Dutch Roll Motion

During the Dutch roll motion, the UAV rolls and yaws in an oscillatory fashion after a yaw disturbance. To approximate the eigenvalues, the rolling moment can be disregarded. This removes the two center columns and rows. By neglecting $C_{Y_{\dot{\beta}}}, C_{n_{\dot{\beta}}}$and C_{Y_r}, with this, the equations for dutchroll were simplified into Equation (7.38).

$$\begin{bmatrix} C_{Y_\beta} - 2\mu_b D_b & -4\mu_b \\ C_{n_\beta} & C_{n_r} - 4\mu_b K_Z^2 D_b \end{bmatrix} \begin{bmatrix} \beta \\ \frac{rb}{2V} \end{bmatrix} = 0 \tag{7.38}$$

Simplified Spiral Motion

When an aircraft is given a sudden roll disturbance with unstable spiral eigenmotion the roll angle will slowly keep increasing. Typically this happens at a very slow rate, which can be corrected by providing an opposite roll input. As the UAV goes into a spiral, it will experience sideslip, yaw, and roll. It can be assumed that all linear and angular accelerations are negligible. This means that $D_b \beta = D_b \frac{pb}{2V} = D_b \frac{rb}{2V} = 0$. Additionally, C_{Y_r} and C_{Y_P} can be ignored, resulting in simplified equations of motion for spiral motion Equation 7.39 [44].

$$\begin{bmatrix} C_{Y_\beta} & C_L & 0 & -4\mu_b \\ 0 & -\frac{1}{2} D_b & 1 & 0 \\ C_{l_\beta} & 0 & C_{l_p} & C_{l_r} \\ C_{n_\beta} & 0 & C_{n_p} & C_{n_r} \end{bmatrix} \begin{bmatrix} \beta \\ \phi \\ \frac{pb}{2V} \\ \frac{rb}{2V} \end{bmatrix} = 0 \tag{7.39}$$

The parameters obtained with the balancing tool and the VSPAero simulation were input into these simplified equations of motion. The results are explained below.

7.12.3. Dynamic Stability Results

The eigenvalues calculated using VSPAero simulation are presented in Table 7.5. These eigenvalues indicate that the UAV exhibits instability in the phugoid and Dutch roll motions. Consequently, it is crucial to modify the design, as this situation is highly undesirable. All eigenmotions, except for the spiral, must be stable to ensure safe flight.

Table 7.5: Initial stability results for every eigenmotion.

Eigenmotion	Eigenvalues	Stable	Time to half amplitude [s]
Short period motion	-5.792±5.050j	Yes	0.120
Phugoid	0.011±0.246j	No	63.457 (double amplitude)
Aperiodic roll	-0.007	Yes	98.553
Dutch roll	0.216	No	3.205 (double amplitude)
Spiral	-0.007	Yes	93.449

The necessary design change can be supported with reference to Figure 7.12. The design will be positioned in the bottom right of the graph, where $E > 0$ and $R < 0$. To achieve the desired convergent Dutch roll and spiral stability, the rolling moment coefficient due to sideslip, C_{l_β}, should be less negative in order to shift left on the graph (2). Alternatively, increasing the weathervane stability coefficient C_{N_β} can cause a shift upward on the graph (1). To enhance the weathervane stability coefficient C_{N_β}, adjustments to the vertical tail sizing are necessary. However, since this may conflict with other ongoing design considerations, such as structural and balance calculations, the decision has been made to instead increase the rolling moment coefficient due to sideslip C_{l_β}.

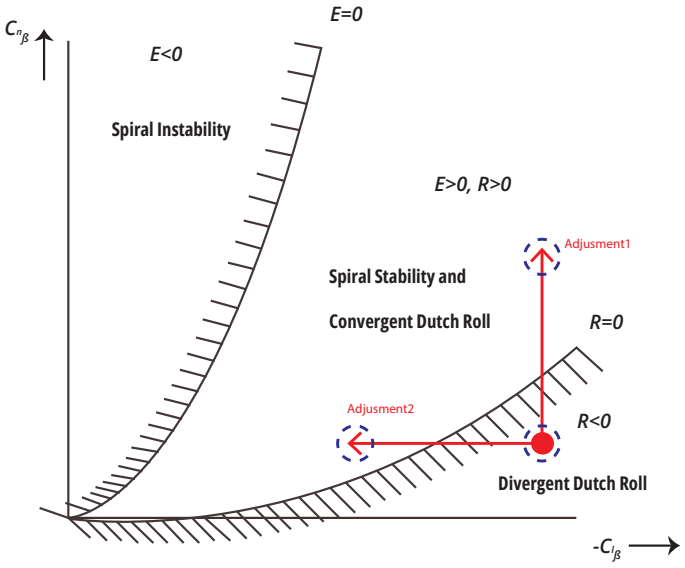

Figure 7.12: Spiral and dutch roll stability curve.

The rolling moment coefficient due to sideslip C_{l_β} can be increased by incorporating anhedral to the wings [44]. Therefore, anhedral was gradually added until stability for the Dutch roll was attained. The anhedral value for the main wing finally resulted in 1.5°. The eigenvalues corresponding to this new design are shown in Table 7.6.

Table 7.6: Stability results for every eigenmotion after design change.

Eigenmotion	Eigenvalues	Stable	Time to half amplitude [s]
Short period motion	-1.097±6.272j	Yes	0.632
Phugoid	-0.001±0.091j	Yes	644.112
Aperiodic roll	-0.008	Yes	87.699
Dutch roll	-0.023± 1.989j	Yes	30.364
Spiral	0.005	No	149.419 (double amplitude)

7.13. Tail Control Surface Design

The controllability of the aircraft depends on the size and position of the control surfaces. Traditionally, control surfaces are sized by simulating the aircraft's response in a state-space system [44]. This approach requires highly accurate values for the control derivatives, with a control force being simulated over the ailerons, rudder, and elevator. However, when applying the coefficients found with the VSPAero aerodynamic simulation, physically impossible results were obtained.

Alternative design methods were studied; for example, elevators are typically sized based on a constraining requirement for horizontal take-off [34]. None of the discovered methods had been developed for hybrid fixed wing-VTOL UAV's, and thus it was decided to select preliminary dimensions for the tail control surfaces empirically. The final dimensions for the rudder and elevator are shown in Table 7.8 and Table 7.7.

Table 7.7: Elevator dimensions [34].

	Ch/Ce	Se/Sh	Bh/Be
Conventional	0.20-0.40	0.15-0.40	0.80-1
FLOWS	0.30	0.30	1

Table 7.8: Rudder dimensions [34].

	Cr/Cv	Sr/Sv	Bh/Be
Conventional	0.15-0.40	0.15-0.35	0.80-1
FLOWS	0.30	0.30	1

The empirical estimation is expected to produce inaccuracies in further simulation. Therefore, it is recommended that further effort is dedicated to the sizing of the control surfaces, for example by performing a higher fidelity aerodynamic simulation and including the outputs in a state-space control analysis.

7.14. Gust Resistance Analysis

As set in requirement **R-SYS-1**, the aircraft must be flyable in wind conditions of up to $14\,\mathrm{m/s}$. For horizontal flight, the most constraining operational case will occur at a monitoring speed of $40\,\mathrm{m/s}$, as discussed in the mission profile in Section 9.3. The stall speed was determined to occur at $26\,\mathrm{m/s}$ in Section 2.2. Therefore, in horizontal flight, even with an incoming wind speed of $14\,\mathrm{m/s}$, the requirement can be met.

To ensure the UAV can operate in winds of up to $14\,\mathrm{m/s}$ in vertical flight, as set in **RTL-AER-5**, a simplified static analysis of aerodynamic forces has been performed. When using the vertical motors for flight, the maximum thrust-to-weight ratio for the heaviest loading case is 1.2, with a thrust force of $3178\,\mathrm{N}$. The maximum angle that can be achieved while maintaining equilibrium (hover) appears when the vertical thrust is equal to the weight, with a value of $2648\,\mathrm{N}$. This results in an angle of $33.56\,°$ and a horizontal thrust of $1756\,\mathrm{N}$, as shown in Figure 7.13.

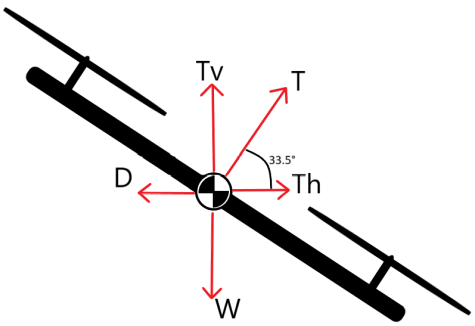

Figure 7.13: Quadcopter free body diagram and maximum body angle.

To fulfill requirement **RTL-AER-5**, the UAV has to be capable of flying at a horizontal velocity of $14\,\mathrm{m/s}$ or more. To find the maximum horizontal velocity as a result of the horizontal thrust, a drag coefficient

and a frontal surface area has to be estimated, as shown in Equation 7.40.

$$T_h = D = 0.5\rho V^2 S \tag{7.40}$$

The top-view technical drawing of the aircraft was used to conservatively estimate the surface of the aircraft at $8\,\mathrm{m}^2$. When angled by $33.56\,°$, the frontal surface area becomes $4.42\,\mathrm{m}^2$. For the drag coefficient, the most conservative value was selected, namely the flat plate drag coefficient of 1.28. This conservative value was chosen to account for the downforce produced by the flow over the wing. Using Equation 7.40, the maximum horizontal velocity was be calculated to be $25.47\,\mathrm{m/s}$.

This estimation results in a maximum gust resistance of $25\,\mathrm{m/s}$ while maintaining hovering flight. However, stability effects and flow downforce are not accounted for, as the model represents a static analysis. Therefore, it is recommended to reiterate this analysis with a higher fidelity model in order to guarantee compliance with **RTL-AER-5**.

7.15. Stability, Balance, and Tail Design Verification

To guarantee compliance with the requirements in Table 7.1, verification methods were defined. They are presented in Table 7.9.

Table 7.9: Stability, balance, and tail design verification methods.

ID	Verification method	Discussion
RTL-AER-1	Demonstration	Integrate system and perform longitudinal stability tests in various flight conditions.
RTL-AER-2	Demonstration	Integrate system and perform stall recovery maneuvers to ensure control at stall speed.
RTL-AER-3	Analysis	Analyze lateral stability using simulation software and wind tunnel tests.
RTL-AER-4	Analysis	Perform CFD analysis to ensure empennage is not in the wing wake during a stall.
RTL-AER-5	Test	Conduct wind tunnel tests to verify wind resistance of 14 m/s in vertical flight.
RTL-AER-6	Test	Conduct wind tunnel tests to verify wind resistance of 14 m/s in horizontal flight.
RTL-STR-1	Analysis	Use finite element analysis to verify tail boom twist is within acceptable limits.
RTL-STR-2	Analysis	Perform structural analysis to ensure tail boom angle is within 1° under ultimate loads.
RTL-STR-3	Test	Apply ultimate loads to tail boom in a test environment and measure stresses and deformations.
RPR-BAL-1	Inspection	Check engine mounts and their positions to ensure they are balanced about the center CG position.
RPR-CSH-1	Inspection	Inspect the arrangement of vertical and horizontal propellers to ensure no clashes during transition.
RLG-BAL-1	Analysis	Perform a geometric analysis to confirm the aft landing gear provides a scrape angle of no less than 15°.
RLG-BAL-2	Test	Conduct load distribution tests to verify the nose landing gear carries between 8% and 15% of the total aircraft weight.

Most of these verification methods can be performed at the Faculty of Aerospace Engineering at TU Delft, for example the wind tunnel tests, structural analysis and CFD. The demonstration tests require assembly of the system and a mock mission. These tests can be performed in combination with tests described in e.g. Section 3.7 at a range with free airspace, such as the local range at ASK 't Harde.

8 | Fuselage Design

This chapter covers the design of the fuselage of the aircraft. As it constrains further design, the sizing of the landing gear is first presented in Section 8.1. Then, the fuselage layout is presented in Section 8.2, and the design of the structure is described in Section 8.3. Finally, Section 8.4 describes the verification of the fuselage design, but also the independent verification of the structural design process performed with the finite element method.

8.1. Landing Gear Design

The landing gear is sized to support the body of the UAV during taxi, vertical take-off, and landing. However, the requirement for safe landing in case of propulsion system failure also needs to be met. Table 8.1 contains the requirements identified for the landing gear.

Table 8.1: Landing gear requirements.

ID	Requirement description	Origin
RLG-VER-1	The landing gear shall allow for vertical take-off and landing.	**R-MIS-5**
RLG-HOR-1	The landing gear shall allow for horizontal landing.	**R-SYS-16**
RLG-SUP-1	The landing gear shall support the UAV maximum take-off weight during taxi, take-off, and landing.	**R-SYS-16**
RLG-COM-1	The landing gear shall be composed of COTS components.	**R-MIS-9**

- **RLG-VER-1** ensures that the critical VTOL capabilities are available.
- **RLG-HOR-1** ensures that the UAV is capable of a horizontal landing from gliding flight, allowing for contingency in case of power generation or propulsion failure.
- **RLG-SUP-1** ensures that the landing gear can support the heaviest possible version of the UAV in all operational conditions.
- **RLG-COM-1** follows from the top-level design intention to rely on proven, already existing components.

RLG-HOR-1 makes it impossible for any strut- or skid-based landing gear to be selected, so a traditional wheel-based assembly is required. This results in typical aircraft landing gear design constraints: pitch, scrape, and tip-back angles limiting the longitudinal position, as well as lateral ground clearance limiting the horizontal position. The former are discussed in Chapter 7, while the latter will be evaluated after the selection of the landing gear based on the calculated wing deflection in Chapter 6.

Several landing gear configurations are available, from the traditional tricycle to quadricycle, taildragger, mono-wheel and bicycle. To limit weight and ensure that components can be found off-the-shelf, it was decided to pursue a traditional tricycle configuration, with a single nose landing gear and a larger main landing gear. The main landing gear is expected to be positioned on the belly of the fuselage, as the high wing configuration would result in overwhelmingly tall (and therefore large and heavy) landing gear struts.

During the wing design process in Chapter 6, a maximum downward deflection of $3.3\,\mathrm{cm}$ was found. Though the landing gear is only to be used for horizontal landing in case of emergency, with no ground maneuvering being expected, clearance for the wing should still be provided. The longitudinal position of the landing gear was calculated during the coupled stability-tail design analysis in Chapter 7, resulting in a required height of $0.59\,\mathrm{m}$ from the ground to the bottom of the fuselage.

The two values above, together with the maximum take-off weight of $274\,\mathrm{kg}$ estimated in Chapter 2, represent the constraints for the landing gear selection procedure.

After a comprehensive market study, two suppliers were discovered, one for the main landing gear and the other for the nose landing gear. The Grove Aircraft Corby Starlet frame proved the lightest from all evaluated options, withstanding a maximum load of $3.34\,\mathrm{kN}$[1]. When equipped with 49-1A wheels and Aero Classic 400-4 8 ply tires[2], the ground-to-fuselage distance is equal to $54.6\,\mathrm{cm}$, less than $5\,\mathrm{cm}$ from the required distance . Therefore, the fuselage structure in the area of the landing gear is to be designed with a downward bulge to allow for the minimum ground distance to be complied with. The Corby Starlet frame is manufactured out of Al7075-T6, and was specifically chosen instead of a composite frame due to its recyclability. The total main landing gear assembly weighs $11.5\,\mathrm{kg}$.

For the nose landing gear, the AeroTelemetry Light Nose Landing Gear assembly was selected. Allowing for steering and braking, this landing gear has a maximum length of $74.9\,\mathrm{cm}$, which is quite higher than the required $0.59\,\mathrm{m}$, and will therefore require special integration. The total mass of the nose landing gear assembly is given as $9.1\,\mathrm{kg}$, with a maximum acceptable load of $1.34\,\mathrm{kN}$[3]. Both landing gears are shown in Figure 8.1 below.

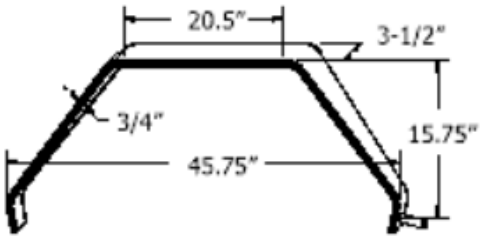

(a) Corby Starlet landing gear frame sketch[1].

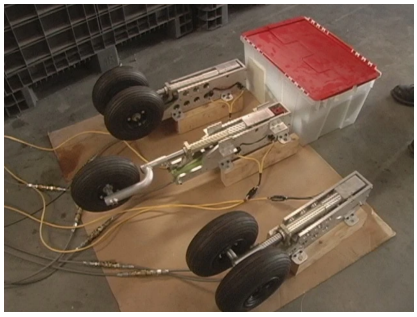

(b) AeroTelemetry nose landing gear (center)[3].

Figure 8.1: Landing gear components.

8.2. Fuselage Layout Design

Once all the fuselage components have been selected, a logical next step would be to determine the position of each component within the structure. In order to facilitate this process and make sure all components are positioned beneficially, requirements are given in Table 8.2.

Table 8.2: Fuselage layout requirements.

ID	Requirement description	Origin
RFU-LAY-1	The fuselage shall have a length-width ratio between 4 and 8.	Aerodynamics
RFU-LAY-2	The maximum shift in c.g. throughout the mission shall be within stability and maneuverability limits.	**R-SYS-11**, **R-SYS-12**
RFU-LAY-3	The electrical components within the fuselage shall be located at a minimum distance of $1.5\,\mathrm{cm}$ from each other.	**TPRC-8**
RFU-LAY-4	The power plant of the UAV shall be located at the rear of the fuselage.	**R-MIS-2**
RFU-LAY-5	The communication subsystem shall not be hindered by the fuselage structure.	**R-MIS-3**, **R-MIS-4**
RFU-LAY-6	The landing gear shall not obstruct the field of view of the monitoring payload and the control camera.	**R-MIS-2**

- **RFU-LAY-1** is an important requirement in order to guarantee beneficial aerodynamic properties of the fuselage [41].
- **RFU-LAY-2** flows from controllability and stability of the UAV. A large shift in the center of gravity may make the UAV unstable, which is why this should be avoided.

[1] https://www.groveaircraft.com/landing_gear.html
[2] https://www.groveaircraft.com/4inch.html
[3] https://www.aerotelemetry.com/light-weight-uav-landing-gear

- **RFU-LAY-3** is important due to the electrical infrastructure. As many of these components will be connected, locating them far apart will increase the mass spent on wiring significantly.
- **RFU-LAY-4** follows from the monitoring requirement. Locating the instruments close to the vibrations and magnets of the internal power plant may diminish the quality of the measurements.
- **RFU-LAY-5** flows from the data transmission and communication requirements. This is important to consider when positioning the communication components, as they may be hindered by other components or structural elements.
- **RFU-LAY-6** flows from the requirement that the UAV shall be able to continuously monitor. This means that the landing gear shall not obstruct the field of view of either the cameras, or the LiDAR.

Before starting the placement of the subsystems, a note should be made on the fuselage layout. Firstly, empty space is kept between components to account for the integration, by means of wiring and structures. Secondly, an iterative process will be undertaken to obtain the final layout, with results available in Chapter 13. The following considerations apply.

Intervention Payload

An important starting point for the fuselage layout determination is the determination of the components that may shift the center of gravity. As the fuel is taken up in the wing-group, the only component which will significantly shift the center of gravity is the intervention payload. Therefore, this intervention payload should be located as closely as possible to the center of gravity. As the intervention payload is a large component, this offers a clear starting point.

Monitoring Payload

The position of the monitoring payload is integral to the success of its objective, and should therefore be considered early on in the layout determination. The choice has been made to position the LiDAR in front of the wings, at the bottom of the UAV. This ensures that the LiDAR can monitor the ground beneath, with its optimal angle of $90\,°$. Furthermore, the monitoring camera can be positioned under the nose of the UAV, as it too will be observing the ground.

Power Plant and Propulsion

As determined in Chapter 5, the power plant of the UAV will consist of four internal combustion engines (ICE's), which all connect to a control unit. These four engines require an air inlet. Furthermore, the UAV consists of one electronic speed controller (ESC) per motor, leading to a total of 5 electronic speed controllers. These components will be located in the back of the fuselage, so as to maximize the distance between the monitoring payload and the power plant.

In addition to the ICE's, the five ESC's require air cooling, meaning these components can be located close together and benefit from common air ducts. For this reason, it has been decided to locate the ESC's in front of the ICE's, with one air inlet on each side of the fuselage. The engine control units are then located in front of these components, as they benefit from a position close to the engine, but do not require cooling. Finally the electric motor and propeller for horizontal propulsion is located at the back of the fuselage to act as a pusher.

Communication

The UAV contains two different communication systems, which each have requirements for their respective position within the fuselage. The first component is the radio communication system, for which the Swiftlink P43 is selected. This component will include an antenna, which is mounted inside the UAV, and requires unobstructed communication with the ground station. Secondly, the MICRO SAT LW has been selected as the satellite communication system of the UAV. This again requires an unobstructed path to the sky, meaning these components can be positioned together under a common radome. This radome is positioned on top of the UAV, near the front, as can be seen in comparable UAV's [59].

Electrical Components and Computers
The electrical components are located near the monitoring devices, in order to reduce the total wiring mass. The choice has been made to implement a clearance between all electrical components to assure that wire harnesses can be implemented as required.

Landing Gear
The landing gear components have a fixed position within the fuselage. The nose landing gear is retractable, in order to allow for monitoring as required. It is positioned as far forward as possible, to satisfy its loading constraint, as explained in the previous section. The main landing gear is positioned beneath the power plant, but will not be retractable as this would increase the mass of the system far beyond the possible aerodynamic benefits.

Final Fuselage Layout
The preliminary layout was dfined based on the component dimensions supplied by each manufacturer. Once all components had been assessed and set in their optimal position, a CAD model was designed to visually assess the placement. Based on this, the final internal layout was created. It is presented with commentary in Chapter 13.

8.3. Fuselage Structural Design
The fuselage is a key component of the UAV, protecting internal components and transferring loads from the wingbox to the landing gear. The sizing of the fuselage structure is an iterative process, which starts by determining the critical load cases. In order to determine these load cases of the fuselage, it is important to examine the different operational environments. In addition, the fuselage of the FLOWS UAV is quite different from conventional aircraft, because it is not connected directly to the tail, which leads to different load cases than conventional fuselages.

The mission profile was analyzed, and critical load cases were identified. In each case, the load was multiplied by a safety factor of 1.5, to account for the difference between the limit load case and the ultimate load resistance (**TPRC-43**) [4]. The overall requirements for the structure of the fuselage are available in Table 8.3.

Table 8.3: Requirements for the structure of the fuselage.

ID	Requirement description	Origin
RFU-STR-1	The aircraft fuselage shall be able to withstand loads caused by a $3.6\,\mathrm{g}$ maneuver.	**R-STK-5**
RFU-STR-2	The aircraft fuselage shall be able to withstand loads caused by landing up to $2.0\,\mathrm{g}$.	**R-STK-5**
RFU-STR-3	The aircraft fuselage skin shall not carry any loads other than aerodynamic forces.	**R-STK-5**
RFU-STR-4	The aircraft fuselage shall be able to withstand loads caused by the horizontal propeller.	**R-STK-5**
RFU-STR-5	The aircraft fuselage deflection shall not interfere with safe operations.	**R-STK-8**
RFU-STR-6	The load bearing structure of the fuselage shall not hinder functionality of the internal subsystems.	**R-MIS-2**
RFU-STR-7	The fuselage structure shall have a precipitation tolerance of up to $50\,\mathrm{mm/h}$.	**R-SYS-2**.

- **RFU-STR-1** flows from the maximum load case during flight. This load occurs during the $3.6\,\mathrm{g}$ maneuver, which results in a load factor of 3.6 [60].
- **RFU-STR-2** follows from the maximum load case during landing and ground operations. This load case is inherently different from the first case, due to the induced forces of the landing gear

[4] https://www.law.cornell.edu/cfr/text/14/25.303

and the weight of the wing acting on the fuselage. The maximum loading for this is taken as $2.0\,\mathrm{g}$ [61].

- **RFU-STR-3** is a result of the many cutouts and obstructions of load paths throughout the skin. Therefore, the choice has been made to not make the skin load bearing. This means that the only loads experienced by the skin will be the aerodynamic loads.
- **RFU-STR-4** takes into account compression loads caused by the propeller. At maximum power, the propeller causes a compressive force of $365\,\mathrm{N}$.
- **RFU-STR-5** flows from the European Union Safety Aviation Agency, which states this requirement in the structural regulations of aircraft [5].
- **RFU-STR-6** is important to consider, as it states that the fuselage structure should not refrain the internal components from fulfilling their purpose.
- **RFU-STR-7** is an important requirement to satisfy, as a large number of components within the fuselage are not waterproof.

8.3.1. Internal Structural Configuration

Due to **RFU-STR-3**, the fuselage structure can be simplified to consist of two distinct parts. The first part will be the longeron, a structural element following the longitudinal body axis of the fuselage. The second element is the frame, which acts as a way of distributing the loads between the longerons, and by reducing the length of the longerons, which in turn counters buckling.

The shape and positioning of the subsystems provides a clear starting point for the determination of the fuselage structure, both in terms of position and layout. The largest, and therefore most limiting component is the intervention payload bay. With a width of $46\,\mathrm{cm}$ and an unobstructed floor due to the payload bay doors, this will determine the location of the lower two longerons, which are therefore set at $156.7\,\mathrm{mm}$ from the center of the fuselage.

Because load transfer between the wings and fuselage is integral for the $3.6\,\mathrm{g}$ maneuver, the choice has been made to run three longerons through the wing box. This combination of five longerons leads to the configuration shown in Figure 8.2. In this figure, the position of the longerons with respect to the frames can be observed. In addition, the choice has been made to give the longerons a thin-walled cylindrical shape, which ensures ease of manufacturing and a relatively high moment of inertia.

The frame spacing is also limited by the intervention payload. As the payload bay has a length of $78\,\mathrm{cm}$, the frame spacing which is able to withstand the loading should be no lower than $78\,\mathrm{cm}$. The frame shape has been set as a thin walled I-beam. Similarly to the longeron, this increases the ease with which it can be manufactured and provides a flat surface to which the fuselage skin can be attached.

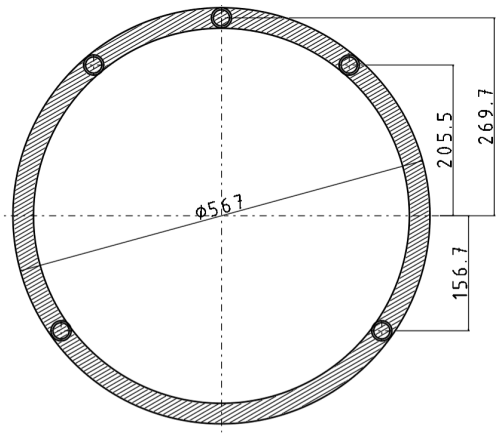

Figure 8.2: Position of the longerons with respect to the frames.

[5] https://www.easa.europa.eu/en/document-library/easy-access-rules/online-publications/easy-access-rules-large-aeroplanes-cs-25?page=13#_Toc256000060

The detailed design of the structural components of the airborne segment begins with an evaluation of the mission profile that should result in the critical load cases being identified. These critical loads are multiplied by the load factors and the loads on the structure are identified.

The aircraft system parameters identified during the Class-II weight estimation, together with data defined during the detail design of other subsystems, act as inputs and constraints on the structural design procedure. The following mission phases were identified:

1. Pre-take-off taxi: UAV is stationary on a horizontal surface, with full fuel tanks.
2. Vertical take-off: UAV vertical motors push the aircraft upwards, with full fuel tanks.
3. Vertical landing: UAV vertical motors allow the aircraft to slowly hover downwards, with either full or empty fuel tanks.
4. Maximum speed: UAV moves horizontally with maximum speed.
5. Monitoring: UAV moves horizontally at monitoring/cruise speed.
6. Hover: UAV hovers in place.

Based on the defined conceptual and preliminary design, the following structural components may be defined:

1. The wing is the largest structural component, and supports the VTOL motors, contains the fuel, and provides flight and attitude control capabilities.
2. The fuselage contains the avionics, data handling, payload bay, and horizontal flight capabilities.
3. The tail contains the horizontal and vertical stabilizer.
4. The VTOL booms contain the vertical motors and connect the wing to the tail.

The defined load cases and components were modeled analytically to calculate the required structural properties, as discussed in what follows.

8.3.2. Structural Modeling

To calculate the necessary structure to comply with the requirements, different failure modes must be analyzed. The following failure modes were analyzed:

- Yielding due to bending. This failure mode is analyzed to size the longerons such that they can withstand the bending loads when performing high-g maneuvers or when landing.
- Yielding due to compression of the frames. The frames must carry the aerodynamic loads, but most importantly must carry the loads from the landing gear shock.
- Buckling of longerons. Due to the bending and the force of the horizontal propeller applied on the fuselage, a compression force is introduced in the fuselage. This can cause the longerons to buckle if the frames are not spaced close enough.

The bending moments introduced are analyzed to find the necessary moment of inertia I_{yy} needed for the fuselage to not yield. A similar approach to the wing structure calculations was taken as described in Section 6.3.4. Each individual component in the fuselage is treated as a point load and the shear stress is calculated as shown in Equation 6.8.

The force of the wing on the fuselage is calculated as an evenly distributed load along the wingbox connection, starting from $x_{W_{start}}$ to $x_{W_{end}}$. During the 3.6g maneuver, the wing load $F_{wing_{3.6g}}$ can be seen as the reaction force, hence it carries the weight of the whole fuselage, shown in Equation 8.1. During landing, the wing acts as a point load on the fuselage structure. The force $F_{wing_{land}}$ shown in Equation 8.2 is the sum of the weights of the wing group. This is multiplied with the landing gravitational factor.

$$F_{wing_{3.6g}} = \frac{W_{fus} * f_{3.6g}}{x_{W_{end}} - x_{W_{start}}} (x_{W_{start}} < x < x_{W_{end}}) \quad (8.1)$$

$$F_{wing_{land}} = -W_{wing} * f_{land} \quad (8.2)$$

The weight of the fuselage itself is modeled as a distributed load along the length of the fuselage and

the shear is calculated following Equation 6.9.

Finally, during landing, the shock of the landing gear on the fuselage is considered as two point loads on the main and nose landing gear position. These forces are calculated as 85% and 15% of the MTOW including the landing gravitational factor, as discussed in Chapter 7. The shear stresses caused by the landing shock load is again calculated as shown in Equation 6.8, with the respective forces and applied position of the force.

The moment during the two most constraining load cases can again be calculated as shown in Equation 6.10. By positioning the longerons in the determined position, the centroid of the fuselage structure can be calculated. The necessary moment of inertia is then calculated as shown in Equation 6.11. Each longeron is modelled as a point mass. This assumption can be made since the distance from the centroid of each longeron is an order of magnitude bigger than the diameter of the longeron cross-section (final longeron cross-section is $27.6\,\mathrm{mm}$). The necessary area $A_{longeron}$ can be calculated as shown in Equation 8.3, when h is the distance from the centroid to the longeron, p is the amount of longerons. This equation can be solved for the area of the longerons. The exact diameter of the longeron is calculated by choosing the thickness of the tube to be one tenth of the diameter, this is done so that thin wall assumption can be applied [31]. Equation 8.4 shows how the final dimensions of the tube such as the diameter d can be calculated.

$$I_{\text{xx}} = \sum_{n=0}^{p} h^2 * A_{longeron} \tag{8.3}$$

$$A_{longeron} = \pi * d * \frac{d}{10} \tag{8.4}$$

The longerons could also fail due to buckling. To prevent buckling, the frames may be placed closer together, or the longeron may increase in size. Throughout the length of the payload bay, no frames may be placed since the bay must be able to open. Hence, this is the longest distance l that the longerons must not buckle. The critical force P_{crit} calculated in Equation 8.6 is the compressive force caused by the thrust F_{thrust} plus the compressive force applied on the longeron due to bending M. The moment must be divided by the distance from the centroid c to get the bending force. The moment of inertia needed of the cross-section of the longeron I_{longeron} can be calculated using Euler buckling of columns calculation shown in Equation 8.5 [31]. The longeron most prone to buckle is the bottom longeron during a 3.6g maneuver, because it has the largest P_{crit}. The maximum moment at the 3.6g maneuver is used as this is the most constraining load case.

$$P_{\text{crit}} = \frac{\pi^2 * E * I_{\text{longeron}}}{l^2} \tag{8.5}$$

$$P_{\text{crit}} = \frac{F_{\text{thrust}}}{n} + \frac{M}{c} \tag{8.6}$$

The final failure mode analyzed is the compression of the frames. The most critical point is the main landing gear shock load. The maximum bending moment M_{max} on a tube with a point load in compression can be expressed as shown in Equation 8.7 [31], where P is the point load applied, and R is the radius of the tube. The maximum bending moment occurs on the top and bottom of the tube, where the load is applied.

$$M_{\text{max}} = \frac{P * R}{\pi} \tag{8.7}$$

$$I_{\text{I-beam}} = \frac{7 * h^4}{120} \tag{8.8}$$

From, M_{max} the necessary moment of inertia can be calculated using Equation 6.11. The height h of the I-beam can be calculated from the moment of inertia needed as shown in Equation 8.8 [31] (because the thickness is one tenth the height of the I-beam, thin-walled analysis is assumed). The same dimensions of the frames are used for all frames in the fuselage to facilitate manufacturing.

8.3.3. Final Fuselage Structure

The material selected for the fuselage was once again Aluminum 6061-T6, as mentioned in Section 6.4. This aluminum alloy provides excellent specific strenth and stiffness, and allows for a high recycling percentage [33].

The results of the structural model, including shear and moment distributions and the maximum deflection, are available in Figure 8.3. From these deflections, the component dimensions can be calculated.

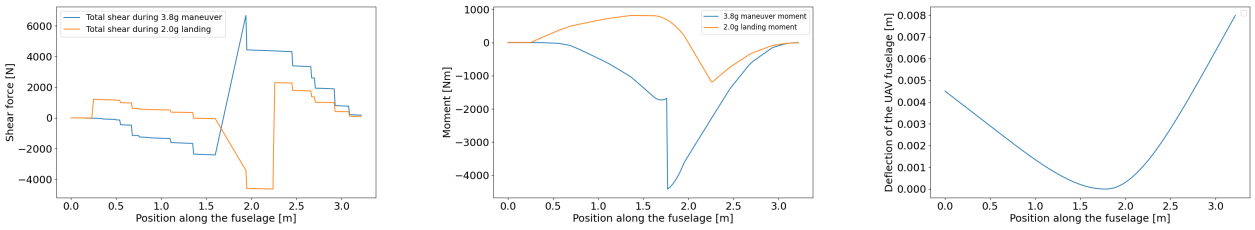

(a) Shear distribution. **(b)** Moment distribution. **(c)** Deflection during 3.6g maneuver.

Figure 8.3: Results of the analytical structural model.

For the longerons, resistance to buckling over a length of $780\,\mathrm{mm}$ proved to require a diameter of $27.5\,\mathrm{mm}$, while for yielding only $8.3\,\mathrm{mm}$ was needed. The plates of the frame I-beams were also calculated to require a length of $23.3\,\mathrm{mm}$ to withstand the compression during landing. The dimensions are shown in Figure 8.4.

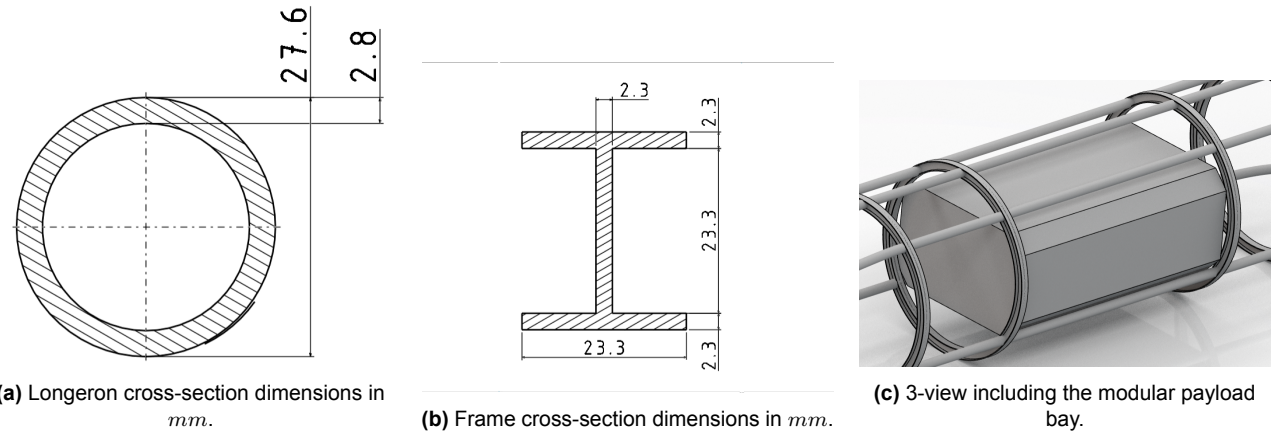

(a) Longeron cross-section dimensions in mm. **(b)** Frame cross-section dimensions in mm. **(c)** 3-view including the modular payload bay.

Figure 8.4: Structural component properties.

As mentioned in **RFU-STR-3**, the skin is expected to not carry any loads except aerodynamic loads. Therefore, a skin thickness of $0.4\,\mathrm{mm}$ was estimated based on literature, which is considered sufficient to withstand the aerodynamic load profile [32]. Using the aluminum density of $2700\,\mathrm{kg/m^3}$ in Section 6.4, the mass of the structure totals to $21.82\,\mathrm{kg}$, as seen in Table 8.4 below.

Table 8.4: Total structural mass of the fuselage.

Component	Amount [-]	Individual mass [kg]
Longeron	5	2.08
Frame	5	1.04
Skin	-	6.22
Mounting	-	8.44
Total	**-**	**30.26**

As observed in Table 8.4, the total structural mass includes an additional $8.44\,\mathrm{kg}$ for mounting. Due to the limited scope of the design project, the exact mounting structure for each individual component in the fuselage has not been designed. Therefore, this mass allocation has been obtained from literature as a conservative estimate [5], leading to a total structural mass of $30.26\,\mathrm{kg}$.

8.4. Fuselage Design Verification

To guarantee compliance with requirements set on the landing gear and fuselage, the verification methods set in Table 8.5 can be used.

Table 8.5: Fuselage design verification methods.

ID	Verification method	Discussion
RLG-VER-1	Demonstration	Integrate system and perform test vertical take-off and landing.
RLG-HOR-1	Demonstration	Integrate system and perform test horizontal landing.
RLG-SUP-1	Demonstration	Apply equivalent load to nose and main landing gear, or integrate system and load to MTOW.
RLG-COM-1	Analysis	Check that the components are not designed in-house.
RFU-LAY-1	Inspection	Measure fuselage length and width.
RFU-LAY-2	Analysis	Use component mass and position to calculate center of gravity shift during operational lifetime.
RFU-LAY-3	Inspection	Measure distance between electrical components.
RFU-LAY-4	Inspection	Check power plant position.
RFU-LAY-5	Demonstration	Test communications system signal from above.
RFU-LAY-6	Demonstration	Integrate components into fuselage and check field of view.
RFU-STR-1	Analysis, Test	Analyze fuselage structure with high-fidelity techniques, then manufacture and test prototype.
RFU-STR-2	Analysis, Test	Analyze fuselage structure with high-fidelity techniques, then manufacture and test prototype.
RFU-STR-3	Analysis	Check skin loads during combined fluid-structure analysis.
RFU-STR-4	Analysis, Test	Analyze fuselage structure with high-fidelity techniques, then manufacture and test prototype with propeller integrated.
RFU-STR-5	Analysis, Test	Analyze fuselage deflection with high-fidelity techniques, then manufacture and test prototype.
RFU-STR-6	Demonstration	Perform integration test with all components in the fuselage.
RFU-STR-7	Test	Test prototype in adverse weather simulation conditions.

Though several verification methods in Table 8.5 require dedicated mechanical/weather testing facilities (for example, the Delft Aerospace Structures and Materials Laboratory in the Faculty of Aerospace Engineering at TU Delft), compliance of the fuselage structure with the maximum load case requirement can be verified with a high-fidelity analysis.

Finite Element Analysis

As described in the verification strategy for **RFU-STR-1**, **RFU-STR-2**, **RFU-STR-3**, **RFU-STR-4**, and **RFU-STR-5**, the fuselage structural design can be verified with an external solver. The ANSYS Mechanical suite was chosen to perform this verification. Due to the limited scope of the project, it was decided to limit the analysis to the most critical aspects of the structural design, namely the heavily-loaded circumferential fuselage frames.

The model of the fuselage frames was used as input geometry, with Al6061-T6 (elastic modulus of $69\,\mathrm{GPa}$, Poisson Ratio of 0.33) being assigned to the geometry. A two-tiered tetragonal mesh was applied to the frame, with $4\,\mathrm{cm}$ elements in the upper half of the frame (which is expected to develop lower stresses) and smaller $0.5\,\mathrm{cm}$ elements in the lower half of the frame. This mesh was observed to converge to the solution in $8\,\mathrm{s}$, and is represented in Figure 8.5a.

To simulate the real world scenario, the most constraining load case was selected, namely the frame that supports the main landing gear (and therefore needs to transfer the highest load during taxi and horizontal landing). To simulate the transfer of this load through the longerons, a $4504\,\mathrm{N}$ static load was applied on the upper surface of the frame, and a fixed support was applied to the bottom of the frame, simulating the connection to the main landing gear. Frictionless boundary conditions were applied to the vertical surfaces of the frame, as the structure is assumed to be stiff in the longitudinal

direction. Therefore, only vertical deflection was analyzed. The loading and boundary conditions are shown in Figure 8.5b.

(a) Fuselage frame finite element mesh. **(b)** Fuselage frame applied loads.

Figure 8.5: Fuselage finite element analysis settings.

Figure 8.5a includes an overview of element skewness. High element skewness can result in unrealistic deformation values. It may be observed that only 7 percent of elements have a skewness above 0.9, with these elements being observed to be the larger elements on the upper side of the frame. As these elements are not in the area of expected maximum stress, the mesh is considered acceptable for the analysis.

The static structural analysis was performed, resulting in a maximum vertical deflection of about $3.7\,\mathrm{mm}$ at the top of the frame, as shown in Figure 8.6a. A maximum stress of $183\,\mathrm{MPa}$ was found in the lower flange of the frame, at the point where the flange connects to the landing gear. The stress distribution for the lower side of the frame is shown in the close-up in Figure 8.6b.

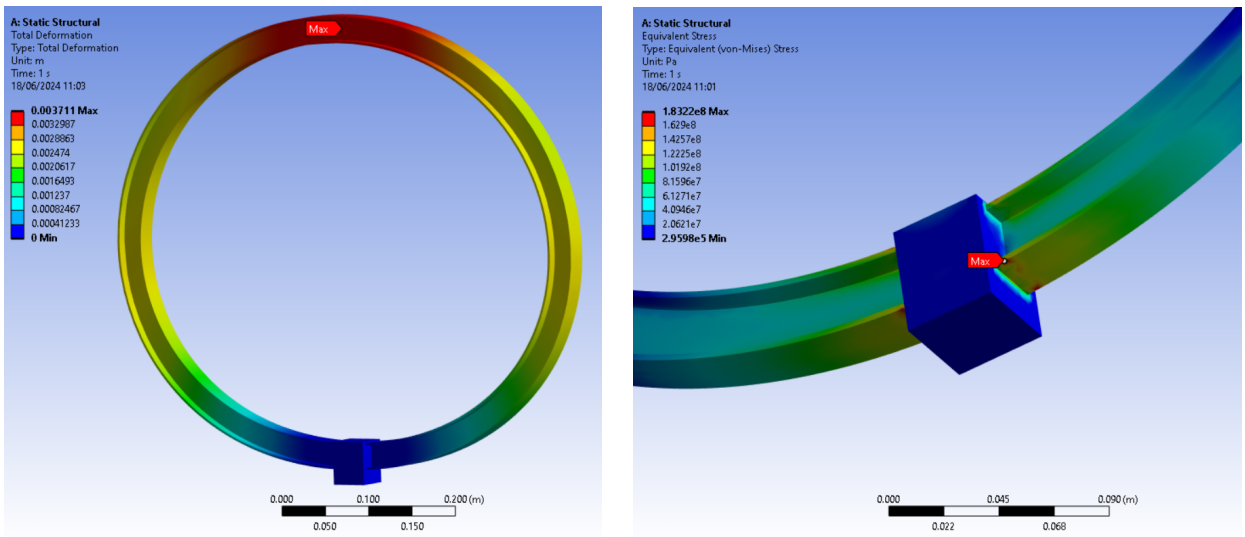

(a) Fuselage frame deformation (exaggerated). **(b)** Local maximum equivalent stress.

Figure 8.6: Fuselage finite element analysis static results.

The static finite element analysis shows that the preliminary structural design is highly conservative, with lower deflections and stresses expected than calculated. However, an aspect that was

not considered previously is the buckling of the frame, a factor to which it is susceptible due to its one-dimensional loading scenario.

The ANSYS Workbench has also allowed for a linear eigenvalue buckling analysis to be performed. The same constraints and loading case as in the static analysis were maintained (with the note that out-of-plane buckling is not considered, as it is expected to be blocked by the stiffener longerons). The first two modes were analyzed, and are shown in Figure 8.7a and Figure 8.7b.

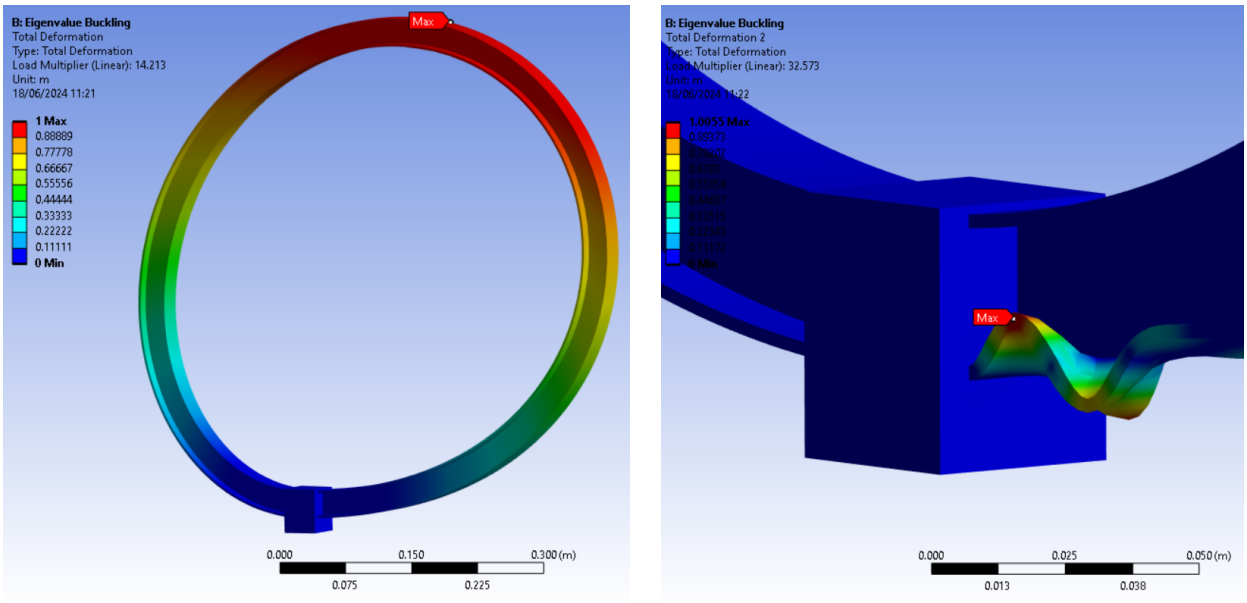

(a) First buckling mode.

(b) Second buckling mode.

Figure 8.7: First two fuselage buckling modes.

As observed in Figure 8.7, the first buckling mode represents full-frame lateral movement of the structure, while the second buckling mode represents localized flange buckling at the connection between the landing gear support and the frame (in agreement with the maximum stress point shown above in Figure 8.6b). The load multiplication factor for these two modes was found to be 14.2 and 32.6 respectively, which means that the $4504\,\mathrm{N}$ load needs to be multiplied with these factors for the buckling mode to occur. As the simulated load represents the maximum load case, it is considered that these buckling modes will not appear during the operational lifetime of the frame.

The finite element analysis has allowed for the structural design of the flight-critical fuselage frame to be verified independently. As discussed in Table 8.5, further verification involves continued analysis of the other structural components, as well as subsystem-level testing in a dedicated facility.

9 | Ground System and Operations

Similar to many UAV systems, the airborne segment is accompanied by a ground segment. In this chapter, first the requirements for the ground system are identified in Section 9.1. Then, the ground segment design is explained in Section 9.2 after which details are given on the mission profile and operations of the entire system in Section 9.3. Finally, verification methods for compliance with the ground system requirements are discussed in Section 9.4.

9.1. Ground Station Requirements

A multitude of requirements for the ground system design have been identified, which are represented in Table 9.1. These requirements are divided into two categories, firstly treating the operational requirements, after going into communications. Finally, after the requirements are presented, each requirement is rationalized appropriately.

Table 9.1: Identified operation requirements of mobile ground system.

ID	Requirement description	Origin
RGR-OPR-1	The ground station UAV deployment zone shall be capable of relocation.	**R-STK-5**
RGR-OPR-2	The mobile ground station shall be able to transport the UAV according to the road haulage regulations established by the European Commission.	**R-STK-8**
RGR-OPR-3	The mobile ground station shall be able to refuel and or charge the UAV to full capacity.	**R-STK-5**
RGR-OPR-4	The mobile ground station shall be equipped for routine maintenance on the UAV.	**R-STK-4**
RGR-OPR-5	The mobile ground station shall contain all necessary equipment to connect the payload to the UAV.	**R-STK-5**
RGR-OPR-6	The mobile ground station shall have integrated storage space for alternative payloads.	**R-SYS-8**
RGR-OPR-7	The mobile ground station shall be able to autonomously power the equipment necessary to perform the mission for no less than 14 days.	**RGR-OPR-3**
RGR-OPR-8	The mobile ground station shall fit into a space of 2.55 x 4 x $12\,\mathrm{m}$.	**RGR-OPR-2**
RGR-OPR-9	The mobile ground station shall weigh no more than $40\,\mathrm{t}$.	**RGR-OPR-2**
RGR-OPR-10	The walls of the mobile ground station shall be manually deployable.	**RSK-TEC-MGS-1.1**
RGR-COM-1	The mobile ground station shall be able to communicate with external sources about flood progression.	**R-STK-2**
RGR-COM-2	The mobile ground station shall autonomously process data provided by the UAV.	**R-MIS-4**
RGR-COM-3	The mobile ground station shall have a direct link antenna to communicate with the UAV.	**R-MIS-4**
RGR-COM-4	The mobile ground station shall have a secondary satellite communication option with the UAV.	**R-MIS-3**
RGR-COM-5	The mobile ground station shall be able to store 336 hours worth of telemetry data locally.	**R-SYS-3**
RGR-COM-6	The mobile ground station shall be able to maintain a bandwidth of no less than $10\,\mathrm{Mbps}$.	**R-MIS-4**
RGR-COM-7	The mobile ground station antenna shall have a link frequency between $30\,\mathrm{MHz}$ and $10\,\mathrm{GHz}$.	**R-MIS-4**
RGR-COM-8	The mobile ground station shall be able to maintain a steady, uninterrupted connection for a range of $200\,\mathrm{km}$.	**R-MIS-3**
RGR-COM-9	The mobile ground station main antenna shall have a $58.73\,\mathrm{km}$ communication range within direct line of sight of the UAV.	**RGR-COM-3**

Continued on next page

Table 9.1: Identified operation requirements of mobile ground system.

ID	Requirement description	Origin
RGR-COM-10	The link shall have a latency of no more than $250\,\mathrm{ms}$ within $8.25\,\mathrm{km}$ of the ground station.	**RGR-COM-3**
RGR-COM-11	The link shall have a latency of no more than$1.25\,\mathrm{s}$ beyond $8.25\,\mathrm{km}$ from the ground station.	**RGR-COM-4**
RGR-COM-12	The mobile ground station shall communicate unprocessed telemetry data with external data processing servers in case of ground station data processing unit failure.	**RSK-TEC-MGS-5**
RGR-COM-13	The mobile ground station shall be able to connect to the cellular network to send and receive data.	**RSK-TEC-MGS-6**

- **RGR-OPR-1** flows from **R-STK-5**. Flexibility in deployment location can be achieved by making the ground station mobile. Additionally, mobility of the ground station reduces downtime, since inactive ground stations could be moved to an area of risk preemptively.
- **RGR-OPR-2** flows from the European public road regulations[1]. As these are considered the strictest in the world, these are taken as a baseline for the ground station requirement.
- **RGR-OPR-3** flows from the circumstance in which the UAV is deployed. As floods may occur for prolonged amounts of time, is it integral that the UAV can be refueled at the ground station.
- **RGR-OPR-4** follows logically from the previous requirement. When monitoring a disaster area for prolonged periods of time, it is important that the mobile ground system is able to repair minor damages that might occur to the UAV during regular operation.
- **RGR-OPR-5** flows from **R-SYS-8**, according to which the UAV is to possess a modular payload bay, so the mobile ground system should contain the correct tools to integrate different payloads.
- **RGR-OPR-6** follows from the previous requirement. The distinct payloads should have an integrated storage place on the mobile ground system.
- **RGR-OPR-7** has been set up so that the operations of the ground systems can be carried out continuously, even if the power grid fails, which is common during disaster events [62]. Serinaldi et al. found that the probability of a flood lasting longer than 7 days is above 10% (excluding avalanche-related floods), and can reach up to 67% for monsoon and snowmelt-related floods [63], fourteen days were therefore chosen to stay above the median length of a monsoonal rain flood, which is the longest type of flooding event.
- **RGR-OPR-8** is again a result of the European road regulations.
- **RGR-OPR-9** flows from the road regulations, similar to **RGR-OPR-8**.
- **RGR-OPR-10** flows from an identified risk, **RSK-TEC-MGS-1.1**, which states the importance of manually deployable container walls (**TRRC-17**), as failure to do so may jeopardize the success of the mission by preventing UAV preparations or take-off.
- **RGR-COM-1** follows directly from **R-STK-2**.
- **RGR-COM-2** follows from the need to process the down-link data in such a way that it is digestible for the operators. For example, by displaying the information on a HUD and displaying sensor data such as live overlaying of photogrammetry and LIDAR data.
- **RGR-COM-3** follows from the existence of the satellite connection imposed by **RG-COM-4**. It cannot be guaranteed that the latency requirement imposed by **RG-COM-10** is met, and therefore a direct link shall be employed.
- **RGR-COM-4** flows from the use of the 4/3 curving radio wave propagation rule, which is valid for low altitudes [64, 65], a minimum ground station height or aircraft altitude of $2549.4\,\mathrm{m}$ can be calculated for direct line of sight at $200\,\mathrm{km}$. Since the UAV may need to operate below $500\,\mathrm{m}$ while performing monitoring or intervention tasks, using only a ground station antenna is unfeasible. Though other options were also investigated, such as a tethered balloon, low-frequency radiowaves or a secondary UAV relay, these options were also found to be unfeasible due to low resistance to inclement weather [66], inconsistent bandwidth [65, 67, 68], or unacceptable

[1] https://transport.ec.europa.eu/transport-modes/road/weights-and-dimensions_en/

design effort. The only remaining feasible option is having a satellite terminal on both the UAV and the ground station to allow for operations outside direct line of sight.

- **RGR-COM-5** uses the justification as **RG-OP-7**, in case of a communications blackout during a flood. Local data storage ensures that non-critical imaging data will not tax the local emergency communication network [63].
- **RGR-COM-6** flows from the link budget as determined in Chapter 3. This is the bit rate which the ground station shall be able to communicate with the UAV.
- **RGR-COM-7** dictates a frequency of $30\,\mathrm{MHz}$ number, which follows from the 30 to $300\,\mathrm{MHz}$ VHF range. From this point, antenna size becomes reasonable, and these frequencies are typically used for air radio [65]. Beyond $10\,\mathrm{GHz}$ the atmospheric attenuation becomes unreasonable. For example, the attenuation at $10\,\mathrm{GHz}$ is only $0.012\,\mathrm{dB/km}$, and at $20\,\mathrm{GHz}$ it climbs to $0.1\,\mathrm{dB/km}$, or an increase of $3\,\mathrm{dB}$ to $20\,\mathrm{dB}$ over $200\,\mathrm{km}$ [69]. Similar drones with high range such as the PD-2 operate in a variety of frequency bands: $433\,\mathrm{MHz}$, $868\,\mathrm{MHz}$, $900\,\mathrm{MHz}$, $2.4\,\mathrm{GHz}$, and $5.8\,\mathrm{GHz}$ [2]. This range is primarily given as a constraint for a possible link budget analysis in detailed design.
- **RGR-COM-8** follows directly from **R-MIS-3**.
- **RGR-COM-9** follows from the cruising height of $150\,\mathrm{m}$ and the ground station height of $4\,\mathrm{m}$ from RG-OP-8. With this altitude, a maximum line of sight distance can be calculated of $58.73\,\mathrm{km}$ using the 4/3 radio wave propagation rule [64].
- **RGR-COM-10** follows from the findings of de Vries [70], demonstrating that delays beyond $250\,\mathrm{ms}$ lead to unacceptable handling qualities, which is not tolerable during a possible manual takeoff and landing of the UAV. Another reason supporting this number is the similarity of this finding with the median reaction time of a human, which is $273\,\mathrm{ms}$ [3]. The $8.25\,\mathrm{km}$ value follows from how far a 4-meter high ground station can see over the horizon, where the $4\,\mathrm{m}$ comes from RG-OP-8, the calculation was performed using the 4/3 rule [64].
- **RGR-COM-11** follows from an analysis of pilot performance during simulated dogfights at different latencies, where it was found that delays above $1.25\,\mathrm{s}$ were unacceptable for manual flying [71]. Even though dogfighting is an extreme example, maneuvering in stormy conditions might require sudden corrections. The $8.25\,\mathrm{km}$ number follows from the rationale of **RG-COM-10**.
- **RGR-COM-12** is an important requirement, allowing the ground station to perform its task of data processing and alerting external parties even when the internal processor fails (**TPRC-38**).
- **RGR-COM-13** hooks into **RGR-COM-12**, which allows the ground station to communicate with external parties (**TRRC-21**).

9.2. Ground Station Design

Following the identification of the requirements discussed above, the decision has been made to base the design of the ground station on a standard high cube 12-meter sea container. This container has a width of $2.35\,\mathrm{m}$, a length of $12\,\mathrm{m}$, and a height of $2.93\,\mathrm{m}$ [4]. Using such a standardized base of operations ensures that it can be transported anywhere with typical land or sea logistics.

The ground segment is to be divided into two 6-meter-long segments. The first segment would contain everything required for operations and minor maintenance, including a small office space, a workbench, space for electronics, generator storage, a fuel tank, personal storage space, and payload storage space. This segment would also contain the antenna dish on top of the container, which would unfold upward to increase its height above the ground.

The second segment would contain the drone itself, including its components, and would be capable of unfolding to allow for assembly and vertical take-off and landing of the airborne segment. The idea is that the drone fuselage, wing, and powerplant would be stored separately, and attached together

[2] https://ukrspecsystems.com/uascomponents/tracking-antenna-system-uav
[3] https://humanbenchmark.com/tests/reactiontime
[4] https://www.tts-transocean.com/en/information/container-dimensions/

after the second segment unfolds. The feasibility of constructing the drone on location is based on the fast deploy design visible on many drones by YANGDA where wings, engines and, empennage can be attached quickly using clips [5].

With the main functionalities explained, significant design effort has been dedicated to the design of individual subsystems for the ground segment. These capabilities are discussed below.

1. **Power and Refueling System:** To adhere to **RG-OP-3**, the ground station is to include an onboard power system. For this, it will provide two different options. The first and preferred option is plugging the station into the local power grid. This allows the ground station to be powered for indefinite lengths of time. However, in case of a power outage, an on-site generation option must also be included.

   For this, the station will contain a battery, capable of running the ground system for 12 hours. This should be enough to run one mission cycle on batteries. To adhere to **RG-OP-7**, the ground station will include a generator and fuel tank. This generator can, when necessary, be activated to recharge the battery and power the systems.

   Additionally, a fuel tank is included to fuel the generator. This fuel tank would require a capacity to power the generator for the 14-day duration. It has been determined that this generator should be a standby generator, as these are designed to run continuously for prolonged durations [6]. This generator can be moved outside of the ground system when operational, to reduce internal heat, prevent dangerous emissions for the operating crew, and reduce noise for the operators.

   By using a generator that runs on the same fuel source as the UAV, a single fuel tank can be used for both powering the ground station and refueling the UAV.

2. **Maintenance and Storage Capabilities:** To adhere to **RGR-OPR-4**, an onboard system for maintenance needs to be included for the ground system. Therefore the mobile ground station includes a workbench where smaller parts can be repaired or prepared for the flight. This only treats damage or effects that occur during normal operation of the UAV. In addition, the ground station should include all tools necessary to assemble the aircraft and to apply the different payloads to adhere to **RGR-OPR-5**.

   In addition, the modular nature of the UAV allows for easy replacement of damaged components such as the tail and vertical propellers. This ensures prolonged operations from the ground station, without the requiring reliability on outside resources.

   The mobile ground station shall also include ample storage space to adhere to **RGR-OPR-6**. For this, it will include storage for personal belongings, food, and basic safety equipment such as fire extinguishers. As well as a storage space for the different payloads.

3. **Command and Data Handling System:** One of the main functionalities of the ground system is to function as a command center for the UAV. For this reason, the preliminary design of the ground system includes a desk with monitors from where the UAV can be controlled and monitored by two operators. The data handling itself is done through the computer present within the mobile ground station.

4. **Data Transmission System:** To adhere to **RGR-COM-9** the ground station will have an RF antenna on top to allow near-range communication with low latency to adhere to **RGR-COM-10** for primarily takeoff and landing. To reach the $200\,\mathrm{km}$ range imposed by **RGR-COM-8**, and to provide onboard internet access for external communication for **RGR-COM-1**, a satellite terminal will be installed on the ground station. Backup internet acess for smaller commands can be handled by surrounding cellular networks, if available.

[5] https://www.yangdaonline.com/vtol/

[6] https://rcaelectric.com/2022/10/25/how-long-can-a-backup-generator-continuously-run/

In Figure 9.1, a graphical representation of the designed ground station is shown. Each component is numbered, with further description below.

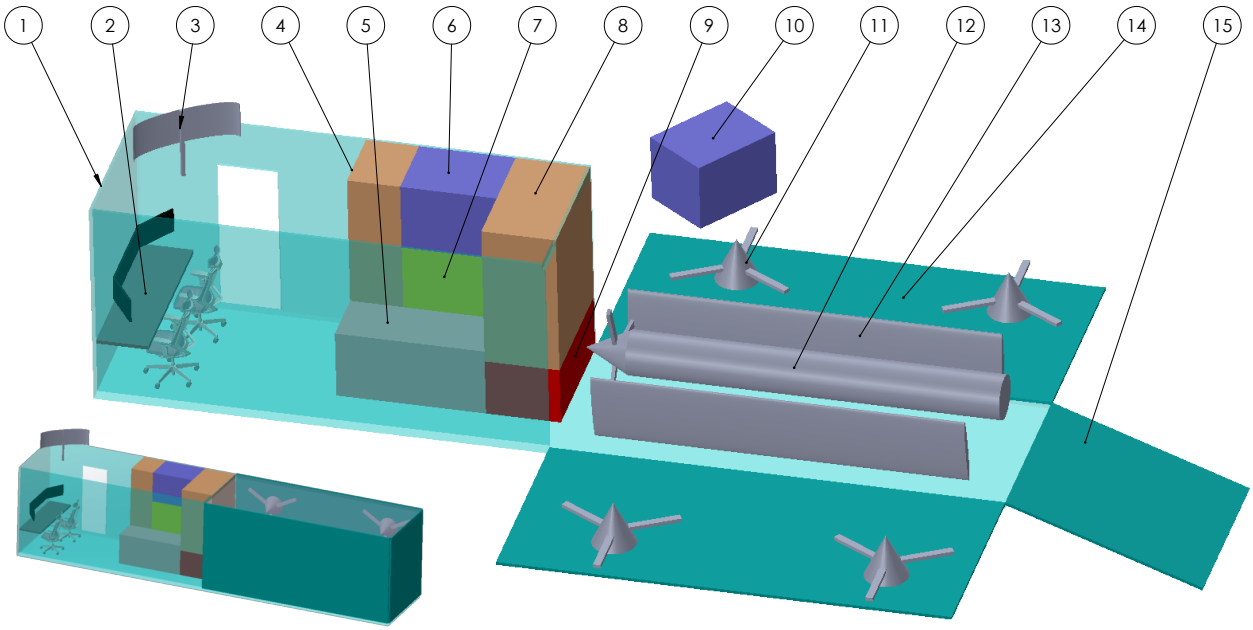

Figure 9.1: Visualization of the ground station layout, with numbers representing each component. The bottom left corner shows the stowed configuration (with the antenna still upright). The roof is made transparent, and the chair model [7]provides a sense of human scale.

1. Container section containing crew during ground operations
2. Command center including monitoring and operating displays
3. Radio dish for medium-distance communication with UAV
4. Storage space for personnel and safety equipment
5. Workbench with storage for UAV spare parts
6. Data handling electronics and a satellite internet terminal
7. Battery pack and electrical systems
8. Payload storage space and assembly/payload tools. It would open from the side of the UAV platform.
9. Fuel tank and refueling system for UAV
10. External generator (normally stored under battery and accessible from outside)
11. VTOL propeller storage during transport (disconnected)
12. UAV fuselage
13. Wing storage during transport (disconnected)
14. Walls of the container, functioning as a VTOL platform for UAV when deployed.
15. Wall of the container, functioning as a ramp for on- and offloading of UAV and supplies when deployed

Notes on Mobile Ground System Design

The configuration described above covers the functionality required for the mission of the UAV, but may still lack some practicalities. Firstly, as floods can last multiple days or even weeks, additional living quarters and sanitary facilities for the crew should be considered. However, this falls within the responsibilities of the client and is thus not considered within the scope of this project. Furthermore, climate control, windows, and insulation would be required in the final design, to provide a comfortable working environment.

[7]https://grabcad.com/library/cr-gw3015e1kz1k-chair-1

Secondly, some safety considerations have been made. In the current layout, the UAV VTOL platform is distanced as far as possible from the ground crew. Also, a second door has been implemented for fire safety, in case electronics or fuel catch fire and escape from the back is not possible.

Next, a small note should be made on the sizing of subsystems within the current layout. As this is still a conceptual design, the exact sizes have not been determined. This acts as a schematic and as an aid for future detail design. However, it does provide a reasonable overview on the budget allocation for such a ground station. For example, the current size of the fuel tank in this infographic (9) is 1.792 x 1 x $0.8\,\mathrm{m}$, already providing $1433.6\,\mathrm{L}$ of fuel, despite its seemingly small size in the figure.

9.3. Mission Profile

Due to the strong integration between the mobile ground system and the UAV, the complete mission can be seen as three separate segments. Firstly, the Joint Segment (abbreviated as JS) consists of the UAV and the mobile ground system together. This is applicable during transport and the setup of the system. Secondly, there is the Airborne Segment (AS), which consists solely of the UAV once it is operated separately from the ground segment. This includes any payload it may carry. Finally, there is the Ground Segment (GS). This consists of the mobile ground system, which during the airborne mission is mostly used to control the UAV, and handle data.

On Page 89, the mission profile is shown for an optimal mission. It is important to note that this diagram only depicts each event happening once. However, in reality, it may be possible to monitor multiple areas, requiring the UAV to go in and out of cruise flight before performing its task again. Similarly, it is also possible to refuel the UAV after landing and repeat a similar mission, without fully packing up the joint segment.

In the following subsections, every mission section is elaborated upon, along with characteristic data per phase. Here, the same identifiers are used as in the mission profile graphic. After the mission phases have been discussed, an overview is given of communication and data handling per phase of the airborne mission phases.

9.3.1. Joint Segment Phases

The following mission profile phases are handled by the joint segment.

- **MP-JS-1 - Transport to determined ground station location**: The mission starts when the operator determines that the deployment of the UAV is necessary. Once this decision has been made, the mobile ground station (which includes the disassembled UAV) will be transported to the deployment location. In this phase, either road, train, air, or naval infrastructure may be used.
- **MP-JS-2 - Arrive at take-off location and start preparations**: Once the destination has been reached, the mobile ground station will start its set-up, which consists of starting up its power supply and deploying the container walls. In addition, the satellite internet terminal is initiated. If available at the determined location, the ground station can connect to the power grid.
- **MP-JS-3 - Assemble UAV and insert required payloads**: During transportation, the UAV is not fully assembled. Therefore, the first step for the UAV is to be assembled, using the tools present on the ground station. Finally, the mission specific payload can be prepared and inserted into the UAV.
- **MP-JS-4 - Shut down and disassemble UAV**: Once the UAV finishes performing its mission, and it has landed back on the ground station, it can be shut down and disassembled. Its components should also be checked for damage, which if applicable can be repaired on the ground station.
- **PM-JS-5 - Prepare ground station and UAV for transport**: In order for the mobile ground system to be transported back to the standby location, it should be prepared for transport. This means retracting the ground station walls, applying the tarp, and stowing loose components.

- **PM-JS-6 - Transport to standby location**: Finally, the mobile ground station can be transported back to its standby location. Here, it can again be stored until the next deployment. Similarly to PM-JS-1, this can be done using existing infrastructure.

9.3.2. Ground Segment Phases

Once the ground segment and the airborne segment separate, their respective functionalities are treated as different mission phases even when running in parallel. In the following list, the ground segment mission phases are elaborated upon. Overall, the combined mission profile is shown in Figure 9.4 on Page 89.

- **MP-GS-1 - Prepare ground station for mission and build up antenna**: This is the first mission phase where the ground segment is treated separately. Here, the control systems are set up, and the antenna stationed atop the station is initiated.
- **MP-GS-2 - Control, communicate and share data with UAV**: For the majority of the mission, this will be the function of the ground station. It will both directly and indirectly control the UAV, and transmit data from external flood monitoring parties. From the UAV, it will receive a variety of data, which is to be discussed in more detail below. During this phase, it is connected to the satellite network.
- **MP-GS-3 - Shut down ground station and pack up antennae**: After the UAV has returned to the mobile ground station, the ground system can be shut down and packed up. Power systems can be disconnected or turned off, and the antenna can be folded down.

9.3.3. Airborne Segment Phases

For the majority of the mission, the UAV will be airborne and therefore it is necessary to assess its different phases throughout the mission. As the mission types vary greatly, the shared phases are summed up below.

- **MP-AS-1 - Perform vertical take-off, transition to horizontal flight, and climb to required altitude**: After assembly, the UAV can perform vertical take-off. The vertical motors elevate the UAV to the transition altitude of $50\,\mathrm{m}$. The UAV will transition to horizontal flight by using the horizontal pusher motor to accelerate to stall velocity. The vertical motors can then be shut off. In horizontal flight, the UAV will climb to a mission-specific altitude. This phase can take between $0.1\,\mathrm{hours}$ and $0.2\,\mathrm{hours}$, depending on the altitude of the required climb. During this time, direct link communication is used to ensure low latency controllability, for which the radio antenna is used.
- **MP-AS-2 - Perform Mission**: After climb, the UAV can perform its mission. This phase can take up to $10\,\mathrm{hours}$, depending on the amount of flight to reach the location and the fuel used to reach it. In this phase, the UAV communication method will transition to satellite communication. During cruise, the drone can either be manually controlled or commanded to follow specified waypoints.
- **MP-AS-3 - Descend, transition to vertical flight and perform vertical landing**: The UAV will descend to the transition altitude of $50\,\mathrm{m}$ and slow to the stall speed of $26\,\frac{\mathrm{m}}{\mathrm{s}}$. From stall speed, the UAV transitions into vertical flight by slowing down beyond stall while turning on the vertical engines to produce lift. In vertical flight, the UAV will perform a vertical landing at the ground station. This phase can take between $0.1\,\mathrm{hours}$ and $0.2\,\mathrm{hours}$, depending on the altitude of the required descent. The communication method will switch back to radio control, to ensure low latency during the vertical landing phase.

9.3.4. Operational Mission Specification

These phases can be varied based on the mission performed. Two distinct types of missions will be performed, however in reality a combination of these mission types might be performed. The first mission type is the monitoring mission, which is optimized for endurance, and aims to cover large

areas to effectively monitor the flooding or risk areas. This mission type is graphically represented in Figure 9.2. In this graphic, the different mission phases, durations and characteristics can be found.

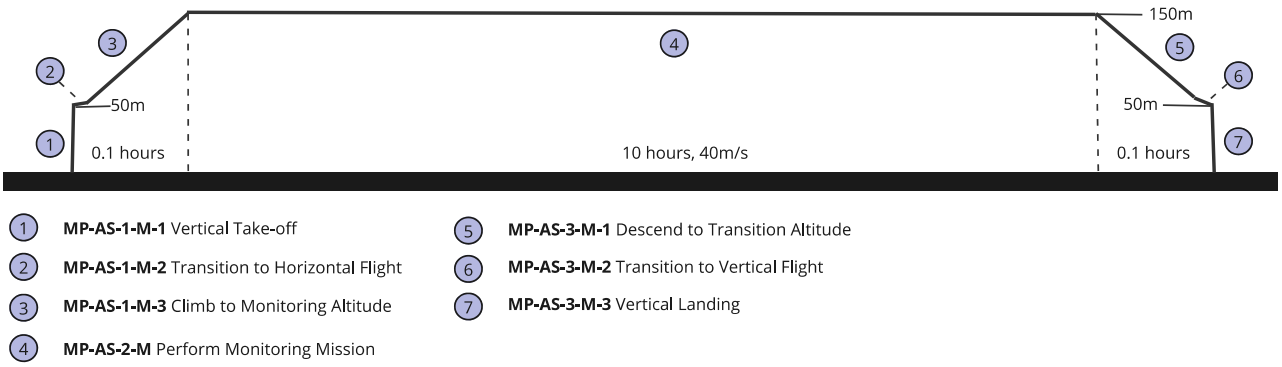

Figure 9.2: Visualization of monitoring mission profile

The second distinct mission profile is the intervention mission, which is a rapid-response mission to drop an intervention payload at a distant location, after which it will fly back at cruise speed. Again, the mission phases, durations and characteristics can be seen in Figure 9.3.

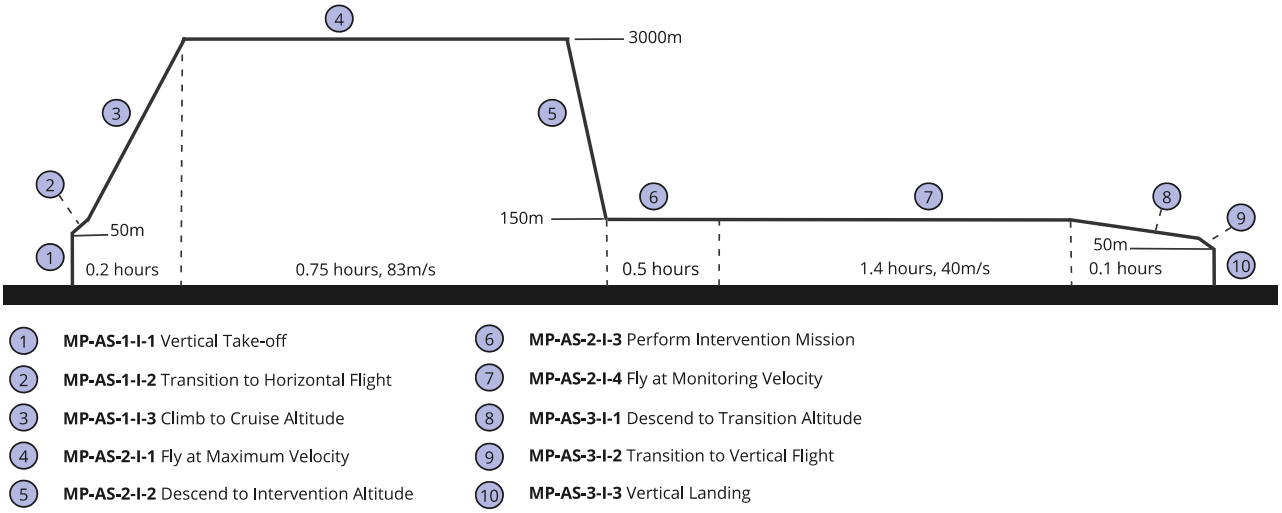

Figure 9.3: Visualization of intervention mission profile

Overall, the combined mission profile is shown in Figure 9.4 on Page 89.

9.4. Ground System Verification

In this section, the verification methods and for the ground station requirements are listed, originating from Table 9.1.

Table 9.2: Ground system requirement verification methods

ID	Verification method	Discussion
RGR-OPR-1	Demonstration	This can easily be demonstrated by moving the ground station using various modes of transport.
RGR-OPR-2	Inspection, Demonstration	The large number of requirements can be satisfied by inspecting and demonstrating the system, to show its compliance.

Continued on next page

Table 9.2: Ground system requirement verification methods

ID	Verification method	Discussion
RGR-OPR-3	Demonstration	The ground system should refuel the UAV to demonstrate the functionality of this requirement.
RGR-OPR-4	Inspection, Demonstration	The necessary components should be inspected, after which a demonstration of maintenance procedures will verify compliance.
RGR-OPR-5	Inspection, Demonstration	The necessary components should be inspected, after which a demonstration of a payload switch will verify the compliance.
RGR-OPR-6	Inspection, Demonstration	The designated spaces should be inspected, after which a demonstration of alternative payload storage will verify the compliance.
RGR-OPR-7	Test	A test should be performed to assess the functioning of the generator, to assess its long-term performance and fuel consumption.
RGR-OPR-8	Inspection	The dimensions of the ground system can easily be verified by inspection.
RGR-OPR-9	Inspection	The ground system can be placed on a specialized scale, and its mass can be verified by inspection.
RGR-OPR-10	Demonstration	The manual deployment of the ground station walls can be demonstrated.
RGR-COM-1	Demonstration	A functional link with external parties can be verified by demonstration the live connection.
RGR-COM-2	Demonstration	The complete data infrastructure can be verified by demonstrating its functionality.
RGR-COM-3	Demonstration	The ground and the airborne segment can be taken a sufficient distance apart to demonstrate the functionality of the link.
RGR-COM-4	Demonstration	A functional link with external parties can be verified by demonstration the live connection.
RGR-COM-5	Test	The data storage component of the ground station can be tested to determine its functional data capacity.
RGR-COM-6	Demonstration	The required data rate can be demonstrated by sending and receiving data of known size, and testing its limits.
RGR-COM-7	Test	This can be tested in a cost-effective manner in a laboratory.
RGR-COM-8	Demonstration	This can be demonstrated by performing a fully integrated flight test and flying further to test communication limits.
RGR-COM-9	Demonstration	This calculation can be verified by performing a flight test and determining at what distance the line-of-sight communication fails.
RGR-COM-10	Test	This can be tested by positioning the communication system on the ground, and moving it further away from the ground system. At the given distance, the connection should lose line-of-sight.
RGR-COM-11	Test	The communication system should be tested in worst-case conditions, to confirm that the maximum latency is not exceeded.
RGR-COM-12	Demonstration	The ground station should send its data over the cellular network to an external processing server, where the data can be analyzed and this requirement can be verified.
RGR-COM-13	Test	The data handling and communication infrastructure of the ground station will receive and send test data over the cellular network.

The verification methods in section 9.4 involve either test, inspection, or demonstration of ground system capabilities. Therefore, they will have to be performed once the ground station is itself integrated (either by refitting a transport container or by manufacturing it directly). It is expected that individual ground control components can be acquired before or during this integration, so individual functionalities related to communications and/or data control may be tested in an accelerated manner. As discussed in Chapter 3, such testing could occur at a rented out range with free airspace, such as the local range at ASK 't Harde.

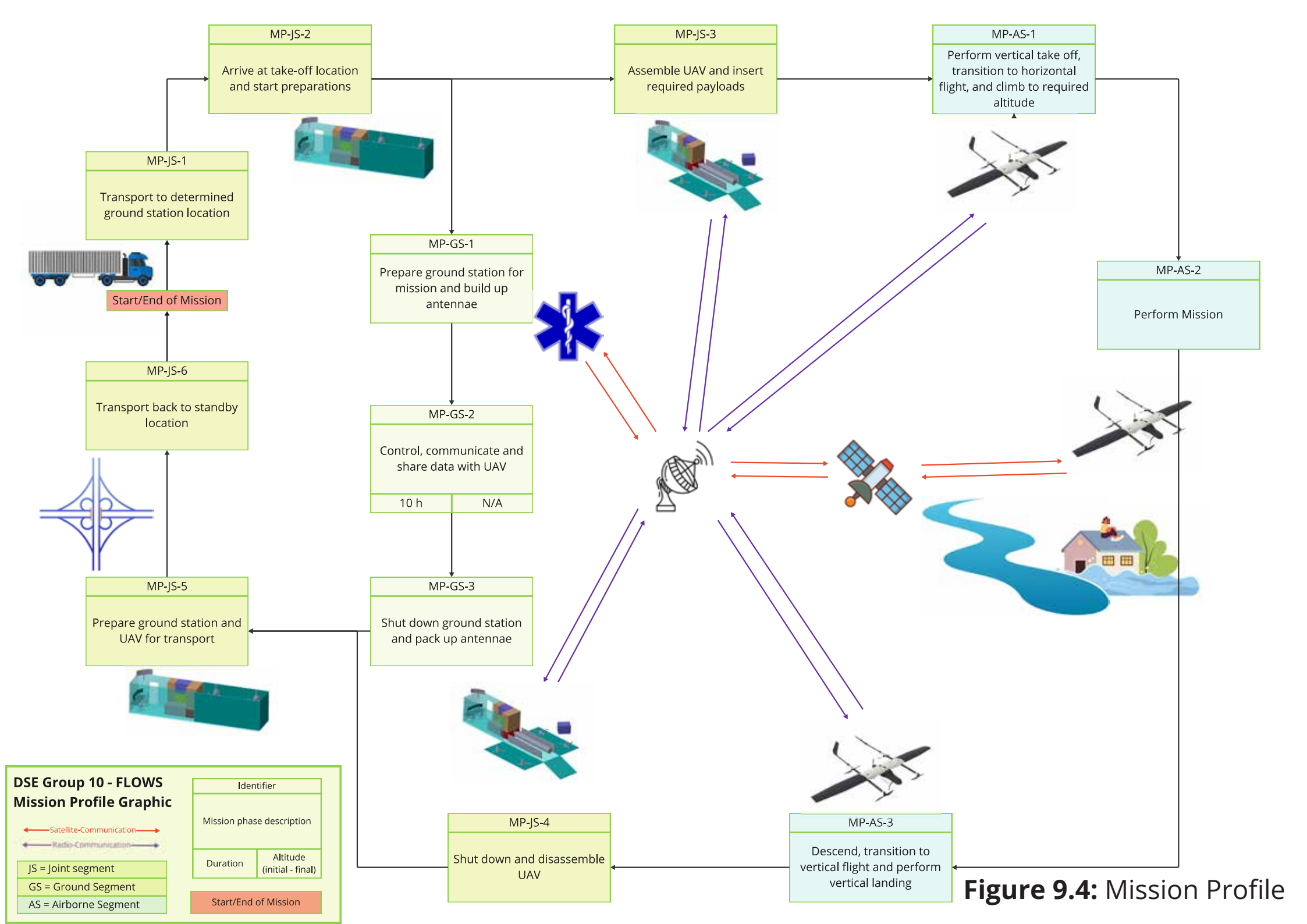

Figure 9.4: Mission Profile

10 | Technical Risk Assessment

Based on the functionality of the FLOWS mission in its entirety, the technical risks concerning the system can be assessed. In detailed design, subsystems designs were worked out, and their specific failure modes are identified in item 10.1. These risks, along with those previously identified, are explained in Section 10.2, together with the framework used for quantification. Then, Section 10.3 covers the strategies employed for contingency and mitigation, and their application to the risks previously described, and Section 10.4 quantifies these aspects in a dedicated risk map.

10.1. Fault Tree Analysis

Within a complex design, determining the possible failure modes that may bring about undesired events and faults is an essential procedure to ensure the safety and reliability of the mission. To identify these events, a fault tree diagram is created by separating the subsystems and analyzing the individual failure modes for each of their components. By identifying the set of events that may cause the failure of a component, they can be subsequently analyzed to determine what action is needed to maintain operation through redundancy, maintenance, or replacement.

The UAV was split up into the following subsystems. The subsystems are split up into smaller failure modes. If any section fails, the UAV will not be able to complete its mission.

1. **Propulsion System Failure**: Issues occurring in either the electric motors or the propellers affect UAV's capability of producing thrust.
2. **Structural Failure**: Issues in any structural component, affecting the UAV's ability to resist physical loads.
3. **Power System Failure**: Issues in the power generation or distribution substructure, affecting any component that requires electricity.
4. **Control System Failure**: Issues in control surfaces and operational architecture, affecting the controllability of the UAV.
5. **Communication System Failure**: Issues in communication to and from the ground station, affecting the data transfer and command handling.
6. **Payload Failure**: Issues in the monitoring or intervention payload, preventing the UAV from performing the mission.

These failure modes were broken down and assessed in detail in a fault tree diagram as shown in Figure 10.1.

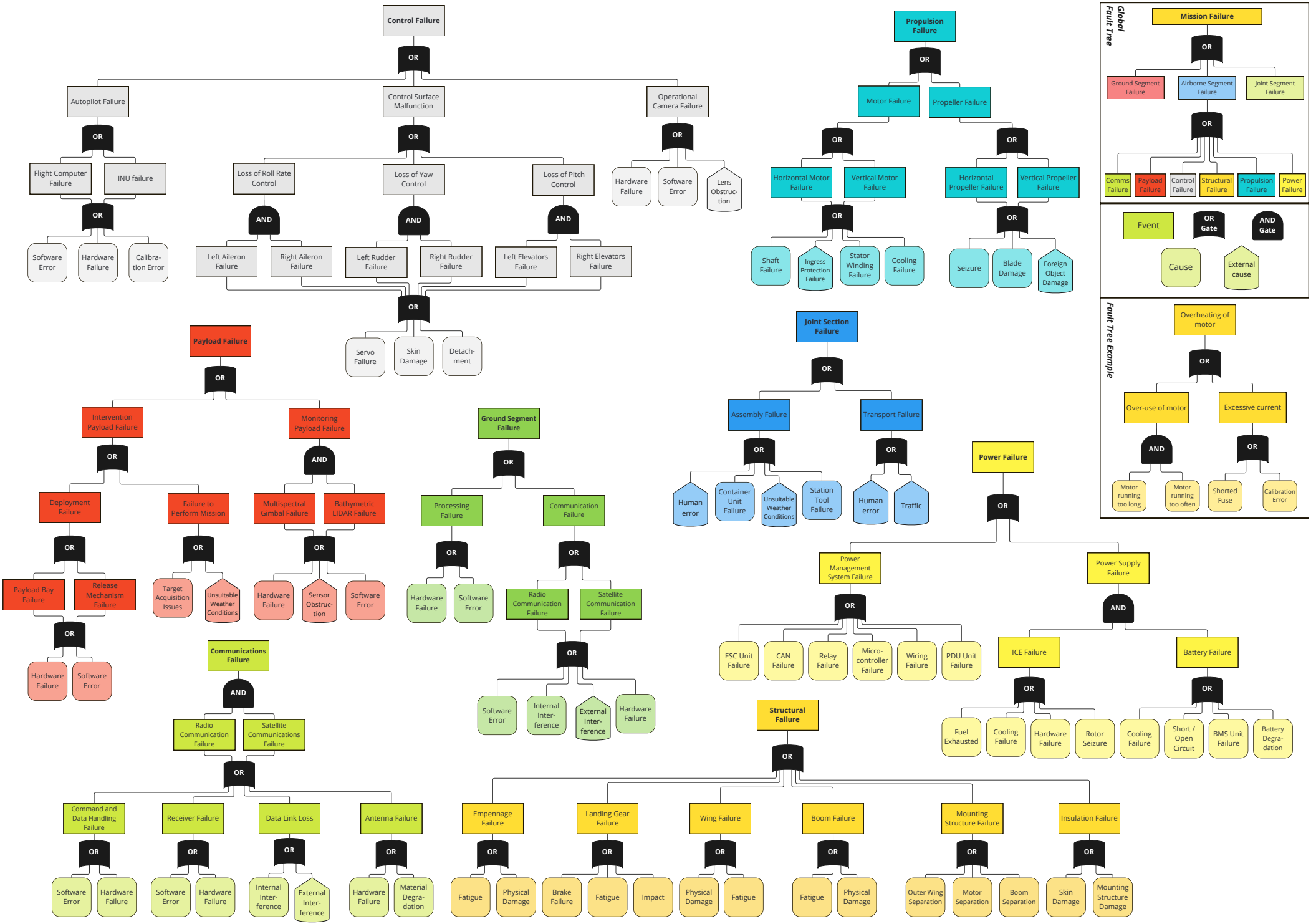

Figure 10.1: Fault Tree

10.2. Risk Assessment

A technical risk analysis is performed to assess what functionalities of the FLOWS system present the highest risk such that they can be mitigated, guaranteeing system performance. Table 10.1 shows the system used for accessing the risk level. This risk is calculated as follows: Risk (**R**) = Likelihood (**L**) x Consequence (**C**), with the description of each of these being presented in Table 10.1. Due to the large engineering effort required to quantify every risk on basis of historical data, these risk scales are qualitative.

Table 10.1: Qualitative scales used during risk assessment.

Potential Likelihood (L)	
1	Extremely Unlikely: Failure condition never expected to occur during operational lifetime.
2	Unlikely / Remote: Failure condition is expected to occur - at most - once during its operational lifetime.
3	Possible / Occasional: Failure condition is expected to occur once or twice during its operational lifetime.
4	Likely / Reasonably Possible: Failure condition is expected to occur several times during its operational lifetime.
5	Almost certain / Frequent: Failure condition is expected to occur during almost every mission during operational lifetime.

Potential Consequence (C)	
1	Negligible: Failure condition has negligible effect on schedule, technical performance, cost or other available resources. There is no observable change in the project.
2	Minor: Failure condition does not significantly impact schedule, technical performance or other available resources. There may be minor delays and/or changes required in available budgets.
3	Major: Failure condition results in noticeable schedule delay and/or change in other available resources. Action must be taken by design team and/or operator in order to resolve the problem.
4	Hazardous: Failure condition results in a major schedule delay or has significant effect on other available resources. Action must be taken by the design team and/or operator to resolve the problem.
5	Catastrophic: Failure condition results in the worst credible outcome and may halt the project to a complete stop due to a lack of resources. Action must be taken by the design team and/or operator to resolve the problem.

Risk Levels
1-3 = Low
4-9 = Medium
10-16 = High
20-25 = Very High

The technical risks associated with FLOWS mission are presented in Table 10.2. The identifiers of the risks are constructed as follows: firstly, RSK-TEC stands for 'Risk Technical' to differentiate it from an organizational risk. Then, the category under which the risk falls is specified. These categories are: JS (Joint Segment), VTOL (Vertical Take-Off and Landing), PROP (Propulsion), PLD (Payload), POW (Power), STR (Structures), ADC (Attitude Determination and Control), CDH (Command and Data Handling), and GS (Ground Segment). In addition, although these are not the main focus of the assessment, there are several risks outside of the mission: PROD (Production), TRANS (Transportation), MAINT (Maintenance), and EOL (End Of Life). Any other risks that do not fall under any of the aforementioned categories are handled in MISC (Miscellaneous). The final part of the identifier contains two numbers separated by a decimal point, the first one specifying the event and the second being the specific cause for that event.

Table 10.2: Initial risk assessment.

ID	Event	Cause	Effect	L	C	R
Production (PROD)						
RSK-TEC-PROD-1.1	Parts not available	Shortage of materials	Production is delayed and possible design revisions are needed if material unavailability is permanent	3	3	9
RSK-TEC-PROD-1.2		Manufacturing of parts by external parties is delayed	Assembly is delayed	4	3	12
RSK-TEC-PROD-2.1	Injury to personnel during	Inadequate handling of heavy equipment or dangerous machinery	Reduced productivity, delay in production times	3	2	6
RSK-TEC-PROD-2.2	production or assembly	Inadequate handling of other risk sources (electronics, hazardous substances, etc.)	Reduced productivity, delay in production times	3	3	9
RSK-TEC-PROD-3.1	Parts or systems fail during testing	Manufacturing defect found during non-destructive testing	New part needs to be manufactured causing delays that might propagate to the assembly phase	3	2	6

Continued on next page

Table 10.2 – continued from previous page

ID	Event	Cause	Effect	L	C	R
RSK-TEC-PROD-3.2		Integrated software fails testing	Software needs bugfixing or redesign causing delays and cost	3	3	9
RSK-TEC-PROD-3.3		Fluid leaks found	Leaks need to be repaired or new parts need to be installed causing delays and cost. Possible damage to other parts due to the fluids	3	3	9
RSK-TEC-PROD-3.4		Fluid leaks found	Leaks need to be repaired or new parts need to be installed causing delays and cost. Possible damage to other parts due to the fluids	3	3	9
RSK-TEC-PROD-3.5		Installation or assembly error	Disassembly and rework required causing delays and additional costs	4	3	12
RSK-TEC-PROD-4.1	Injury to personnel during testing	Inadequate handling of equipment or testing machinery	Reduced productivity, delay in production times	2	3	6
Transportation (TRANS)						
RSK-TEC-TRANS-1.1	Part or assembly is damaged during transport	Inadequate packaging of hardware	Parts need repairing causing delays and cost	2	2	4
RSK-TEC-TRANS-1.2		Hardware is dropped during handling	Parts need repairing causing delays and cost	3	2	6
RSK-TEC-TRANS-1.3		Hoisting equipment malfunctions during transport	Assembly needs repairing, causing delays and cost	1	3	3
RSK-TEC-TRANS-2.1	Injury to personnel during transport	Inadequate handling of heavy or hazardous equipment	Reduced productivity, delay in transport times	3	2	6
RSK-TEC-TRANS-3.1	Parts go missing	Parts are lost during transport	Time is needed to find the missing parts or new parts must be manufactured which also increases cost	2	2	4
RSK-TEC-TRANS-3.2		Access by unauthorized personnel	Time is needed to find the missing parts or new parts must be manufactured which also increases cost	2	2	4
Joint Segment (JS)						
RSK-TEC-JS-1.1	Faulty mission plan	Incorect payload and fuel estimated to perform mission	Mission cannot be performed and a new mission with a different payload and/or fuel must be planned causing delays	2	3	6
RSK-TEC-JS-1.2		Situation drastically changes after system deployment	Mission cannot be performed and a new mission with a different payload must be planned causing delays	3	3	9
RSK-TEC-JS-1.3	Container walls cannot be deployed	Wall deployment mechanism actuators fail	The ground system cannot be deployed and the UAV cannot be assembled	3	3	9
RSK-TEC-JS-1.4	System cannot be deployed	System fails one or more pre-flight calibration tests	Parts might need repairing or replacement	3	3	9
RSK-TEC-JS-1.5	The wind impairs ground station deployment	The deployable walls cannot be deployed	The ground system cannot be deployed and the UAV cannot be assembled	3	3	9
RSK-TEC-JS-1.6		The heavy winds prevent or jeopardize the assembly of the UAV	The UAV cannot be assembled, or becomes damaged during the assembly attempt	4	4	16
RSK-TEC-JS-1.7	Ground station tools fail	No power available from external power grid	The UAV assembly and deployment is delayed or not possible	3	3	9
RSK-TEC-JS-1.8		The assembly tool itself fails		3	3	9
RSK-TEC-JS-2.1	Ground station relocation is delayed	Traffic present on roads	The ground station cannot perform its mission on time	4	3	12
RSK-TEC-JS-2.2		Selected location is not available or reachable	Ground station must move to an alternate location	3	3	9
RSK-TEC-JS-2.3	System cannot be deployed	System is damaged during transport	System needs to be repaired with spare parts if available, else the mission cannot be performed and must be planned for a later date	2	3	6
Vertical Take-Off and Landing (VTOL)						
RSK-TEC-VTOL-1.1	System cannot take off	Weather conditions are incomptaible with vertical take-off capabilities	Mission is delayed or cannot be performed at all	3	4	12
RSK-TEC-VTOL-1.2		Obstructed take-off surface or surrounding area	Relocation of take-off site is required and may cause delays to the mission	2	2	4
RSK-TEC-VTOL-2.1	System cannot land	Weather conditions are incomptaible with landing capabilities	Loitering is needed to wait until better weather conditions or a horizontal emergency landing must be performed	3	3	9

Continued on next page

Table 10.2 – continued from previous page

ID	Event	Cause	Effect	L	C	R
RSK-TEC-VTOL-2.2		System cannot transition to vertical flight mode	Horizontal emergency landing is required	2	3	6
RSK-TEC-VTOL-2.3		Obstructed landing surface	Relocation of landing site is required and may cause delays to the mission	2	2	4
Propulsion (PROP)						
RSK-TEC-PROP-1.1	Failure of horizontal or vertical motor	Shaft failure	Motor failure, loss of propulsion function; emergency landing is necessary	2	4	8
RSK-TEC-PROP-1.2		Ingress protection failure		3	4	12
RSK-TEC-PROP-1.3		Stator winding failure		2	4	8
RSK-TEC-PROP-1.4		Cooling failure		3	4	12
RSK-TEC-PROP-1.5		ESC Unit failure		2	4	8
RSK-TEC-PROP-2.1	Failure of horizontal or vertical propeller	Seizure	Propeller failure, loss of propulsion function; emergency landing is necessary	2	4	8
RSK-TEC-PROP-2.2		Blade damage		2	4	8
RSK-TEC-PROP-2.3		Foreign object damage		3	4	12
Payload (PLD)						
RSK-TEC-PLD-1.1	Deployment failure	Payload bay or release mechanism hardware failure	Loss of intervention payload functions; mission may be terminated and return to base for repairs may be required	3	3	9
RSK-TEC-PLD-1.2		Payload bay or release mechanism software error		4	3	12
RSK-TEC-PLD-1.3	Failure to perform mission	Target acquisition issues		4	3	12
RSK-TEC-PLD-1.4		Unsuitable weather conditions		3	3	9
RSK-TEC-PLD-2.1	Multispectral Gimbal failure or Bathymetric LIDAR failure	Hardware failure	Loss of monitoring payload functions, loss of data measurement and gathering; mission may be terminated and return to base for repairs may be required	2	3	6
RSK-TEC-PLD-2.2		Sensor obstruction		5	3	15
RSK-TEC-PLD-2.3		Software error		2	3	6
Power (POW)						
RSK-TEC-POW-1.1	Power Management System failure	CAN failure	Power Management System failure; all systems become inoperative, unpowered emergency landing may result in collateral damage	3	5	15
RSK-TEC-POW-1.2		Relay failure		2	5	10
RSK-TEC-POW-1.3		Microcontroller failure		2	5	10
RSK-TEC-POW-1.4		Wiring failure		4	5	20
RSK-TEC-POW-1.5		PDU Unit failure		2	5	10
RSK-TEC-POW-2.1	ICE failure	Fuel is exhausted	Power supply failure; loss of power; emergency landing is required	3	5	15
RSK-TEC-POW-2.2		Cooling failure		3	5	15
RSK-TEC-POW-2.3		Hardware failure		3	5	15
RSK-TEC-POW-2.4		Rotor seizure		2	5	10
RSK-TEC-POW-2.5	Battery failure	Cooling failure	Power supply failure; loss of power; emergency landing is required	3	5	15
RSK-TEC-POW-2.6		Short/Open circuit		3	5	15
RSK-TEC-POW-2.7		BMS Unit failure		2	5	10
RSK-TEC-POW-2.8		Battery degradation		3	5	15
Structures (STR)						

Continued on next page

Table 10.2 – continued from previous page

ID	Event	Cause	Effect	L	C	R
RSK-TEC-STR-1.1	Structural failure of empennage	Fatigue, physical damage	Primary structural failure; total loss of aircraft functions	3	5	15
RSK-TEC-STR-2.1	Structural failure of wing			3	5	15
RSK-TEC-STR-3.1	Structural failure of boom			3	5	15
RSK-TEC-STR-4.1	Structural failure of mounting structure	Fatigue, physical damage	Secondary structural failure; emergency landing and repair is necessary	3	3	9
RSK-TEC-STR-5.1	Structural failure of landing gear	Fatigue, physical damage, brake failure	Secondary structural failure; loss of VTOL functions, horizontal emergency landing is required	3	4	12
RSK-TEC-STR-6.1	Insulation failure	Fatigue, physical damage, mounting structure misalignment	Secondary structural failure; substances can enter the UAV and contaminate hardware; emergency landing and repair is necessary	3	4	12
Attitude Determination and Control (ADC)						
RSK-TEC-ADC-1.1	Flight Computer or INU failure	Software error	Autopilot failure, increased pilot workload; emergency landing is required	3	4	12
RSK-TEC-ADC-1.2		Hardware failure		2	4	8
RSK-TEC-ADC-2.1	Aileron, rudder, or elevator failure	Servo failure	Control surface malfunction, loss of roll rate, yaw, or pitch control; emergency landing is required	2	3	6
RSK-TEC-ADC-2.2		Fatigue		3	3	9
RSK-TEC-ADC-2.3		Physical damage		3	3	9
RSK-TEC-ADC-3.1	Control camera failure	Hardware failure	Control failure: loss of pilot vision; emergency landing is required	2	5	10
RSK-TEC-ADC-3.2		Software error		2	5	10
RSK-TEC-ADC-3.3		Lens obstruction		5	5	25
Command and Data Handling (CDH)						
RSK-TEC-CDH-1.1	Data handling unit failure	Hardware failure	Radio or satellite communication failure: attitude, control, and/or measurement data is (partially) lost, corrupted or incorrect. Emergency landing is required	2	4	8
RSK-TEC-CDH-1.2		Software error		2	4	8
RSK-TEC-CDH-2.1	Receiver or antenna failure	Material degradation		4	4	16
RSK-TEC-CDH-2.2		Software error		2	4	8
RSK-TEC-CDH-3.1	Data link loss	Internal signal interference		3	3	9
RSK-TEC-CDH-3.2		External signal interference		5	3	15
Ground Segement (GS)						
RSK-TEC-GS-1.1	The ground station is not processing data	The data processing unit is not functioning	The data supplied by the UAV is not processed on the ground station and the mission is not successful	1	4	4
RSK-TEC-GS-1.2		The data processing unit is not receiving the data correctly	The data cannot be processed on the ground station and the mission is not successful	2	4	8
RSK-TEC-GS-2.1	Ground station radio communication fails	Signal is blocked by buildings or terrain	The UAV cannot be contacted by the ground station resulting in a loss of low-latency control	4	4	16
RSK-TEC-GS-2.2		Radio antennae itself is not functioning		2	4	8
RSK-TEC-GS-2.3	The ground station does not have a satellite connection	The satellite internet terminal is not functioning	The ground station does not have a long-distance connection to the UAV and possibly cannot receive data from external parties	3	4	12
RSK-TEC-GS-2.4		The area of deployment does not have satellite coverage		2	4	8
Maintenance (MAINT)						
RSK-TEC-MAINT-1.1	UAV requires update or redesign	A common problem is discovered during the operational life of the system	Depending on the severity an update to all operational systems might be required	4	3	12

Continued on next page

Table 10.2 – continued from previous page

ID	Event	Cause	Effect	L	C	R
RSK-TEC-MAINT-1.2		An uncommon but critical problem is discovered during the operational life of the system	All operational systems must be grounded until the problem has been resolved	2	5	10
RSK-TEC-MAINT-2.1	Damage goes unnoticed after mission	Inadequate post-flight maintenance check	Damage may propogate over time and cause failures during the next mission	3	4	12
RSK-TEC-MAINT-2.2		Damage could not be found with methods used	Damage may propogate over time and cause failures during the next mission	3	4	12
End Of Life (EOL)						
RSK-TEC-EOL-1.1	Parts are not reusable	Damage is found in part at end of life	In case of no available storage space, part is discarded and inventory is decreased by part value	4	3	12
RSK-TEC-EOL-1.2		No buyers interested in the part	In case of no available storage space, part is discarded and inventory is decreased by part value	3	3	9
RSK-TEC-EOL-2.1	EOL procedure cannot be performed	Company producing UAV does not exist anymore	Owners of the UAV don't follow the EOL procedures and unnessecary waste is produced	2	3	6
RSK-TEC-EOL-2.2		Regulations change making recycling impossible	Parts that were intended to be recycled become waste	2	2	4
Miscellaneous (MISC)						
RSK-TEC-MISC-1.1	UAV causes panic to public	Sound of the UAV scares people	People think they cannot flee from the flood as they believe they are in danger	4	2	8
RSK-TEC-MISC-1.2		People mistake the UAV as military weapon	People think they cannot flee from the flood as they believe they are in danger	4	2	8
RSK-TEC-MISC-2.1	Unidentified risks	Technical risks are not foreseen	No contingency plan available to reduce the effect of the risk when it occurs	4	3	12

10.3. Risk Reduction

The risks presented in Table 10.2 were analyzed and two types of measures were developed to address them. On one hand, mitigation strategies in the form of preventive risk controls were designed to reduce the likelihood of risk events. On the other, contingency plans in the form of reactive risk controls were defined to reduce their severity. These mitigation plans and contingency plans have their own identifier, as some strategies can be applied to several risks. The IDs for the mitigation strategies start with the abbreviation TPRC (Technical Preventive Risk Control) and end with a number specifying the exact strategy. Similarly, the contingency plans use the abbreviation TRRC (Technical Reactive Risk Control) with a number to construct the ID.

Risk Control Measures

All mitigation strategies and contingency plans can be found in Table 10.3 and Table 10.4 respectively, together with responsible individuals. If these measures are to be implemented during the operational life of the system, the operator of the system is deemed responsible.

Table 10.3: Technical Preventive Risk Control

ID	Description	Responsible
TPRC-1	Monitor the commercial market for possible delays	Materials Engineer
TPRC-2	Avoid using materials that have a history of shortages	Materials Engineer
TPRC-3	Order, store, and/or produce parts in batches (reserve quantities)	Materials Engineer
TPRC-4	Maintain product and/or material inventory and delivery checklist, e.g. part tracking system with (bar)codes	Chief Engineer
TPRC-5	Order from trustworthy part suppliers	Chief Engineer
TPRC-6	Order off the shelf components instead of custom parts	Chief Engineer
TPRC-7	Account for delays in assembly planning	Project Manager
TPRC-8	Implement handling, installation, engineering validation testing, and/or design verification (e.g. functional, performance, environmental, safety) testing procedures	Risk Manager
TPRC-9	Make use of PPE (Personal Protective Equipment, e.g. safety shoes, gloves, glasses)	Risk Manager
TPRC-10	Employ only licensed operators	Risk Manager
TPRC-11	Incorporate validation of physical, mathematical, or sofware model integrated in system environment	Technical Quality Control
TPRC-12	Implement certified software, i.e. Design Assurance Levels (DALs)	Software Manager

Continued on next page

Table 10.3 – continued from previous page

ID	Description	Responsible Member
TPRC-13	Perform Qualification Model Testing	Technical Quality Control
TPRC-14	Implement quality control by external experts	Technical Quality Control
TPRC-15	Use hoisting equipment that is suitable for its intended function and meets machine directive or equivalent	Risk Manager
TPRC-16	Ensure safeguarding of parts (i.e. secure storage and transport)	Risk Manager
TPRC-17	Incorporate fuel reserves into system	Chief Engineer
TPRC-18	Perform occasional maintenance in accordance with maintenance checklist	Operator
TPRC-19	Perform weather forecasting prior to flight to ensure sufficient flight conditions	Operator
TPRC-20	Accommodate for high gusts and turbulence resistance	Flight Performance Engineer
TPRC-21	Incorporate conventional landing capabilities (under extreme weather conditions)	Chief Engineer
TPRC-22	Appoint designated take-off and landing platforms at remote area, clear of any obstacles	Operator
TPRC-23	Implement pre-flight checklist (in chronological order) for the establishment of data links and operating of ADC system, airflow sensors, monitor and control cameras, control mechanisms, motors, propellers, and payload deployment bay	Operator
TPRC-24	Incorporate control system redundancy by use of built-in Flight Computer failure redundancy	Control Engineer
TPRC-25	Assess and monitor maintenance intervals of each component	Operator
TPRC-26	Incorporate signal redundancy in link budget	Ground Systems Engineer
TPRC-27	Ensure non-threatening noise levels of propulsion system with respect to general public	Propulsion Engineer
TPRC-28	Design verification and validation tests that aim to simulate the long term functioning of the system	Technical Quality Control
TPRC-29	Find possible buyers before the part's end of life	Materials Engineer
TPRC-30	Distribute recycling and waste management methods with users	Materials Engineer
TPRC-31	Avoid use of highly experimental materials where recycling regulations have not yet matured	Materials Engineer
TPRC-32	Maintain the technical risk assessment during further development	Risk Manager
TPRC-33	Select nearby backup deployment location in advance for the mobile ground station	Ground Systems Engineer
TPRC-34	Employ backup battery system and generator in the mobile ground station	Ground Systems Engineer
TPRC-35	Limit amount of different tools necessary and carry backup tools and parts on ground station	Ground Systems Engineer
TPRC-36	Use detachable radio antenna of the ground station to deploy at a different location	Ground Systems Engineer
TPRC-37	Supply ground station with a small backup radio antenna for landing and take-off	Ground Systems Engineer
TPRC-38	Implement independent back-up data processing unit on the ground station	Ground Systems Engineer
TPRC-39	Mount radio antenna of the ground system on an extendable structure	Ground Systems Engineer
TPRC-40	Constrain UAV components to ground station until fully assembled	Ground Systems Engineer
TPRC-41	Design protective housing for horizontal and vertical motors	Propulsion Engineer
TPRC-42	Use of multispectral (infrared + visual) camera to more easily identify targets under any conditions	Sensor Array Engineer
TPRC-43	Incorporate design safety factors	Structures Engineer
TPRC-44	Establish two communication links (radio + satellite) with ground station for redundancy	Ground Systems Engineer
TPRC-45	Integrate receiver and antenna into a protective radome structure	Ground Systems Engineer

Table 10.4: Technical Reactive Risk Control

ID	Description	Responsible Member
TRRC-1	Search for different materials that are currently available	Materials Engineer
TRRC-2	Search for different companies that can produce the part more quickly	Materials Engineer
TRRC-3	Consider substitute personnel	Risk Manager
TRRC-4	Order, store, and/or produce parts in batches (reserve quantities)	Materials Engineer
TRRC-5	Use short, straight fluid lines in the wing	Integration Manager
TRRC-6	Move to a different location where conditions allow for continued mission operation	Operator
TRRC-7	Transition to vertical flight if VTOL system has a seperate propulsion system that is still functioning	Operator
TRRC-8	Use unpowered gliding capabilities	Flight Performance Enginer
TRRC-9	Perform Particular Risk Analysis (identification and management of events external to the system)	Risk Manager
TRRC-10	Incorporate redundant sensor design by using two multispectral cameras	Sensor Array Engineer

Continued on next page

Table 10.4 – continued from previous page

ID	Description	Responsible Member
TRRC-11	Incorporate control system redundancy by use of built-in Flight Computer failure redundancy	Control Engineer
TRRC-12	Incorporate conventional landing capabilities (under extreme weather conditions)	Flight Performance Enginer
TRRC-13	Implement automated return-to-base or emergency landing procedure in case of loss of communication	Ground Systems Engineer
TRRC-14	Implement infrastructure to communicate with emergency services (e.g. NL alert) and alert the general public	Chief Engineer
TRRC-15	Establish recycling and/or waste management methods	Materials Engineer
TRRC-16	Establish additional repurposing concepts for parts external to the usual EOL procedure	Materials Engineer
TRRC-17	Ensure manual deployment option for the container walls	Ground Systems Engineer
TRRC-18	Communicate with first responders and authorities about the quickest route to deployment location	Operator
TRRC-19	Send data to external server for processing upon ground station failure	Ground Systems Engineer
TRRC-20	Orient, position and design the ground system in a way to reduce wind effects	Chief Engineer
TRRC-21	Use nearby cellular network for internet connection, if available	Ground Systems Engineer
TRRC-22	Establish error diagnostics protocol for the ground system radio antenna	Ground Systems Engineer
TRRC-23	Power avionics and ADCS with back-up battery to ensure controlled glide during propulsion failure	Power Engineer
TRRC-24	Accommodate for high gusts and turbulence resistance	Flight Performance Enginer
TRRC-25	Incorporate fuel reserves into system	Chief Engineer
TRRC-26	Incorporate fail-safe philosophy into design	Structures Engineer
TRRC-27	Implement thrust vectoring strategies to counter loss of control	Propulsion Engineer

10.4. Mitigated Risks and Risk Maps

The objective of the risk management process is to reduce risk by correctly implementing the mitigation strategies and contingency plans described above. In Table 10.5, the strategies applied to each risk are specified, along with the updated risk score and the engineer responsible for applying the mitigation strategy and contingency plan for that specific risk. If no clear responsible engineer could be assigned, the risk manager was deemed responsible.

Table 10.5: Applied risk mitigation methods and contingency plans per risk

ID	Old R	Mitigation Strategy	New L	Contingency Plan	New C	New R	Responsible Engineer
RSK-TEC-PROD-1.1	9	TPRC-1, TPRC-2, TPRC-3, TPRC-4	2	TRRC-1	3	6	Materials
RSK-TEC-PROD-1.2	12	TPRC-3, TPRC-5, TPRC-6, TPRC-7	3	TRRC-2	2	6	Materials
RSK-TEC-PROD-2.1	6	TPRC-8, TPRC-9, TPRC-10	2	TRRC-3	1	2	Risk Manager
RSK-TEC-PROD-2.2	9	TPRC-8, TPRC-9, TPRC-10	2	TRRC-3	3	6	Risk Manager
RSK-TEC-PROD-3.1	6	TPRC-5	2	TRRC-4	1	2	Risk Manager
RSK-TEC-PROD-3.2	9	TPRC-11, TPRC-12	1	N/A	3	3	Software Manager
RSK-TEC-PROD-3.3	9	TPRC-11	3	TRRC-5	2	6	Integration Manager
RSK-TEC-PROD-3.4	8	TPRC-13	1	N/A	4	4	Risk Manager
RSK-TEC-PROD-3.5	12	TPRC-8, TPRC-14	3	N/A	3	9	Technical Quality Control
RSK-TEC-PROD-4.1	6	TPRC-8, TPRC-9	2	N/A	3	6	Risk Manager
RSK-TEC-TRANS-1.1	4	TPRC-8	1	TRRC-4	1	1	Risk Manager
RSK-TEC-TRANS-1.2	6	TPRC-8	2	TRRC-4	1	2	Risk Manager
RSK-TEC-TRANS-1.3	3	TPRC-15	1	TRRC-4	2	2	Risk Manager
RSK-TEC-TRANS-2.1	6	TPRC-8, TPRC-9	2	TRRC-3	1	2	Risk Manager
RSK-TEC-TRANS-3.1	4	TPRC-4	2	TRRC-4	1	2	Risk Manager
RSK-TEC-TRANS-3.2	4	TPRC-16	1	TRRC-4	1	1	Risk Manager
RSK-TEC-JS-1.1	6	TPRC-17	1	N/A	3	3	Chief
RSK-TEC-JS-1.2	9	TPRC-17	2	N/A	3	6	Chief
RSK-TEC-JS-1.3	9	TPRC-18	2	TRRC-17	2	4	Ground Systems
RSK-TEC-JS-1.4	9	TPRC-11, TPRC-18	2		3	6	Risk Manager

Continued on next page

Table 10.5 – continued from previous page

ID	Old R	Mitigation Strategy	New L	Contingency Plan	New C	New R	Responsible Engineer
RSK-TEC-JS-1.5	9	TPRC-19, TPRC-20	2	TRRC-6, TRRC-17, TRRC-20	2	4	Ground Systems
RSK-TEC-JS-1.6	16	TPRC-8, TPRC-19 TPRC-40	3	TRRC-6, TRRC-20	2	6	Ground Systems
RSK-TEC-JS-1.7	9	TPRC-34	1	N/A	3	3	Ground Systems
RSK-TEC-JS-1.8	9	TPRC-35	2	N/A	3	6	Chief
RSK-TEC-JS-2.1	12	TPRC-33	3	TRRC-18	1	3	Ground Systems
RSK-TEC-JS-2.2	9	TPRC-33	3	TRRC-6	2	6	Ground Systems
RSK-TEC-JS-2.3	6	TPRC-8, TPRC-15	1	N/A	3	3	Risk Manager
RSK-TEC-VTOL-1.1	12	TPRC-19, TPRC-20	2	TRRC-6	3	6	Chief
RSK-TEC-VTOL-1.2	4	TPRC-22	1	TRRC-6	1	1	Risk Manager
RSK-TEC-VTOL-2.1	9	TPRC-19, TPRC-20, TPRC-21	3	TRRC-6, TRRC-25	2	6	Flight Performance
RSK-TEC-VTOL-2.2	6	TPRC-21, TPRC-23	2	TRRC-12	1	2	Flight Performance
RSK-TEC-VTOL-2.3	4	TPRC-22	1	TRRC-6	1	1	Flight Performance
RSK-TEC-PROP-1.1	8	TPRC-18, TPRC-23	2	TRRC-7, TRRC-8, TRRC-9, TRRC-23	3	6	Propulsion
RSK-TEC-PROP-1.2	12	TPRC-41	2		3	6	Propulsion
RSK-TEC-PROP-1.3	8	TPRC-18, TPRC-23	1		3	3	Propulsion
RSK-TEC-PROP-1.4	12	TPRC-11, TPRC-23	2		3	6	Propulsion
RSK-TEC-PROP-1.5	8	TPRC-23	1		3	3	Power
RSK-TEC-PROP-2.1	8	TPRC-18, TPRC-23	2	TRRC-7, TRRC-8, TRRC-9	3	6	Propulsion
RSK-TEC-PROP-2.2	8	TPRC-18, TPRC-23	1		3	3	Propulsion
RSK-TEC-PROP-2.3	12	N/A	3		3	9	Propulsion
RSK-TEC-PLD-1.1	9	TPRC-18, TPRC-23	2	N/A	3	6	Mechanisms
RSK-TEC-PLD-1.2	12	TPRC-12, TPRC-23	2	N/A	3	6	Mechanisms
RSK-TEC-PLD-1.3	12	TPRC-11, TPRC-23, TPRC-42	2	TRRC-25	4	8	Intervention
RSK-TEC-PLD-1.4	9	TPRC-19, TPRC-20, TPRC-42	1	TRRC-6, TRRC-12, TRRC-24	3	3	Intervention
RSK-TEC-PLD-2.1	6	TPRC-18, TPRC-23	1	TRRC-10	2	2	Sensor Array
RSK-TEC-PLD-2.2	15	TPRC-23	4	TRRC-10	2	8	Sensor Array
RSK-TEC-PLD-2.3	6	TPRC-12, TPRC-23	2	TRRC-10	2	4	Sensor Array
RSK-TEC-POW-1.1	15	TPRC-8, TPRC-12, TPRC-23	2	TRRC-8, TRRC-12	4	8	Power
RSK-TEC-POW-1.2	10	TPRC-8, TPRC-23	1	TRRC-8, TRRC-12	4	4	Power
RSK-TEC-POW-1.3	10	TPRC-8, TPRC-23	1	TRRC-8, TRRC-12	4	4	Power
RSK-TEC-POW-1.4	20	TPRC-8, TPRC-14, TPRC-23	2	TRRC-8, TRRC-12	4	8	Power
RSK-TEC-POW-1.5	10	TPRC-8, TPRC-23	1	TRRC-8, TRRC-12	4	4	Power
RSK-TEC-POW-2.1	15	TPRC-17, TPRC-23	2	TRRC-23	4	8	Power
RSK-TEC-POW-2.2	15	TPRC-11, TPRC-23	2	TRRC-23	4	8	Power
RSK-TEC-POW-2.3	15	TPRC-18 TPRC-23	2	TRRC-23	4	8	Power
RSK-TEC-POW-2.4	10	TPRC-18, TPRC-23	1	TRRC-23	4	4	Power
RSK-TEC-POW-2.5	15	TPRC-11, TPRC-23	2	TRRC-8, TRRC-12	4	8	Power
RSK-TEC-POW-2.6	15	TPRC-8, TPRC-14, TPRC-23	2	TRRC-8, TRRC-12	4	8	Power
RSK-TEC-POW-2.7	10	TPRC-8, TPRC-23	1	TRRC-8, TRRC-12	4	4	Power
RSK-TEC-POW-2.8	15	TPRC-8, TPRC-23, TPRC-25	2	TRRC-8, TRRC-12	4	8	Power
RSK-TEC-STR-1.1	15	TPRC-18, TPRC-25, TPRC-43	1	N/A	5	5	Structures
RSK-TEC-STR-2.1	15	TPRC-18, TPRC-25, TPRC-43	1	N/A	5	5	Structures
RSK-TEC-STR-3.1	15	TPRC-18, TPRC-25, TPRC-43	1	N/A	5	5	Structures
RSK-TEC-STR-4.1	9	TPRC-18, TPRC-25, TPRC-43	2	TRRC-26	3	6	Structures
RSK-TEC-STR-5.1	12	TPRC-18, TPRC-25, TPRC-43	2	TRRC-12	3	6	Structures
RSK-TEC-STR-6.1	12	TPRC-18, TPRC-25, TPRC-43	2	N/A	4	8	Structures
RSK-TEC-ADC-1.1	12	TPRC-12, TPRC-23	2	TRRC-11	3	6	Control
RSK-TEC-ADC-1.2	8	TPRC-18, TPRC-23	2	TRRC-11, TRRC-13	3	6	Control
RSK-TEC-ADC-2.1	6	TPRC-18, TPRC-23	2	TRRC-13, TRRC-27	2	4	Control
RSK-TEC-ADC-2.2	9	TPRC-18, TPRC-25, TPRC-43	2	TRRC-13, TRRC-27	2	4	Control
RSK-TEC-ADC-2.3	9	TPRC-18, TPRC-25, TPRC-43	2	TRRC-13, TRRC-27	2	4	Control
RSK-TEC-ADC-3.1	10	TPRC-18, TPRC-23	1	TRRC-10, TRRC-13,	3	3	Control
RSK-TEC-ADC-3.2	10	TPRC-12, TPRC-23	2	TRRC-10, TRRC-13,	3	6	Control

Continued on next page

Table 10.5 – continued from previous page

ID	Old R	Mitigation Strategy	New L	Contingency Plan	New C	New R	Responsible Engineer
RSK-TEC-ADC-3.3	25	TPRC-23	4	TRRC-9, TRRC-10, TRRC-13	2	8	Control
RSK-TEC-CDH-1.1	8	TPRC-23, TPRC-25	1	TRRC-13	3	3	Ground Systems
RSK-TEC-CDH-1.2	8	TPRC-12, TPRC-23	1	TRRC-13	3	3	Ground Systems
RSK-TEC-CDH-2.1	16	TPRC-23, TPRC-25, TPRC-45	1	TRRC-13	3	3	Ground Systems
RSK-TEC-CDH-2.2	8	TPRC-12, TPRC-23	1	TRRC-13	3	3	Ground Systems
RSK-TEC-CDH-3.1	9	TPRC-26, TPRC-44	3	TRRC-13	3	9	Ground Systems
RSK-TEC-CDH-3.2	15	TPRC-26, TPRC-44	3	TRRC-13	3	9	Ground Systems
RSK-TEC-GS-1.1	4	TPRC-38	1	TRRC-19	2	2	Ground Systems
RSK-TEC-GS-1.2	8	TPRC-38	1	TRRC-19	2	2	Ground Systems
RSK-TEC-GS-2.1	16	TPRC-22, TPRC-26, TPRC-33, TPRC-36, TPRC-39, TPRC-44	2	TRRC-6, TRRC-13	2	4	Ground Systems
RSK-TEC-GS-2.2	8	TPRC-23, TPRC-37	1	TRRC-13	3	3	Ground Systems
RSK-TEC-GS-2.3	12	TPRC-11. TPRC-26, TPRC-44	3	TRRC-21	2	6	Ground Systems
RSK-TEC-GS-2.4	8	TPRC-39	2	TRRC-6, TRRC-21	2	4	Ground Systems
RSK-TEC-MAINT-1.1	12	TPRC-28	4	N/A	2	8	Integration Manager
RSK-TEC-MAINT-1.2	10	TPRC-28	2	N/A	4	8	Integration Manager
RSK-TEC-MAINT-2.1	12	TPRC-14, TPRC-18	1	N/A	4	4	Risk Manager
RSK-TEC-MAINT-2.2	12	TPRC-18, TPRC-25	2	N/A	4	8	Risk Manager
RSK-TEC-EOL-1.1	12	N/A	3	TRRC-15	2	6	Materials
RSK-TEC-EOL-1.2	9	TPRC-29	1	TRRC-15	2	2	Materials
RSK-TEC-EOL-2.1	6	TPRC-30	1	N/A	3	3	Project Manager
RSK-TEC-EOL-2.2	4	TPRC-31	1	TRRC-16	2	2	Materials
RSK-TEC-MISC-1.1	8	TPRC-27	3	TRRC-14	1	3	Chief
RSK-TEC-MISC-1.2	8	N/A	4	TRRC-14	1	4	Chief
RSK-TEC-MISC-2.1	12	TPRC-32	3	N/A	3	9	Risk Manager

The change in risk levels due to the application of the mitigation strategies and contingency plans is visualized in Table 10.6. In the risks maps each cell contains the number of risks with that exact likelihood and consequence. A clear shift to the lower left corner is visible when comparing the two maps. However, a significant amount of risks with a medium risk level remains. Their mitigation strategy and contingency plans must be monitored closely to ensure that the risk is minimized.

Table 10.6: Risk maps before (left) and after (right) applying the mitigation strategies and the contingency plans.

Risk Map (pre-mitigation)

Likelihood (L)	1	2	3	4	5
5			2		1
4		2	8	3	1
3		4	19	10	10
2		6	8	13	8
1			1	1	

Consequence (C)

Risk Map (post-mitigation)

Likelihood (L)	1	2	3	4	5
5					
4	1	3			
3	2	7	5		
2	6	6	20	12	
1	4	6	15	7	3

Consequence (C)

Overall, the risk assessment is an important tool used during the design process. While the number of risks identified will likely not increase any further given the final phase of the design, they may be re-evaluated to give way to specific requirements formulated from new mitigation methods and contingency plans. All likelihood and consequence levels are estimations and are subject to change, as these were estimated at different times in the design process. For this reason, certain risks may be under- or overestimated.

11 | Lifecycle Assessment

The advancement of sustainability in the design process is a continuous process, based on the framework of the UN Sustainable Development Goals (SDG's). As observed in Figure 11.1, the design contributes to sustainability by supporting SDG 11 (Sustainable Cities and Communities) and representing SDG 13 (Climate Action) by participating in climate mitigation efforts. In turn, the SDG's influence the design, leading to specific design intentions from the design team (recycling and reuse of materials, reduced cost to ensure accessibility, funding from the Green Climate Fund, etc).

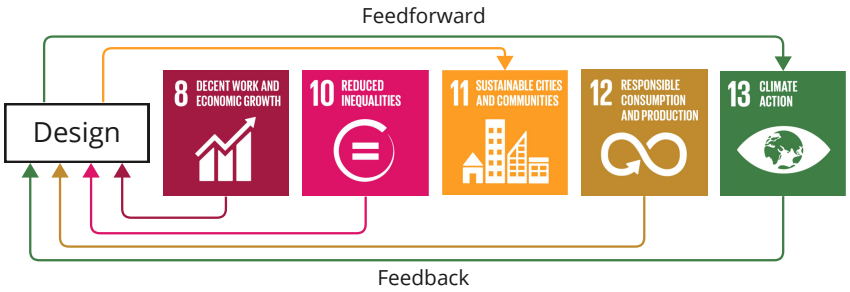

Figure 11.1: Sustainability framework [72].

This chapter describes the design team's approach to sustainable development, relying on a comprehensive and multilayered lifecycle assessment. Each individual phase in the life of the product was analyzed, and the equivalent carbon dioxide emissions were calculated, resulting in a final key performance indicator for lifecycle emissions. First, the production process was examined, with the material procurement and manufacturing and assembly procedures being covered in Section 11.1 and Section 11.2 respectively. Then, the total emissions for the production process and operational lifetime of the system were calculated in Section 11.3. For the final phase of the analysis, recycling and reuse practices were set up in Section 11.4.

11.1. Beginning of Life: Material Procurement

Before the parts for the UAV can be manufactured, materials need to be sourced. The FLOWS UAV predominantly uses commercially off-the-shelf components but requires custom fabrications for the structures. These structures include the fuselage, wings, booms, and control surfaces. As discussed in Chapter 6, the selected structural material is Aluminum 6061-T6. Aluminum 6061 is an alloy consisting of up to 98.56% aluminum and containing trace amounts of magnesium, silicon, iron, copper, chromium, zinc, tin, and manganese [1]. T6 stands for the temper of the material, which is a heat treatment that provides the maximum yield strength [2]. As the alloy is dominated by aluminum, the emissions are identified for the procurement and manufacturing processes of only aluminum.

The production of Al6061 is a two-step process of recycling aluminum and carrying out the alloying procedure. The finished product is not yet tempered, as this happens after the manufacturing of parts. The emissions for the recycling and alloying of aluminum are estimated in tons of CO_2 and MWh of electricity per ton of finished material[3]:

- **Aluminum Recycling**: The recycling of pre-used aluminum emits 0.5 tons of CO_2 per ton aluminum. [4]

[1] https://www.astm.org/b0209m-14.html
[2] https://www.makeitfrom.com/material-properties/6061-T6-Aluminum/
[3] https://www.carbonchain.com/blog/understand-your-aluminum-emissions
[4] https://www.climateaction.org/news/carbon-footprint-of-recycled-aluminium

- **6061 Alloying**: Electrolysis to melt aluminum for alloying uses $15.37\,\mathrm{MWh}$ of electricity per ton aluminum. [3]

Due to the multitude of methods of electricity production, emissions from smelting can vary from 3 to 18 tons of CO_2 per ton of aluminum, depending on what energy source is used [3]. Using renewable energy sources like hydroelectric energy, emissions can be limited to 4 tons of CO_2 per ton of aluminum, though this does limit the material sourcing to a handful of countries Figure 11.2 [3]. It is recommended to have the aluminum sourced from Norway, Sweden, or France, as these countries are able to produce low-emission aluminum at the time of writing [3].

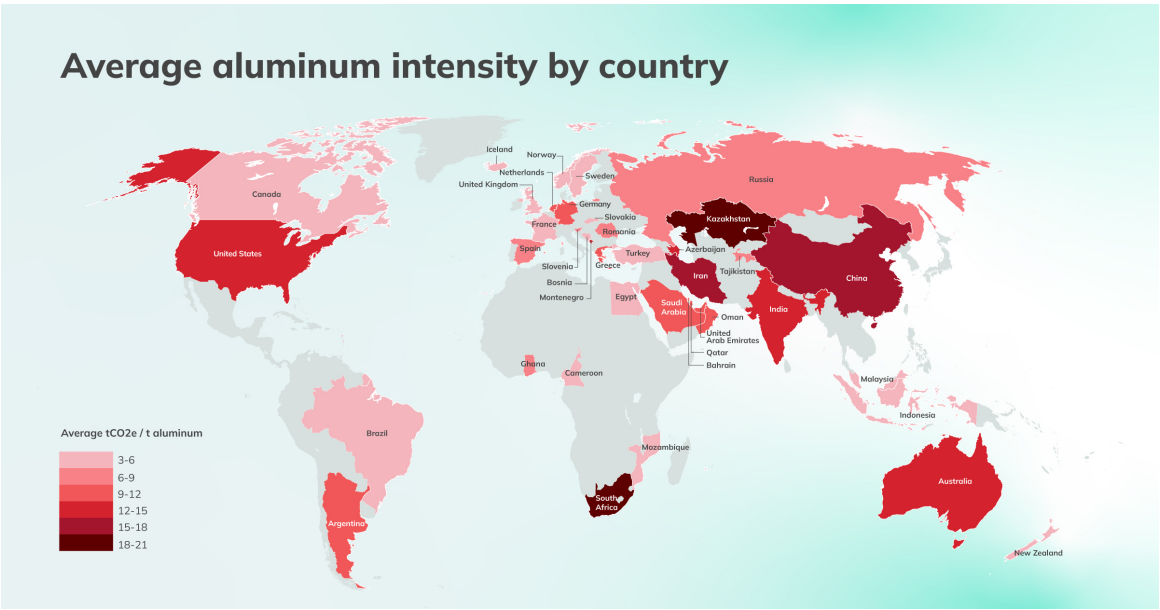

Figure 11.2: Map displaying tons of CO_2 emissions per ton of aluminum used for electrolysis.

With the material acquisition evaluated, the amount of emissions caused by its processing can be evaluated, for the purposes of a more detailed emission analysis to be carried out in Section 11.3. For the production of the required material, CO_2 emissions have been estimated at $4.5\,\mathrm{kg}$ per kg of aluminum. However, the amount of raw material needed for the production of each part can only be determined by identifying the manufacturing and assembly procedures.

11.2. Manufacturing and Assembly Procedures

The process of deforming and machining Aluminum 6061 into usable parts for the structural assembly consists of multiple manufacturing methods[5]. For each of the methods used, their emissions and waste can be estimated to determine not only how much raw material is needed as input to obtain a part of the expected weight, but also the emissions caused by the manufacturing process [6].

- **Extrusion** is a forming method that can be used to create frame stringers and longerons. The process produces $0.31\,\mathrm{tons}\,CO_2$ per ton of aluminum.
- **Forming** is used on the frame stringers and longerons in an annealed condition of $413\,^{\circ}\mathrm{C}$ to get them into shape. The process produces $0.37\,\mathrm{tons}\,CO_2$ per ton of aluminum [7].
- **Forging** is used to create thin sheets out of ingots. The process produces $0.37\,\mathrm{tons}\,CO_2$ per ton of aluminum [7].
- **Rubber forming** is used for the skin and sheet metal to create double-curved sheets needed for complex skin structures. The process produces $0.36\,\mathrm{tons}\,CO_2$ per ton of aluminum [7].

[5] https://www.azom.com/article.aspx?ArticleID=6636
[6] https://international-aluminium.org/statistics/greenhouse-gas-emissions-aluminium-sector/

- **Machining** is done in an annealed condition of $413\,°\mathrm{C}$ to work small details and finish the edges of parts. The process produces $0.36\,\mathrm{tons}\ CO_2$ per ton of aluminum [7].
- **Artificial Aging** is used to perform precipitation hardening. When parts are completed they can be artificially aged to T6 using precipitation hardening. The precipitation hardening is performed at $160\,°\mathrm{C}$ for $18\,\mathrm{hours}$ and $177\,°\mathrm{C}$ for $8\,\mathrm{hours}$, both followed by air cooling. The process produces $0.36\,\mathrm{tons}\ CO_2$ per ton of aluminum [7].
- **Riveting** is used to assemble the parts of the UAV into a single structure.

The fuselage skin, wing, and empennage will mostly consist of sheet metal, for which forging, rubber forming, machining and artificial aging are used. The longerons, booms, and frames are made using extrusion, forming, machining, and artificial aging.

When it comes to material waste, in working with metal, it is estimated that 15.9% of the inputted raw material is wasted in the manufacturing processes [7]. Therefore, for an expected total structural mass of $72.013\,\mathrm{kg}$, **an initial raw mass of aluminum of** $83.46\,\mathrm{kg}$ **is needed.**

The actual emission rates of the manufacturing processes can be verified during the production of the parts by measuring the CO_2 emissions with a simple sensor [8].

11.3. Lifecycle Emission Estimation

Once the system assembly has been completed, the vehicle can start its operational lifetime, carrying out missions until it reaches end-of-life. Both the manufacturing and the subsequent operation of the system result in the production of waste, which will be evaluated in the form of carbon dioxide emissions, as already mentioned at the beginning of this chapter.

Starting with the production emissions, they include the raw material procurement, described in Section 11.1, and the manufacturing and assembly procedures it must undergo, explored in Section 11.2. The production of the $83.46\,\mathrm{kg}$ of raw aluminum needed for the manufacturing of the structure leads to a carbon dioxide emission mass of $375.6\,\mathrm{kg}$, given the production relation of $4.5\,\mathrm{kg}$ of CO_2 per aluminum previously defined.

As for the manufacturing, the mass input for the production of each part can be obtained by increasing the expected final part mass by the waste percentage of the manufacturing processes. That, coupled with the data regarding carbon dioxide emissions for each process, determined in Section 11.2, leads to the total carbon dioxide emissions for the production of each part, as shown in Table 11.1.

Table 11.1: Part production emissions.

Part	Manufacturing processes	CO2/Al [kg/kg]	Input mass [kg]	Manufacturing emissions [kg CO2]
Fuselage skin	Forging, rubber forming, machining, artificial aging	1.45	7.2	10.4
Wing	Forging, rubber forming, machining, artificial aging	1.45	32.2	46.7
Empennage	Forging, rubber forming, machining, artificial aging	1.45	5.8	8.4
Longerons	Extrusion, forming, machining, artificial aging	1.4	12.1	16.9
Booms	Extrusion, forming, machining, artificial aging	1.4	20.2	28.2
Frames	Extrusion, forming, machining, artificial aging	1.4	6.03	8.4

[7] https://www.dallan.com/en/news/raw-material-saving-case-study/

[8] https://www.azocleantech.com/article.aspx?ArticleID=830

Therefore, the total production emissions for the procurement and manufacturing of the material into the complete structural frame leads to a total $494.6\,\mathrm{kg}$ of carbon dioxide emissions.

This analysis focused on the production emissions of the manufacturing and assembly process of the structural frame, but it does not take into account the integration of the subsystem components, which are also elements to be manufactured by the suppliers, a process which also results in emissions. However, information about the manufacturing and waste management practices of the COTS suppliers is not made available, suggesting that any conclusions reached through such a research could not be validated. Therefore, the production of the components that are to be acquired off-the-shelf is not considered in this analysis.

The emissions caused by the operations of the system can instead be found by determining the mass of carbon dioxide produced by the combustion of the fuel by the engines, since that is the primary means of waste production during operations. For this analysis, both monitoring and intervention mission profiles, described in Section 9.3, are investigated.

First, data regarding the fuel used by the engine and the engine itself must be identified. The engines used in the vehicle, which are selected in Section 5.1, use aviation kerosene as fuel, which has an energy density ED_{ker} of $46.3\,\mathrm{MJ/kg}$ [9] and an emission rate Em_{ker} of $263.9\,\mathrm{g_{[CO2]}\,kW\,h^{-1}}$, represented in grams of carbon dioxide produced per primary energy content [10]. The brake specific fuel consumption $BSFC$ of the engine, which for this analysis is taken to be $255\,\mathrm{g/kWh}$, is important to relate the fuel burnt by the engine and the energy it produces.

The energy density of the kerosene is used to compute how much primary energy a certain amount of fuel can produce. That energy can then be compared to the energy produced by the engine $E_{\text{eng}} = \frac{m_{\text{fuel}}}{BSFC}$ with the same amount of fuel in order to get a measure of the efficiency of the engine.

$$E_{\text{ker}} = ED_{\text{ker}} m_{\text{fuel}} \tag{11.1}$$

$$\eta_{\text{eng}} = \frac{E_{\text{eng}}}{E_{\text{ker}}} \tag{11.2}$$

Once that is done, the energy that the engine must provide in order to enact one of the flight phases in the mission profiles under study can be used to calculate the corresponding primary energy needed from the fuel from rewriting Equation 11.2, which is in turn used to determine the carbon dioxide emissions relative to that primary energy production by simply multiplying that energy with the emission rate Em_{ker}.

Therefore, by knowing the energy required for each phase of the monitoring and intervention mission profiles, the carbon dioxide emissions associated with each one can be calculated. **One nominal monitoring mission therefore produces $58.4\,\mathrm{kg}$ of CO_2, while the intervention mission produces $44.3\,\mathrm{kg}$ of CO_2.** Importantly, this emissions estimate covers only carbon dioxide emissions, as they are the best documented emissions for aerospace systems.

11.4. End of Life: Recycling & Reuse

The last step of the lifecycle analysis consists of determining the procedures that must take place once the system reaches the end of its operational lifespan. To successfully meet **R-MIS-10**, all drone components are to be repurposed for use or otherwise recycled according to the ISO-14001:2015 standard [73]. Moreover, recycling and reuse must be researched and applied whenever possible in order to maximize efficiency and bring forth a more circular design process[11]. This standard provides a framework and a structured approach to handling waste through the conceptualization of an Environmental Management System.

[9] https://transportgeography.org/contents/chapter4/transportation-and-energy/combustibles-energy-content/

[10] https://www.volker-quaschning.de/datserv/CO2-spez/index_e.php

[11] https://www.eea.europa.eu/highlights/reuse-and-recycling-are-key

The Environmental Management System (EMS) defines the rules governing the interaction of a certain business with the environment [73]. In the specific case of the FLOWS system, the EMS represents the policy developed to manage the decommissioning of the physical architecture. As the design progresses, targeted design effort could be put into ensuring sustainable sourcing of materials, as discussed in Section 11.1. Such efforts would also be included in the EMS.

To comply with ISO-14001:2015's legal requirements, the EMS needs to set specific objectives and targets. These targets should be pursued through a clearly defined environmental policy, which should itself be monitored and reported on [73].

Once it is deemed that the system is not able to perform its mission anymore, it is said to have reached its end-of-life stage and is subsequently de-commissioned, at which point the recyclability and the reusability of its components is to be assessed in order to minimize waste. This process encompasses both the aviation domain and the non-aviation, general waste management domain. This is an important distinction to make, as each sector has its own regulations on the valuation and possible reuse of the components.

Starting with the aviation field, components that are either still fully operational, or are capable of returning to an operational status after undergoing repairs, are identified and disassembled with the purpose of being brought back into service. Once this process is complete, the system will have lost any airworthyness, after which it shifts to the waste management field. Here, a complete dismantling of the system occurs, during which some parts of the aircraft are repurposed and certified for reuse in non-aerospace sectors. What remains is waste that is to be recycled whenever possible, or disposed of when recycling is not an option. A display of how this procedure is applied to a standard aircraft is displayed in Figure 11.3 [74].

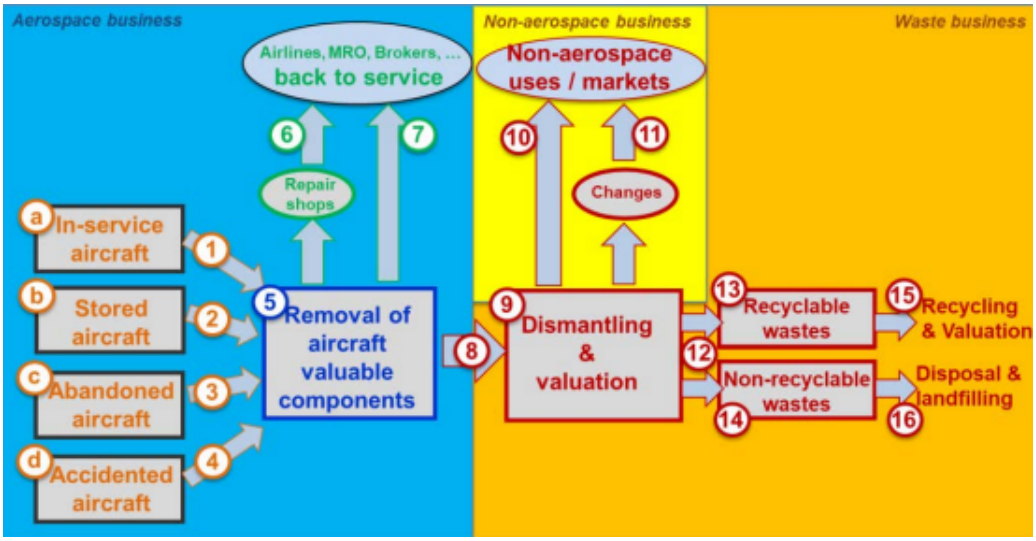

Figure 11.3: Recycling and reuse for a standard aircraft.

The airborne segment can be considered to be made up of its components, which are listed in Table 13.2, as well as the structural frame and any additional assembly structures discussed in Section 11.2. The subsystem components can be gathered in the following categories:

- Attitude Determination & Control
- Avionics
- Command & Data Handling
- Monitoring & Intervention Payload
- Propulsion System
- Electrical Power System

- Landing Gear System

Each of the components in these categories is to be disassembled and checked for operational performance, after which it is either ready for reuse or it needs to be repaired and recertified before it can be reused. If that is not possible, then the components will be dismantled into further pieces, which will be either repurposed for other applications or recycled whenever possible.

The structural frame will be made up of different segments that are then assembled together, so it can also undergo disassembly in order to find any section of the infrastructure that is able to be reused, most likely in the production of another FLOWS airborne segment. If that is not possible, the material will be recycled, given the remarkable affinity of aluminium with recycling [12].

Finally, for the assembly of the structural frame, reuse of fasteners is not recommended because of the inability to reliably test whether the fasteners were taken past their yield point during operations [13]. For this reason, the fasteners will flow directly to recycling or disposal.

After having discussed how recycling and reuse procedures would apply to the FLOWS mission, it can be concluded that the system infrastructure is entirely recyclable and reusable once it reaches end-of-life after a nominal operational lifespan. The only exception to this consists of the case in which the system reaches end-of-life due to an event that irreparably damages a component, meaning that its reuse would be compromised and its repurposing and recycling would depend on the part and material content of said component, which is not guaranteed to be fully reusable and recyclable.

The lifecycle assessment has resulted in a preliminary estimate of 83.46 kilograms for the required quantity of Aluminum 6061-T6 for the structural components of the aircraft. An estimate of 494.6 kilograms of carbon dioxide was reached for the manufacturing of the aircraft structure, with an operational emissions estimate between 44 and 58 kilograms of carbon dioxide. Further development for sustainability involves the definition of a manufacturing and assembly plan, as well as sourcing of a material supplier, which are to improve the accuracy of the emissions estimates significantly. Other analyses, including of energy expenditure and total material flows, can be performed as contact is made with component manufacturers and individual component data is obtained.

[12] https://greentumble.com/how-is-aluminum-recycled

[13] https://www.fastenal.com/content/feds/pdf/2017/02/Reuse%20of%20Fasteners%20rev%202017-02-21.pdf

12 | Economic Analysis

In this chapter, the market position of the final product is assessed. In Section 12.1, the total project cost is broken down into various expenses that are each assessed. Thereafter, possible business plans are evaluated in Section 12.2 and their effect on the product price is described. Then, a market analysis is performed in Section 12.3 and customer cases are assessed in Section 12.4 to identify the market gap and possible customers. Finally, the fit of the FLOWS system into the market is described in Section 12.5.

12.1. Cost Breakdown

To gain a better understanding of the product's position within the market, an initial estimate of the price needs to be made. In Figure 12.1, the Cost Breakdown Structure (CBS) is given. The total annual expenses have been divided into capital expenditures (CapEx) - the development, production, and management cost - and operating expenses (OpEx) - analogous to operation cost - to differentiate between long-term and day-to-day costs. Any CapEx are to be carried by the designer, whilst any OpEx will have to be carried by the customer in addition to paying the unit price.

	Annual Total Expenses								
	Capital Expenditures (CapEx)						Operating Expenses (OpEx)		
	Development cost		**Production cost**		**Management cost**		**Operation cost**		**Total**
Labor	Engineering [€300k]	Project Management [€100k]	Manufacture [€3.5k / unit]	Production Management [€1k / unit]	Inventory [€4k / unit]	Product Handling [€2k / unit]	System Deployment [€115k / unit]	Operation Management [€30k / unit]	**Fixed: €510k Variable: €186.5k**
		R&D [€150k]		Product Manufacturing [€2k / unit]				Operator [€80k / unit]	
		Prototyping [€50k]		Transport [€500 / unit]		Transport [€1k / unit]		Operator Training [€5k / unit]	
	Qualification Process [€200k]	Testing [€50k]	Quality Control [€4k / unit]	Inspection [€1k / unit]			Continued Operation [€10k + 60k / unit]	Maintenance [€15k / unit]	
		Documentation [€50k]		Testing [€2k / unit]		Waste Management and Recycling [€1k / unit]		Aircraft Licence [N/A]	
		Certification [€100k]		Documentation [€1k / unit]				TT&C Services [€10k + 45k / unit]	
Property, Plant, and Equipment (PP&E)	Facilities [€25k]	Research [€10k]	Production Facilities [€15k]		Facilities [€50k]	Storage [€30k]	Maintenance Facilities [€15k]		**Fixed: €185k Variable: €270.2k**
		Prototyping / Testing [€15k]	Raw Material [€200 / unit]			Processing [€20k]			
	Prototyping Material [€2.5k]		Off-the-Shelf Components [€270k / unit]		Tooling and Machinery [€50k]		Ground Tools and Maintenance Equipment [€10k]		
	Development Tooling and Machinery [€7.5k]		Production Tooling and Machinery [€10k]						
Misc	Utilities [€5k]		Utilities [€10k]		Utilities [€10k]		Utilities [€10k + €2k / unit]		**Fixed: €208.5k Variable: €6k**
	Feasibility Study [€13.5k]				Decommission Support [€10k]		System Improvement [€75k]		
	Future Development Research [€75k]						Product Insurance [€4k / unit]		
Total	**Fixed: €628.5k Variable: N/A**		**Fixed: €35k Variable: €277.7k**		**Fixed: €120k Variable: €4k**		**Fixed: €120k Variable: €181k**		**Fixed: €903.5k Variable: €462.7k**

Figure 12.1: Cost breakdown structure.

Each cost is split up into their respective labor, Property, Plant, and Equipment (PP&E), and miscellaneous costs. In addition, a distinction is made between fixed costs and variable costs. Variable costs are costs made dependent on the number of units produced, while fixed costs are costs made irrespective of this quantity. The methodology for the estimation of each cost is elaborated on in what follows.

12.1.1. Development Cost Estimate

Development costs entail further development of the preliminary design presented by the team to fully realize the product. This requires the following:

- **Labor:** A team of engineers is assumed to further develop the design for 8 hours a day over 255 working days per year [1]. The team consists of two Project Managers, three R&D engineers, and one Prototyping Engineer. Furthermore, a group of four Certification and Testing Engineers collaborate on testing the design, documenting results, and certifying according to regulations. The salary of each engineer is estimated at €25/hour [2].
- **PP&E:** A research (office space) and testing facility is assumed in Rotterdam at €200/m^2 [3], with the facilities being $50\,\mathrm{m}^2$ and $75\,\mathrm{m}^2$ in size. Additional costs account for prototyping materials as well as testing equipment, which namely consists of a drill, press, workbenches, and a tool kit trolley. Office equipment primarily includes desks, computers, monitors, and chairs [4].
- **Misc:** To estimate total utility cost, average utility costs are assumed at €40/m^2 [5]. The feasibility study is assumed to cost approximately 1% of the total project costs [6]. Lastly, future development is assumed to encompass no more than two Engineers and one Manager working at most half a year, with the possibility of later introducing Prototyping and Testing Engineers.

12.1.2. Production Cost Estimate

Production costs encompass all the manufacturing and assembly activities of the verified design. This requires the following:

- **Labor:** Production is assumed to require at least three Product Manufacturers working for €15/hour [2]. At maximum efficiency, one unit is estimated to take one week to manufacture, equivalent to 120 working hours. The produced parts shall be assessed for their quality by four Engineers who perform inspection, testing, and documentation under a similar engineering salary of €25/hour [2]. Furthermore, all production activities shall be overseen by at least one Production Manager. Last but not least, transport of raw material is performed via air freight at a rate of €5/kg [7].
- **PP&E:** The production facility and corresponding tooling is estimated to cost the same as those for the testing facility. The amount of raw material needed to manufacture structural components - recycled aluminum - will be purchased at a market price of €1.10/kg [8] assuming a waste of 16% [9]. The costs for the COTS components have also been added, excluding the cost of the optional LIDAR payload.
- **Misc:** The only miscellaneous item here is utility cost. It is assumed that at least twice as many costs are made on utilities than during development due to the energy-intensive processes.

12.1.3. Management Cost Estimate

Management costs entail handling, warehousing, and distribution of the manufactured products. This requires the following:

- **Labor:** Similar to production, it is assumed that it takes no more than a week for two warehouse workers at €20/hour [2] to properly prepare and distribute a unit to the customer. Meanwhile, two other Assemblers at €15/hour [2] manage any incoming waste and recycle where it is deemed fit. Transport costs are computed similarly to those for production, but now assuming shipping of the complete system.
- **PP&E:** For storage and processing, a facility twice as large as the research and testing facility is assumed. Tools and machinery are equivalent to those for production, but with the addition

[1] https://netherlands.workingdays.org/workingdays_holidays_2024.htm
[2] https://www.payscale.com/research/NL/Country=Netherlands/Salary
[3] https://www.statista.com/statistics/638925/prime-office-rents-in-netherlands-by-location/
[4] https://nl.rs-online.com/web/c/power-tools-soldering-welding/
[5] https://www.cbs.nl/-/media/_excel/2023/08/energy-consumption-offices-netherlands-2019.xls
[6] https://www.whitehutchinson.com/leisure/articles/100.shtml
[7] https://www.freightos.com/freight-resources/air-freight-rates-cost-prices/
[8] https://oudmetaalhandel.nl/en/metal-purchase/aluminium/
[9] https://www.dallan.com/en/news/raw-material-saving-case-study/

of a forklift.
- **Misc:** Miscellaneous items encompass utilities and decommission support. Utility costs are equivalent to those for production. Decommissioning support concerns all costs and expenses devoted to ceasing the operation of the project. While no real cost can be estimated, approximately 10% of the management cost has been allocated to account for such activities.

12.1.4. Operation Cost Estimate
Operation costs entail all costs with respect to the infrastructure required in order to support the operation of the product. This requires the following:

- **Labor:** Two Operators working for €35/hour are required to operate a unit in the ground station for three days a week, as well as an Operation Manager at €25/hour [2] who oversees all operation processes. Each employee is also given a one-week training course to learn how to work with the system. Furthermore, maintenance checks are performed by a Maintenance Engineer working at €25/hour [2] at varying levels of frequency and thoroughness: superficial 1-hour pre- and post-flight checks, proper 8-hour system inspections after every 100 flight hours, and rigorous 16-hour maintenance checks performed annually. An aircraft license for operation in airspace is considered negligible and the UAV is exempted from any other charges as it would likely fall under ”humanitarian flight” [10]. However, fees for the use of communication frequencies do have to be accounted for, both for operation in the radio frequency spectrum in shared airspace [11] as well as service costs for communication with the O3b satellite network [12].
- **PP&E:** Maintenance is performed in a hangar of similar size and with similar tooling to those for production.
- **Misc:** Utilities are similar to those for production and management, with the addition of ground station energy usage and used Jet-A1 fuel [12]. UAV insurance is assumed higher than average for drones as the system is involved in complex operations and exposed to large risks [13]. While further system improvement cannot be estimated, it is assumed that implementation will not cost more than costs allocated for future development research.

The project-level expenditures calculated in the CBS are therefore summarized in Table 12.1.

Table 12.1: Total fixed and variable capital and operating expenses for the FLOWS product.

	Capital Expenditures	**Operating Expenses**
Fixed	€783.5k	€120.0k
Variable	€281.7k	€181.0k

12.2. Business Plan Evaluation
Following the results presented in Table 12.1, two business plans are presented below. For each program, the financial ambitions are presented, and it is shown how these feed back into the unit price.

Model 1: Non-Profit Program
The first model presents the scenario for a non-profit organization that aims to provide the lowest possible product costs for its customers. In this case, the lowest possible unit price equals the variable capital expenditures: **€281.7k**. The annual fixed capital expenditures, **€783.5k**, will have to be covered either by subsidies or partners, as there are no incoming revenues.

[10] https://eaip.lvnl.nl/web/2023-04-06-AIRAC/html/eAIP/EH-GEN-4.2-en-GB.html
[11] https://wetten.overheid.nl/BWBR0048814/2024-01-01/0
[12] https://jet-a1-fuel.com/jeta1
[13] https://www.skywatch.ai/blog/how-much-should-your-drone-insurance-cost

Model 2: Commercial Program

The second model presents the scenario for a for-profit organization that aims to make a profit from the sale of the FLOWS product. While the organization will initially have a net loss of **€783.5k**, this will diminish over time as more units are sold. For a unit price of **€300.0k**, a profit margin of €18.3k is realized. Consequently, the break-even point - which is the point at which zero profit is made - will be reached after 43 units are sold. These results are also visualized in Figure 12.2 below.

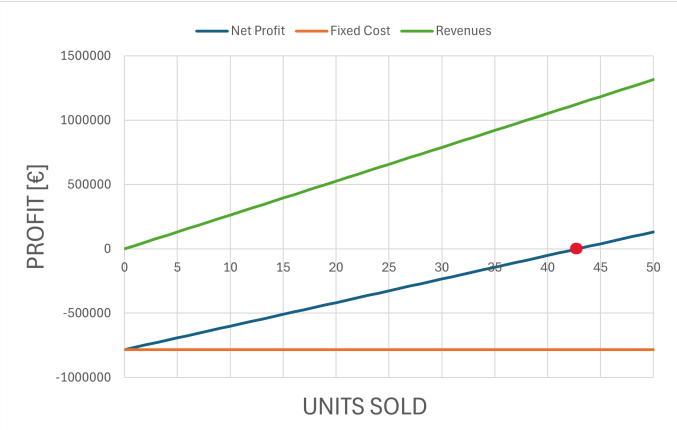

Figure 12.2: Fixed cost, revenues, and net profit versus units sold.

12.3. Product and Niche Definition

The designed product is defined as an integrated flood monitoring and intervention system composed of an unmanned aerial vehicle and its ground station. As justified in Chapter 13, the system demonstrates functionalities in water level monitoring, riverbed topography monitoring, debris identification, stationary flood control system monitoring, and humanitarian aid delivery.

The flood monitoring data obtained by the system has three main functions: data-driven flood modeling, rapid decision-making for flood warning, and damage assessment. Up-to-date information about current conditions and waterborne debris can be transmitted directly to first responders, allowing for swift planning of rescue operations. Furthermore, the flexible intervention payload allows for open-ended missions to be designed to support ground-based intervention.

The system performs several interconnected functions, thus operating as a breakthrough product in several markets:

1. **Flood Monitoring**
   Currently, the flood monitoring system market is dominated by stationary sensors, developed for mounting in fixed locations (rivers, roads, storm drains, coasts, railways etc). Several suppliers for such systems exist, providing both individual sensors and integrated sensor and data handling solutions. Companies such as Xylem[14], Linkwise[15], and World Sensing[16] routinely offer Internet of Things (IoT)-based flood monitoring services. These systems lack flexibility and require significant initial investment, as well as decentralized maintenance for sensors, some of which may be mounted in remote locations. Furthermore, they rely on proprietary infrastructure, thus locking the customer into the use of their specific system.
   Recently, UAV systems have begun to be used for specific monitoring functions in flood situations, such as for railway monitoring or cellular towers. However, in such cases, vehicles deployed for these use were small-scale repurposed all-purpose drones[17].

[14] https://www.ysi.com/applications/flooding
[15] https://linkwisetech.com/applications/flood-monitoring-system/
[16] https://www.worldsensing.com/flood-monitoring/
[17] https://www.boldbusiness.com/digital/drone-use-in-houston-flood/

2. **Riverbed Topography**
   Current riverbed topography monitoring systems rely on ground or waterborne LiDAR, or more rarely airborne LiDAR based on small general aviation aircraft. These systems require significant investment and high setup time, leading to low flexibility. Bathymetric (underwater topography) studies with UAV systems are so far restricted to technology demonstrators with retrofitted commercial drones in research contexts [75].
3. **Flood Response**
   Intervention and response during extreme weather events are usually performed by first responders and emergency (military and civilian) services, using traditional infrastructure: rescue boats, helicopters, and response crews. Debris identification is also performed by first responders visually. No dedicated autonomous airborne intervention systems exist on the market.

The capabilities analysis provides a clear starting point for the assessment of the demand for such a product, with customers interested in any of these three capabilities representing the focus of the market study.

12.4. Customer Case Studies

In the aerospace industry, typical assessments of the market for a certain product involve the study of the total addressable market (TAM), serviceable available market (SAM), and serviceable obtainable market (SOM)[18]. The TAM-SAM-SOM model allows for a quantitative analysis of the existing and projected market for a product to be performed, resulting in values for the market size and budgets. This approach was deemed unfeasible for the FLOWS product, for the following reasons:

1. No market currently exists for airborne integrated flood monitoring and response systems. Any projection of the market demand would inevitably require unsupported assumptions.
2. The design team is limited in both time and econometric modeling capabilities.
3. Due to the typically prohibitive initial capital expenditure of these capabilities, their importance to saving human lives, and their typical lack of profitability, these systems are universally managed by public institutions, such as the German Umwelt Bundesamt (Federal Environment Agency) or the Bangladeshi Ministry of Disaster Management and Relief. This results in different economic perspectives when compared to the private market (quotes, sustainability audits, budgetary accountability).

Therefore, to obtain insights into the available market, a small-scale case study assessment method was chosen. The total addressable market is represented in a qualitative manner in Figure 12.3, based on the public/private distinction.

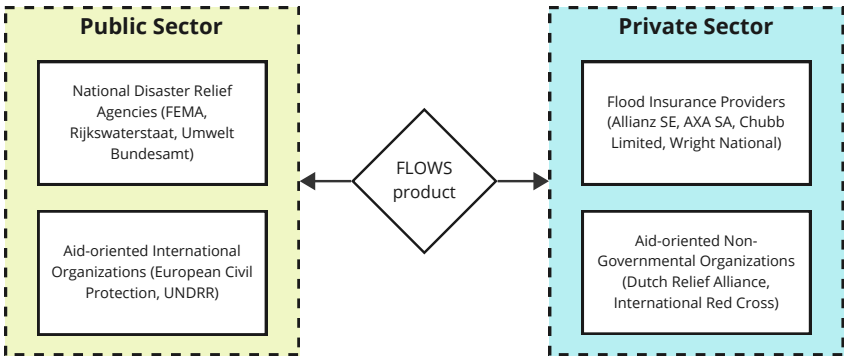

Figure 12.3: Qualitative total addressable market.

[18] https://www.thebusinessplanshop.com/blog/en/entry/tam_sam_som

Four case studies, one for each case in Figure 12.3, were performed. They are discussed in what follows.

12.4.1. Case Study 1: Federal Emergency Management Agency

Part of the United States Department of Homeland Security, the Federal Emergency Management Agency (FEMA) coordinates the response to disasters that occur in the territory of the United States[19]. FEMA is only allowed to respond if the disaster overwhelms local and state response authorities. The Agency also provides these authorities with experts in specialized fields and funds for response personnel training, and directs individuals and small businesses to low-interest loans for rebuilding.

FEMA headquarters hosts the National Response Coordination Center (NRCC), which supports operations during major disasters and emergencies at a regional level[20]. In the NRCC, the Agency collaborates with other authorities to focus on projected, potential, or escalating crises, ensuring resource deployment to the affected area, as shown in the coordination diagram in Figure 12.4[21]. One of the resources uniquely available to FEMA is represented by Mobile Emergency Response Support (MERS) teams, which provide communications support to local public safety, allowing first responders to communicate with the outside world[22].

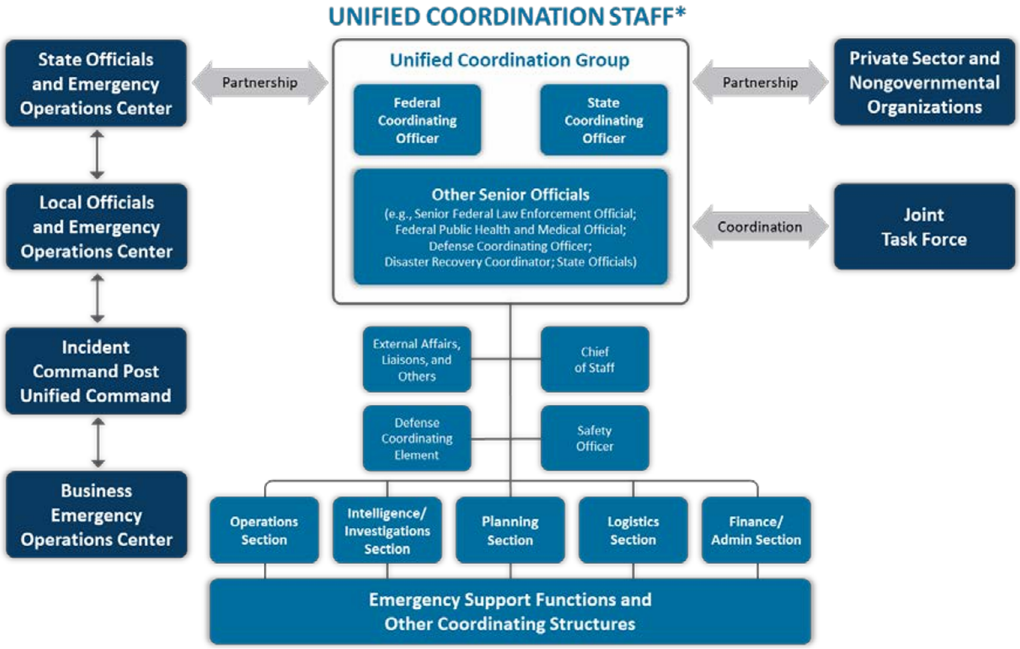

Figure 12.4: FEMA response coordination framework.

It may be observed that both the top-level objectives of the Agency and its Emergency Support Functions (ESF's) correlate well with the functionalities provided by the product[23]. The FLOWS system allows for high-endurance monitoring of disasters, delivering critical information to the NRCC (ESF 5). Furthermore, in support of MERS teams, the airborne segment may be fitted with a transponder link, extending the range of communications for first responders (ESF 9).

FEMA and its subsidiaries already have experience with UAV-collected data on flood damage. In collaboration with local disaster response authorities, infrastructure engineering firm Bolton & Menk

[19] https://www.fema.gov/about

[20] https://www.fema.gov/press-release/20210318/fema-activates-national-response-coordination-center-preparation-hurricane

[21] https://www.fema.gov/emergency-managers/national-preparedness/frameworks/response

[22] https://www.fema.gov/about/offices/field-operations/disaster-emergency-communications

[23] https://www.fema.gov/emergency-managers/national-preparedness/frameworks/response#esf

deployed two FPV UAV's to monitor flood levels and damage during the 2019 flooding of Jordan, Minnesota[24]. This monitoring allowed first responders to better prioritize resources, and, beyond the initial response phase, allowed for documentation of the extent of flood damage, important for federal relief funding and insurance documentation (as discussed in the third case study).

From a business perspective, FEMA Industry Liaison Program requires the submission of a Vendor Profile Form, which describes the capabilities of the product[25]. With a total procurement budget of $190M over FY2023, and grants for the Flood Hazard Mapping and Risk Analysis Program worth a total of $350M, the Agency shows significant financial resources, allowing for the possible purchase of several dozen FLOWS units and distribution to MERS teams and state-level response authorities[26].

12.4.2. Case Study 2: United Nations Office for Disaster Risk Reduction

The United Nations Office of Disaster Risk Reduction (UNDRR) leads the United Nations effort in the coordination of disaster risk reduction, building relationships between national governments, intergovernmental organizations, and the private sector[27]. The UNDRR works within the 2015-2030 Sendai Framework for Disaster Risk Reduction, a set of targets and action points designed to protect development gains from the risk of disaster.

One of the UNDRR's core objectives is mobilizing financing for climate resilience and adaptation projects[28], with a total budget of $53.5M over FY2023, and no less than $5M in procurement grants from the European Union alone[29]. Given the relatively low unit cost of the FLOWS system, these grants could allow for the purchase of several units, operator training, and service of risk-prone areas in the developing world.

12.4.3. Case Study 3: Allianz SE

Allianz SE is a German multinational insurance and asset management company and is the largest financial services company in Europe[30]. The company is an early adopter of using drones to assess post-disaster damage, especially at sites unsafe for humans to enter. Just in 2017, Allianz Global Corporate & Specialty, the corporate insurance subdivision, managed 52 drone flights in areas affected by natural disasters such as Hurricanes Maria and Harvey[31].

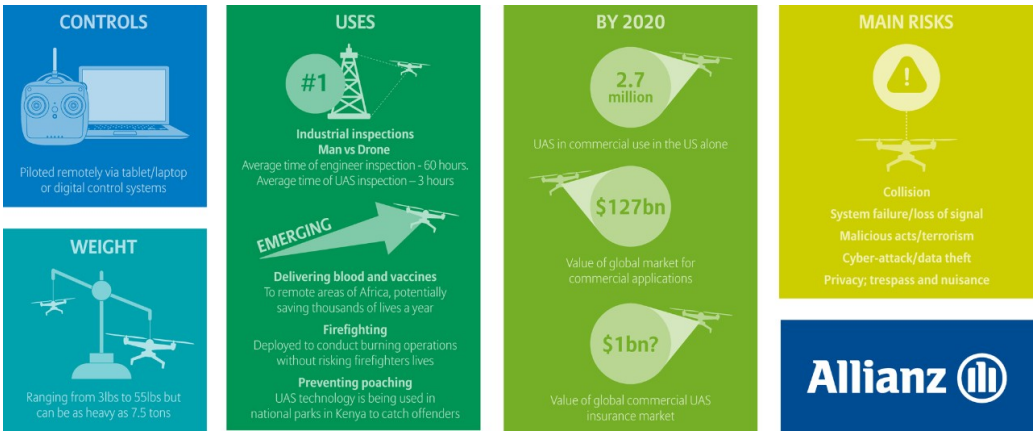

Figure 12.5: Allianz material on drone use.

[24] https://storymaps.arcgis.com/stories/a7cf393b38a44ae0a457b916995392fa
[25] https://www.fema.gov/business-industry/doing-business
[26] https://www.dhs.gov/publication/congressional-budget-justification-fiscal-year-fy-2023
[27] https://www.undrr.org/our-work
[28] https://www.undrr.org/financing-prevention
[29] https://www.undrr.org/about-undrr/funding
[30] https://www.allianz.com/en/about-us/company.html
[31] https://www.allianz.com/en/press/news/commitment/environment/190912_Allianz-drones-and-hurricanes-flying-masters-of-disasters.html

Until 2016, insurance companies in the United States were required to petition the Federal Aviation Administration for permission to use UAV's for damage assessment, with a complex legal process[32]. After the liberalization of the regulations, the use of FPV drones after national disasters exploded, in order to track and monitor hundreds to thousands of insurance claims. Insurers can also make use of drone maps, which create a common set of data and a clear record of the damage[33].

From an economic perspective, AGCS shows a strong asset base of more than $13B[34] for FY2023. Its massive financial resources allow for the possible purchase of several FLOWS units, which can be transported out to areas affected by disasters as required.

12.4.4. Case Study 4: Dutch Relief Alliance

The Dutch Relief Alliance (DRA) represents a coalition of 14 Dutch humanitarian non-governmental organizations working together with the Ministry of Foreign Affairs[35]. These partners coordinate their efforts through Joint Responses, which can be tailored to both acute and protracted crises. This dual response mode allows for both fulfilling a spike in need in 72 hours and sustainable longer-term responses with predictable multi-year funding.

The DRA works in eight intervention sectors, as shown in Figure 12.6: education, health, nutrition, shelter, food security, cash assistance, protection, and water, working with local partners to deliver humanitarian aid where it is most needed[36]. This approach correlates with the intervention payload capabilities of the FLOWS system, unlocking new opportunities for critical aid deliveries during acute crises.

Figure 12.6: Dutch Relief Alliance aid breakdown.

With a total budget of more than $70M over FY2022, the DRA mobilizes millions of dollars for each acute crisis response, providing aid to local communities during droughts and hurricanes[37]. The purchase of a FLOWS system would allow the Alliance to directly support these communities during a flood event, then easily relocate to where these capabilities are most needed.

12.5. Product-Market Fit

The FLOWS system represents a novel flood monitoring and response architecture, showing far higher flexibility when compared to static flood monitoring sensor arrays, while also incorporating dedicated intervention capabilities. As observed in the case studies above, the estimated unit cost of

[32] https://www.cbinsights.com/research/drone-property-insurance/
[33] https://www.dronedeploy.com/blog/dronotec-hurricane-irma
[34] https://commercial.allianz.com/about-us/financials.html#annual
[35] https://dutchrelief.org/about-us/
[36] https://dutchrelief.org/downloads/
[37] https://dutchrelief.org/wp-content/uploads/2023/11/Annual-Report-2022.pdf

$300k fits well within the procurement capabilities of the assessed organizations. Furthermore, due to its versatility, the product's capabilities correlate with the mission and needs of each customer, resulting in a high product-market fit. The conclusions of the economic assessment have been synthesized in the SWOT diagram in Figure 12.7.

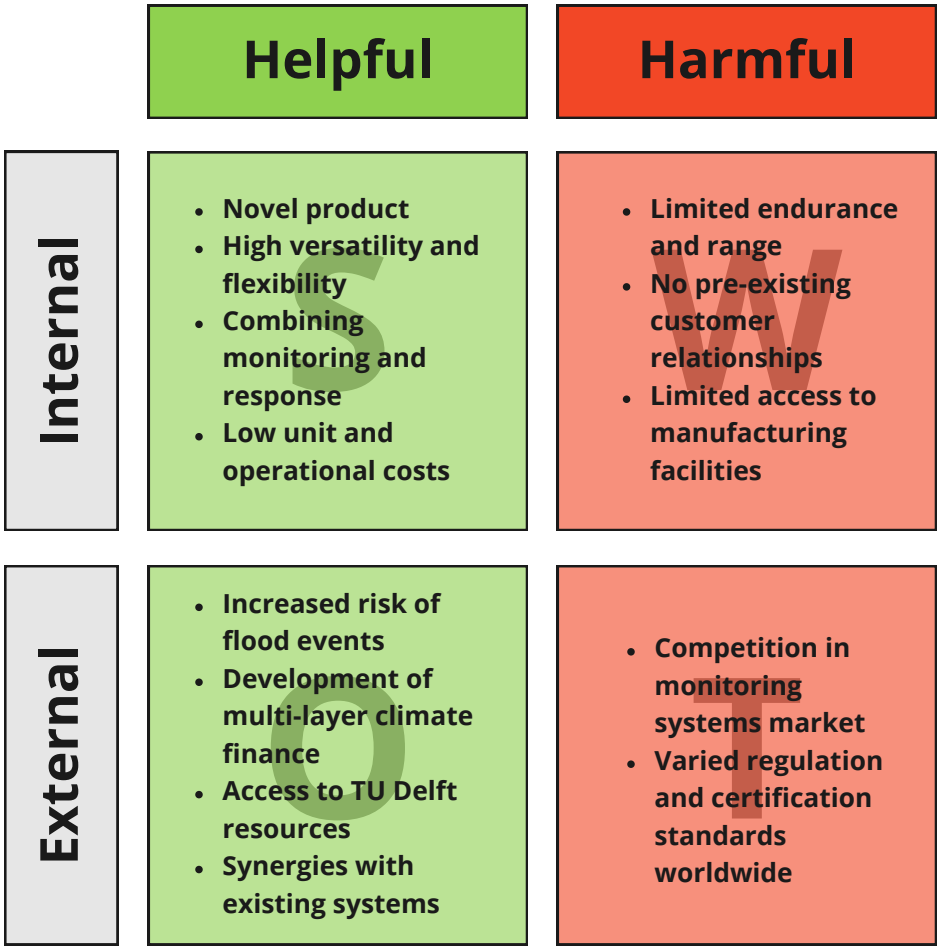

Figure 12.7: Market analysis conclusions in SWOT form.

This economic assessment has provided insights into the needs of the projected customers and allowed for a better understanding of the market niche filled by the FLOWS system. However, the qualitative and empirical nature of the case study methodology means that significant quantitative insights have not been obtained. For further development, it is recommended to incorporate econometric analyses, identifying customer classes in order to develop a robust market segmentation following the TAM-SAM-SOM model.

13 | Final Design

This chapter shows the final layout of the airborne system. Section 13.1 shows the final geometry including a 3-view drawing, the internal layout of the fuselage, a list of parts, and the hardware and software diagrams. Section 13.2 shows a final drag polar analysis. Section 13.3 explains the necessary fuel for the different missions. Subsequently, Section 13.4 illustrates the final payload range diagram of the UAV. Section 13.5 discusses the final design and its possible discrepancies. The integration strategy of subsystems is explained in Section 13.6. The requirements are verified in Section 13.7 and the budget breakdown of the mass, power, and cost is explained in Section 13.8. Finally, the functional flow and breakdown diagrams are shown in Section 13.9.

13.1. Final Airborne Segment Layout

The final aircraft configuration consists of a main wing with a twin boom configuration. Each boom has an individual empennage. A pusher propeller provides the thrust required during horizontal flight while four vertical propeller provide the capability to take-off, hover, and land vertically. The final MTOM is $272.1\,\mathrm{kg}$ and the OEM is $230.2\,\mathrm{kg}$. An overview of the OEM can be seen in Table 13.2.

13.1.1. External Geometry and 3-view Drawing

The exact geometry parameters for the final design are given in Table 13.1. A 3-view technical drawing, shown in Figure 13.1, depicts the aircraft configuration from the front and back, side, top, and an isometric view.

Table 13.1: Table of the final design geometry. *Span for horizontal and vertical stabilizers are given as distance from root chord to tip chord. **Full-length of the fuselage from tip of pitot tube to tip of pusher propeller spinner.

Wing geometry	**Wing**	**Horizontal stabilizer**	**Vertical stabilizer**
Aspect ratio	20	5	2
Taper ratio	0.4	0.5	0.5
Quarter chord sweep	0°	5°	20°
Dihedral	-1.5°	0°	0°
Wingspan	$9.89\,\mathrm{m}$	$0.421\,\mathrm{m}$*	$0.861\,\mathrm{m}$*
Root chord	$0.706\,\mathrm{m}$	$0.112\,\mathrm{m}$	$0.574\,\mathrm{m}$
Fuselage geometry		**Propeller geometry**	
Length	$3.51\,\mathrm{m}$**	VTOL blade diameter	63” ($1.6\,\mathrm{m}$)
Maximum diameter	$0.59\,\mathrm{m}$	Pusher blade diameter	$1.4\,\mathrm{m}$
Cylindrical diameter	$0.568\,\mathrm{m}$	Pusher blade pitch 0.7R	28°
Landing gear geometry		**Boom geometry**	
Ground clearance	$0.51\,\mathrm{m}$	Length	$5.39\,\mathrm{m}$
Wheel diameter	11.5”	Diameter	0.15
Scrape angle	13.3°	Maximum bulge diameter	$0.288\,\mathrm{m}$

A final note should be given on the scrape angle of the aft landing gear. Originally, this was planned as 15°, however, this resulted in the fuselage requiring a bulge to lower it further. Measuring the scraping angle in the configuration without a bulge yields a result of 13.4°, which still fits within the acceptable range of 12° to 15° [39], without adding unnecessary structural mass and drag due to the structural reinforcement.

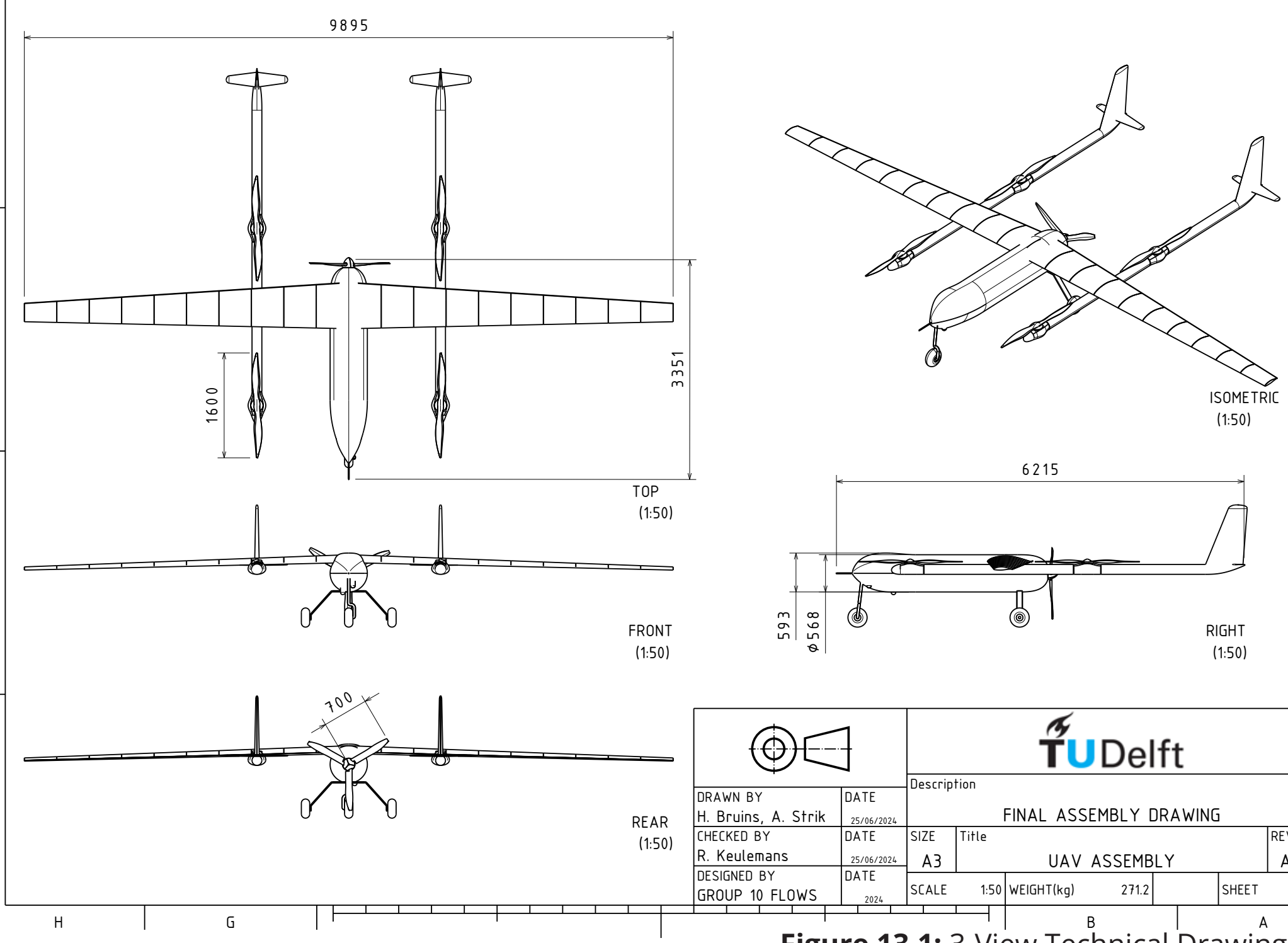

Figure 13.1: 3-View Technical Drawing

13.1.2. Internal Layout

Most of the internal components within the UAV are fit into the fuselage. This layout has been created using the motivations and reasoning presented in Chapter 8, and is presented in a cross section in Figure 13.2. The different components within are described below the figure.

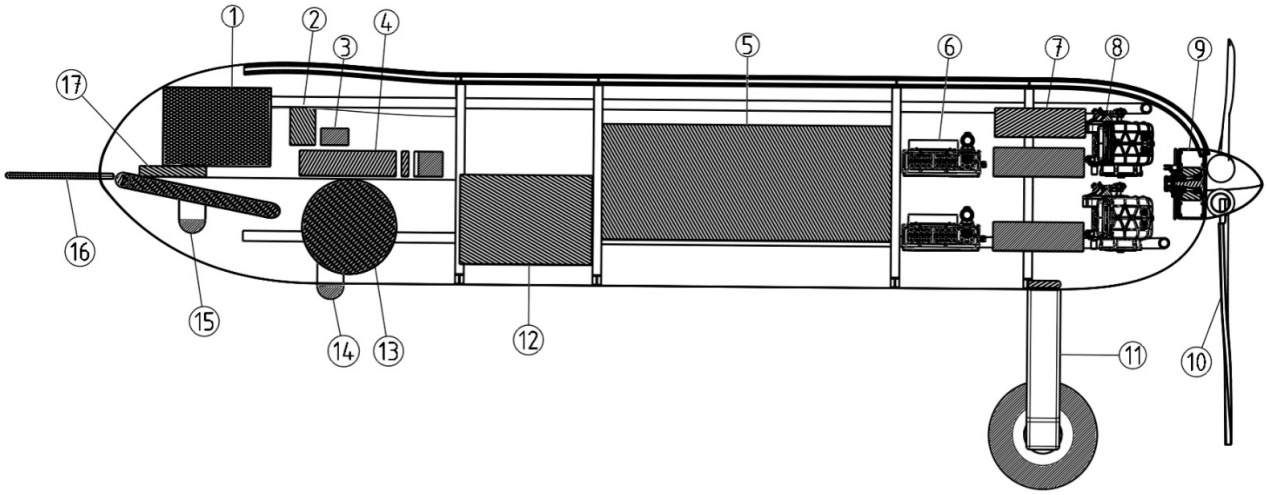

Figure 13.2: A graphic representation of the fuselage cross section, showing the various internal components.

1. SATCOM Communication System
2. Compression Computer for LiDAR Data
3. Flight and Mission Computer
4. Electrical Subsystem (Multiple Components)
5. Intervention Payload Bay
6. ICE Controller
7. Electronic Speed Controller
8. Internal Combustion Engine and Generator
9. Electrical Motor (Pusher Engine)
10. Pusher Propeller
11. Non-retractable Main Landing Gear
12. Bathymetric LiDAR
13. Retractable Nose Landing Gear
14. Monitoring Camera (Photogrammetry)
15. Operator UAV Control Camera
16. Pitot Tube
17. Direct link Radio Communication System

13.1.3. Component List

In this section, an overview is given of all selected and designed parts for the designed UAV. For each part, Table 13.2 shows the identifier, the part and its technical name (as given by the manufacturer), the amount of parts used. It also provides technical details such as mass, peak power and a cost estimate. Note that negative power means that power is used, while positive power means it is produced.

The identifiers are divided into subsystems, including Payload (PLD), Attitude Determination and Control (ADC), Avionics (AVI), Command and Data Handling (CDH), Power and Propulsion (PROP), Landing Gear (LG), Electronics (ELEC), and Structural (STR). As the structures are not COTS components, these do not have a name or a value for the cost.

Table 13.2: Overview of the selected and designed components of the UAV.

Identifier	Part	Name	Qty	Mass [kg]	Power [W]	Cost [€]
FL-PLD-1	Monitoring Camera	Trillium HD25-LV	1	0.34	-75	5,190
FL-PLD-2	LiDAR	Riegl VQ-840 GE	1	9.5	-220	1,000,000
FL-PLD-3	Compression Computer	Saab RVC-E	1	1.2	-25	2,500

Continued on next page

Table 13.2: Overview of the selected and designed components of the UAV (continued).

Identifier	Part	Name	Qty	Mass [kg]	Power [W]	Cost [€]
FL-PLD-4	Payload Bay	N/A	1	31.7	N/A	N/A
FL-PLD-5	Payload Bay Servo	SD-01B	1	1.5		500
FL-ADC-1	Control Camera	Trillium HD25-LV	1	0.34	-75	5,190
FL-ADC-2	Mission Computer	Vector MCC	1	0.16	-2.5	2,000
FL-ADC-3	Wing Servo	SD-01B	2	1.5		500
FL-AVI-1	Pitot Tube	Airmobi Long Pitot Tube	1	0.2	N/A	111
FL-AVI-2	AoA Vane	SMV-1 Flow Vane	1	0.03	-0.67	1,000
FL-AVI-3	Flight Computer	Vector 600	1	0.18	-2.5	3500
FL-CDH-1	Radio Link	Swiftlink P43 A2G	1	0.42	-90	18,592
FL-CDH-2	SatCom System	MICRO SAT LW	1	4.2	-25	125,000
FL-PROP-1	ICE Generator	RW79	4	4.87	+16,128	15,500
FL-PROP-2	ICE Controller	RW79	4	4.13	N/A	N/A
FL-PROP-3	Vertical Motor	EMRAX188 (AC)	4	7.1	-15,000	4,000
FL-PROP-4	Vertical Propeller	FLUXER PRO 63x22	4	1.08	N/A	725
FL-PROP-5	Horizontal Motor	EMRAX188 (CC)	1	7.6	-37000	4,000
FL-PROP-6	Horizontal Propeller	TU Delft X-PROP	1	3.5	N/A	N/A
FL-PROP-7	Electronic Speed Controller	AMPX-90A	4	1.8	0	1,914
FL-LG-1	Nose Landing Gear	Aerotelemetry Light-Weight UAV landing gear	1	9.1	N/A	1,500
FL-LG-2	Main Landing Gear		1	12	N/A	1,500
FL-ELEC-1	Power Distribution Unit	VISIONAIRtronics 1800W dual PDU	1	2.7	N/A	1,000
FL-ELEC-2	Backup Battery	MaxAmps Li-ion 2800 10S1P	1	0.48	+396	194
FL-ELEC-3	Microchip	ATmega16M1-MU	1	<0.001	-1.65	6
FL-ELEC-4	Power Module	Wurth Elektronik 173950378	1	0.002	-12	6
FL-ELEC-5	Power Module	Wurth Elektronik 173011235	1	0.002	-60	5
FL-ELEC-6	Battery Manager	VISIONAIRtronics 15S BMSB	1	N/A	N/A	300
FL-ELEC-7	Wire Harness	N/A	1	22	N/A	N/A
FL-STR-1	Fuselage Longerons	N/A	5	2.08	N/A	N/A
FL-STR-2	Fuselage Frames	N/A	5	1.04	N/A	N/A
FL-STR-3	Fuselage Skin	N/A	1	6.22	N/A	N/A
FL-STR-4	Component Mounting	N/A	1	8.44	N/A	N/A
FL-STR-5	Wingbox Structure	N/A	1	19.55	N/A	N/A
FL-STR-6	Wing Skin	N/A	1	5.46	N/A	N/A
FL-STR-7	Wing Rib Structure	N/A	1	2.78	N/A	N/A
FL-STR-8	Boom Structure	N/A	2	8.7	N/A	N/A
FL-STR-9	Empennage Structure	N/A	2	2.5	N/A	N/A

13.1.4. Hardware and Software Block Diagrams

The hardware block diagram given in Figure 13.3 describes the schematic architecture of the aircraft, including components of monitoring, intervention, data handling, and other instrumentation payload. Each block represents a hardware element, with the arrows indicating the relation between the various subsystems in the UAV. Some arrows indicate a stream of data (e.g. the visual camera providing camera data to the flight computer), whilst others indicate how one hardware item controls another (e.g. the PDU sending an electrical signal to each servo that controls their respective control surface).

The monitoring subsystem has two sets of HD25-LV cameras: one for monitoring, the other for pilot vision to remotely control the UAV. Each of the sets will sample data at a specific frequency, which is to be processed together with other sensor data by the VECTOR-600 flight computer. The flight computer may store data to an internal hard drive in case of loss of communications, which can be accessed after completion of the mission. The flight computer may also receive and transmit signals via either of the antennas that will be installed onto the UAV (i.e. the Swiftlink P43 for a direct link, the Micro SAT LW for communication via satellite) in order to communicate with the ground station.

The avionics mainly consists of the VECTOR-600, which has an internal Air Data, Attitude, and Heading Reference System (ADAHRS). The ADAHRS is composed of attitude *sensors* like an accelerometer, gyroscope, a GPS, and a magnetometer to determine the UAV's attitude. Whether controlled automatically or manually, aircraft control messages can subsequently be sent from the flight computer to the PDU to demand a specific control surface orientation from the servos or power rating from the engines.

The software block diagram given in Figure 13.4 concerns the logic of the software that will be integrated into the flight computer across the duration of the mission and is written in one of the many types of UML diagrams - a State Machine Diagram, which depicts the states of the system (take-off, cruise, monitoring, landing, etc) and determines in which state the UAV will be. The filled circle marks the beginning of the mission, whereas the dotted circle marks the end of the mission. Then, with very simplified if-statements marked in bold, the system moves from one state to the next by performing the actions listed along the arrow. An additional circle filled with a diamond helps visualize the relation between the UAV and external systems with regards to received commands and telemetry.

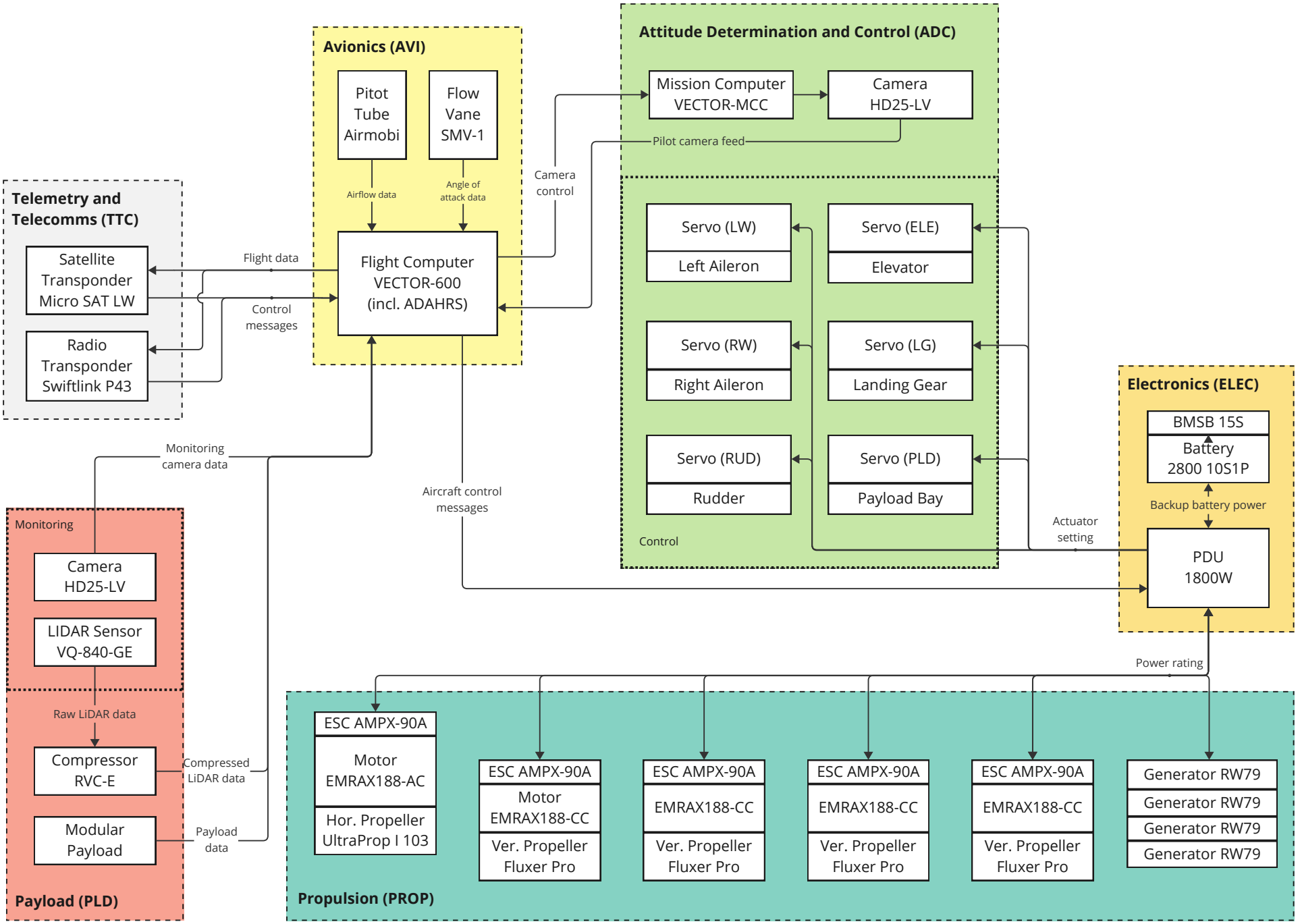

Figure 13.3: Hardware Diagram

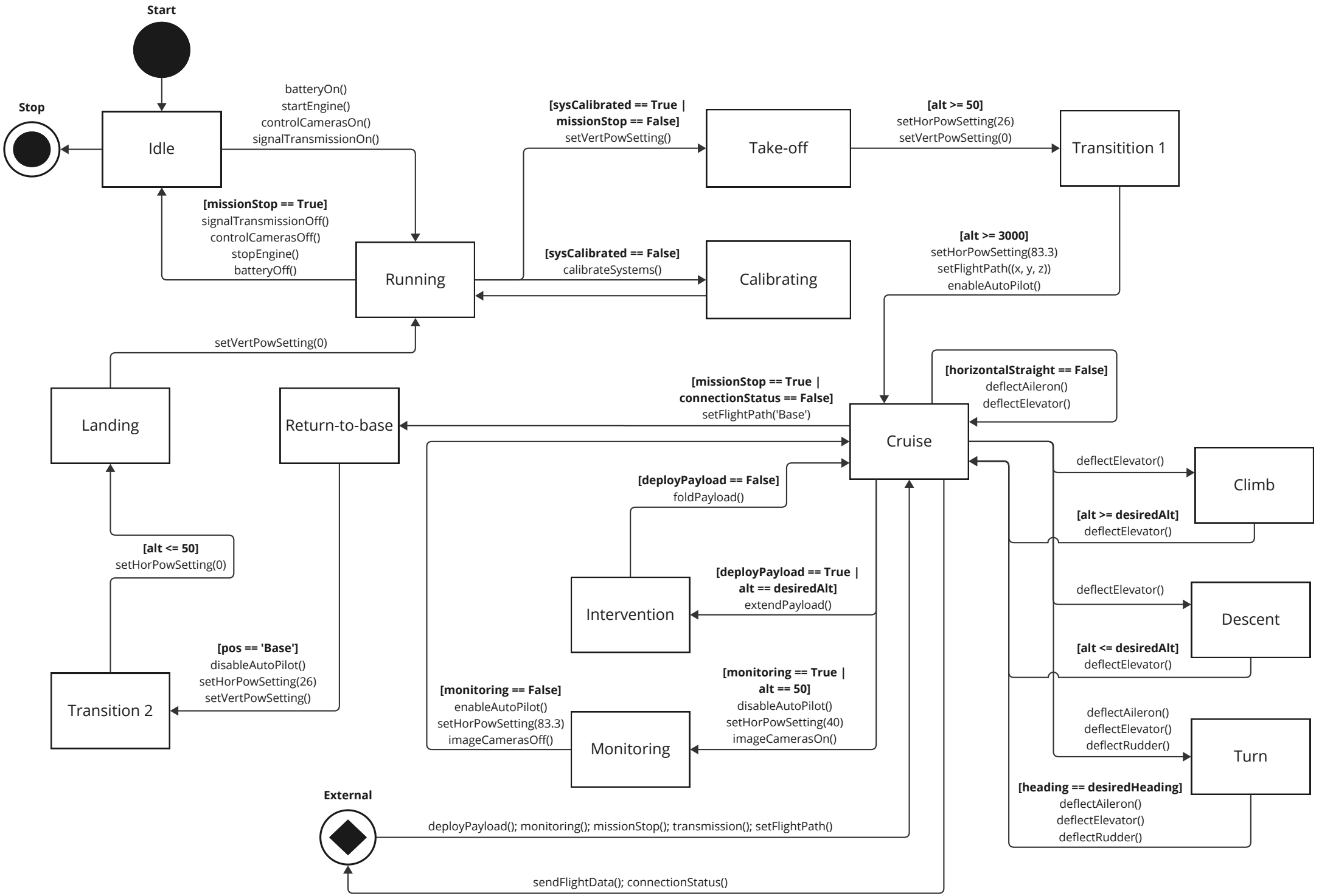

Figure 13.4: Software Diagram

13.2. Final Aerodynamic Analysis

The aerodynamic performance of the aircraft is incredibly important to the FLOWS mission, as it requires both high endurance and high velocities to be achieved. The values for the dimensionless lift and drag coefficients were found with an aerodynamic analysis using the vortex lattice method in OpenVSP. This method is useful for finding change the induced drag and the parasitic drag of large surfaces such as the fuselage. However, since the propellers for VTOL and the exposed landing gear add significant drag, another method for estimating the zero-lift drag coefficient C_{D_0} was used. An estimation of this C_{D_0} was calculated using using a method for finding the drag of stopped propellers by Raymer combined with CFD data from VSPAero [76]:

$$C_{D_{0_{prop}}} = \frac{C_{D_{\text{prop}}}^{\text{MR}} S_{\text{prop}}^{\text{MR}}}{S_{total}} \tag{13.1}$$

$$C_{D_{\text{prop}}}^{\text{MR}} = 0.1 \frac{N_{\text{blades}} c_{\text{blade}}}{\pi r_{\text{pro}}} \tag{13.2}$$

$$\frac{S_{\text{prop}}^{\text{MR}}}{S_{total}} = \frac{0.288 \cdot 4}{11.82} = 0.0014 \tag{13.3}$$

$$C_{D_{\text{prop}}}^{\text{MR}} = 0.1 \frac{3 \cdot 0.12041}{\pi \cdot 0.8} = 0.0144 \tag{13.4}$$

Equation 13.1 and Equation 13.2 account for the drag of the VTOL propellers during horizontal flight, which is combined with the zero lift drag coefficient of the aerodynamic analysis in OpenVSP for a model without propellers. The simulated zero lift drag coefficient was found to be $C_{D_0} = 0.0145$. Finally, the parasitic drag contribution of the landing gear was added. This was estimated using empirical data as 19% of the total C_{D_0} [77]. The final value obtained is shown in Equation 13.5.

$$C_{D_0} = \frac{0.0145 + 0.0014}{1 - 0.19} = 0.0196 \tag{13.5}$$

This value for the zero lift drag coefficient was used to offset the induced drag found by OpenVSP to construct the total drag polar. The drag polar is presented in Figure 13.5 and the relation between $C_L^{3/2}$ and C_D is given in Figure 13.6.

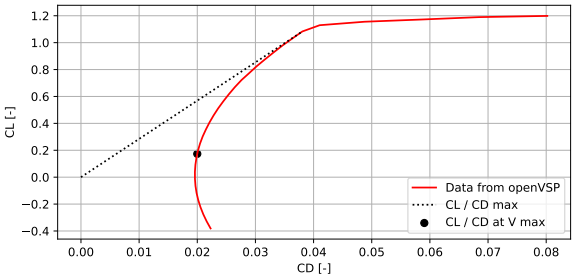

Figure 13.5: Relation between C_L and C_D.

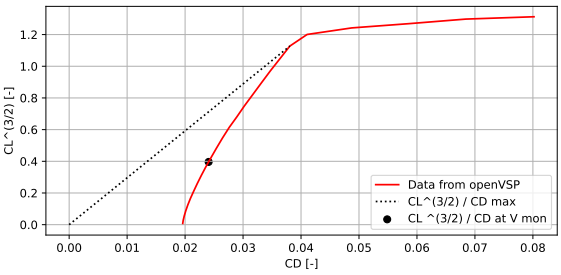

Figure 13.6: Relation between $C_L^{3/2}$ and C_D.

In both figures, the maximum slope is also shown, as this is the flight condition at which maximum range and endurance are obtained. However, since the range of $200\,\text{km}$ must be traveled at $300\,\text{km/h}$, the actual value used is lower than this optimum, causing a decrease in efficiency. Similarly, in Figure 13.6, the flight conditions used for the monitoring mission are considered sub-optimal. This was done to allow for control in rough weather, as the optimum flight condition would have a velocity very close to the stall speed.

The aerodynamic performance of the aircraft is summarized in Table **??**. Due to the sharp angle, the drag polar makes for C_L values above 1.0 the maximum lift over drag occurs at the same lift and drag coefficients as the maximum $C_L^{3/2}$ over drag. It is important to note that the maximum lift coefficient was found to be 1.26 (not shown in Figure 13.5) which means that the stall speed is slightly higher than $26\,\text{m/s}$. For fuel mass calculations a monitoring speed of $41\,\text{m/s}$ was used to make sure that the calculations allow for a wind resistance of more than $14\,\text{m/s}$.

Table 13.3: Summary of aerodynamic performance at most important flight conditions.

Flight Condition	Velocity	Altitude	C_L	C_D	C_L/C_D	$C_L^{3/2}/C_D$
monitoring	$41.00\,\mathrm{m/s}$	$150\,\mathrm{m}$	0.5393	0.0241	22.38	16.46
max velocity	$83.33\,\mathrm{m/s}$	$3000\,\mathrm{m}$	0.1734	0.0200	8.67	3.610
max C_L/C_D	$28.88\,\mathrm{m/s}$	$150\,\mathrm{m}$	1.0831	0.0381	28.45	29.61

13.3. Fuel Mass Calculations

The performance of the design is measured by its capability to perform the two missions defined in Chapter 9, and, if one of the missions can be performed with a take-off mass less than the MTOW, its performance can even exceed the required performance.

The fuel mass required for both missions involves calculations for VTOL maneuvers, power consumption of instruments and fuel for horizontal flight at different speeds. The fuel needed for VTOL maneuvers is calculated simply by calculating the power required for vertical climb at maximum vertical thrust and thus maximum vertical rate of climb. This power is obtained by multiplying the weight of the aircraft by a factor of 1.2, from requirement **RPR-PRP-1**, and reading the power consumption from the data table in Figure 4.2.

Then, the power consumption of all energy consuming instruments during the maneuver is added to this power to obtain the total power consumption. All VTOL maneuvers are assumed to be 160 seconds of pure climb at sea level. This means that the total fuel mass calculated is conservative as most VTOL maneuvers will not consist of pure climb (e.g. landing maneuvers).

Next, this power is converted to fuel mass required by multiplying it with the Brake Specific Fuel Consumption (BSFC), given by the manufacturer as $255\,\mathrm{g/kWh}$, and the duration of the maneuver. The weight and thus the power consumption are assumed to be constant during these maneuvers. In a similar way, the power consumption of instruments during horizontal flight is calculated. However since the fuel mass, and thus the weight of the aircraft, changes during flight a different method is required. For this, Equation 13.6 and Equation 13.7 are used, rewritten such that the fuel weight is calculated [78].

$$R = \frac{\eta_p}{c_p}\frac{C_L}{C_D}\ln\left(\frac{W_{fin}+W_{fuel}}{W_{fin}}\right) \quad (13.6) \qquad E = \frac{\eta_p\sqrt{2\rho S}}{c_p}\frac{C_L^{3/2}}{C_D}\left(\frac{1}{\sqrt{W_{fin}}}-\frac{1}{\sqrt{W_{fin}+W_{fuel}}}\right) \quad (13.7)$$

Now, using Breguet's range equation shown in Equation 13.6, the range is calculated with the propulsive efficiency η_p, the BSFC c_p, the lift over drag ratio at a certain airspeed and altitude $\frac{C_L}{C_D}$, and finally the weight at the beginning of the horizontal flight and the final weight after all the fuel is burned.

The Breguet equation assumes the lift coefficent and the drag coefficient to stay constant during flight, but, since the weight of the aircraft reduces as fuel is burned, this will mean that either airspeed or air density must be reduced to produce as much lift as the weight of the aircraft. Since the Breguet equation is used to calculate the fuel mass required to fly $200\,\mathrm{km}$ at a velocity of $300\,\mathrm{km/h}$, it was decided to increase air density and thus climb to higher altitudes as fuel is burned. In reality, an operator would likely reduce the angle of attack and thus the lift coefficient to maintain altitude and speed.

In Equation 13.7, the endurance in seconds is given as a function of mostly the same inputs as the Breguet equation. However, the surface area of the wing S is added and the ratio of $\frac{C_L^{3/2}}{C_D}$ are also now required. This formula for endurance is not necessarily the maximum endurance, but rather the endurance at constant altitude and velocity, which is also important, since the this allows for a constant point density of the LIDAR system during monitoring.

The final value required to calculate the fuel mass was the propulsive efficiency during horizontal flight. This efficiency stems from 3 sources of energy loss: the propeller, the motor and the ESC. The propeller efficiency is calculated using the graphs in Figure 4.3. Based on the thrust required the advance ratio of the propeller is found and based on this advance ratio the propeller efficiency is found. This efficiency was found to be 0.84 at the maximum velocity and 0.82 for monitoring velocity.

The motor efficiency was calculated using the RPM of the propeller and the power input, to find the torque produced by the motor in Figure 4.4. The motor efficiency can then be found in Figure 13.7.
Using this graph, the motor efficiency was found to be 96 % at maximum velocity and 86% at monitoring velocity. Finally, the efficiency of the ESC is stated by the manufacturer to be greater than 98 %, so that value was used for all speeds. This resulted in a total propulsive efficiency of 79 % at maximum velocity and a propulsive efficiency of 69 % at monitoring velocity.

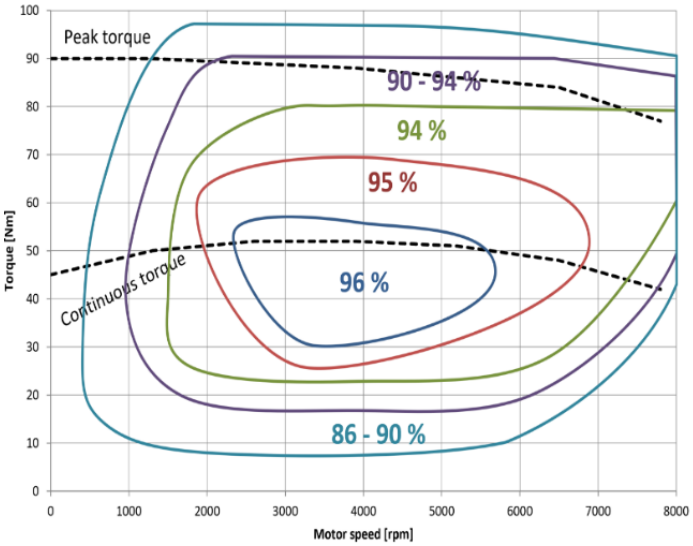

Figure 13.7: Efficiency of the Emrax 188 as a function of torque and RPM.

Finally, the fuel mass can be calculated for each mission phase. This was done by assuming landing to happen at operational empty weight, and working backwards to find the total fuel mass at take-off. The results are presented in Table **??**. The total fuel masses add up to $10.21\,\mathrm{kg}$ for the intervention mission and $17.73\,\mathrm{kg}$ for the monitoring mission. Since maximum payload is carried in the intervention mission this mission results in the highest take-off weight, which is the same as the MTOW, as the maximum payload mass was sized such that an intervention mission takes off at MTOW. This means that an endurance of more than 10 hours is achievable. If no intervention payload would be added, a total fuel mass of $41.91\,\mathrm{kg}$ could be added, which would result in a maximum endurance of 23 hours and 4 minutes.

Table 13.4: Fuel mass breakdown of different mission phases

Mission phase (intervention)	Fuel mass [kg]
Take-off	0.7176
Flight at V max	5.597
Payload deployment	1.270
Flight at V mon	2.058
Landing	0.5656

Mission phase (monitoring)	Fuel Mass [kg]
Take-off	0.6323
10h of monitoring	16.53
Landing	0.5656

13.4. Final Performance Analysis

Given the propulsive efficiency at different flight conditions and the power and thrust required at these different flight conditions can be computed. The results are summarized in Table 13.5. All flight conditions in this table assume the mass to equal the MTOW such that these are the maximum values.

Table 13.5: Selected thrust and power at MTOW at different flight conditions.

Description	Symbol	VTOL	V_{max} at 3 km altitude	V_{mon} at 150 m altitude
Thrust required	T	3202 N	311.74 N	129.88 N
Power output of propellers	P_{out}	49 970 W	5325 W	25 978 W
Power used by instruments	P_{inst}	434.3 W	434.3 W	679.3 W
Power required from ICE	P_{ICE}	63 968 W	33 306 W	8384 W
Propulsive efficiency	η_p	0.787 [−]	0.790 [−]	0.691 [−]

The values presented in Table 13.5 can be used to discuss the limitations of the design. Firstly, it can be seen that the MTOW has been designed such that the maximum continuous power output of the power generation system is used. For the other flight conditions, the power required from the generator is significantly lower than the maximum continuous power produced. This means that even if the parasitic drag is 1.93 times larger than the current drag estimate, the same maximum velocity can still be achieved, although it must be noted that a more powerful electric motor might be required.

This implies that the payload mass must be reduced to allow for the extra fuel needed to perform the mission without increasing the mass above MTOM. The horizontal propeller was verified to be capable of achieving 1.93 times the thrust at the same maximum velocity. The final payload range diagram is visible in Figure 13.8. It can be observed that the maximum endurance of 23 hours well exceeds the 10-hour requirement, at the cost of some payload mass. This result shows satisfactory margins for detailed design for meeting the endurance requirement.

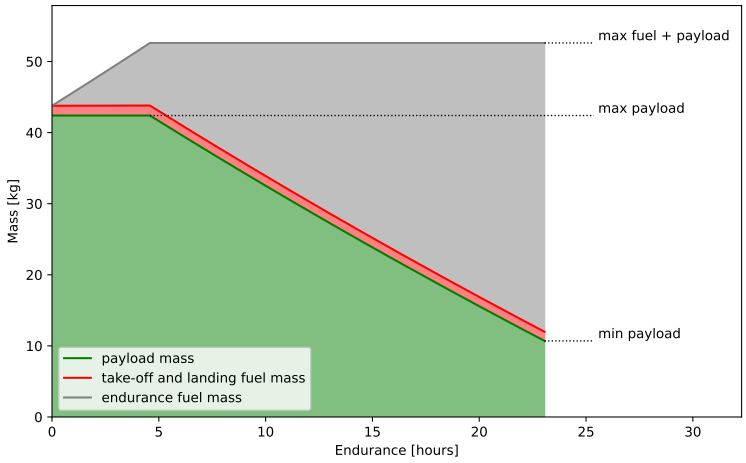

Figure 13.8: Payload-endurance diagram for the final design.

The payload-endurance diagram in Figure 13.8 was constructed assuming that horizontal flight happens at an altitude of $150\,\mathrm{m}$ at $41\,\mathrm{m/s}$ without deploying the payload. In reality, flying at higher speeds will reduce the endurance, and deployment of the payload at some point in the mission will increase endurance again.

13.5. Final Design Sensitivity

The mass estimates for the fuel mass are significantly lower than the previous estimates for the fuel mass. The fuel mass may change in later stages of the design if the drag found during field testing is different from the simulations. Similarly, the propulsive efficiency might be different from efficiencies claimed by manufacturers. The mission phases considered do not include climb phases, which would have been more accurate. The calculations for the fuel mass also do not include a safety factor for possible trapped fuels, or fuel for diversions in case of emergency. Because of these simplifications, it might prove that the payload mass needs to be reduced to allow for extra fuel to be carried.

Another inaccuracy in the calculations is the stall speed of $26\,\mathrm{m/s}$ as this is still an estimated value. The aerodynamic analysis in OpenVSP found a maximum lift coefficient of 1.26 at an angle of attack of 15 degrees (which would allow for a stall speed of $26.6\,\mathrm{m/s}$). This, however, is possibly too optimistic, as stall is very difficult to model in CFD and the actual maximum lift coefficient will have to be found through wind tunnel testing or field testing. If stall speed is found to be much worse than expected, an increase in wing area close to the wing root will be required to improve stall characteristics.

13.6. Integration Strategy

The final design consists of many completed sub-systems. To assemble these into one UAV, some considerations have to be made. The final design shows where each part is to be placed, but mounting structures must be assessed to allow assembly and disassembly. The individual mounting structures are beyond the scope of this project, but a strategy for development is made here.

Critical locations need to be identified. These are the boom mounting points to the wing and wing mounting points to the fuselage, as these mounting points carry external loads and need to be disassembled between deployments, whereas internal mounting structures for integrated parts are much less critical and can be permanent. Part-specific mounting structures need to be developed and designed for durability and ease of assembly. The internal component mounting can be made much simpler because these parts are not disassembled.

Designing these mounting structures needs to be done in such a way that power and control subsystem components and wiring can be connected to parts beyond the mounting where necessary. It is also important to match mounting structures to the available physical dimensions. This can be done by integrating the structures into the three-dimensional CAD model containing all parts.

The electrical power system also needs to be integrated into the UAV. The power distribution and subsystem are worked out in Chapter 5, but individual wiring and holes allowing for this in structures have to be designed. Wiring to connect the antenna, flight computer, receiver, and parts relying on information from these systems also need to be connected by wiring to transfer information. These connections sometimes have to be made through structures, so calculations have to be performed to ensure the structure can still bear the required loads with the changes.

The control surfaces need to be developed in more detail. Specifically, the hinge position and structure, the position of the servos and the wiring. Wiring will happen within the wing structure and the servo will be mounted on the wingbox. The integration of fuel systems within the wingbox also has to be developed. Space for fuel tanks is available in the wing box including pumps, and pipes. However a detailed design is needed for the connection between the fuel tank and the engines, and an opening to refill the tank.

Finally, the intervention payload structure requires the development of remote control payload doors and mounting/release structure. The mounting structure should be changeable to allow for different intervention payloads, as the bay should be modular in design.

13.7. Requirement Compliance Matrix

To ensure that all project requirements set on the UAV and mission design are fulfilled, a requirement compliance matrix has been created. The requirement matrix gives a clear overview of the verification status and strategy for the stakeholder, mission, and system requirements. Requirements are marked with a check mark if the requirement has been analyzed in the design process. requirements in need of further analysis or those not complied with are marked with a cross. In the final column, a brief description is given on the verification methodology for each requirement.

Table 13.6: Requirement compliance matrix.

Requirement ID & description	Mark	Verification	Compliance Method
R-STK-1 : The system shall effectively monitor landscape.	✓	Analysis	Photogrammetry data has an estimated horizontal accuracy of $2.5\,\mathrm{cm}^2$ from Section 3.1.
R-STK-2 : The system shall quickly provide data for warning about flood risk.	✓	Analysis	The communications system is designed to transfer at least $10\,\mathrm{Mb/s}$ at a latency of no more than $150\,\mathrm{ms}$ as mentioned in Chapter 3.
R-STK-3 : The system shall aid in maintaining lives and the surrounding environment.	✓	Analysis	The UAV is capable of sending data capable of providing usable information to first responders, in addition to providing humanitarian aid supplies described in Chapter 3.
R-STK-4 : The system shall have affordable operational costs.	✓	Analysis	The total operational cost is no more than €301k calculated in Section 12.1, which is deemed affordable in Section 12.4. This requirement should be changed to be quantitative.
R-STK-5 : The system shall be able to be deployed and operated in a variety of environments.	✓	Analysis	The system is designed to be capable of deployment on any open, flat surface, as described in Section 9.3. No runway or power infrastructure is needed. In addition, the ground station is capable of relocation.
R-STK-6 : The system shall not endanger the civilians in the region where it operates and the first responders active in the area.	✓	Analysis	The system is designed to not interact with civilians or first responders unless controlled by an operator, as described in Section 9.3.
R-STK-7 : The system shall not compromise the functioning of other flood prevention and protection systems.	✓	Analysis	The system is not designed to interact with other flood prevention and protection systems.
R-STK-8 : The system shall operate according to existing UAV regulations.	×	Inspection	Inspection of all UAV regulations has not been performed. It is recommended that potential buyers investigate local regulations before purchasing.
R-STK-9 : The system components shall be reusable at end of life.	✓	Analysis	Reusability and recyclability of components is discussed in Chapter 11 and assessed for each subsystem.
R-MIS-1 : The system shall allow for total airborne operational endurance of no less than 10 hours at the lowest latitude-related flyability conditions as described by FAA weather tolerance data.	×	Analysis	The endurance of the UAV at minimum payload has been identified in Section 13.4 to be no less than $22\,\mathrm{h}$ at the most critical. Lattitude-related compliance of each component should be verified individually.
R-MIS-2 : The system shall allow for monitoring of water levels, riverbed topography, surface debris, and stationary flood protection mechanisms.	✓	Inspection	A monitoring payload capable of monitoring water levels, riverbed topography, surface debris, stationary flood protection mechanisms has been developed in Section 3.1.
R-MIS-3 : The system shall allow for remote control and data transmission from a range of no less than $200\,\mathrm{km}$.	✓	Inspection of comm system datasheet	Two communications systems were chosen capable of communication link at a distance up to $200\,\mathrm{km}$ in Section 3.5.
R-MIS-4 : The system shall allow for the continuous transmission of data about monitored areas to the ground segment.	✓	Analysis	The communications system is designed to transfer at least $10\,\mathrm{Mb/s}$, for a calculated monitoring payload data rate of no higher than $2.47\,\mathrm{Mb/s}$ described in Section 3.1.

Continued on next page

Table 13.6: Requirement compliance matrix.

Requirement ID & description	Mark	Verification	Compliance Method
R-MIS-5 : The system shall allow for vertical take-off and landing from any ground surface at lowest latitude-related flyability conditions as described by the FAA weather tolerance data.	×	Analysis, Demonstration	VTOL has been calculated for an assumed flat ground surface. The requirement has to be rewritten, or a more thorough analysis of VTOL has to be performed.
R-MIS-6 : The system shall allow for deployment and operations under moderate to high turbulence conditions as described by the FAA weather tolerance data.	×	Analysis	The method of assembly has been described in Section 13.6. Precipitation tolerance has to be verified on physical assembly.
R-MIS-7 : The system shall allow for safe autonomous landing in case of propulsion system failure.	✓	Analysis, Demonstration	The UAV is capable of a gliding landing in case of propulsion system failure, and can be autonomously landed using the selected Autopilot computer from Chapter 3.
R-MIS-8 : The payload shall comply with existing EASA UAV regulations.	×	Inspection of EASA UAV regulations	The payload has not been verified to pass EASA UAV regulations.
R-MIS-9 : The system shall allow for reuse or recycling of all assembly components at end of life according to ISO-14001:2015.	✓	Analysis	The Life Cycle Analysis describes the reuse and recycle strategy applied to all parts in Chapter 11.
R-MIS-10 : The system shall allow for versatile payload loading.	✓	Inspection, Demonstration	The payload bay is designed to be modular and support varying payloads up to $29\,\mathrm{kg}$, mentioned in Chapter 3.
R-SYS-1 : The system shall have a maximum wind resistance of $14\,\mathrm{m/s}$.	×	Analysis of angled flat plate	The horizontal flight an vertical flight wind resistance have been identified in Section 7.14. The monitoring flight envelope should changed to accommodate the increase in stall speed, or an improved aerodynamic analysis is required.
R-SYS-2 : The system shall have a precipitation tolerance of $50\,\mathrm{mm/h}$.	×	Test, Inspection	The method of assembly has been described in Section 13.6. Precipitation tolerance has to be verified on physical assembly.
R-SYS-3 : The system shall have an onboard data storage of TBD.	×	N/A	This requirement was deemed unnecessary, as loss of communications halts data collection.
R-SYS-4 : The propulsion system shall be able to transition between VTOL and horizontal flight.	✓	Analysis	The propulsion system designed in Chapter 4 to be capable of providing enough power to the vertical and horizontal engine.
R-SYS-5 : The system shall have an operational temperature range of -20 $°C$ to 46 $°C$.	×	Analysis	Verification of operation at these temperatures has to be performed for all components and the assembly.
R-SYS-7 : The UAV shall have a modular sensing payload system with predefined interfaces for data and power.	✓	Analysis	A modular monitoring payload has been designed in Section 3.1, consisting of a LIDAR and a multi-spectral camera.
R-SYS-8 : The UAV shall have a modular intervention payload bay.	✓	Analysis	The payload bay has been designed to carry a variety of intervention payloads, as described in chapter 3.
R-SYS-9 : The UAV shall have an autonomous landing mode.	✓	Analysis, Demonstration	The selected autopilot computer allows for autonomous landing, as described in chapter 3.

Continued on next page

Table 13.6: Requirement compliance matrix.

Requirement ID & description	Mark	Verification	Compliance Method
R-SYS-10 : The UAV shall have a manual flying mode.	✓	Analysis, Test	The UAV has been designed to receive and send flight control data, which in combination with a flight computer, allows for manual control, as stated in chapter 3.
R-SYS-11 : The system flight profile shall be dynamically stable.	✓	Analysis	A dynamic stability analysis of the system is performed in Section 7.12, which has shown compliance.
R-SYS-12 : The system flight profile shall be controllable.	✓	Analysis	The controllability of the system has been analyzed in Section 7.13.
R-SYS-13 : The software related to the control of the UAV shall have a Design Assurance Level (DAL) of Level A.	×	Analysis, Test	The design of the UAV software has not been analyzed. This should be determined for each subsystem component.
R-SYS-14 : The UAV shall not produce more than $130\,\mathrm{dB}$ measured at $100\,\mathrm{m}$ from the ground.	✓	Analysis	The noise level of the UAV is calculated in Section 4.5, which shows compliance by analysis.
R-SYS-15 : The UAV shall be capable of a glide ratio of 22 at a velocity of no more than $40\,\mathrm{m/s}$	✓	Analysis	The glide ratio has been determined to be 22.38 at a velocity of $40\,\mathrm{m/s}$ in Section 13.2.
R-SYS-16 : The UAV shall be capable of a horizontal landing from gliding flight.	✓	Analysis, Demonstration	Landing gear for horizontal landing up to a load factor of N = 2.0 has been designed in Section 8.1.

As is evident from Table 13.6, there are multiple requirements which have not been met. The nature of these requirements should be noted as most of those not met are not performance requirements. With further analysis and an increased depth of research, it is expected that these requirements can be met without large design changes.

Further subsystem requirements have been set up in the design of subsystems. Payload & Communications, Propulsion, and Power subsystem requirements are verified in Section 3.7, Section 4.6, and Section 5.3 respectively. Wing, stability & control, and fuselage subsystem requirements are verified in Section 6.6, Section 7.15, and Section 8.4 respectively. The ground system subsystem requirements were verified in Section 9.4.

13.8. Budget Breakdown

Initial estimates of the mass, cost, and power were made at the start of the design process. The system was split into five subsystems, namely: payload, structure, communications and control, fuel/energy source, and propulsion. With the final design complete, a more accurate breakdown can now be assessed and compared.

Table 13.7 shows the mass budget breakdown from the conceptual phase to the final phase. The final propulsion system became heavier than in the initial design iteration. Due to the initial estimate for the energy density of the motor (which was made based on statistical data of various electric motor dimensions), the motors turned out to be heavier than previously calculated. Another reason is that the initial sizing procedure did not take into account all extra electronics needed for the propulsion system to run. The fuel mass is less than first expected. The efficiency of the motors and ICE of the actual components were higher than originally calculated for, making the propulsion system more fuel efficient. Payload, structures, and communications and control stayed within the acceptable margin of error of the budget breakdown, especially compared to the preliminary design. Due to components being off the shelf, the payload, communications and control, fuel and propulsion are considered accurate values as the exact masses are known. For the structure, there is a certain uncertainty as

connections between structural parts were not considered. Nonetheless, the structural calculations were done in a conservative manner and thus the extra mass gives a margin of error.

Table 13.8 shows the conceptual and final power allocation. During the preliminary phase, no power budget diagram was developed. It should be noted that this power breakdown is during a monitoring mission. The high discrepancies can be explained by the fact that the propulsion system changed from series-hybrid with a battery to a series-hybrid with a generator. All power is first converted into electricity and then distributed into the systems. Another important note to make is that the initial estimation was made for smaller scale UAV's. The exact power of each component was calculated and is shown in Section 13.1.3. Hence, the values are considered accurate.

The last breakdown delves into the cost of each subsystem, shown in Table 13.9. In this case, the cost of the communications and control was underestimated. The satellite communication system takes up around 1/3 of the total production cost of the UAV. The structures cost include material procurement, manufacturing and management of the structure. It should be noted that the LIDAR is not included in the cost breakdown, as it costs multiple times the unit cost of the UAV (more information in Section 13.1.3), and represents an optional payload for the monitoring of riverbed topography. The accuracy of the structures cost is deemed less accurate than the other subsystems, as it is not off the shelf and manufacturing processes need to be designed and implemented.

Table 13.7: Mass breakdown per subsystem for different design phases.

Subsystem	Conceptual	Preliminary	Final
Payload	7%	4%-20%	5%-17%
Structure	27%	35%	36%
Communications and control	4%	10%	6%
Fuel/energy source	40%	15%- 31%	4%-15%
Propulsion	22%	20%	38%

Table 13.8: Power breakdown per subsystem for different design phases.

Subsystem	Conceptual	Preliminary	Final
Payload	18%	-	4%
Structure	0%	-	0
Communications and control	20%	-	5%
Fuel/energy source	9%	-	0
Propulsion	53%	-	91%

Table 13.9: Cost breakdown per susbsystem for different design phases.

Subsystem	Conceptual	Preliminary	Final
Payload	28%	-	3%
Structure	43%	-	3%
Communications and control	11%	-	58%
Fuel/energy source	-	-	1%
Propulsion	18%	-	35%

13.9. Functional Breakdown and Flow Diagram

Within the functional breakdown diagram, an overview of system functionalities is depicted. This is divided into three categories, first treating the production of the system, then the operation of the system when performing missions, and finally the end-of-life process. The breakdown of functions is represented in Figure 13.9 on Page 132.

The relation between these functionalities is depicted in the functional flow diagram, where the flow of the functions is shown through the production, mission and end-of-life. In addition, this depicts any iterative loops and repetitions present in the shown functions. This is graphically represented in Figure 13.10 on Page 133.

- F - TOTAL: Perform FLOWS Mission
  - F.1 - TOTAL: Produce system
    - F.1.1 - TOTAL: Produce parts
      - F.1.1.1 - TOTAL: Order COTS components
      - F.1.1.2 - AIR: Collect materials
      - F.1.1.3 - AIR: Manufacture parts
      - F.1.1.4 - AIR: Perform non-destructive testing
      - F.1.1.5 - AIR: Deliver parts to assembly
    - F.1.2 - AIR: Assemble parts
      - F.1.2.1 - AIR: Assemble subassemblies
      - F.1.2.2 - AIR: Assemble final assembly
      - F.1.2.3 - AIR: Install wire harness
      - F.1.2.4 - TOTAL: Install software
    - F.1.3 - TOTAL: Verification and Validation
      - F.1.3.1 - TOTAL: Test software
      - F.1.3.2 - AIR: Test hardware
      - F.1.3.3 - AIR: Environmental laboratory testing
      - F.1.3.4 - TOTAL: Test mechanisms
        - F.1.3.4.1 - TOTAL: Test actuators
        - F.1.3.4.2 - AIR: Test landing gear
        - F.1.3.4.3 - AIR: Test control surfaces
      - F.1.3.5 - TOTAL: Perform test mission
        - F.1.3.5.1 - AIR: Test telemetry
        - F.1.3.5.2 - TOTAL: Test communication
        - F.1.3.5.3 - TOTAL: Test intervention payloads
    - F.1.4 - TOTAL: Deliver system to client
      - F.1.4.1 - TOTAL: Prepare system for transport
      - F.1.4.2 - TOTAL: Transport system
  - F.2 - TOTAL: Perform mission
    - F.2.1 - GROUND: Plan mission
      - F.2.1.1 - GROUND: Set take-off and landing location
      - F.2.1.2 - GROUND: Set measurement areas/points
      - F.2.1.3 - GROUND: Determine mission profile and payload
    - F.2.2 - TOTAL: Deploy system
      - F.2.2.1 - TOTAL: Transport UAV to take-off location
      - F.2.2.2 - AIR: Assemble UAV
      - F.2.2.3 - GROUND: Prepare ground station
      - F.2.2.4 - AIR: Place UAV in take-off position
      - F.2.2.5 - AIR: Turn on system
      - F.2.2.6 - AIR: Perform sensor calibration
      - F.2.2.7 - TOTAL: Test subsystems
        - F.2.2.7.1 - AIR: Test control systems
        - F.2.2.7.2 - AIR: Test navigation systems
        - F.2.2.7.3 - AIR: Test avionics systems
        - F.2.2.7.4 - AIR: Test monitoring system
        - F.2.2.7.5 - AIR: Test propulsion systems
        - F.2.2.7.6 - TOTAL: Test communication systems
      - F.2.2.8 - AIR: Apply intervention payload
        - F.2.2.8.1 - AIR: Load the required intervention payload
        - F.2.2.8.2 - AIR: Test intervention activation system
    - F.2.3 - AIR: Initiate flight
      - F.2.3.1 - AIR: Perform vertical take-off
      - F.2.3.2 - AIR: Climb to required altitude
      - F.2.3.3 - AIR: Transition to horizontal flight
    - F.2.4 - AIR: Perform cruise
      - F.2.4.1 - AIR: Adjust altitude to desired altitude
      - F.2.4.2 - AIR: Adjust speed to cruise speed
      - F.2.4.3 - AIR: Follow flight path
    - F.2.5 - AIR: Monitor environment
      - F.2.5.1 - AIR: Adjust flight conditions
      - F.2.5.2 - AIR: Activate sensors
      - F.2.5.3 - AIR: Perform LIDAR measurements
      - F.2.5.4 - AIR: Perform photogrammetry
    - F.2.6 - AIR: Perform intervention
      - F.2.6.1 - AIR: Locate area of interest
      - F.2.6.2 - AIR: Adjust flight conditions
      - F.2.6.3 - AIR: Activate payload
    - F.2.7 - AIR: Perform vertical landing
      - F.2.7.1 - AIR: Adjust horizontal speed
      - F.2.7.2 - AIR: Transition to VTOL mode
      - F.2.7.3 - AIR: Descend vertically
      - F.2.7.4 - AIR: Perform touchdown
    - F.2.8 - TOTAL: Pack system
      - F.2.8.1 - TOTAL: Turn system off
      - F.2.8.2 - AIR: Post-mission check for UAV damage
      - F.2.8.3 - TOTAL: Disassemble system
    - F.2.9 - TOTAL: Perform communication
      - F.2.9.1 - TOTAL: Establish connection between UAV and GC
      - F.2.9.2 - AIR: Send flight data
      - F.2.9.3 - AIR: Receive control data
      - F.2.9.4 - AIR: Compress monitoring and control data
      - F.2.9.5 - AIR: Send monitoring and control data
    - F.2.10 - AIR: Determine attitude and position
      - F.2.10.1.1 - AIR: Integrate accelerations
      - F.2.10.1.2 - AIR: Process GPS data
      - F.2.10.1.3 - AIR: Perform in flight sensor recalibration
    - E
  - F.3 - TOTAL: Assess the end-of-life of the system
    - F.3.1 - TOTAL: Store system for decommission
      - F.3.1.1 - TOTAL: Transport to storage location
      - F.3.1.2 - TOTAL: Store total system
    - F.3.2 - AIR: Disassemble UAV
      - F.3.2.1 - AIR: Extract and separate parts
      - F.3.2.2 - AIR: Clean parts
      - F.3.2.3 - AIR: Assess quality of parts
      - F.3.2.4 - AIR: Document quality and reuseability
    - F.3.3 - TOTAL: Repurpose parts
      - F.3.3.1 - TOTAL: Re-certify parts
      - F.3.3.2 - TOTAL: Reintegrate reusable parts
      - F.3.3.3 - TOTAL: Sell redundant parts
      - F.3.3.4 - TOTAL: Recycle non-reusable parts
- E
  - F.2.11 - TOTAL: Perform maintenance
    - F.2.11.1 - TOTAL: Inspect damage
    - F.2.11.2 - TOTAL: Perform repairs
    - F.2.11.3 - TOTAL: Verify integration of repairs
  - F.2.12 - TOTAL: Perform horizontal landing
    - F.2.12.1 - TOTAL: Find landing location
    - F.2.12.2 - AIR: Adjust velocity
    - F.2.12.3 - AIR: Extend nose landing gear
    - F.2.12.4 - AIR: Perform touchdown

DSE GROUP 10 - FLOWS
FUNCTIONAL BREAKDOWN STRUCTURE

Input → Z → Output
Portal

Connection →

Identifier - segment
Function

Level 0
Level 1
Level 2
Level 3
Level 4

Segment definition

• TOTAL • AIR • GROUND	full FLOWS system airborne segment ground segment

Figure 13.9: Functional Breakdown

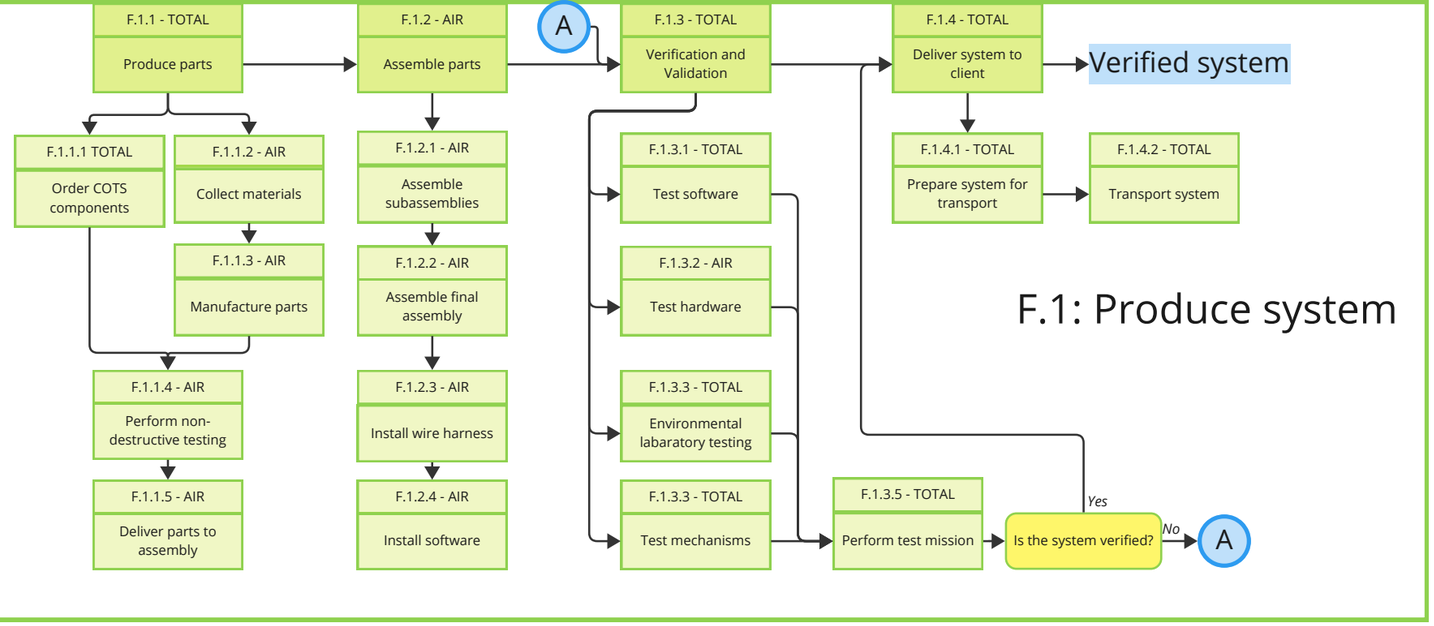

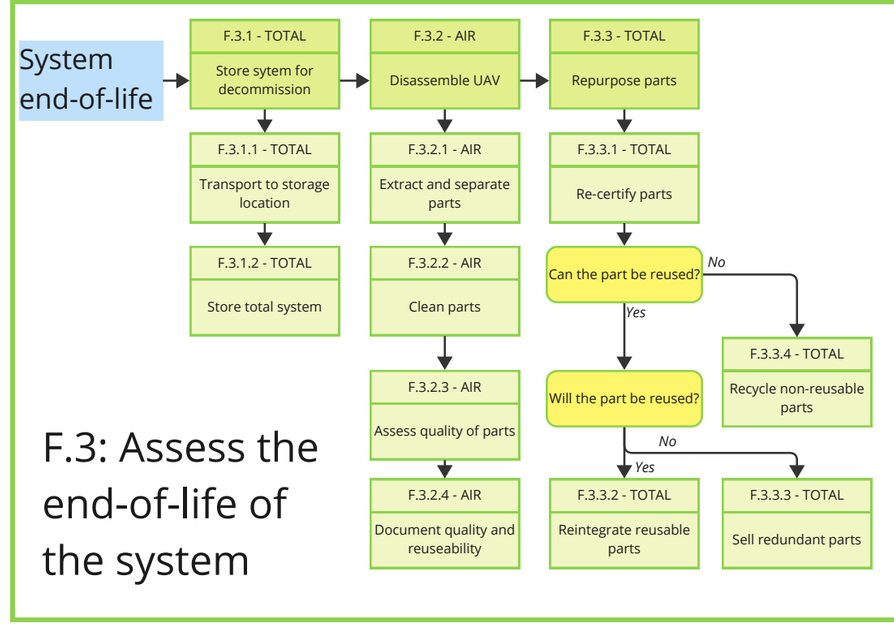

DSE GROUP 10 - FLOWS FUNCTIONAL FLOW STRUCTURE

Identifier
Function

Level 0
Level 1
Level 2
Level 3
Level 4

Segment definition

• TOTAL • AIR • GROUND	full FLOWS system airborne segment ground segment

Question (or flow)

Input Z Output
Portal

Connection

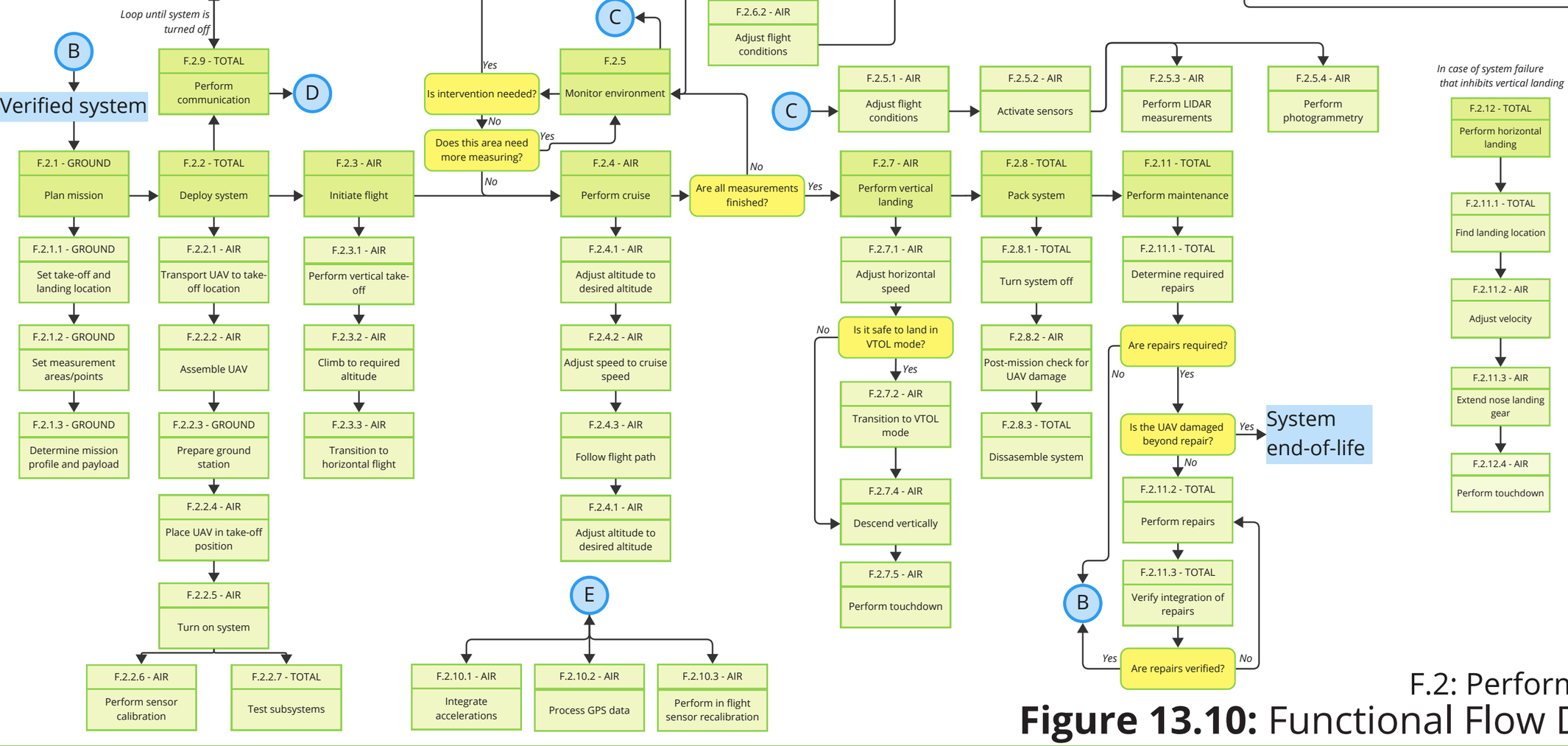

F.2: Perform mission

Figure 13.10: Functional Flow Diagram

14 | Project Conclusion

In this chapter, the next steps of the project are discussed. First, the project design and development logic is presented in Section 14.1. Secondly, the future validation efforts are elaborated upon in Section 14.2. Then, the future project plans are shown in a Gantt chart, in Section 14.3. Finally, the conclusions drawn by the design team at the end of the project are presented in Section 14.4.

14.1. Project Design and Development Logic

The design of the FLOWS architecture is carried out in the context of the Design Synthesis Exercise. Though the objective of the project, as described in Chapter 1, is to design a flood monitoring and response system, this objective does not necessarily represent the final outcome.

To study the steps that are to be pursued after the formal completion of the DSE project, the Project Design and Development logic was performed. It is available in visual format in Figure 14.1. The yellow blocks show what tasks need to be performed before the design is complete. The orange blocks provide an overview of the entire system: the required inputs, processing activities, and expected outputs. The green blocks visualize the short-term outcome of the project, while the blue blocks represent the long-term expected outcome.

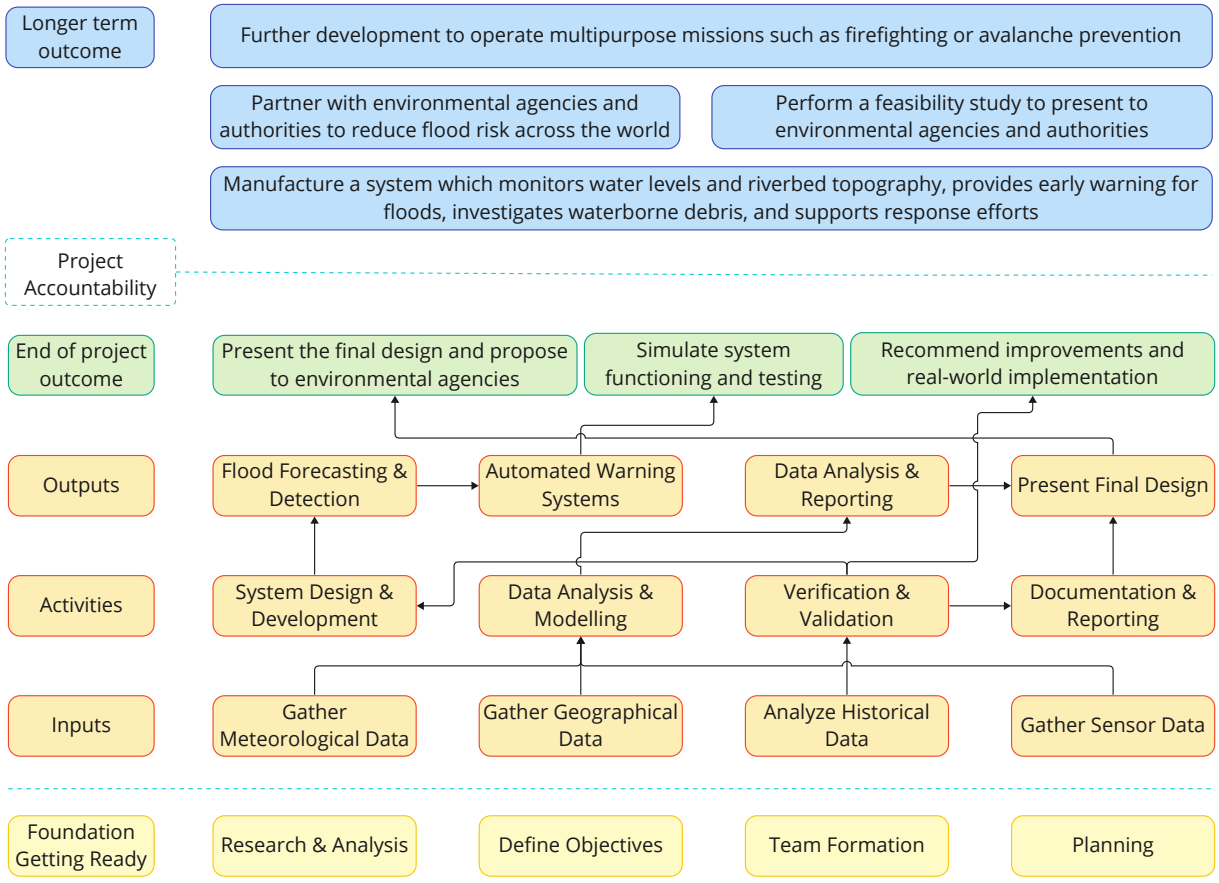

Figure 14.1: Project Design and Development Logic visualization.

As described in Figure 14.1, the expected outcome of the DSE project is to complete the design of a system for flood monitoring and response. However, further steps may be pursued, including but not limited to official feasibility studies for the clients described above. These options are to be explored continuously and updated as the design matures.

14.2. Validation Activities

In the validation process of the final design, various testing methods are used to ensure the system's compliance with the stakeholder requirements and the expected functionality of the system.

The validation methods for each stakeholder requirement are chosen and explained in Table 14.1, portraying how each requirement is to be tested.

Table 14.1: Validation methods for stakeholder requirements.

Identifier	Method	Rationale
R-STK-1	Field Testing	Field Testing involves conducting tests in actual operational environments to validate the UAV's effectiveness in monitoring landscapes. This ensures that the UAV can handle real-world variables and terrain diversity effectively.
R-STK-2	Operational Testing	Operational Testing in scenarios simulating emergency flood situations to validate the UAV's ability to quickly provide accurate and timely data, crucial for effective warning and mitigation actions.
R-STK-3	Simulation, Live Demonstration	Simulation and Live Demonstration to validate the UAV's effectiveness in aiding lifesaving and environmental protection efforts under different emergency scenarios, demonstrating its utility and impact in critical situations.
R-STK-4	Cost-Benefit Analysis	Cost-Benefit Analysis to validate that operations remain within the projected budget while achieving desired outcomes, ensuring economic feasibility.
R-STK-5	Environmental Testing	Environmental Testing in various simulated environments to validate the UAV's adaptability and robustness, ensuring it performs reliably across a wide range of operational conditions.
R-STK-6	Safety Audits, Risk Assessments	Safety Audits and Risk Assessment tests carried out to validate that the UAV operations do not endanger civilians and first responders, confirming its safety protocols are effective.
R-STK-7	Integration Testing	Integration Testing with other flood prevention systems to validate that the UAV does not interfere with or compromise these systems, ensuring compatibility and cooperative functionality.
R-STK-8	Regulatory Compliance Review	Regulatory Compliance Review to validate that UAV operations conform to existing UAV regulations, ensuring all operational aspects are legally compliant and documented.
R-STK-9	Lifecycle Analysis	Lifecycle Analysis to validate the reusability and end-of-life processing of system components, ensuring they meet sustainability goals.

For the validation methods, the following expected expenses have been quantified:

1. **Field Testing:** Two weeks will be dedicated to the field testing of the validation procedure on a rental aerodrome. The cost of aerodrome rental is considered to be of a **High** magnitude, since costs for ATC and ground personnel also need to be included. All performance tests and landscape monitoring will happen in the first week. The monitoring tests will concentrate on the landscape's capacity to be monitored in order to create a digital visualization.
2. **Operational Testing:** This method of testing will take place in the second week of the aerodrome rental. During operational testing, the focus will lie on the performance of the UAV in emergency situations. For this, an emergency environment needs to be simulated to allow the study of water level increases. For example, the environment in a water park may be used, though this would result in far increased costs, possibly of **High** magnitude.
3. **Simulation, Live Demonstration:** The simulation and live demonstration includes the effectiveness in aiding lifesaving and environmental protection efforts as described in Table 14.1. This validation method will take place in the second week of the aerodrome rental as well. Pointers will be placed on a certain location on the aerodrome. The task is to let the UAV identify this specific location and provide humanitarian aid payload such as life vests while hovering above the area. The costs of the aerodrome are once again considered **High** [1].

[1] https://hca-airport.dk/en/rent-a-runway/

4. **Cost-Benefit Analysis:** With the cost-benefit analysis, operational costs will be analyzed alongside any costs that would be mitigated by the operations of FLOWS. Preventing expenses through the operations of the FLOWS system would facilitate justifying any possibly high operational costs, with the ultimate goal of ensuring that the FLOWS mission is beneficial. This makes this validation method crucial in determining the worth of utilizing the system, with **Low** costs expected due to specialized support being required. This will be an addition to the existing cost-risk analysis.
5. **Environmental Testing:** This refers to the testing of the UAV in specific environments, which are relevant to stakeholders. This means subjecting the design to a variety of environments, such as gust loads in a wind-tunnel, subjecting it to a range of temperatures and subjecting it to moisture and precipitation. It also includes tests such as vibrations testing and other flight load testing.
   Certain specialized facilities may be required, such as the McKinley Climatic Laboratory [2], which can simulate temperature, moisture and precipitation ranges. Due to it being a governmental and military laboratory, a cost estimate is expected to be **High**. In addition, a gust wind tunnel and a loading laboratory are necessary, which are estimated to have a **Medium** price range [3]. Another reason for **High** expected costs is the chance of irreparable product damage and subsequent loss, considering the significant stress applied at ultimate loading.
6. **Safety Audit and Risk Assessments:** The operational areas are to be studied, with specific procedures for ensuring safe interactions with both general population and first responders. Possible risks will be assessed and safety audits will be performed to optimize overall certainty. Expected costs are **Low**.
7. **Integration Testing:** The integration test validates that the UAV is able to communicate without issues with external flood monitoring and emergency services. This test can be performed from a laboratory by simulating the data supplied by the UAV, and processing this together with external data at the mobile ground station. A second validation test should be performed once the UAV is airborne and collecting data autonomously. The cost is expected to be low **Low**, as it will probably not require additional facilities.
8. **Regulatory Compliance Review:** In order for the UAV to be active it must comply to regulatory rules in the country of operation. Therefore, the FLOWS design will be inspected by local examiners in order to obtain an approval certificate that validates legal compliance. Costs may be **High** as the system is opened up to more markets and FAA compliance costs are high.
9. **Lifecycle Analysis:** The lifecycle study aims to investigate reusability and end-of-life processing of system components, also through the compilation of an Environmental Management System as described in Chapter 11. Though a preliminary analysis has been performed, it is recommended to continue it as the design matures.

14.3. Project Gantt Chart

The plan for the remaining design phases, as is detailed in Figure 14.2, highlights the necessary steps to be taken following the DSE project deadline. This includes further verification, production, validation, and finalization. After the DSE deadline, the next phase of the project is scheduled to take place between June 28th, 2024, and May 8th, 2025. This timeframe allows for thorough verification of the design, the implementation of production processes, rigorous validation testing, and the finalization of all elements to ensure the complete and successful completion of the project.

[2] https://www.eglin.af.mil/News/Article-Display/Article/1086166/mckinley-climatic-laboratory/
[3] https://www.aa.washington.edu/AERL/KWT/rateguide

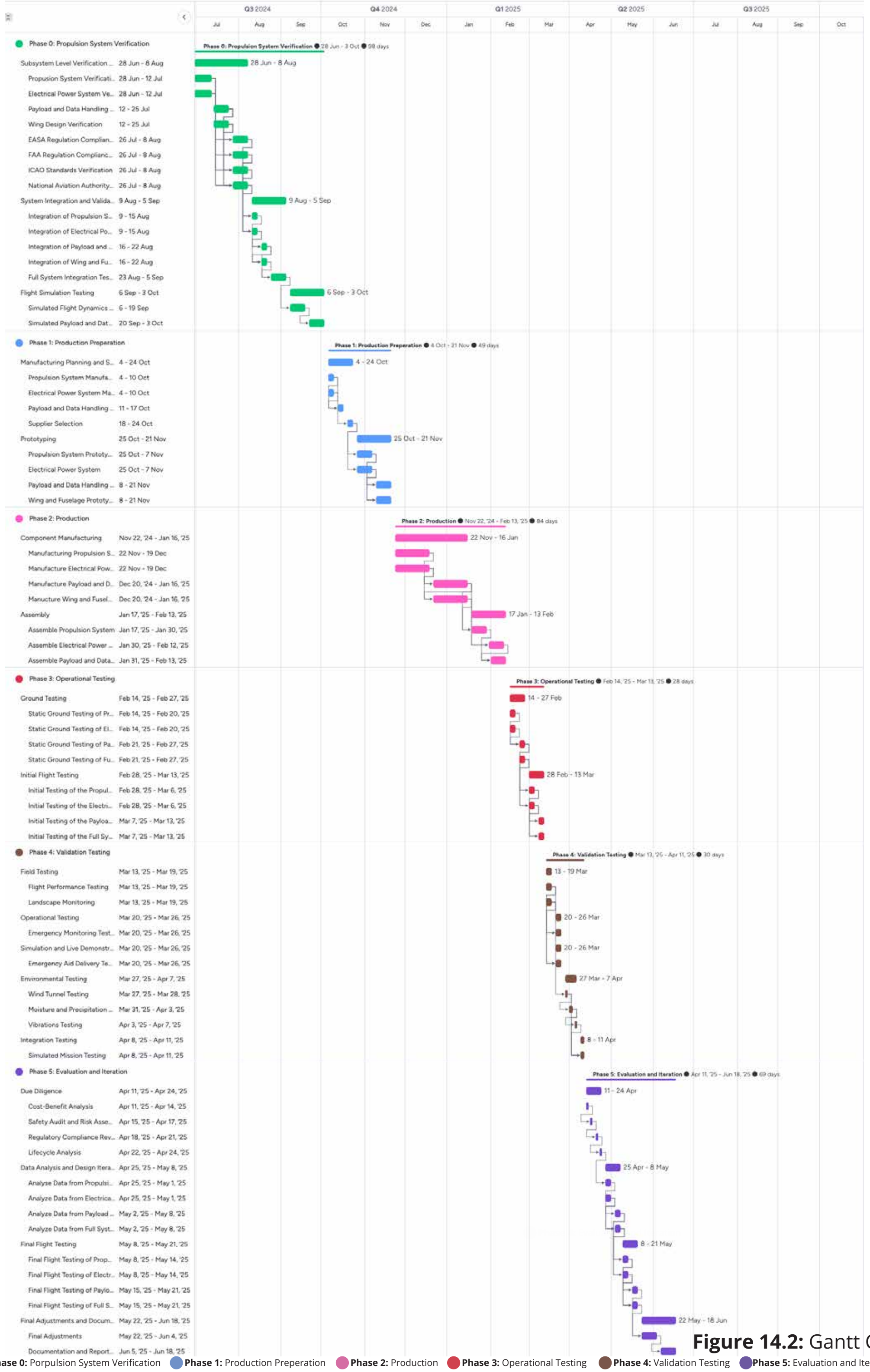

Figure 14.2: Gantt Chart

Phase 0: Porpulsion System Verification **Phase 1:** Production Preperation **Phase 2:** Production **Phase 3:** Operational Testing **Phase 4:** Validation Testing **Phase 5:** Evaluation and Iteration

14.4. Conclusion

As a result of climate change, riverine floods are becoming increasingly frequent, and within Europe alone, have cost thousands of lives in the past decade [4]. One of the largest obstacles faced by first responders in flooding is that the affected areas are difficult to monitor, and even more difficult to reach. This demands a novel flood forecasting, warning and response system, of which the necessity has been defined as follows.

Design a system to monitor water levels and riverbed topography, provide early warning for floods, investigate waterborne debris, and support response efforts.

Over the course of ten weeks, the FLOWS design team has been dedicated to the design of a flood monitoring and intervention system. This system includes a ground segment and airborne segment, which work in tandem to ensure fast responses, versatile mission profiles, and broad deployability. Due to the versatility of the monitoring payload, and the modularity of the payload bay, the expectation is that this system will not solely be employed for flooding situations, but will become a staple in environmental monitoring and humanitarian aid.

Multiple obstacles were encountered during this design process, of which the most prominent examples are discussed briefly. The most immediate obstacle of this design project seemed to be the lack of comparable UAV's. Because of this, relying on historical data and empirical relations was difficult in the early design phases. This was countered by exploring a large variety of concepts, and considering seemingly unconventional designs.

Once an initial sizing was performed, it was quickly established that the required UAV size was unconventional. This resulted in difficulties with aircraft performance, namely that VTOL for the determined take-off weight was not broadly explored, let alone applied. An example of this is the propeller sizing, for which little to no information was available. However, by consulting experts and applying a variety of methods, this obstacle was also overcome by the design team. The peak power requirement of the VTOL phase of the mission formed another obstacle, as this required the analysis of different power systems, which finally led to the selection of a series hybrid generator system.

All in all, this research has proven the feasibility of a VTOL UAV with a payload capacity of over $30\,\mathrm{kg}$, and impressive performance characteristics such as an endurance of up to $23\,\mathrm{hours}$. On top of this, there has been a focus on sustainability over the course of the design project. This resulted in a high fuel efficiency, and low emissions per mission. In addition, the sustainability of the design was assessed by selecting materials and components which allow for recycling and reuse. It was found that this design has filled a significant niche in the market, and provides a unique combination of performance, sustainability and cost effectiveness.

Close to the conclusion of the design project, the design team would like to thank all members of the supervisory team for their support at all stages of the design. Their guidance and feedback has enabled the team members to use their individual strengths to the best possible effect, collaborating towards a unique final design. Moreover, the design team would like to thank the experts who have shared their knowledge over the course of the design projects, providing the critical support required to overcome various obstacles.

On behalf of the FLOWS design team, thank you for reading.

[4] https://www.eea.europa.eu/en/newsroom/news/climate-health-risks-posed-by-floods

References

[1] J. Rentschler, M. Salhab, and B.A. Jafino. “Flood exposure and poverty in 188 countries”. In: *Nature Communications* (2022). DOI: 10.1038/s41467-022-30727-4.

[2] Ş. Zekâi. *Flood Modeling, Prediction and Mitigation*. 1st ed. Cham, Switzerland: Springer, 2018.

[3] DSE Group 10. *FLOWS Baseline Report*. AE3200. Version 1.1. Delft, Netherlands: Delft University of Technology, May 2024.

[4] DSE Group 10. *FLOWS Midterm Report*. AE3200. Version 1.1. Delft, Netherlands: Delft University of Technology, May 2024.

[5] J. Gundlach. *Designing Unmanned Aircraft Systems: A Comprehensive Approach*. 1st ed. Reston, Virginia: American Institute of Aeronautics and Astronautics, Inc, 2012.

[6] J. Zong et al. “Evaluation and Comparison of Hybrid Wing VTOL UAV with Four Different Electric Propulsion Systems”. In: *Aerospace* 8.9 (2021). URL: https://www.mdpi.com/2226-4310/8/9/256.

[7] A. Szafarczyk and Toś C. “The Use of Green Laser in LiDAR Bathymetry: State of the Art and Recent Advancements”. In: *Sensors* 23.1 (2023). ISSN: 1424-8220. DOI: 10.3390/s23010292. URL: https://www.mdpi.com/1424-8220/23/1/292.

[8] *RIEGL VQ-840-GE, Lightweight and Compact Topo-Bathymetric Airborne Laser Scanner*.

[9] RIEGL. *Personal Communication*. May 2024.

[10] L et al Ferranti. “SkyCell: A Prototyping Platform for 5G Aerial Base Stations”. In: *IEEE 21st International Symposium on ”A World of Wireless, Mobile and Multimedia Networks”* (2020).

[11] V. Estrela et al. *Imaging and Sensing for Unmanned Aircraft Systems*. Institution of Engineering and Technology, 2020, pp. 6–7. ISBN: 978-1-78561-642-6.

[12] T. Hill. “Satellite Communication System Study for Unmanned Autonomous Aircraft (UAVs)”. In: (Jan. 2016). DOI: 10.13140/RG.2.2.24876.31366.

[13] K. Amerasinghe. *H.264 For The Rest Of Us*. Adobe Inc.

[14] M. Swartz and D. Wallace. “The Influence of Frame Rate and Resolution Reduction on Human Performance”. In: (1992). DOI: 10.1177/154193129203601817.

[15] N. Haala, M. Cramer, and M. Rothermel. “QUALITY OF 3D POINT CLOUDS FROM HIGHLY OVERLAPPING UAV IMAGERY”. In: (2013). DOI: 10.5194/isprsarchives-XL-1-W2-183-2013.

[16] Y. Feng, S. Liu, and Y. Zhu. “Real-Time Spatio-Temporal LiDAR Point Cloud Compression”. In: (2020). DOI: 10.48550/arXiv.2008.06972.

[17] H.C. Lee. “KU-BAND LINK BUDGET ANALYSIS OF UAV WITH ATMOSPHERIC LOSSES”. In: (2006). DOI: 1-4244-0378-2/06/$20.00.

[18] S. van Berkel and X. van Kooten. “Ground station user interface and data link: An implementation for unmanned aerial vehicles”. Technical Project. TU Delft, 2012.

[19] R. Nederlof. *Personal Communication*. May 2024.

[20] R. Nederlof et al. “Experimental Investigation of the Aerodynamic Performance of a Propeller at Positive and Negative Thrust and Power”. In: *AIAA Aviation Forum* (2022). URL: https://arc.aiaa.org/doi/epdf/10.2514/6.2022-3893.

[21] M. Simões. “Optimizing a Coaxial Propulsion System to a Quadcopter Cédric”. In: 2014. URL: https://api.semanticscholar.org/CorpusID:10956021.

[22] SAE Mobilus Academic Library. *Prediction Procedure for Near-Field and Far-Field Propeller Noise*. 2024. URL: https://www.sae.org/publications/technical-papers/content/AIR1407/ (visited on 06/12/2024).

[23] UAVHE. *Personal Communication*. June 2024.

[24] J. Gundlach. *Desinging Unmanned Aircraft Systems*. Aurora Flight Sciences, 2012. ISBN: 978-1-62410-261-5.

[25] A. Elham et al. *ADSEE II Lecture Notes*. Delft University of Technology, 2013.

[26] E. Torenbeek. *Synthesis of Subsonic Airplane Design*. English. 1st ed. Dordrecht: Springer, 1982.

[27] M. Tan (TA) I. Kroo (PI). *Applied Aerodynamics Lecture Notes*. Stanford University, 2023.

[28] J.D. Anderson. *Fundamentals of Aerodynamics*. 6th international ed. New York, United States: McGraw Hill Education, 2017.

[29] H. Masoumi and F. Jalili. “Inverse and direct optimization shape of airfoil using hybrid algorithm Big Bang-Big Crunch and Particle Swarm Optimization”. In: *Journal of Theoretical and Applied Mechanics* (2019). URL: https://api.semanticscholar.org/CorpusID:197411375.

[30] R. Budynas and K. Nisbett. *Mechanical Engineering Design*. McGraw Hill, 2019.

[31] T. H. G. Megson. *Aircraft Structures for Engineering Students*. English. Elsevier, 2021.

[32] N. Krajangsawasdi. *Structural Wing Sizing in Preliminary Aircraft Design*. 2016.

[33] M.F. Ashby. *Materials and the Environment Eco-Informed Material Choice*. Butterworth-Heinemann, 2013.

[34] M.H. Sadraey. *Aircraft design: A systems engineering approach*. Aerospace Series. Chichester: John Wiley and Sons, 2013. ISBN: 9781118352700. DOI: 10.1002/9781118352700. URL: http://dx.doi.org/10.1002/9781118352700.

[35] B. Litherland. *VSPAERO Basics*. 2024. URL: https://vspu.larc.nasa.gov/training-content/chapter-3-model-analysis-in-openvsp/vspaero-basics/#:~:text=VSPAERO%20is%20a%20potential%20flow,Dave%20Kinney%20at%20NASA%20Ames (visited on 06/11/2024).

[36] L. Payne. *VSPAERO VERIFICATION TESTING*. 2024. URL: https://dokumen.tips/documents/1-vspaero-verification-testing-17-empirical-systems-aerospace-inc-bertin-smith.html?page=1 (visited on 06/10/2024).

[37] K. Ju-Hoe and T. Takeshi. "OPENVSP BASED AERODYNAMIC DESIGN OPTIMIZATION TOOL BUILDING METHOD AND ITS APPLICATION TO TAILLESS UAV". In: *ICAS 2022* (2022).

[38] D. Scholz. *Aircraft Design Chapter 9: Empennage General Design*. Hamburg University of Applied Sciences, 2016.

[39] N.S. Currey. *Aircraft landing gear design : principles and practices*. 1988. URL: https://api.semanticscholar.org/CorpusID:107420191.

[40] G. Nugroho, Y.D. Hutagaol, and Z. Galih. "Aerodynamic Performance Analysis of VTOL Arm Configurations of a VTOL Plane UAV Using a Computational Fluid Dynamics Simulation". In: *Drones* 6.12 (2022). ISSN: 2504-446X. DOI: 10.3390/drones6120392. URL: https://www.mdpi.com/2504-446X/6/12/392.

[41] J. Roskam. *Airplane design. Pt. 3. Layout design of cockpit, fuselage, wing and empennage: cutaways and inboard profiles*. English. Ottawa, Kansas: Roskam Aviation and Engineering, 1985.

[42] McDonnel Douglas Corp. *USAF Stability and Control Datcom*. Air Force Flight Dyn. Lab., US Air Force., 1976.

[43] J. McDavid and B Kühner. "Empennage Sizing: The Tail Lever Arm as a Percentage of Fuselage Length Determined from Statistics". Technical Project. HAW-Hamburg, 2017.

[44] J.A. Mulder et al. *Flight Dynamics Lecture Notes*. Delft University of Technology, 2013.

[45] E. K. A. Gill, F. Oliviero, and B.V.S. Jyoti. *Systems Engineering & Aerospace Design Lecture Slides*. 2024.

[46] J. Murua et al. "T-Tail flutter: Potential-flow modelling and experimental validation". In: June 2013.

[47] J. Roskam. *Airplane design. Pt. 2. Preliminary configuration design and integration of the propulsion system*. English. Ottawa, Kansas: Roskam Aviation and Engineering, 1985.

[48] D. Ciliberti. "A new vertical tailplane design procedure through CFD". MA thesis. Università degli Studi di Napoli, Sept. 2012. DOI: 10.13140/2.1.1975.9367.

[49] J. Roskam. *Airplane design. Pt. 6. Preliminary calculation of aerodynamic, thrust and power characteristics*. English. Ottawa, Kansas: Roskam Aviation and Engineering, 1987.

[50] R.C. Struett. "Empennage Sizing and Aircraft Stability using Matlab". Technical Project. California Polytechnic State University, 2012.

[51] C.D. Perkins and R.E. Hage. *Airplane Performance, Stability and Control*. English. New York: Wiley, 1949. ISBN: 047168046X and 9780471680468.

[52] R.C. Hibbeler. *Mechanics of Materials*. 10th ed. in SI units. Harlow, United Kingdom: Pearson, 2017.

[53] M.F. Ashby, H. Shercliff, and D. Cebon. *Materials: engineering, science, processing and designs*. 4th ed. Oxford, United Kingdom: Butterworth-Heinemann, 2019.

[54] T.L. Lomax. *Structural Loads Analysis : Theory and Practice for Commercial Aircraft*. American Institute of Aeronautics and Astronautics, 1995. ISBN: 978-1-56347-114-8.

[55] Q. Bai and Y. Bai. *Subsea Pipeline Design, Analysis, and Installation*. Elsevier, 2014. ISBN: 978-0-12-386888-6.

[56] R. Burden, A. Burden, and D. Faires. *Numerical Analysis*. 10th ed. England: CENGAGE learning, 2016.

[57] A. Essari. "ESTIMATION OF EMPENNAGE DESIGN WEIGHT IN CONCEPTUAL DESIGN PHASE FOR TACTICAL UAVs". In: Nov. 2018, pp. 675–685. DOI: 10.21467/proceedings.4.35.

[58] M. Abdulla. "Prediction of Wing Downwash Using CFD". In: *INCAS Bulletin* 7 (June 2015), pp. 6–07. DOI: 10.13111/2066-8201.2015.7.2.10.

[59] Operational Test The Office of the Director and Evaluation. *MQ-9 Reaper Armed Unmanned Aircraft System (UAS)*.

[60] *STANAG 4671 Unmanned Aerial Vehicles Systems Airworthiness Requirements (USAR)*. Standard. Brussels: NATO Standardization Agency, May 2007.

[61] *Design Dive Speed*. Tech. rep. Washington, D.C.: U.S. Department of Transportation, Federal Aviation Administration, Mar. 1997.

[62] F. Mahdavian et al. "Communication blackouts in power outages: Findings from scenario exercises in Germany and France". In: *International Journal*

of Disaster Risk Reduction 46 (2020), p. 101628. ISSN: 2212-4209. DOI: https://doi.org/10.1016/j.ijdrr.2020.101628. URL: https://www.sciencedirect.com/science/article/pii/S2212420920301941.

[63] F. Serinaldi et al. “Flood propagation and duration in large river basins: a data-driven analysis for reinsurance purposes”. In: *Natural Hazards* 94 (Oct. 2018), pp. 71–92. DOI: 10.1007/s11069-018-3374-0.

[64] W.A. Doerry. “Earth Curvature and Atmospheric Refraction Effects on Radar Signal Propagation”. In: *Sandia National Laboratories* 10690 (Jan. 2013).

[65] J.S. Seybold. *Introduction to RF Propagation*. 1th ed. Hoboken, New Jersey: Wiley, 2005.

[66] D. Dexheimer et al. “Tethered Balloon System (TBS) Instrument Handbook”. In: *U.S. Department of Energy* 206 (Mar. 2024).

[67] A. Kurian. “Latency Analysis and Reduction in a 4G Network”. MA thesis. Delft University of Technology, 2018.

[68] J.C.W. Adamse. “UAV deployment for flood-resilient mobile networks: a data-driven analysis for the Netherlands”. Bachelor’s Thesis. University of Twente, 2023.

[69] L.J. Ippolito. “Attenuation by Atmospheric Gases”. In: *Radiowave Propagation in Satellite Communications*. Dordrecht: Springer Netherlands, 1986, pp. 25–37. ISBN: 978-94-011-7027-7. DOI: 10.1007/978-94-011-7027-7_3. URL: https://doi.org/10.1007/978-94-011-7027-7_3.

[70] S. de Vries. “UAVs and Control Delays”. In: *TNO-DV3* (Sept. 2005), p. 52.

[71] D. Thirtyacre. “The Effects of Remotely Piloted Aircraft Command and Control Latency during Within-Visual-Range Air-To-Air Combat”. MA thesis. Embry-Riddle Aeronautical University, 2021.

[72] United Nations. *Resolution A/RES/70/1: The 2030 Agenda for Sustainable Development*. 2015.

[73] *Environmental Management Systems*. Standard. International Organization for Standardization, 2015.

[74] *Destination Green. The Next Chapter*. Standard. International Civil Aviation Organization, 2019.

[75] D. Wang et al. “Evaluation of a New Lightweight UAV-Borne Topo-Bathymetric LiDAR for Shallow Water Bathymetry and Object Detection”. In: *Sensors* 22.4 (2022). ISSN: 1424-8220. DOI: 10.3390/s22041379. URL: https://www.mdpi.com/1424-8220/22/4/1379.

[76] D. Raymer. *Aircraft Design: A Conceptual Approach, Sixth Edition*. Sept. 2018. ISBN: 978-1-62410-490-9. DOI: 10.2514/4.104909.

[77] F. Pollet et al. “A common framework for the design optimization of fixed-wing, multicopter and VTOL UAV configurations”. In: Sept. 2022.

[78] *Range and Endurance*. Apr. 2003.